



Abschlußbericht

SO 167 - LOUISVILLE

Louisville Rücken: Dynamik und Magmatismus eines Mantelplumes
und sein Einfluß auf die Tonga – Kermadec Subduktionszone

Louisville Ridge: Dynamics and Magmatism of a Mantle Plume and its
Influence on the Tonga – Kermadec Subduction System

Suva, Fiji – Wellington, New Zealand

12 October – 02 December 2002

BMBF 03G0167 A/B

Projektleiter:

Prof. P. Stoffers, Prof. P. Herzig

SO-167 ABSCHLUßBERICHT

INHALTSVERZEICHNIS

AUFGABENSTELLUNG UND ZUSAMMENFASSUNG DER ERGEBNISSE

EINGEREICHTE PUBLIKATIONEN

1. Hydrothermal alteration associated with shallow submarine volcanoes of the Tonga island arc, SW-Pacific
U. Schwarz-Schampera, P.M. Herzig, H.L. Gibson, T.J. Worthington, P. Stoffers
Economic Geology
2. Hydrothermal activity and magma genesis along a propagating back-arc basin: the Valu Fa Ridge (southern Lau Basin)
S. Fretzdorff, U. Schwarz-Schampera, H. Gibson, C.-D. Garbe-Schönberg, F. Hauff, P. Stoffers
Journal of Geophysical Research
3. Osborn Trough: structure, geochemistry and implications of a mid-Cretaceous paleosspreading center in the south Pacific
T.J. Worthington, R. Hekinian, P. Stoffers, T. Kuhn, F. Hauff
Earth and Planetary Science Letters

PUBLIKATIONEN IN VORBEREITUNG

4. Louisville Ridge: characterization of alkaline lavas from a mantle plume and their eruption through lithosphere of increasing age
T.J. Worthington, R. Hekinian, P. Stoffers, C.-D. Garbe-Schönberg, F. Hauff
Earth and Planetary Science Letters

KONFERENZBEITRÄGE

5. Forschungsfahrt SO-167 LOUISVILLE: Erste Ergebnisse
P. Stoffers, T. Worthington, Shipboard Scientific Party
SONNE Statusseminar, Hamburg 2003
6. Mineralisationsprozesse und ihre zeitliche Variabilität im Bereich des Tonga Inselbogens und des südlichen Lau Beckes: Erste Ergebnisse der Forschungsfahrt SO-167 LOUISVILLE
U. Schwarz-Schampera, P. Stoffers, R. Hekinian, H. Gibson, P. Herzig, T. Kuhn, S. Fretzdorff, A. Kindermann, K. Schreiber
SONNE Statusseminar, Hamburg 2003

7. Magmatically induced hydrothermal processes and their temporal variability in the southern Lau Basin and the nearby Tonga island arc, SW-Pacific
U. Schwarz-Schampera, H. Gibson, P. Herzig, P. Stoffers
GAC-MAC, Vancouver 2003
8. Auriferous pyrite mineralization in the Tonga island arc, SW-Pacific: first evidence for shallow submarine hydrothermal activity
U. Schwarz-Schampera, P.M. Herzig, H. Gibson, P. Stoffers
SGA, Athens 2003
9. Louisville Ridge and the south Tonga arc: first results
T. Worthington, P. Stoffers, C. Timm, M. Zimmerer, D. Garbe-Schönberg
State of the Arc 3, Mt Hood (USA) 2003
10. Hydrothermal processes in island arcs: new evidences from the Tonga arc
U. Schwarz-Schampera, H. Gibson, P. Stoffers
ODP, Bremen 2004
11. First evidence for shallow submarine hydrothermal activity in the Tonga island arc, SW-Pacific
U. Schwarz-Schampera, P. Stoffers, H. Gibson, P.M. Herzig
Soundings Newsletter, 2004
12. Effects of subducting the Louisville Ridge and Osbourn Trough beneath the south Tonga arc
T. Worthington, P. Stoffers, C. Timm, M. Zimmerer, D. Garbe-Schönberg
Goldschmidt, Copenhagen 2004
13. Hf-Nd isotope characterization of the Tonga-Kermadec sub-arc mantle
T.J. Worthington, C. Münker, P. Stoffers, J.A. Gamble, I.C. Wright
AGU Fall Meeting, San Francisco 2004
14. Mineralisationsprozesse und ihre zeitliche Variabilität im Bereich des südlichen Tonga Inselbogens: Ergebnisse der Forschungsfahrt SO-167 LOUISVILLE
U. Schwarz-Schampera, P. Stoffers, K. Schreiber, S. Fretzdorff, H. Gibson, P. Herzig, T. Kuhn, R. Hekinian, T. Worthington
SONNE Statusseminar, Warnemünde 2005
15. Magmengenetische Prozesse entlang des Valu Fa Rückens, Lau Becken, SW-Pazifik (SO 167)
S. Fretzdorff, P. Stoffers, U. Schwarz-Schampera, T. Worthington
SONNE Statusseminar, Warnemünde 2005
16. Der südliche Tonga Inselbogen: Einfluss der Subduktion des Louisville Rückens und Osbourn Troughs auf den Magmatismus
T.J. Worthington, P. Stoffers, C. Timm, M. Zimmerer, C.D. Garbe-Schönberg, S. Fretzdorff
SONNE Statusseminar, Warnemünde 2005
17. Charakterisierung des Tonga-Kermadec Mantelkeils mit Hf-Nd Isotopen
T.J. Worthington, C. Münker, P. Stoffers, J.A. Gamble, I.C. Wright

SONNE Statusseminar, Warnemünde 2005

18. Shallow submarine hydrothermal activity in the Tonga island arc, SW-Pacific
U. Schwarz-Schampera, P. Stoffers
DMG, Aachen 2005

DIPLOMARBEIT

19. Submarine weathering of vesicular lavas from the Louisville Ridge
N. Bigalke
20. Petrology of the Ata Island Area, South Tonga
C. Timm
21. Geochemie und Mineralogie der südlichen Tonga-Vulkane
M. Zimmerer

AUFGABENSTELLUNG UND ZUSAMMENFASSUNG DER ERGEBNISSE

Aufgabenstellung:

Die Beprobung und Untersuchung des südlichen Tonga-Inselbogens, des Valu Fa Rückens, des Osbourn Trough und des Louisville Rückens wurden während der Forschungskampagne SO 167 durchgeführt.

Die Hauptziele des Projektes waren:

- Untersuchung der Beziehung zwischen Tektonik, Magmatismus und Hydrothermalismus im Bereich des Valu Fa Rückens und der südlichen submarinen Tonga Inselbogenvulkane
- Klärung des Ursprungs und Alters des Osbourn- Trough
- Die geochemische Charakterisierung der Gesteine des Louisville Rückens
- Klärung der Frage, ob eine geochemische Signatur des subduzierten Louisville Rückens in den Inselbogenmagmen zu finden ist
- Kartierung der submarinen Vulkane des südlichen Tonga-Inselbogens

Voraussetzungen, unter denen das Vorhaben durchgeführt wurde:

Da die Arbeitsgebiete in der EEZ von Tonga als auch Neuseeland lagen, war die Arbeitsgenehmigung dieser Staaten eine wichtige Voraussetzung für die Durchführung der Forschungskampagne. Mit der Arbeitserlaubnis war die Auflage verbunden, Information über die Ergebnisse der Reise (Kartenmaterial, Fahrtbericht) weiterzureichen.

Planung und Ablauf des Vorhabens

Die Forschungsfahrt SO-167 fand im Zeitraum 12. Oktober 2002 – 02. Dezember 2002 statt. Ausgangs- und Endhafen waren Suva, Fiji und Wellington, Neuseeland. Insgesamt wurden 130 Dredge-, 9 TV-Greifer-, 8 OFOS- und 29 Plankton-Stationen durchgeführt.

Zusammenarbeit mit anderen Stellen

Die SO-167 Reise war ein internationales Projekt, an dem neben den Universitäten Kiel und Freiberg, das Senckenberg Institut in Frankfurt, das National Institute of Water and Atmospheric Research, Wellington, Neuseeland, die Laurentian and Toronto University, Canada und das Ministry of Lands, Survey and Natural Resources, Tonga beteiligt waren.

Ergebnisse:

Nachfolgend wird eine kurze Zusammenfassung der wichtigsten bisher erzielten Ergebnisse gegeben. Die entsprechenden Publikationen und Tagungsbeiträge sind im Anhang wiedergegeben.

1) Hydrothermale Alteration und Mineralisation im Topbereich zweier flachmariner Vulkane des südlichen Tonga Inselbogens, SW-Pazifik

Im südlichen Tonga Inselbogen wurden Proben intensiv alterierter vulkanoklastischer Basalte und Andesite von zwei flachmarinen Vulkanen in Wassertiefen zwischen 450 und 200 m gewonnen. Die hydrothermal alterierten vulkanischen Gesteine sind mit Kalderastrukturen und neovulkanischen Basaltkegeln im Topbereich der beiden Vulkane assoziiert. Die intensive argillitische Alteration und Silifizierung sind das Ergebnis zirkulierender säureproduzierender, schwefelreicher Gase und kieselsäurereicher Fluide. Die Alteration ist durch das Auftreten von Natroalunit, Illit-Kaolinit, polymorpher Kieselsäure, rhombischem Kalifeldspat, Anhydrit, Baryt und gediegen Schwefel gekennzeichnet. In den alterierten Gesteinen treten darüber hinaus disseminierte Sulfide (bis zu 5 Vol.%) auf, darunter Pyrit, Markasit, Chalkopyrit, Arsenopyrit, Pyrrhotin, Isocubanit, Realgar, Stibnit sowie Magnetit, Hämatit, Rutil und gediegen Gold. Koexistierender Pyrit, Magnetit und Hämatit, niedrige Buntmetallgehalte und leichte Schwefelisotopenverhältnisse der Sulfide unterscheiden sich deutlich von typischen Hydrothermalsystemen an mittelozeanischen Rücken und kennzeichnen vergleichsweise oxidierende Fluide, wie sie typisch für Inselbogenvulkane sind. Die plattige Ausbildung des Natroalunits und charakteristische Schwefelisotopenverhältnisse koexistierender Alunit-Pyrit-Verwachsungen weisen auf die Freisetzung und Disproportionierung von magmatischem SO₂ hin. Die Art der Alteration und Mineralisation an beiden Vulkanen deutet auf ein hohes Potenzial für Cu und Au Mineralisationen ähnlich den Vorkommen in anderen flachmarinen Inselbögen hin.

2) Magmengenese und hydrothermale Aktivität entlang des Valu Fa Rückens (südliches Lau Becken)

Der Valu Fa Rücken, die südliche Fortsetzung des Lau Beckens, ist ca. 165 km lang und 5 bis 6 km breit. Südlich von 22°45'S propagiert die Spreizungsachse in miozäne Inselbogenkruste. Während der Forschungsfahrt SO 167 wurde die Spreizungsachse des Valu Fa Rückens zwischen 22°12'S und 22°52'S eingehend untersucht. Bathymetrische Aufzeichnungen sowie eine detaillierte Probenahme wurden entlang und südlich der aktiven Spreizungsachse durchgeführt. Ziel war es, hydrothermale und vulkanische Aktivität zu lokalisieren und zu beproben. Die Untersuchungen der vulkanischen Gesteine konzentrieren sich im Wesentlichen auf magmengenetische Fragestellungen. Dabei geben die Haupt- und Spurenelementzusammensetzungen sowie die Isotopenverhältnisse (Sr, Nd, Pb) der Laven Einblicke in fraktionelle Kristallisations- und Aufschmelzprozesse sowie die Zusammensetzung der Mantelquelle des südlichen Valu Fa Rückens. Des Weiteren wurde der Einfluss der Subduktionsvorgänge auf die Laven der Valu Fa Spreizungszone untersucht, insbesondere welche Komponenten aus der subduzierten Platte in den Mantelkeil transportiert werden. Im Bereich von 22°25'S sind Laven mit SiO₂ Gehalten von bis zu 72 Gew.% eruptiert. Bisher ist das Auftreten von solch hoch-differenzierten Gesteinen einzigartig und unterstützt die geophysikalischen Beobachtungen, dass eine Magmenkammer im zentralen Bereich des Valu Fa Rückens vorhanden ist, in der die Magmen unter intensiven fraktionellen

Kristallisationsprozessen generiert worden sind. Niedrige $\text{Na}_{8,0}$ -Gehalte weisen auf einen hohen Aufschmelzgrad der Proben hin. Der $\text{Na}_{8,0}$ -Gehalt korreliert mit der Abnahme der Entfernung zum Inselbogen in südlicher Richtung, was bedeutet, dass der Aufschmelzgrad am südlichen Ende der Spreizungsachse erheblich höher ist als z.B. im Bereich des Vai Lili Hydrothermalfeldes. Diese Beobachtung wird durch die Variation der Nb/Yb Verhältnisse entlang des back-arc Rückens unterstützt. Aufschmelzgrade der Valu Fa Laven liegen deutlich höher als N-MORB - nach Modellierungsberechnungen bei ca. 20% bis Hine Hina und ca. 25% unterhalb des südlichsten Segments. Ce/Pb Verhältnisse nehmen entlang der Spreizungsachse in südlicher Richtung ab, was auf einen Fluideintrag aus der subduzierten Platte in die Magmenquelle der Laven mit abnehmender Distanz zum Inselbogen hinweist. Es handelt sich hauptsächlich um Fluide aus der alterierten Kruste und/oder Sedimentfluide, ein geringer Anteil einer Sedimentschmelze in der Magmenquelle scheint aufgrund erhöhter Th/Nb Verhältnisse im südlichsten Bereich der Spreizungsachse vorhanden zu sein. Die neu gewonnenen Proben weisen die charakteristischen Pb-Isotopenverhältnisse eines pazifischen MORBs auf und liegen grösstenteils im geochemischen Feld des zentralen Tonga Inselbogens und den Laven der ODP Bohrung 834 & 839 westlich des Lau Beckens. Der geochemische Einfluss indischer MORBs reicht somit wahrscheinlich vom zentralen Lau Becken bis nördlich des Vai Lili Hydrothermalfeldes und wird in diesem Bereich von pazifischem MORB "verdrängt". Entlang des gesamten Untersuchungsgebietes wurde kein aktiver Hydrothermalismus nachgewiesen, lediglich diffuse niedrig-temperierte Quellaustritte sind im Bereich des Vai Lili Hydrothermalfeldes zu beobachten.

3) Osbourn Trough: Morphologie und Geochemie einer kretazischen Spreizungsachse im Südpazifik

Während der SO 167 Expedition wurde ein 145 km breiter Streifen des ca. 900 km langen Osbourn Troughs detailliert kartiert. Die bathymetrische Karte zeigt drei Segmente, die durch 23-35 km breite, zur Achse senkrecht streichende, Becken versetzt sind. Die Achsen dieser Segmente sind 10 bis 15 km breit und sind durch sogenannte *inside corner highs*, die 1000 – 1200m herausragen, gekennzeichnet. Die steilen Hänge der verschiedenen Segmente konnten erfolgreich beprobt werden. Die Dredgeproben bestehen hauptsächlich aus vulkanischen Brekzien, die mit dicken Mn-Fe Krusten überzogen sind. Lavafragmente wurden herauspräpariert und analysiert. Durch intensive Seewasseralteration sind die Na_2O -, K_2O - Gehalte und die leichten seltenen Erdelemente (Ce ausgenommen) der Proben erhöht. Die geochemische Signatur der immobilen Elemente zeigt allerdings die primäre Zusammensetzung der Laven, die mit der von mittelozeanischen Rückenbasalten (MORB) zu vergleichen ist. Dabei zeigen die radiogenen Isotopenverhältnisse, dass die Osbourn Trough Proben eine pazifische MORB-Mantelsignatur aufweisen. Die Morphologie sowie die Geochemie der Osbourn Trough Laven deuten daraufhin, dass es sich bei dieser Struktur um eine Paläo-Spreizungsachse aus der mittleren Kreidezeit handelt. Dies würde bedeuten, dass das Manihiki und Hikurangi Plateau früher zusammenhängend war und eine große Flutbasaltprovinz gebildet haben. Beide Regionen liegen heute in gleicher Entfernung zum Osbourn Trough. Der Beginn der Spreizungsaktivität entlang des Osbourn Troughs fällt zusammen mit dem Ende der Spreizungsbewegungen des Pazifik – Phoenix Rückens und des Auseinanderbrechens des Manihiki Plateaus vor ca. 118 Ma. Die Spreizung entlang des Osbourn Troughs kam wahrscheinlich zum Stillstand, als das Hikurangi Plateau mit der südwärts gerichteten Subduktion des Chatham Rise (östliches Neuseeland und Teil des Gondwana Kontinentalrandes) vor ca. 86 Ma kollidierte.

4) Louisville Rücken: Geochemische Charakterisierung von Alkali Mantelplume Laven

Im Rahmen der Expedition SO 167 konnten elf Seamounts des Louisville Rückens zwischen dem Tonga-Kermadec Trench (Osborn Seamount, 78Ma) und ein großer Vulkan bei 168°W (45Ma) beprobt werden. Die Probenahme mittels Dredgen wurde jeweils in Richtung der Hauptschildbildungsphasen der Vulkanzentren durchgeführt. Einige der Laven weisen marine Alterationserscheinungen auf. Glaskruste und Olivinkristalle sind durch sekundäre Phasen ersetzt worden und Hohlräume mit Kalzit, Phillipsit und Tonmineralen ausgefüllt, Plagioklas- und Klinopyroxenkristalle sind unbeeinflusst. Bei den beprobten Laven handelt es sich hauptsächlich um Basanite und Alkalibasalte, Anzeichen einer tholeiitischen Schildbildungsphase sind nicht vorhanden. Inkompatible Elementverhältnisse der Proben zeigen, dass mit abnehmender partieller Schmelzbildung der Magmen das Alter der Lithosphäre über dem Louisville Plume zunimmt bzw. die Entfernung vom Tonga – Kermadec Trench in Richtung Osten (Osborn seamount: ~10 Ma; 168°W: ~55 Ma). Ein Trend ist außerdem in den radiogenen Isotopenverhältnissen der Proben zu beobachten. Nd und Pb Isotopenverhältnisse nehmen mit zunehmender Entfernung vom Tonga - Kermadec Trench ab, wobei $^{87}\text{Sr}/^{86}\text{Sr}$ ansteigt. Seamounts, die jünger als 60 Ma sind, weisen im Vergleich zu den älteren Vulkanzentren eine größere Variation der radiogenen Isotopenverhältnisse auf. Die Louisville Laven liegen innerhalb des globalen MORB Feldes angrenzend an FOZO, wobei alle Laven radiogener sind als die unterliegende Lithosphäre. Es können keine HIMU, EM-I oder EM II Signaturen in den Proben nachgewiesen werden.

5) Der südliche Tonga Inselbogen: Einfluss der Subduktion des Louisville Rückens und Osborn Troughs auf den Magmatismus

Die Subduktion der Plume-Spur des Louisville Rückens sowie des spätkretazischen Spreizungszentrums des Osborn Troughs findet unter einem 450 km langen Segment des südlichen Tonga Inselbogens statt. Der überwiegend submarine südliche Tonga Inselbogen war vorher nicht untersucht, und nur eine vulkanische Insel (Ata) tritt dort auf. Vermessungen und Beprobungen während der Ausfahrt SO167 des FS SONNE zeigen eine durchgehende vulkanische Front mit einer Breite von 10 bis 15 km bestehend aus 27 aktiven Stratovulkanen mit typischen basalen Durchmessern von 10 bis 25 km und Höhen von 1 bis 2 km. Die Vulkanfront ist nur in der Nähe von Ata gestört, wo zehn größere und zahlreiche kleinere Vulkane die Breite auf 50 km erweitern. Die größere Breite reflektiert eine transiente 40 km westwärts gerichtete Migration der Inselbogenfront und verstärkten Vulkanismus durch die Entwässerung des Louisville Rückens unter dem Inselbogen.

Die Vulkane des südlichen Tonga Inselbogens zeigen deutlich stärkere geochemische und isotopische Variationen als die besser bekannten subaerischen Vulkane des zentralen Tonga Bogens. Mg-reiche Basalte, Andesite und Rhyodacite treten in Zusammenhang mit Calderen auf (oft >6 km im Durchmesser). Die Laven definieren eine niedrig-K Suite mit starker Anreicherung der fluid-mobilen Elemente und extremer Verarmung der fluid-immobilen Elemente relativ zu MORB [z.B. $(\text{La}/\text{Yb})_{\text{N}} < 1,1$; Nb/Yb 0,09-0,27]. Spezifische Inkompatiblenverhältnisse weisen Unterschiede zwischen den Laven verschiedener Vulkane auf und deuten eine zufällige Verteilung in diesem Segment des Inselbogens an. Diese Charakteristika sind langlebig und können mit einer Interaktion des aufsteigenden Magmas mit der Lithosphäre je nach Lage des Vulkans erklärt werden. Damit unterstützen diese Daten Modelle einer signifikanten Überprägung von ozeanischen Magmen in der Lithosphäre.

Die Subduktion des Louisville Rückens unter den Inselbogen führt zu einer Eruption von Laven mit $(\text{La}/\text{Yb})_{\text{N}} > 1,1$, höheren Th/U und anderen Anomalien vor und während der westlich gerichteten Migration der vulkanischen Front. Im Gegensatz dazu haben die Laven,

die während der östlich gerichteten Rückkehr der Front eruptieren, relativ normale Zusammensetzungen und deuten damit eine schnelle Durchwanderung der Fluide durch den Mantelkeil an. Vulkane über dem subduzierten Osborn Trough zwischen 23,5 und 24,7°S weisen einen markanten Wechsel von Calderen zu Diatrem-ähnlichen Kratern mit Tiefen bis zu 1,1 km auf. Die damit zusammenhängenden Wechsel der magmatischen Volatilgehalte, die diese Eruptionen auslösen, reflektieren vermutlich die Entwässerung eines stark serpentinisierten Mantels des Osborn Troughs.

6) Charakterisierung des Tonga-Kermadec Mantelkeils mit Hf-Nd Isotopen

Die Magmenbildung an Subduktionszonen wird wesentlich durch den Eintrag von Fluiden und/oder Schmelze aus der abtauchenden Platte beeinflusst. Der thermische, physikalische und chemische Zustand der abtauchenden Platte und des Bereichs zwischen dieser Platte und dem Mantelkeil unter der vulkanischen Front ist unbekannt, so dass die Anwendung von experimentellen Daten zur Entwässerung und Aufschmelzung sowie zur Massenbilanzierung unzulänglich sind. Die Bestimmung der Zusammensetzung des Mantelkeils ist daher wichtig, um die vorgeschlagenen Modelle zu überprüfen. Einfache Modelle der Konvektion im Mantelkeil vom Backarc zur Front des Inselbogens sind unvollständig und erklären z.B. nicht, warum es keine Korrelation zwischen der Verarmung des Mantelkeils und der Backarc Breite oder Dehnungsrate gibt. Zur Untersuchung der Dynamik der Konvektion im Mantelkeil wurden Hf-Nd Isotopenverhältnisse an Laven eines Großteils des Tonga-Kermadec Inselbogens (Proben von SO167 sowie älterer Fahrten) durchgeführt. Diese Elemente haben den Vorteil, dass sie fluidimmobil sind (Hf stark und Nd moderat) relativ zu den sehr mobilen und daher hauptsächlich aus der subduzierten Platte stammenden Elementen Sr und Pb. Vorherige Sr-Nd-Pb Isotopenstudien von Lau Backarc Laven zeigten, dass Indischer MORB Mantel (IMM) Pazifischen MORB Mantel (PMM) während der Öffnung des Beckens ersetzt hat und nun unter dem zentralen Tonga Inselbogen liegt. Im Gegensatz dazu liegt PMM unter dem Valu Fa Rücken und unter dem Havre Trough, so dass ein Übergang von IMM zu PMM unter dem südlichen Tonga Inselbogen vermutet wurde.

Hf Isotopenverhältnisse der Tonga-Kermadec Inselbogenlaven liegen zwischen +12 und +16 ϵ -Einheiten und sind 1-2 ϵ -Einheiten niedriger als die des Lau Beckens. Die Tonga Laven liegen generell im oberen Teil dieses Bereichs, während die Kermadec Laven stärker variieren. Alle Tonga-Kermadec Laven fallen in das Feld des IMM in ϵ Hf und ϵ Nd und zeigen, dass IMM-ähnlicher Mantel unter dem gesamten Inselbogen zwischen 15 und 35°S liegt. Dieses Ergebnis wird weiter verstärkt durch die Subtraktion der 20 bis 40% Nd, die aus der subduzierten Platte mit PMM Zusammensetzung stammen. ϵ Hf zeigt eine schwache negative Korrelation mit Hf/Yb und zunehmender geographischer Breite, die mit einer schwachen Hf Zufuhr aus subduzierten vulkanischen Sedimenten unter den Kermadec Inselbogen erklärt werden kann. Unsere Daten liefern keinen Hinweis auf eine Schmelze aus der subduzierten Platte, obwohl die Platte unter dem südlichen Kermadec Inselbogen wärmer ist wegen der langsameren Subduktion. Das Auftreten von IMM unter dem Tonga-Kermadec Inselbogen, aber PMM unter dem südlichen Lau Becken und Havre Trough, ist im Widerspruch zu einem einfachen südostwärts gerichteten Einstrom von IMM in das Tonga-Kermadec System während der Öffnung des Lau-Havre Backarc Beckens. Stattdessen scheinen die Verteilung der Grenze zwischen IMM und PMM, die Dynamik im Mantelkeil und die Herkunft der IMM-ähnlichen Signatur wesentlich komplexer.

Nutzen und Verwertbarkeit der Ergebnisse

Die sehr erfolgreiche Forschungskampagne hat international ein großes Echo gefunden und hat einen wichtigen Beitrag zur aktuellen Diskussion über Mantelplumes und Subduktionsprozesse.

Die durch die SO-167 erzielten wissenschaftlichen Ergebnisse sind eingeflossen in den internationalen IODP Bohrvorschlag 636, IODP Drilling of the Louisville Seamount Trail: Implications for geodynamic mantle flow models and the geochemical evolution of primary hotspots.

Darüber hinaus bilden die Daten der SO-167 eine wichtige Grundlage für eine vom Scripps Institute of Oceanography Anfang 2006 im Bereich der Louisville-Kette geplante Forschungsfahrt

Die Entdeckung und detaillierte Kartierung von großen, relativ flachen submarinen seamounts im Bereich der Tonga Inseln ist für die Fischerei des Inselstaates von Bedeutung.

Ferner sind unsere Daten von großem Interesse für LINZ (Lands Information New Zealand) für die Frage der Ausdehnung der EEZ Neuseelands.

**Hydrothermal Alteration Associated with Shallow Submarine Volcanoes
of the Tonga Island Arc, SW-Pacific**

Ulrich Schwarz-Schampera

*Ore Deposit Research Group, Federal Institute for Geosciences and Natural Resources,
30655 Hannover, Germany*

Peter M. Herzig

*Freiberg University of Mining and Technology, Department of Economic Geology and Leibniz
Laboratory for Applied Marine Research, 09596 Freiberg, Germany*

Harold L. Gibson

Department of Geology, Laurentian University, Sudbury, Ontario, Canada P3E 2C6

Tim J. Worthington and Peter Stoffers

Department of Geosciences, Christian Albrechts University Kiel, 24118 Kiel, Germany

Abstract

Samples of intensely altered volcanoclastic basalt and andesite have been recovered from two shallow submarine arc volcanoes of the Tonga island arc in water depths between 450 and 200 m. The hydrothermally altered volcanic rocks are associated with caldera structures and neovolcanic cones within the upper parts of the two volcanoes. The intense argillic alteration and silicification are products of acid-generating sulfurous gases and siliceous fluids associated with hydrothermal activity on the volcanoes. The alteration consists of natroalunite, illite-kaolinite, silica polymorphs, rhombic K-feldspar, anhydrite, barite, and native sulfur. Disseminated sulfides (up to 5 vol.%) occur throughout the altered rocks and include pyrite, marcasite, chalcopyrite, arsenopyrite, pyrrhotite, intermediate solid solution (iss), realgar and stibnite together with magnetite, hematite, rutile and native Au. The coexisting pyrite, magnetite, and hematite, low base metal contents, and the low sulphur isotope values for the sulfides contrast with typical mid-ocean ridge hydrothermal systems and indicate relatively oxidized fluids typical of arc volcanoes. The platy habit of natroalunite and sulfur isotope ratios of coexisting alunite and pyrite are consistent with possible derivation from magmatic SO₂. The style of alteration at both volcanoes also may indicate a potential for Cu and Au mineralization similar to that observed at other shallow submarine arcs.

Introduction

During cruise SO-167 of the German *R/V Sonne*, 27 large active or recently active submarine volcanoes along the southern Tonga island arc system were mapped and sampled for the first time (Stoffers et al., 2003; Schwarz-Schampera et al., 2003, Fig. 1A). On two of the volcanoes (Efuefu sites, Uli'uli site), extensive hydrothermal alteration was found in volcanic rocks recovered from water depths of 450 m and 200. At both locations, the volcanic rocks consist of young and glassy lapilli- to ash-sized basaltic to andesitic volcanoclastic scoria. Altered volcanic rocks with fine-grained disseminated sulfides were dredged at three locations from the Efuefu (Tongan for "ashes") site at Volcano 1, one at a neovolcanic scoria cone at the western rim of the central caldera, one on the flank of the volcano outside the caldera, and one at the northern inner caldera wall (Fig. 1B, C). Samples of hydrothermally altered volcanic rock from the Uli'uli (Tongan for "black") site at Volcano 19 are associated with a neovolcanic cone and explosion crater in the central part of an older caldera (Fig. 1D, E). This contribution documents the main features of hydrothermal alteration and mineralization at the two volcanoes.

Regional Geological Setting

The Tonga trench is a type example of an immature, intra-oceanic, extension-dominated and non-accretionary convergent margin where Pacific plate lithosphere is subducted beneath a volcanic island arc chain (Karig, 1970; Hawkins, 1974; Gill, 1976; Tappin et al., 1994). Relative plate convergence is at $\sim 290^\circ$ and subduction is presently near perpendicular to the trench at a rate of about 16 cm/year (including an 8 cm/year opening rate in the Lau basin; Pelletier and Louat, 1989; DeMets et al., 1990). Along its southern end, at approximately 26°S , the trench is impinged upon by the Louisville Ridge, a NNW-trending chain of hotspot-related guyots and seamounts on the Pacific Plate (Dupont and Herzer, 1985; Lonsdale, 1986). The trend of the Louisville Ridge and the convergence direction of the Tonga trench are oblique. As a consequence, the collision zone and subduction of this aseismic ridge has progressively moved southwards along the Tongan trench during the past ~ 5 my (Yan and Kroenke, 1993) at a rate of approximately 18 cm/year (Lonsdale, 1986; MacLeod, 1994, 1996). This rate is roughly equivalent to the rate of southward propagation of the Eastern Lau Spreading Center/Valu Fa Ridge within the Lau back-arc basin (Parson and Hawkins, 1994). The effects of collision upon the trench are evident near 26°S , which also marks the boundary between the Tonga and Kermadec forearcs. In the vicinity of the collision zone near 26°S , seismicity and volcanic activity are virtually absent, and the trench axis is unusually shallow, with a maximum depth of less than 6,000 m (Dupont and Herzer, 1985).

Active arc volcanism is occurring along the Tofua volcanic arc, located on the western edge of the shallow forearc platform of the Tonga ridge. The actual Tonga island arc includes two

chains of islands parallel to the trench, separated from each other by the deep, sedimented Tofua Trough (Raitt et al., 1955). The eastern chain, the Tonga ridge, is part of a remnant arc complex, split in the late Miocene to form the active Lau back-arc basin (Karig, 1970; Parson et al., 1992) and includes extinct, coralline-capped Eocene to Miocene volcanic islands. The western chain, the Tofua arc, comprises active submarine and subaerial volcanoes erupting basalt, basaltic andesites, and dacites (e.g., Ewart et al., 1977). West of the Tofua Arc lies the extensional and southward propagating Lau basin, which separates the Tofua volcanic arc from the other half of the remnant arc, the volcanic Lau ridge (Cole et al., 1990). The Tonga arc has existed since Eocene time when it formed as part of the ancient Melanesian arc, which included fragments of what are now the Fiji, Lau, Tonga, and New Hebrides arcs. The west-dipping subduction that built the Melanesian arc was initiated sometime after the early Eocene (Herzer and Exon, 1985). Volcanism in the Tonga system continued through the Miocene along the Lau ridge. Opening of the Lau basin had started by at least 7.0 Ma (Parson et al., 1992), split the Lau ridge from the Tonga platform and led to the development of the presently active Tofua arc. During the rifting and opening of the Lau basin, the new Tonga ('Tofua') arc developed on the trench side of the basin on rifted blocks of the Lau ridge arc. Activity dates from ~ 3.0 Ma (middle Pliocene; Tappin et al., 1994), although the Tofua arc may have initiated earlier further north and propagated south in advance of the back-arc spreading centers (Parson and Hawkins, 1994). The Lau basin has a triangular shape as a consequence of the eastwards clockwise rotation of the Tonga ridge as the basin opened (MacLeod, 1994; Sager et al., 1994; Olbertz et al., 1997).

Arc Volcanoes and Associated Hydrothermal Sites

First detailed mapping and sampling of 27 volcanoes of the southern Tonga arc were carried out for this study from the *R/V Sonne* during October/November 2002 (Stoffers et al., 2003). Mapping and sampling were conducted by the SIMRAD swath bathymetry system on board *Sonne* and by dredging. Two areas of shallow submarine hydrothermal activity (Efuefu sites, Uli'uli site) were discovered at two island arc volcanoes (volcanoes 1 and 19). Both volcanoes form part of the southern Tonga frontal arc south of 21° S (Fig. 1A). These volcanoes lie west of the Tonga plateau and post-date the earliest phases of Lau back-arc rifting (Parson et al., 1992; Tappin et al., 1994). Hydrothermal alteration and mineralization are spatially associated with the caldera within the upper parts of the two arc volcanoes. Within these structures, hydrothermal activity occurs at volcanically active cones or the inner and outer caldera walls. The sampling locations of hydrothermal alteration and mineralization, taken from the respective dredge track positions, are given in Table 1.

Volcano 1 (21°09'S, 175°45'W) has a basal diameter of ~ 28 km and rise from a water depth of 1,400 m up to 300 m. It hosts a 7 km-long by 4.5 km-wide, NW-SE-elongated oval

central caldera with the caldera floor lying at a water depth of about 450 m, surrounded by 200-250-m high caldera walls (Fig. 1B, C). The walls occur at a water depth between 150 mbsl (meters below sea level) and 250 mbsl. The volcano hosts two young symmetrical volcanic cones rising approximately 300 and 350 m from their caldera floors, respectively (Fig. 1B, C). Both cones are separated by a sharp, NNW-SSE-oriented volcanic ridge of approximately the same height and a length of about 1 km, possibly representing part of the former western caldera boundary or a cross-cutting tectonic structure within the caldera. Cone A (Efuefu I) occurs to the northwest, close to the actual western rim of the caldera, where the caldera wall is less distinct and deeper than in the northern, eastern and southern parts. Cone A has a diameter of 1.3 km and obtains a cone-shaped top at a height of approximately 150 m below sea level. It rises 300 m above the caldera floor and appears to be localized along a regional, NE-SW trending structure. Cone B is located approximately 1,100 m to the southeast. This cone has a diameter of 1.2 km, a summit at 90 m below surface and rises 350 m above the caldera floor. It is interpreted as the youngest feature of the summit and generally exhibits a more complicated shape. A crater 100 m-deep and 300 m-wide occurs at its northern base. The cone is characterized by two peaks approximately 200 m apart. The northern peak occurs on the SW side of a small round crater or collapse structure about 50 m in diameter that shallows towards the NW. Immediately to the south of this peak, the cone obtains a second collapse structure. The southern peak is located right at the junction of a three-fold ridge. The SW flank of volcano 1 is cut by a series of major faults, with the northernmost trending W-E with an offset of 100 - 200 m and the more southern ones trending SW-NE with a maximum offset of 100 m. These faults appear to govern both the northern and southern boundaries of the summit caldera, and also the location of the post-caldera cones. The northern flank of volcano 1 exhibits high relief attributed to outcropping lavas, whereas to the south the flanks are smoothed and presumably buried by volcanoclastics or caldera ejecta. All structures in the caldera of volcano 1 as well as the caldera itself show an asymmetric shape with a steep western wall and a smooth eastern slope. It is suggested that this is largely related to a westward shift in tectonic and magmatic activity which could be observed along the entire southern Tonga island arc (Stoffers et al., 2003).

Volcano 1 was covered by four dredge stations. Sampling the mid-flanks of the north ridge (167-03-DR) revealed fresh variably porphyritic vesicular to non-vesicular plagioclase basalt and aphyric dacite likely representing at least two recent flank eruptions in the North. No mineralization was recorded at this site. Sampling of the mid-western flank downslope of the young post-caldera cone A (167-04-DR, Efuefu I; Fig. 1C) retrieved aphyric basalt and fresh plagioclase basalt. The aphyric basalt constructs major parts of the cone A, is largely scoriaceous and appears to represent bombs. Strong hydrothermal alteration and intense

sulfide mineralization are associated with the scoriaceous material. Station 167-05-DR was located on the mid-flank of the SW caldera wall. The occurrence of different flow units composed of vesicular to non-vesicular aphyric to plagioclase-phyric basalt and andesite suggests either a large variety of volcanic flows or a high amount of debris from the caldera rim and the post caldera cone B at this site. The occurrence of angular fragments and the lack of significant weathering rather suggest limited transportation. Fragments of hydrothermally altered and mineralized material very similar to 167-04-DR were recovered from this site (Efuefu II; Fig. 1C). The sampling of the inner NE caldera wall (167-09-DR) retrieved weakly weathered porphyritic plagioclase-pyroxene basalt, aphyric basalt, and plagioclase basalt. The weakly weathered nature of these lavas suggests that the caldera-forming eruption at volcano no. 1 occurred a few 10,000 rather than some 100,000 years ago. Hydrothermal precipitates at this sampling location (Efuefu III; Fig. 1C) are characterized by intensely altered and poorly mineralized basaltic scoria which again lacks any indications for sulfide oxidation.

Volcano 19 (24°48'S, 177°01'W) has a rather flat and wide shape, obtains a NW-SE elongation and a base of approximately 14 km by 12 km in diameter (Fig. 1D). The volcano rises from a water depth of 1,400 mbsl up to 470 m, has smooth flanks, and hosts a large NW-SE elongated central caldera, about 4.6 km by 2.8 km in size and poorly preserved on its eastern and northern walls (Fig. 1E). The caldera is distinctly asymmetric with a deep depression in the NW part and a much shallower caldera floor in the SE. The caldera floor occurs at a water depth of about 1,050 m and 750 m, respectively and is surrounded by 300 m to 400-m high caldera walls. The caldera hosts a single central young volcanic cone rising approximately 580 m and 280 m from its caldera floor, respectively (Fig. 1D, E). The cone is 1.7 km in diameter at its base and has an irregular three-fold shape, most likely related to a fissure-fed eruption style. The top at about 450 mbsl occupies the center of this structure. The depression in the NW part is formed by a more recent crater 1.8 km in diameter and 250 m-deep (Fig. 1D, E). It is likely that its formation has blasted away much of the western wall of the old caldera. The cone has partly collapsed into this young crater, and also down the outer southern flank of the volcano. Two small edifices 250 m in diameter and <100 m-high occur on the floor of the young crater and might represent neovolcanic cones. At least 15 small cones, each <200 m across and <100 m-high, have broken through the smooth SW and NE flanks of the volcano. They form a SW-NE volcanic lineament that passes through the summit of the volcano and a satellite cone 500 m-high with a basal diameter of 2.5 km further to the SW. Volcano 19 adjoins a strongly tectonized ridge to the NW.

Samples were collected from two dredge stations. Sampling the inner NE wall of the young western crater recovered numerous lava flows including both vesicular and non-vesicular olivine-plagioclase basalt, plagioclase basalt, and plagioclase andesite. No mineralization

was recorded at this site. The dredge at the western flank of the cone filling the caldera retrieved a similar sequence of equal variety at water depths of 595 to 469 m (167-100-DR). A small fraction of the samples consist of boulders of young but intensely hydrothermally altered andesitic volcanoclastic breccias with angular to subrounded scoriaceous fragments. Interstices between the fragments are strongly mineralized by pyrite and the fragments display argillic alteration. The occurrence of intensely altered and mineralized boulders lacking significant sulfide oxidation likely attests to ongoing hydrothermal activity higher up on the cone. The dredge stations indicate probably that numerous small eruptions ranging from olivine basalt to plagioclase andesite have taken place within the summit area over the last few thousand years.

Host Rocks

Hydrothermal mineralization at the two arc volcanoes is closely associated with central to slightly offset (basaltic-) andesitic cinder cones within prominent calderas, or with caldera walls. Host rocks are porous fine- to coarse-grained aphyric scoriaceous volcanoclastic breccia and plagioclase porphyritic andesitic breccias. The occurrence of high portions of volcanic glass, chilled margins and fractures within and around lithic fragments suggests quench fragmentation for most of the scoriaceous material. These rocks are variably sorted and poorly bedded and contain clasts between <1 mm and 0.5 cm at both sites. Coarser volcanic breccias, with clasts up to 2 cm, were recovered from the different Efuenu sites. The fine-grained volcanoclastic matrix and the outer parts of the larger clasts are most intensely mineralized. These rocks typically display advanced alteration and contain abundant amorphous silica cementing the clasts and partly replacing the fragments.

Least-altered volcanic glass from both volcanoes is andesitic in composition and volcanic host rocks of the Efuenu and Uli'uli sites are best described as low-potassium basaltic andesites (Table 2).

The arc volcano setting, the shallow water depths, the formation of scoriaceous basaltic andesites and the style of mineralization indicate that very shallow submarine pyroclastic eruptions (water depths of < 1,000 m up to 200 m) played a significant role in the formation of the arc volcanoes, at least in the latter part of their constructional history. The basaltic-andesitic scoria cones at volcanoes 1 and 19 were undoubtedly a product of explosive strombolian to surtseyian eruptions.

Hydrothermal Alteration

The mineralized volcanoclastic breccias display distinct blue-green bleaching and pale grey colours attesting to significant sulfide, quartz and clay (argillic) alteration that indurate single fragments as well as the breccia matrix. The dominant alteration is argillic and silicification

(Table 3; Fig. 2). The intense clay alteration and silicification of the andesites at both arc volcanoes is likely a product of acid-generating sulphurous gases and siliceous hydrothermal fluids emanating from the vents. The alteration is characterized by typical colloform pyrite and intense intergrowths with illite, smectite, traces of kaolinite, cristobalite, natro-alunite, anhydrite, minor K-feldspar, barite and native sulfur. Argillic alteration is characterized by fibrous clay mineral (illite, smectite, kaolinite) coatings of vesicles and fractures, replacing scoriaceous fragments, and cementing the volcanoclastic material (2A). The argillic alteration however, is not always penetrative but often affects the outer portions of (unzoned) plagioclase phenocrysts whereas the inner core does not show any obvious alteration features. While clay alteration affects smaller fragments and the matrix, larger and dense lithic fragments lack evidence of intense alteration besides minor chloritization and rare calcite. The degree and style of silicification is variable and characterized by different silica polymorphs (cristobalite \pm tridymite, opal CT, amorphous silica, quartz; Fig. 2B). Single lithic fragments and matrix may be totally silicified by opal CT and cristobalite \pm tridymite, but the most intense sulfide mineralization occurs without significant silicification. A fine network of cristobalite, opal CT and amorphous silica is often observed to crosscut the matrix of volcanoclastic breccias, suggesting hydrofracturing and sudden silica precipitation. Single open spaces display aggregates and needles of μm -scale euhedral quartz crystals. Massive areas and fibrous aggregates of cristobalite and opal CT represent an irregular type of alteration at the Efuefu sites. The principal type of chalcedonic areas is several centimetres wide, vein-like and occupies very narrow, irregularly intersecting fractures that may grade into small brecciated intensely silicified volcanic clasts or end in fibrous aggregates. More massive areas replace the andesitic volcanoclastic host rock which was previously altered to vuggy silica (Fig. 2C). A certain light to dark grey banding is mainly related to variable pyrite contents. Disseminated pyrite is also abundant in the clay-altered scoriaceous ash. The pyrite occurs as fine grains (<1 mm) throughout the matrix of the ash and locally impregnating larger, altered fragments (Uli'uli site). Anhydrite and barite blades are very fine-grained (<0.5 mm) and may occur in the open spaces of scoria fragments. Those sulfates are closely associated with sulfide mineralization and the occurrence of natro-alunite and colloform to almost euhedral native sulfur (Fig. 2D). Natro-alunite is fine-grained (30 – 50 μm), shows a characteristic platy habit and coexists with the sulfide mineralization as can be seen from a close association and local intergrowths (Fig. 2E, F). The presence of K-feldspar and its rhombic habit suggests that it might represent adularia (Fig. 2G). The association with natro-alunite in samples from the Efuefu I and II sites may be the result of highly variable fluid compositions and sulfidation states and probably represent different mineralization stages. Rutile is a prominent alteration product forming fine-grained needle-shaped aggregates within the altered volcanoclastic fragments (Fig. 2H). Notable contents of mullite

occur at the Efuefu III site. The occurrence certainly attests to significant aluminous alteration and high formation temperatures with the thermal transformation of kaolinite or pyrophyllite (Anton, 1969; Gao & Yao, 1992; Wang & Zhang, 1997). Magma invading a vent-hosted hydrothermal system produces thermal decomposition reactions in the altered material and the formation of mullite (Wood, 1994). Thin, fine-grained, greenish overgrowths along fracture surfaces within lithic fragments are interpreted as atacamite (Efuefu III). The beginning oxidation of pyrite results in a distinct red staining at surfaces and forms thin oxidized crusts on the scoriaceous boulders.

Mineralization

The mineralization is characterized by pervasive sulfide and iron oxide disseminations. A summary of the ore mineralogy is given in Table 3. SEM photographs and colour photomicrographs of the alteration and mineralization are shown in Figures 2 and 3.

Ore mineralogy is simple and uniform and is dominated by Fe- and Cu-sulfides, hematite, and magnetite. Fine-grained but pervasive disseminated pyrite (usually < 10 μ m) and magnetite or hematite (usually 10 to 50 μ m up to 1 mm) account for approximately 80 percent of the ore minerals, and the remaining includes variable amounts of fine-grained chalcopyrite, marcasite, cobaltian pyrite, cupriferous pyrite, pyrrhotite, intermediate solid solution (iss), rutile, arsenopyrite, stibnite, realgar, and native gold (with decreasing order).

Mineralization at the two island arc volcanoes can be divided into two basic ore types. The Efuefu vent site comprises samples dominated by the ore mineral assemblage pyrite-chalcopyrite-hematite-magnetite, where pyrite ranges between 30 and 90 modal % of the sulfides, and chalcopyrite between 70 and 10 modal %. Magnetite and/or hematite account for up to 40 modal % of the ore. The remaining sulfide phases are less than 5 % and occur either as fine-grained intergrowths (pyrrhotite, marcasite) or as isolated, disseminated, very fine-grained subhedral to euhedral phases (arsenopyrite, realgar, stibnite). The Uli'uli vent site is characterized by a dense intergrowth of dominating pyrite (60 to 80 modal %) and subordinate marcasite (20 to 40 modal %). Hematite is the dominating iron oxide and occurs as a very fine-grained pervasive dusting throughout the matrix. It accounts for up to 15 % of the ore.

At the Efuefu sites, samples often show zoning where pyrite enrichment is associated with outer zones surrounding a siliceous and argillic interior, as well as with intense veining and coatings of lithic fragments. Pyrite occurs as fine-grained, pervasive disseminated grains, but is best developed where it occurs: 1) coating vesicles within scoriaceous fragments (coatings up to 2 mm thickness), 2) lining fractures and open spaces, and 3) within the matrix between larger fragments. However, a fine pervasive pyrite dusting is also associated with smaller, more compact lithic fragments, interstices, and as a coating of larger scoria fragments (Fig.

3A, B). More massive aggregates of pyrite are rare and restricted to large vesicles or open spaces related to vuggy silica (Fig. 3A). Structurally controlled pyrite mineralization along fractures, associated with chalcedonic quartz, suggests hydrothermal fracturing and healing. Pyrite as well as marcasite and magnetite show the whole range from colloform to euhedral crystals (Fig. 3C, D). Magnetite ranges from several 10s of μm -sized colloform aggregates (Fig. 3F) to mm-sized, equigranular crystals. Hematite forms laths of equigranular crystals, dendritic and platy growth (Fig. 3G). In general, the association chalcopryrite-hematite predominates at the Efuefu I site whereas Efuefu II and III are characterized by predominant pyrite-magnetite intergrowths.

Gold occurs as few discrete grains in association with magnetite, pyrite, and arsenopyrite at Efuefu II. The grains are heterogeneously distributed, very fine-grained ($< 5 \mu\text{m}$), and forms irregular grains (Fig. 3H). The association with magnetite showing inclusions of pyrite constrains the gold precipitation at the magnetite/pyrite buffer.

Chalcopryrite is usually sub- to euhedral, more coarse-grained than pyrite and almost exclusively intergrown with pyrite, hematite and subordinate magnetite (Fig. 3C, D). At the Efuefu I site, it also forms larger aggregates and grain agglomerates several millimetres in size. Chalcopryrite displays weak interference colours. Evidence for weak recrystallization can be drawn from inclusions of intermediate solid solutions (iss) and frequent magnetite. The inclusions do not show any obvious crystallographic control but likely mark previous grain boundaries. There is no clear evidence for a paragenetic sequence but pyrite, chalcopryrite, hematite and magnetite are essentially cogenetic. This is concluded from colloform pyrite-magnetite intergrowths, chalcopryrite-pyrite-magnetite, and chalcopryrite-hematite assemblages, and the fact that all four phases occur as host minerals for and mineral inclusions in their cogenetic phases. The association with both, magnetite and hematite suggest highly variable redox conditions in the mineralizing fluids close to the $\text{Fe}^{2+}/\text{Fe}^{3+}$ buffer. Marcasite occurs in more distal, low-temperature parts of the vents (Efuefu II, III). This can be concluded from the rather weak hydrothermal alteration of the associated plagioclase phenocrysts where euhedral grains and more massiv coatings of marcasite are scattered around the altered rims. Marcasite occurs in monomineralic aggregates, isolated laths and recrystallized grains with few, locally recrystallized pyrite inclusions. It is associated with fine grains and patches of hematite. Arsenopyrite, realgar and stibnite were identified by optical microscopy and SEM. They are usually very fine-grained (5-30 μm), sub- to euhedral and disseminated throughout the matrix of the Efuefu site. Arsenopyrite obtains locally triangular shape and is associated with cogenetic disseminated and fine-grained magnetite and pyrrhotite, and later pyrite (Fig. 3L). Magnetite inclusions in arsenopyrite can be observed. Stibnite was identified by SEM at Efuefu III (Fig. 3I). It obtains very fine grain sizes ($< 10\mu\text{m}$) and is closely associated with pervasive disseminated marcasite, rare hematite,

subhedral rutile, and chalcedonic quartz in vesicles of andesitic clasts. Realgar is usually fine-grained (<100 μm), but also occurs as mm-large coarse euhedral crystals (Fig. 3K). It is associated with laths and colloform sooty dusting of hematite, and fine-grained pervasive pyrite in porous, highly argillic altered scoria. It locally forms concentric overgrowths on pyrite. Rutile is closely associated with the most altered scoriaceous clasts and occurs disseminated in the matrix (Fig. 2H). It may occur in agglomerates of magnetite-pyrite or marcasite with subordinate hematite but is also intergrown with crystalline and chalcedonic quartz in vesicles, where no other ore minerals are present.

The sulfide mineralization in general can be distinguished in terms of proximity to the vent areas. Most proximal mineralization is characterized by the cogenetic high-temperature assemblage pyrite-magnetite and chalcopyrite-hematite. Less proximal sulfide mineralization contains cogenetic arsenopyrite-magnetite-pyrrhotite-rutile, whereas distal, low-temperature paragenesis is mainly composed of stibnite-realgar-marcasite-hematite. The Uli'uli vent area is characterized by early marcasite that is overgrown by later pyrite and hematite in a prograde hydrothermal system (Fig. 3E).

Microanalysis

A JEOL JXA-8600 Superprobe was used to characterize the chemical composition of the ore mineral assemblage (Table 4). Pyrite as the main ore-forming sulfide is essentially stoichiometric throughout the Efuefu and Uli'uli hydrothermal sites, although notable concentrations of Cu (up to 1.61 and 7.14 wt. %, respectively), Co (up to 1.47 and 0.3 wt. %, respectively), Zn (up to 0.14 and 0.3 wt.%), and Ni (up to 0.3 wt.%) occur in single grains. Distinct Co contents, in particular, resemble that of cobaltian pyrite commonly found in high-temperature, cupriferous ores in massive sulfide deposits (e.g., Huston et al., 1995; Hannington et al., 1999). Highly elevated Cu concentrations in pyrite are not related to (sub-) microscopic inclusions of chalcopyrite but may derive from impurities in the pyrite lattice. Chemical zonation within pyrite of both sites is shown by changes in Cu, As, and Zn concentrations (Fig. 4M, N). The Cu, and in part Zn and As, are clearly confined to distinct structural zones within the pyrite lattice. It can be suggested that cupriferous pyrite may point to its origin from high-temperature intermediate solid solution (iss). High Cu, however, is not associated with elevated Zn in the same analysis. It is important to note that elevated Cu contents often but not exclusively correlate with high Co, Ni, and As values. The concentrations of Au, Ag, Bi, Hg, Se are mainly at or below the detection limits. Slightly elevated contents attest to correlations between Bi and Ag, as well as with elevated Hg and Zn. Where Se is above the limit of detection, it is confined to elevated Zn values. Slight correlations exist between Au and As.

Pyrrhotite and partly marcasite show enrichments in Cu and Co similar to pyrite. Pyrrhotite inclusions in magnetite from the Efuefu II site contain notable Cu (up to 1.07 wt. %), Co (up to 0.29 wt. %) and Ni (0.2 wt. %) contents. Marcasite may obtain high Cu and elevated Se values (up to 0.77 wt. % and 0.12 wt. %, respectively). Concentrations of any other element are at or below the respective detection levels. Marcasite at Uli'uli shows locally elevated Cu contents (up to 0.32 wt. %) and As, Se, Hg, Ag, and Bi values at or slightly above the detection limits, respectively. Marcasite at Efuefu clearly postdates the primary pyrite-magnetite and chalcopyrite-hematite mineralization and is likely related to lower temperature hydrothermal fluids. The close association and intergrowths of late marcasite and early pyrite suggest that the elevated Cu contents might be related to pyrite replacement rather than represent primary Cu fractionation into marcasite.

Chalcopyrite shows essentially stoichiometric composition but may contain notable trace element and slightly elevated Au concentrations which may reach up to 0.15 wt. % Ag, 0.21 wt. % Co, 0.44 wt. % As, and 0.1 wt. % Au, respectively.

Intermediate solid solution (iss) is characterized by a highly variable composition with respect to its Cu and Zn contents (Fig. 3N). The Cu/Zn ratio varies accordingly between 0.01 and 13.4. The iss is very Zn-rich and essentially the only Zn carrier at the Efuefu vents. Besides As (up to 0.3 wt. %), all other trace elements are at or well below their detection limits.

Arsenopyrite has a largely stoichiometric composition with slightly elevated Se (up to 0.23 wt. %) and Co (up to 0.1 wt. %) contents. The Au content is essentially below the detection limit of the microprobe.

Magnetite and hematite are characterized by significant Ti (up to 10.69 wt. % and 19.67 wt. % TiO₂, respectively) and V (up to 4.62 wt. % and 2.32 wt. % V₂O₃, respectively) contents (Table 4). Magnetite is also characterized by elevated Mg (up to 3.11 wt. %), Al (up to 2.51 wt. %), and Mn (up to 0.54 wt. %). Elevated SiO₂ contents are probably the result of the stimulation of the host minerals as are notable concentrations of Mg, Al, and Si in hematite.

Geochemistry

Pyrite and chalcopyrite disseminations are pervasive and account for less than 5 % of the total mass. Dominating pyrite/marcasite and magnetite/hematite mineralization is reflected by distinct Fe and S contents (average 7.53 wt. % Fe and 3.49 wt. % S for Uli'uli; 5.46 wt. % Fe and 4.70 wt. % S for Efuefu). It is interesting to note, that alteration and mineralization resulted in the decrease of the total Fe content, when compared to the unaltered protoliths (Table 2). Despite significant sulfide and Fe-oxide mineralization, dilution by the andesitic host rock however results in low total amounts of economic mineralization. The most intensely mineralized samples from the Efuefu vent area contain up to 370 ppm Cu, 12 ppm

Pb, 0.15 ppm Au, 295 ppm As, 0.3 ppm Hg, 26 ppm Se, 13 ppm Mo, 6.1 ppm Te, 400 ppm Ba, 2.5 ppm U. The Uli'uli site is characterized by values of up to 213 ppm Cu, 15 ppm Pb, 0.1 ppm Au, 0.4 ppm Hg, 27 ppm Se, 5 ppm Mo, 2 ppm Te, 200 ppm Ba, 1.9 ppm U (Table 2). At both sites, mineralization displays notable trace element concentrations of elements above the detection limits usually attributed to high-temperature hydrothermal activity such as Co (avg. 31 ppm (Efuefu) and 37 ppm (Uli'uli)), Se (avg. 12 ppm (Efuefu) and 15 ppm (Uli'uli)), and Mo (avg. 6 ppm (Efuefu) and 3 ppm (Uli'uli)). The concentrations of elements commonly enriched in island arc systems like Te (avg. 2.7 ppm (Efuefu) and 1.3 ppm (Uli'uli)), Hg ((avg. 103 ppb (Efuefu) and 35 ppb (Uli'uli)), Tl (avg. 0.8 ppm (Efuefu) and 0.1 ppm (Uli'uli)), Bi (avg. 0.3 ppm (Efuefu) and <0.1 ppm (Uli'uli)), Sn ((avg. 0.8 ppm (Efuefu) and 1.3 ppm (Uli'uli)) are slightly elevated or close to the detection limits of the respective elements.

Mass balance calculations based on the normalization of mineralized samples to the least altered basaltic andesites of both volcanoes (Table 2) result in distinctive element enrichment/depletion patterns (Fig. 4). The Efuefu sites are characterized by moderate Ti, Na, Nb gains and local Al, K, Rb, Sr, and Ce enrichments but also by significant losses of Al, Fe, Mn, Ca, K, Mg, P, Sr, Y, Ce, when compared to the suggested protolith composition (Fig. 4A). The latter group of elements is commonly referred to as fluid mobile under reduced and low pH conditions during seawater hydrothermal alteration. This is likely related to the hydrothermal decomposition of plagioclase and pyroxenes as well as andesitic glass. The lack of any silica enrichment despite of significant silicification processes is largely attributed to the limited number of analyses. The Efuefu sites display a distinct S-Au-As-Se-Tl-Hg-Te-U enrichment pattern, associated with slight gains in Cu-Sb-Co-Ni-Th-Ba (Fig. 4A). The enrichment of this suite is also represented by element correlations above the 95% significance level. Compared to the unaltered basaltic andesites, alteration resulted in significant Zn-Pb-Ge and subordinate Sb-Cu-Co-Ni-V-Th-Ba losses.

Alteration at the Uli'uli site is characterized by gains in Ti, K, Rb, Sr, Zr, Nb, and Ce and significant Al, Fe, Mn, Ca, Na, Mg, P, and Y losses when compared to the basaltic andesite protolith (Fig. 4B). The ore geochemistry displays significant S-As-Se-Te-Pb-Au-U and moderate Tl-Hg-Cu-Co-Ni gains while the suite Sb-Zn-Co-Ni-Mn-Ge-V may be depleted.

In order to consider the economic potential of the vent sites, the geochemical composition of the mineralization, i.e., the element suite Cu-Pb-Au-As-Sb-Hg-Tl-Se-Te, was calculated to an ideal 100 % massive sulfide composition. As pyrite is the dominant sulfide mineral, its composition was considered representative of a theoretical massive sulfide ore and the geochemical results were calculated accordingly (Table 5). The results suggest a significant potential for ore-grade Cu and Au enrichments in the sulfide precipitates of the Efuefu sites and similar enrichment grades but lower levels at the Uli'uli site.

Sulfur Isotopes

The sulfur isotope ratios of sulfides (pyrite, combined pyrite-marcasite and pyrite-chalcopyrite) and sulfates (alunite) were analyzed at Freiberg University of Mining and Technology, using a Finnigan Delta E mass spectrometer and the procedures of Ueda and Krouse (1986) and KIBA (Sasaki et al., 1979), respectively. Sulfide mineral separates were prepared by panning and hand picking under a binocular microscope. Sulfur was extracted from the sulfides by digestion in $\text{CrCl}_2\text{-HCl}$ and precipitation as AgS_2 , prior to isotope analysis. Sulfur from alunite was extracted by dissolution in NaOH solution and precipitation of barite. The results are reported relative to the Canyon Diablo Troilite (CDT). The reproducibility of the results is better than 0.2 per mil.

The range of isotopic compositions of the sulfides is typical of volcanic-derived sulfur in seafloor hydrothermal systems likely reflecting variable contributions from a deeper magmatic source. The sulfur isotope ratios of the entire suite of sulfide samples show a large variability in $\delta^{34}\text{S}$ ranging from -17.5 to +2.0 per mil ($n = 16$) for the Efuefu sites and from -5.1 to -0.2 per mil ($n = 4$) for the Uli'uli site (Table 6). The range at both sites is likely related to the variable mixture of sulfides (i.e., pyrite-chalcopyrite and pyrite-marcasite) with different proportions and resulting isotope fractionations. The wide range in $\delta^{34}\text{S}$ values may also indicate that the sulfides did not derive their sulfur from the same source but from multiple sources that are likely represented by magmatic and seawater-derived hydrothermal fluids. The different sites at Efuefu show major differences in their isotopic composition. It is evident that chalcopyrite-bearing mineralization has slightly heavier sulfur isotope ratios between -0.2 and -2.9 per mil ($n = 6$) whereas pyrite-dominated samples show a much larger range and lighter signatures from +2.0 to -17.5 per mil ($n = 10$). The Efuefu I site is characterized by $\delta^{34}\text{S}$ values from -2.9 to +2.0 per mil (average -0.8 per mil; $n = 6$), Efuefu II from -2.0 to -9.8 per mil (avg. -6.0 per mil; $n = 5$), and sulfur isotopes at Efuefu III range between -5.4 and -17.5 per mil (avg. -10.9 per mil; $n = 5$). Framboidal pyrite and marcasite in samples collected at the Efuefu III site have the lowest $\delta^{34}\text{S}$ values, from -12.1 to -17.5 per mil ($n = 3$), possibly indicating the influence of bacteriogenic sulfate reduction. Average value for sulfur isotope signatures at Uli'uli is -2.8 per mil ($n = 4$).

The $\delta^{34}\text{S}$ values close to zero per mil are thought to have formed from a combination of sulfur leached from the underlying basaltic andesites and reduced seawater sulfate, similar to that found in a majority of seafloor hydrothermal systems (e.g., Shanks et al., 1995; Petersen et al., 2002). The overall negative sulfur isotope ratios, however, more closely resemble the $\delta^{34}\text{S}$ values of sulfides in a number of seafloor hydrothermal systems (Fig. 5), where a contribution of magmatic volatiles to the hydrothermal fluids has been shown (e.g., Hine Hina field in the southern Lau basin, the Desmos Site in the Manus Basin, the Brothers

Seamount in the Southern Kermadec arc, and the Conical Seamount in the New Ireland Fore-arc; Gamo et al., 1997, Herzig et al., 1998, Gemmell et al., 1999, de Ronde et al., 2000, Schwarz-Schampera et al., 2001, Petersen et al., 2002).

Eight analyses of alunite (\pm anhydrite and barite), coexisting with pyrite (Fig. 2E, F), indicate a wide range of $\delta^{34}\text{S}$ values for sulfate between 0.5 and 18.9 per mil. This is characteristically lower than the actual seawater sulfur isotopic composition of +21 per mil and at least some of the aqueous sulfate appears to have exchanged significantly with H_2S in the hydrothermal fluids. The wide range indicates that isotopic equilibrium was probably not achieved. When compared to the values for pyrite in the same samples (Table 6), the sulfate values are 6.6 to 33.0 per mil higher than that of coexisting pyrite. This is related to the expected isotopic fractionation between sulfate and sulfide in the hydrothermal fluids. The $\Delta^{34}\text{S}_{\text{SO}_4\text{-S}}$ values for the sulfate-pyrite pairs of the majority of the measurements are largely in the range for equilibrium between alunite and pyrite following the disproportionation of magmatically derived SO_2 (e.g., $\Delta^{34}\text{S}_{\text{al-py}} = 16\text{-}28\text{‰}$ for a temperature range of $200^\circ - 350^\circ\text{C}$; Rye et al., 1992; Arribas et al., 1995; Arribas, 1995). However, $\Delta^{34}\text{S}_{\text{al-py}}$ values of 6.6 per mil, as it is determined at the Efuefu I site, would require temperatures well over 400°C and $\text{H}_2\text{S}/\text{SO}_4$ ratios in the hydrothermal fluid of less than 1 (Rye et al., 1992). The occurrence of abundant hematite, in close intergrowths with chalcopyrite as well as alunite, barite and anhydrite, and minor pyrite attests to rather oxidizing conditions at the central cone of volcano No. 1 (sample 167-04-DR-10E) and low $\text{H}_2\text{S}/\text{SO}_4$ ratios of <1 may therefore be suggested. At the other sites, the sulfur isotope ratios for alunite display a rather variable contribution of seawater sulfate to the hydrothermal fluids ranging from a value close to zero per mil at the Efuefu III site to ratios close to seawater sulfate compositions (Efuefu III, Uli'uli).

The calculated $\Delta^{34}\text{S}_{\text{SO}_4\text{-S}}$ pairs may suggest equilibrium between alunite and pyrite and elevated formation temperatures. If any sulfate-sulfide equilibrium is proposed for the Efuefu and Uli'uli sites, the use of the sulfur isotope fractionation equation for alunite-pyrite after Ohmoto and Rye (1979) and the calculation of fractionation temperatures results in a wide and non-reliable temperature range (Table 7). Single temperatures for the Efuefu I and III sites clearly prove disequilibrium, while that for Efuefu II, two samples from Efuefu II and those for Uli'uli seem reliable. As described above, the wide range of sulfate and sulfide sulfur isotope signatures most likely attests to intense exchange of aqueous sulfate with H_2S in the hydrothermal fluids and any temperature estimates based on sulfur isotope fractionation will not produce reliable data. However, in order to provide better understanding of the sulfur isotope fractionation processes, a more detailed study using laser ablation analyses on pyrite-alunite intergrowth is necessary.

Discussion and Conclusions

Alteration and mineralization of samples recovered from the two new active Efuefu and Uli'uli vent sites at large and complex, multi-stage volcanic edifices (volcanoes 1 and 19) of the southern Tonga arc share important characteristics of geothermal vents in subaerial environments and contribute to a growing number of epithermal-style and transitional types of seafloor mineralization being recognized in the Kermadec arc system (e.g., Wright et al., 1998; Stoffers et al., 1999a, b; de Ronde et al., 2003), in the New Ireland fore-arc (Petersen et al., 2002) and along the volcanic front of the Izu-Ogasawara arc (Suiyo seamount and Mjojjin knoll; Watanabe and Kajimura, 1993, 1994, Iizasa et al., 1999). The altered and mineralized samples share similarities with alteration and mineralization described from subaerial, epithermal-style, high-sulfidation Au deposits, and those reported from shallow submarine hydrothermal vent fields such as the Kermadec and Izu-Bonin arcs (e.g., Hannington et al., 1999; Iizasa et al., 1999; Stoffers et al., 1999b; Glasby et al., 2000; de Ronde et al., 2001; Petersen et al., 2002).

Due to the fact that the samples were retrieved by dredging, their actual position, relationships to the surrounding volcanic rocks as well as the presence of active hydrothermal discharge is unknown. However, considering their weak oxidized outer surfaces, very limited occurrence of oxidation products (i.e., goethite, atacamite), and the persistence of anhydrite in the alteration assemblage, typically characterized by retrograde solubility and fast dissolution, they most likely represent precipitates from active hydrothermal venting. The vent mineralogy at both volcanoes attests to relatively high-temperature proximal Cu-dominated discharge and more distal marcasite-, As-Sb- and silica-dominated activity. The lack of evidence for chimney-type mineralization and sulfide crusts as well as the association with variably hydrothermally altered rocks most likely suggests that activity is represented by unfocused hydrothermal discharge of diffusive percolating hydrothermal fluids. In regular seafloor hydrothermal vent fields along spreading zones and rifts, diffuse discharge zones are associated with vibrant biological communities occurring at relatively low fluid temperatures (<50°C). Their absence in all recovered samples likely suggests rather hostile conditions that are typically represented by the physicochemical properties (e.g., high acidity and temperatures) of the discharging fluids. Diffusive activity may be related to the earliest form of discharge in a new hydrothermal field or indicate the last stages of high-temperature activity in a waning hydrothermal system as high-temperature upflow collapses around a cooling subvolcanic intrusion. While the latter seems unlikely because of the pervasive but irregular and zoned hydrothermal alteration of the basaltic-andesitic host rocks, this fact favours the possibility of currently evolving hydrothermal systems at volcanoes 1 and 19 due to irregular degassing above the respective magma chambers.

The widespread distribution of mineralization at the central cinder cone as well as the southern outer and the northern inner walls and the occurrence of intensely mineralized boulders at all Efuefu sites suggest extensive and widespread hydrothermal activity at volcano 1. The caldera boundaries and the development of post-caldera cones are controlled by active structures subparallel to plate convergence and perpendicular to the trench and it is obvious that hydrothermal activity, the deep penetration of fluid pathways, and/or perhaps magmatic degassing largely follow those structures. It is interesting to note that activity is not associated with the youngest magmatic event, the construction of cinder cone B, but occurs at the older cone A. Degassing and fluid evolution obviously postdate the early constructive magmatic event within the caldera and may be related to the gradual build up of melt and the intrusion of magma at the nearby cone B. The association with the eruptive center at cone A in the young central caldera as well as the disseminated mineralization may indicate that the hydrothermal venting is quite immature and ephemeral. However, the development of a sustained, thermally intensifying hydrothermal cell in proximity to a high-level magma chamber may be suggested.

The alteration assemblages at volcanoes 1 and 19 resemble those typically found in subaerial geothermal deposits (e.g., Heald et al., 1987, Hedenquist, 1987, Hedenquist et al., 1994, 1998; Arribas, 1995) as well as in shallow submarine hydrothermal vent fields (e.g., Conical Seamount, New Ireland fore-arc; Petersen et al., 2003) and share characteristics with alteration associated with epithermal-style mineralization. Alteration mineralogy is likely represented by advanced argillic alteration in close association with pervasive silicification. It is mainly characterized by zonal inward decomposition of plagioclase phenocrysts and microliths in the matrix. The intense clay alteration and silicification of the andesites is likely a product of acid-generating sulphurous gases and siliceous hydrothermal fluids emanating from the vents. Among the most diagnostic minerals are natroalunite, in close intergrowth with pyrite and native sulfur as well as rhombic K-feldspar in association with kaolinite-illite. Magmatic hydrothermal, acid sulfate alteration results from the attack on the wall rocks by sulfuric acid, produced by the disproportionation of SO_2 , and followed by the coprecipitation of sulfur in its reduced, neutral and oxidized state. Some of the H_2S in the fluid reacts with iron-bearing minerals in the host rock to form pyrite (and chalcopyrite); the remainder is oxidized to sulfuric acid which attacks the wall rock to produce a zone of steam-heated acid sulfate alteration. These alunites are usually very fine-grained with a diagnostic platy to rhombohedral habit that is commonly interpreted as being a product of steam-heated sulfate precipitation that originates from magmatic SO_2 degassing (e.g., Arribas, 1995; Herzig et al., 1998). The high sulfidation stage mineralization is also suggested by the occurrence of vuggy silica textures, strong silicification of lithic fragments and matrix, and disseminated

pyrite and chalcopyrite. Mineral phases like arsenopyrite, realgar, and stibnite may attest to elevated sulfur activities in the mineralizing fluids.

The occurrence of rhombic K-feldspar, possibly adularia, in association with potassic clay minerals is regarded as diagnostic for low-sulfidation states in subaerial epithermal-type mineralization (e.g., Heald et al., 1987; Arribas, 1995). Its coexistence with platy natroalunite in the same sample suite strongly suggest highly variable fluid compositions and sulfidation states at Efuefu and Uli'uli, most likely related to boiling processes.

The occurrence of mullite is rather unusual in hydrothermal systems. It was described from the vent-hosted hydrothermal systems at Ruapehu and White Island andesite volcanoes in New Zealand (Wood, 1994) and provides insight into the mineralogical reactions that may occur during magma invasion in an active hydrothermal system. The heating of argillic altered material to magmatic temperatures likely produces thermal decomposition reactions of kaolinite and illite with the formation of mullite. It displays the significant and pervasive aluminous alteration in an active magmatic system at volcano 1 and may attest to recurrent hydrothermal and magmatic activity at Efuefu.

Another characteristic alteration product is the penetrative silicification. There is clear evidence for quench fragmentation of the scoriaceous material that has probably led to shrinking during the deposition on the seafloor. The development of open spaces and channelways within the scoriaceous material certainly allows for fluid migration and associated pervasive disseminated hydrothermal alteration and mineralization. Extensive silica precipitation along fine cracks running through the scoriaceous material and fragments, however, also provide evidence for possible hydrofracturing due to fluid overpressure that might be related to boiling processes, and sealing due to the sudden and rapid precipitation of pyrite, silica or clay minerals.

Most Efuefu and Uli'uli samples do not visually contain any other sulfide but pyrite. However, the setting as well as metallogenic evidences like the close intergrowths of pyrite with magnetite typically constrain conditions of preferential gold and perhaps base metal transportation. Besides fine-grained disseminated chalcopyrite and rare intermediate solid solution, no base metal sulfides were observed visually nor was significant geochemical enrichment detected. This is regarded characteristic of similar subaerial and shallow submarine settings where the mineralizing fluids have undergone phase separation. There are strong indications for a magmatic steam environment at both locations where virtually all of the sulfur is present as SO_2 released from a magmatic reservoir at fairly shallow depth, high temperatures and low pressures without reduction during its ascent. The contribution of magmatic volatiles to the hydrothermal system is consistent with the observed ranges of $\delta^{34}\text{S}$ values in coexisting alunite and pyrite, although full equilibration between aqueous sulfide and sulfate in the hydrothermal fluid was not achieved. At very shallow water depths,

solubility for gold and main base metals (i.e., Cu, Zn, Pb) are likely kept within the deeper zones and do not extend higher up in the discharge zone. The instability of metal-chloride complexes through boiling processes may lead to immediate precipitation at depth. As a result, the precipitates at the seafloor are notably depleted in most metals. The precipitates at Efuefu and Uli'uli form in water depths of 700 to 330 m and 600 to 470 m, respectively and, given the boiling curve for typical seafloor hydrothermal fluids (e.g., de Ronde et al., 2003; Hannington et al., 2003), form well above the supposed subcritical boiling point. As a consequence, both sites carry low totals of metals besides notable Cu concentrations. It is obvious that the formation of extensive chalcopyrite at both sites is largely hampered by limited Cu concentrations in the mineralizing fluids possibly due to precipitation processes at depth.

Boiling processes may also account for highly variable redox conditions in the mineralizing fluids. This is indicated by the coprecipitation of sulfide, sulfate and native sulfur and related distinct sulfur isotope fractionation but also by the coprecipitation of ferric and ferrous iron and the close intergrowths of variable proportions of hematite, magnetite, and pyrite. Coprecipitation may constrain fairly high oxygen and hydrogen fugacities as well as high H₂S activities (e.g., Gibert et al., 2002, Frank et al., 2002, Stefansson and Seward, 2003). These conditions at the hematite/magnetite buffer are favourable for enhanced gold solubility and therefore bear a significant potential for elevated gold contents in the mineralizing fluids. Gold mineralization, however, is rather limited in the studied samples. At Conical Seamount, the main gold stage is not associated with minerals regarded as diagnostic of acid conditions (Petersen et al., 2002). Instead, gold enrichment is rather associated with the evolution from alunite-bearing to nonalunite-bearing assemblages and an increase in H₂S/SO₄ with time, which is consistent with a shift in $\delta^{34}\text{S}_{\text{H}_2\text{S}}$ from lighter to heavier values. Based on this assumption, we conclude that fluid evolution at both Tongan vent sites has not yet achieved considerable gold saturation resulting in limited gold precipitation in the studied samples.

The generation of large deposits of Au and Cu is favoured in suprasubduction zone settings, widely represented along the Tonga-Kermadec island arc system. While normal subduction processes do not appear to favour the generation of large Au and Cu deposits, the favorable tectonic settings include the onset and termination of periods of flat subduction (Kay and Mpodozis, 2001), the reversal of polarity of a subduction zone (Solomon, 1990), the cessation of subduction due to collision (McInnes and Cameron, 1994; Sillitoe, 1997), and oxidation of the mantle wedge (Mungall, 2002). Among these hypotheses, the oxidation of the mantle wedge above the subducting slab most likely applies for the southern Tonga arc and may be ascribed to the collision and subduction of the aseismic Louisville ridge. The collision zone has progressively moved southwards along the Tongan trench during the past ~ 5 my (Yan and Kroenke, 1993) and therefore affected the style of volcanic activity in the

southern Tonga arc for a long period of time. The occurrence of variably sorted and poorly bedded scoriaceous, plagioclase-phyric basaltic andesites and basaltic-andesitic bombs as well as their geochemical composition (Table 2) indicate explosive volcanism and therefore, high volatile contents in the magmas along the southern Tonga arc. The hydrothermal activity at volcanoes along the collision zone suggests enrichment of volatiles in the subduction zone and their recycling during magmatic processes. This may produce melts with elevated oxygen fugacities and enriched in fluid-mobile elements (e.g., Noll et al., 1996). The removal of chalcophile elements from the mantle wedge into the Tonga arc magmas can only occur if sulfide is absent from the melted source rock, requiring oxidation of the mantle wedge to values of $\log fO_2 > FMQ+2$ (Mungall, 2002). The only agent capable of effecting this change is ferric iron, carried in solution by slab-derived partial melts. Based on our work, we suggest the subduction and partial melting of enriched and hydrous OIB material and the introduction of ferric iron likely resulting in the oxidation of the mantle wedge. Significant redox potential and large proportions of ferric iron in the lavas of the Louisville ridge can be concluded from their obvious alteration due to the long exposition to and the interaction with seawater (Stoffers et al., 2003). Partial melting and addition of Fe_2O_3 may brought the Tonga arc mantle wedge to higher oxygen fugacities and above the SSO buffer (cf., Mungall, 2002) potentially leading to elevated Cu and Au contents in the arc volcanic rocks and associated hydrothermal fluids and precipitates.

The present sampling of the Efuefu and the Uli'uli sites at the two volcanoes suggest that large parts of at least volcano 1 may be mineralized. The style of mineralization suggests a large potential for Cu and Au mineralization. The lack of careful and detailed seafloor mapping and sampling at both sites, however, largely prevents a proper assessment of the extent and character of mineralization. Based on this study, we conclude that the Efuefu and Uli'uli sites contribute to the new style of shallow water seafloor mineralization defined by the Conical, Suiyo, and Myojin Knoll seamounts, with characteristics similar to subaerial epithermal systems.

Acknowledgements

Principal funding for this research was provided by the German Federal Ministry for Education and Research (BMBF Grant 03 G 0167 to PS and PMH). Additional support was provided by the Leibniz-Program of the German Research Foundation. We thank masters, officers, and crew of the R/V Sonne for their expert technical assistance during our research cruise along the Tonga island arc and the Lau basin, and K. Schreiber, K.-P. Becker and R. Liebscher for analytical help. The manuscript was much improved through critical reviews.

References

- Anton, O., 1969, Study on the thermal transformation of pyrophyllite: *Revue Roumaine de Geologie, Geophysique et Geographie, Serie de Geologie*, v. 13, p. 29-38.
- Arribas, A. Jr., 1995, Characteristics of high sulfidation deposits, and their relation to magmatic fluid, *in* Thompson, J.F.H., ed., *Magmas, fluids, and ore deposits: Mineralogical Society of Canada, Short Course*, vol. 23, 419-454.
- Arribas, A., Cunningham, C.G., Rytuba, J.J., Rye, R.O., Kelly, W.C., Podwysocki, M.H., McKee, E.H., and Tosdal, R.M., 1995, Geology, geochronology, fluid inclusions, and isotope geochemistry of the Rodalquilar gold alunite deposit, Spain: *Economic Geology*, v. 90, p. 795-822.
- Cole, J.W., Graham, I.J., and Gibson, I.L., 1990, Magmatic evolution of late Cenozoic volcanic rocks of the Lau Ridge, Fiji: *Contributions to Mineralogy and Petrology*, v. 104, p. 540-554.
- DeMets, C., Gordon, R.G., and Stein, S., 1990, Current plate motions: *Geophysical Journal International*, v. 101, p. 425-478.
- de Ronde, C., Hannington, M.D., Stoffers, P., Wright, I., Gennerich, H.-H., Browne, P., and Herzig, P.M., 2000, Massive sulfide mineralization associated with a frontal arc volcano: Brothers hydrothermal system, Southern Kermadec arc, New Zealand, *in* Gemmell, J.B., and Pongratz, J., eds., *Volcanic environments and massive sulfide deposits: Hobart, University of Tasmania, Centre for Ore Deposit Research, Special Publication 3*, p. 37-38.
- de Ronde, C.E.J., Baker, E.T., Massoth, G.J., Lupton, J.E., Wright, I.C., Feely, R.A., and Greene, R.G., 2001, Intra-oceanic subduction-related hydrothermal venting, Kermadec volcanic arc, New Zealand: *Earth and Planetary Science Letters*, v. 193, p. 359-369.
- de Ronde, C.E.J., Faure, K., Bray, C.J., Chappell, D.A., and Wright, I.C., 2003, Hydrothermal fluids associated with seafloor mineralization at two southern Kermadec arc volcanoes, offshore New Zealand: *Mineralium Deposita*, v. 38, p. 217-233.
- Dupont, J., and Herzer, R.H., 1985, Effect of subduction of the Louisville Ridge on the structure and morphology of the Tonga Arc, *in* Scholl, D.W., and Vallier, T.L., eds., *Geology and offshore resources of Pacific island arcs-Tonga region: Circum-Pacific Council for Energy and Mineral Resources, Earth science series*, v. 2, p. 323-332.
- Ewart, A., Brothers, R.N., and Mateen, A., 1977, An outline of the geology and geochemistry, and the possible petrogenetic evolution of the volcanic rocks of the Tonga-Kermadec-New Zealand island arc: *Journal of Volcanology and Geothermal Research*, v. 2, p. 205-250.
- Frank, M.R., Candela, P.A., Piccoli, P.M., and Glascock, M.D., 2002, Gold solubility, speciation, and partitioning as a function of HCl in the brine-silicate melt-metallic gold system at 800 degrees C and 100 MPa, *in* Candela, P.A., ed., *A special issue dedicated to Heinrich D. Holland: Geochimica et Cosmochimica Acta*. v. 66. p. 3719-3732.

- Gamo, T., Okamura, K., Charlou, J.-L., Urabe, T., Auzende, J.-M., Ishibashi, J., Shitashima, K., Chiba, H., and ManusFlux Shipboard Scientific Party, 1997, Acidic and sulfate-rich hydrothermal fluids from the Manus back-arc basin, Papua New Guinea: *Geology*, v. 25, p. 139-142.
- Gao, Z., and Yao, L., 1992, A study on the thermal transformation of Suzhou kaolinite, *in* Tu, G., and Ouyang, Z., eds., *Developments in geochemistry*: Seismological Press, Beijing, p. 156-163.
- Gemmell, J.B., Binns, R.A., and Parr, J.M., 1999, Submarine, high sulfidation alteration within DESMOS caldera, Manus Basin, PNG, *in* Stanley, C.J., et al., eds., *Mineral Deposits: Processes to processing: Fifth Biennial SGA Meeting and the Tenth Quadrennial IAGOD Symposium*, London, Proceedings, p. 503-506.
- Gill, J.B., 1976, Composition and age of Lau Basin and ridge volcanic rocks: implications for evolution of an interarc basin and remnant arc. *Geological Society America Bulletin*, v. 87, p. 1384-1395.
- Gibert, F., Pascal, M.L., Pichavant, M., 2002, Gold solubility and speciation in hydrothermal solutions; experimental study of stability of hydrosulfide complex of gold (AuHS^-) at 350 to 450°C and 500 bars: *Geochimica et Cosmochimica Acta*. v. 62, p. 2931-2947.
- Glasby, G.P., Iizasa, K., Yuasa, M., and Usui, A., 2000, Submarine hydrothermal mineralization on the Izu-Bonin Arc, south of Japan; an overview: *Marine Georesources and Geotechnology*, v. 18, p. 141-176.
- Hannington, M.D., Poulsen, K.H., Thompson, J.F.H., and Sillitoe, R.H., 1999, Volcanogenic gold in the massive sulfide environment: *Reviews in Economic Geology*, v. 8, p. 325-356.
- Hannington, M.D., de Ronde, C., and Petersen, S., 2003, The spectrum of ore-forming fluids in the VMS environment: Modern and ancient: *The Geological Society of America (GSA)*, Seattle, USA, 2003, Proceedings, p. 1-1.
- Hawkins, J.W. Jr, 1974, Geology of the Lau Basin, a marginal sea behind the Tonga Arc, *in* Burk, C.A., and Drake, C.L., eds., *The geology of continental margins*: Springer, New York, p. 505-520.
- Heald, P., Foley, N.K., and Hayba, D.O., 1987, Comparative anatomy of volcanic-hosted epithermal deposits; acid-sulfate and adularia-sericite types: *Economic Geology*, v. 82, p. 1-26.
- Hedenquist, J.W., 1987, Volcanic-related hydrothermal systems in the Circum-Pacific basin and their potential for mineralization: *Mining Geology*, v. 37, p. 347-364.
- Hedenquist, J.W., Matsuhisa, Y., Izawa, E., White, N.C., Giggenbach, W.F., and Aoki, M., 1994, Geology, geochemistry, and origin of high sulfidation Cu-Au mineralization in the Nansatsu district, Japan: *Economic Geology*, v. 89, p. 1-30.

- Hedenquist, J.W., Arribas, A., Jr., and Reynolds, T.J., 1998, Evolution of an intrusion-centered hydrothermal system: Far-Southeast Lepanto porphyry and epithermal Cu-Au deposits, Philippines: *Economic Geology*, v. 93, p. 373-404.
- Herzer, R.H., and Exxon, N.F., 1985, Structure and basin analysis of the southern Tonga forearc, *in* Scholl, D.W., and Vallier, T.L., eds., *Geology and offshore resources of Pacific island arcs - Tonga region*: Circum-Pacific Council for Energy and Mineral Resources, Earth Sciences Series, v. 2, p. 55-73.
- Herzig, P.M., Hannington, M.D., and Arribas, A., 1998, Sulfur isotopic composition of the hydrothermal precipitates from the Lau back-arc: Implications from magmatic contributions to seafloor hydrothermal systems: *Mineralium Deposita*, v. 33, p. 226-237.
- Iizasa, K., Fiske, R.S., Ishizuka, O., Yuasa, M., Hashimoto, J., Ishibashi, J., Naka, J., Horii, Y., Fujiwara, Y., Imai, A., and Koyama, S., 1999, A Kuroko-type polymetallic sulfide deposit in a submarine silicic caldera: *Science*, v. 283, p. 975-977.
- Karig, D.E., 1970, Ridges and basins of the Tonga-Kermadec island arc system: *Journal of Geophysical Research*, v. 75, p. 239-254.
- Kay, S.M., and Mpodozis, C., 2001, Central Andean ore deposits linked to evolving shallow subduction systems and thickening crust: *GSA Today*, v. 11, no. 3, p. 4-9.
- Lonsdale, P., 1986, A multibeam reconnaissance of the Tonga Trench axis and its intersection with the Louisville guyot chain: *Marine Geophysical Researches*, v.8, p. 295-327.
- MacLeod, C.J., 1994, Structure of the outer Tonga forearc at Site 841, *in* Hawkins, J.W., Parson, L.M., Allan, J.F., et al., eds., *Proceedings ODP Scientific Results Leg 135*. College Station, Texas (Ocean Drilling Program), p 313-329.
- MacLeod, C.J., 1996, Geodynamics of the Tonga subduction zone and Lau backarc basin, *in* Anonymous (eds.) *AGU Fall Meeting: EOS Transactions*, American Geophysical Union, v. 77 (46), p. 325.
- McInnes, B.I.A., and Cameron, E.M., 1994, Carbonated, alkaline hybridizing melts from a sub-arc environment: Mantle wedge samples from the Tabar-Lihir-Tanga-Feni arc, Papua New Guinea: *Earth and Planetary Science Letters*, v. 122, p. 125-141.
- Mungall, J.E., 2002, Roasting the mantle: Slab melting and the genesis of major Au and Au-rich Cu deposits: *Geology*, v. 30/10, p. 915-918.
- Noll, P.D., Newsom, H.E., Leeman, W.P., and Ryan, J.G., 1996, The role of hydrothermal fluids in the production of subduction zone magmas: Evidence from siderophile and chalcophile trace elements and boron: *Geochimica et Cosmochimica Acta*, v. 60, p. 587-611.
- Ohmoto, H., and Rye, R.O., 1979, Isotopes of sulphur and carbon, *in* Barnes, H. L., ed., *Geochemistry of hydrothermal ore deposits*: New York, Wiley Intersci., p. 509-567.

- Olbertz, D., Wortel, M.J.R., and Hansen, U., 1997, Trench migration and subduction zone geometry: *Geophysical Research Letters*, v. 24, p. 221-224.
- Parson, L.M., and Hawkins, J.W., 1994, Two-stage ridge propagation and the geological history of the Lau backarc basin, *in* Hawkins, J.W., Parson, L.M., Allan, J.F., et al., eds., *Proceedings ODP Scientific Results Leg 135: College Station, Texas (Ocean Drilling Program)*, p 819-828.
- Parson, L.M., Hawkins, J.W., and Allan, J.F. et al., 1992, *Proceedings ODP, Initial Report, 135: College Station, TX (Ocean Drilling Program)*, 1320 p.
- Pelletier, B., and Louat, R., 1989, Seismotectonics and present-day relative plate motions in the Tonga-Lau and Kermadec-Havre region: *Tectonophysics* v. 165, p. 237-250.
- Petersen, S., Herzig, P.M., and Hannington, M.D., 2000, Third dimension of a presently forming VMS deposit: TAG hydrothermal mound, Mid-Atlantic Ridge, 26°N: *Mineralium Deposita*, v. 35, p. 233-259.
- Petersen, S., Herzig, P.M., Hannington, M.D., Jonasson, I.R., and Arribas, Jr., A., 2002, Submarine gold mineralization near Lihir Island, New Ireland fore-arc, Papua New Guinea: *Economic Geology*, v. 97, p. 1795-1812.
- Raitt, R.W., Fisher, R.L., and Mason, R.G., 1955, Tonga trench, *in* Anonymous, eds., *Crust of the earth (a symposium)*, p. 237-254.
- Rye, R.O., Bethke, P.M., and Wassermann, M.D., 1992, The stable isotope geochemistry of acid sulfate alteration: *Economic Geology*, v. 87, p. 225-262.
- Sager, W.W., MacLeod, C.J., and Abrahamsen, N., 1994, Paleomagnetic constraints on Tonga arc tectonic rotation from sediments drilled at Sites 840 and 841, Ocean Drilling Program Leg 135, *in* Hawkins, J.W., Parson, L.M., Allan, J.F., et al., eds., *Proceedings ODP Scientific Results Leg 135. College Station, Texas (Ocean Drilling Program)*, p 763-783.
- Sasaki, A., Arikawa, Y., and Folinsbee, R.E., 1979, KIBA reagent method of sulfur extraction applied to isotope work: *Bulletin of the Geological Survey of Japan*, v. 30, p. 241-245.
- Schwarz-Schampera, U., Herzig, P.M., Hannington, M.D., and Stoffers, P., 2001, Shallow submarine epithermal-style As-Sb-Hg-Au mineralization in the active Kermadec arc, New Zealand, *in* Piestrzynski, A. et al., eds., *Mineral Deposits at the Beginning of the 21st century: Joint Sixth Biennial SGA-SEG Meeting, Krakow, Proceedings*, p. 333-335.
- Schwarz-Schampera, U., Herzig, P.M., Gibson, H., and Stoffers, P., 2003, Auriferous pyrite mineralization in the Tonga island arc, SW-Pacific: First evidence for shallow submarine hydrothermal activity, *in* Eliopoulos et al., eds., *Mineral exploration and sustainable development: Seventh Biennial SGA meeting, Athens, Proceedings*, p. 179-182.
- Shanks, W.C. III, Böhlke, J.K., and Seal, R.R. II, 1995, Stable isotopes in mid-ocean ridge hydrothermal systems: Interactions between fluids, minerals, and organisms, *in* Humphris,

- S.E., Zierenberg, R.A., Mullineaux, L.S., and Thompson, R.E., eds., Seafloor hydrothermal systems: Physical, chemical, biological, and geological interactions: American Geophysical Union, Monograph 91, p. 194-221.
- Sillitoe, R.H., 1997, Characteristics and controls of the largest porphyry copper-gold and epithermal gold deposits in the circum-Pacific region: *Australian Journal of Earth Sciences*, v. 44, p. 373-388.
- Solomon, M., 1990, Subduction, arc reversal, and the origin of porphyry copper-gold deposits in island arcs: *Geology*, v. 18, p. 630-633.
- Stefansson, A., and Seward, T.M., 2003, The hydrolysis of gold(I) in aqueous solutions to 600°C and 1500 bar: *Geochimica et Cosmochimica Acta*. v. 67, p. 1677-1688.
- Stoffers, P., Wright, I., and Shipboard Scientific Party, 1999a, Cruise Report SONNE 135 HAVRE TROUGH: Havre Trough – Taupo Volcanic Zone: Tectonic, magmatic and hydrothermal processes; Reports Institut für Geowissenschaften, Universität Kiel Nr. 1, 250 pp.
- Stoffers, P., Hannington, M., Wright, I., Herzig, P., de Ronde, C., and Shipboard Scientific Party, 1999b, Elemental mercury at submarine hydrothermal vents in the Bay of Plenty, Taupo Volcanic Zone, New Zealand: *Geology* v. 27, p. 931-934.
- Stoffers, P., Worthington, T., Schwarz-Schampera, U., Ackermann, D., Beaudoin, Y., Bigalke, N., Fretzdorff, S., Gibson, H., Hekinian, R., Kindermann, A., Kuhn, T., Main, W., Schreiber, K., Timm, C., Tonga'onevai, S., Türkay, M., Unverricht, D., Vailea, A., and Zimmerer, M., 2003, Cruise Report SONNE 167 LOUISVILLE: Louisville Ridge: Dynamics and magmatism of a mantle plume and its influence on the Tonga-Kermadec subduction system: Reports Institut für Geowissenschaften, Universität Kiel Nr. 20, 276 pp.
- Tappin, D.R., Bruns, T.R., and Geist, E.L., 1994, Rifting of the Tonga/ Lau Ridge and formation of the Lau backarc basin; evidence from Site 840 on the Tonga Ridge, *in* Hawkins, J.W., Parson, L.M. et al., eds., Proceedings ODP, Scientific Results Leg 135: College Station, Texas (Ocean Drilling Program), p. 367-371.
- Ueda, A., and Krouse, H.R., 1986, Direct conversion of sulfide and sulfate minerals to SO₂ for isotope analyses: *Geochemical Journal*, v. 20, p. 209-212.
- Wang, L., and Zhang, Z., 1997, High-temperature phases of pyrophyllite and their evolutionary characteristics: *Chines Science Bulletin*, v. 42, p. 140-144.
- Watanabe, K., and Kajimura, T., 1993, Topography, geology, and hydrothermal deposits at Suiyo seamount: *Deep Sea Research, JAMSTEC Symposium, Proceedings*, v. 9, p. 77-89 (in Japanese with English abstract).
- Watanabe, K., and Kajimura, T., 1994, The hydrothermal mineralization at Suiyo seamount, Izu-Ogasawara arc: *Resource Geology*, v. 44, p. 133-140 (in Japanese).

- Wood, P.C., 1994, Mineralogy at the magma-hydrothermal system interface in andesite volcanoes, New Zealand: *Geology*, v. 22, p. 75-78.
- Wright, I.C., de Ronde, C.E.J., Faure, K., and Gamble, J.A., 1998, Discovery of hydrothermal sulfide mineralization from southern Kermadec arc volcanoes: *Earth and Planetary Science Letters*, v. 164, p. 335-343.
- Yan, C.Y., and Kroenke, L.W., 1993, A plate tectonic reconstruction of the Southwest Pacific, 0-100 Ma, *in* Berger, W.H., Kroenke, L.W., Janecek, T.R. et al., eds, *Proceedings ODP, Ontong Java Plateau, Scientific Results Leg 130: College Station, Texas (Ocean Drilling Program)*, p. 697-709.

Figure Captions:

Figure 1. A. Location and bathymetry of the southern Tonga island arc and parts of the southern Lau back-arc basin (central and southern Valu Fa ridge) in the back of the westward-dipping Tonga-Kermadec subduction zone, SW-Pacific. B. Bathymetric relief of volcano 1 forming one out of two major stratovolcanoes in a large contiguous complex. The summit area is dominated by a large oval caldera and two large post-caldera volcanic cones. C. Three-dimensional view of volcano 1 showing the distinctive caldera and the neovolcanic central cones. Stars refer to the Efuefu sites of hydrothermal activity taken from the respective dredge positions. D. Bathymetric relief of volcano 19, a large volcano with smooth flanks that rise to a complex summit, dominated by an old crater, an infilling cone, and a younger western crater. E. Three-dimensional view of volcano 19 showing the distinctive summit crater, the small neovolcanic cone, and the spectacular new crater in the western part. The star refers to the Uli'uli site of hydrothermal sampling taken from the respective dredge position.

Figure 2. Alteration mineralogy of scoriaceous volcanoclastic basaltic-andesitic breccias of arc volcanoes nos. 1 (Efuefu sites) and 19 (Uli'uli site) in the Tonga island arc (secondary electron images). A) Argillic alteration with fibrous clay mineral coating (dense intergrowth of illite, smectite, kaolinite, anhydrite, and amorphous silica) of a vesicle (Efuefu III). B) Authigenic hexagonal quartz polymorph (β -quartz or β -tridymite?) representing the variable style of silicification (Efuefu I). C) Cellular, vuggy silica-type alteration with few fine-grained crystals of pyrite and magnetite (Efuefu I). D) Close association of subhedral grains of native sulfur and streaks of colloform pyrite (Efuefu III). E) Close intergrowth of typically fine-grained coexisting pyrite, marcasite, and platy natro-alunite (Uli'uli). F) Close intergrowth of coexisting euhedral pyrite and rhombohedral natroalunite, commonly interpreted as being a product of steam-heated sulfate precipitation (Efuefu II). G) Abundant K-feldspar (Kf) forming

a cluster within a pyrite-bearing pore-space. The rhombic habit suggests that it might represent adularia (Efuefu I). H) Fine-grained, needle-shaped rutile, partly overgrown by amorphous silica (Efuefu III).

Figure 3. Colour and binocular photomicrographs, and SEM pictures of sulfide mineralization and textures at the Efuefu and Uli'uli sites. A) Discovery sample (167-04DR) of the Efuefu hydrothermal vent site. The sample is a 20 by 15 centimeters block of hydrothermally altered aphyric scoriaceous volcanoclastic breccia. Mineralization consists of pyrite and chalcopyrite and lines fractures and open spaces presumably related to vuggy silica-type alteration (cm-scale). B) Discovery sample (167-100DR) of the Uli'uli hydrothermal vent site. A 15 by 10 centimeter large fragment of scoriaceous volcanoclastic breccia is mineralized with very fine-grained sooty pyrite-marcasite coating vesicles within and in between scoriaceous fragments (cm-scale). C) Intergrowth of pyrite (py), chalcopyrite (cp), and hematite (ht) in a matrix of porous amorphous silica and argillic-altered scoriaceous fragments. The intergrowth lacks any indication for secondary alteration and oxidation and attests to variable ferrous/ferric redox conditions during precipitation (167-04DR). D) Fine-grained disseminated pyrite (py) – chalcopyrite (cp) intergrowth in a matrix of altered scoriaceous clasts. The sulfides display indistinct collomorphous textures (167-04DR). E) Close intergrowth of pyrite (py) and marcasite (mc). It is obvious that pyrite is replacing marcasite in a prograde hydrothermal system. Pyrite-marcasite is closely associated with cogenetic alunite (cf., Fig. 2C) (167-100DR). F) Collomorphous and porous magnetite in an open space filling (167-05DR). G) Platy hematite as a fracture filling in a scoriaceous fragment (167-04DR). H) Native gold, intergrown with magnetite (mt) in a matrix of amorphous to opaline silica. The magnetite contains numerous coexisting blebs of pyrite (py) constraining mineralization processes at the magnetite/pyrite buffer (167-05DR). I) Example of fine-grained stibnite (stb) associated with rhombohedral K-feldspar and pyrite (167-09DR). K) Binocular photograph of coarse-grained realgar (rg) associated with microcrystalline quartz and pyrite (py) in an open space filling (167-09DR). L) Association of magnetite and arsenopyrite in a matrix of amorphous silica (167-05DR). M) Microprobe element map of pyrite showing the zonal distribution of Cu reaching up to 7.14 wt.%. It is evident that the Uli'uli hydrothermal fluids attained enhanced Cu solubility but obviously did not reach the saturation for the formation of chalcopyrite (167-100DR). N) Microprobe element map of pyrite showing very fine-grained inclusions of intermediate solid solution. The composition is highly variable and may include highly elevated Zn concentrations. Pyrite shows also a zonal enrichment in As (167-04DR).

Figure 4. Mass balance calculations based on the normalization of mineralized samples at Efuefu (A) and Uli'uli (B) to the least altered basaltic andesites at volcanoes 1 and 19, respectively. Enrichments are represented by elements which are regarded typical in geothermal environments (e.g., Au, As, Se, Hg, Te).

Figure 5. Sulfur isotope ratios of sulfides and alunite from the Efuefu and Uli'uli hydrothermal sites, Southern Tonga Island Arc, in comparison to other seafloor hydrothermal systems in various tectonic settings (data from Herzig et al., 1998, Gemmell et al., 1999, de Ronde et al., 2000, 2003, Petersen et al., 2000, 2003, and references therein). EPR East Pacific Rise (mid-ocean spreading ridge); IB Izu-Bonin arc; KA Kermadec arc (frontal island arcs); CS Conical Seamount (rifted fore-arc); MB Manus Basin; OT Okinawa Trough (back-arc basins); HH Hine Hina; VL Vai Lili; WC White Church (Lau back-arc basin). SW Seawater.

Table 1. Hydrothermal sites, sample locations, and water depths of shallow submarine hydrothermal systems at arc volcanoes of the active southern Tonga volcanic arc, SW-Pacific.

Volcano	Hydrothermal Site	Location	Latitude	Longitude	Water Depth
# 1	Efuefu I	scoria cone	21°08.80' S	175°46.00' W	472 - 330 m
# 1	Efuefu II	S caldera rim	21°10.70' S	175°45.40' W	719 - 612 m
# 1	Efuefu III	NW caldera wall	21°07.70' S	175°43.70' W	474 - 325 m
# 19	Uli'uli	scoria cone	24°48.30' S	177°00.30' W	595 - 469 m

Table 2. Representative Geochemical Analyses of Mineralized and Unaltered Basaltic Andesites at the Etefuu (Volcano 1) and Uli'uli (Volcano 19) Hydrothermal Sites, Southern Tonga Island Arc, SW-Pacific

	Least Altered					Mineralized and Clay and Silica Altered										Least Altered					Mineralized and Clay and Silica Altered									
	Uli'uli					Etefuu I					Etefuu II					Etefuu III														
	100 DR-D	100DR-1	100DR-2	100 DR-A	100 DR-B	100 DR-C	04 DR-11	04DR10-1	04DR10-2	04DR10-3	04DR9-1	04DR9-2	04 DR-9	04 DR-10E	04 DR-10F	05DR20-1	05DR20-2	05 DR-17	05 DR-20	09DR-1	09DR-2	09DR-3	09 DR-A	09 DR-B	09 DR-C					
SiO ₂ (wt. %)	52.64	na	na	na	na	53.40	56.69	na	na	na	na	na	na	na	52.08	na	na	na	na	na	na	na	na	na	62.55					
TiO ₂	0.97	0.98	1.01	1.18	1.12	1.61	0.71	0.56	0.48	0.58	0.70	0.70	0.85	0.67	0.66	0.58	0.58	0.76	0.72	0.90	0.93	0.84	1.09	1.20	0.87					
Al ₂ O ₃	15.23	7.61	6.57	10.17	9.96	14.61	14.52	8.15	6.50	9.82	10.27	9.85	10.56	11.90	14.30	6.41	6.90	18.19	9.20	8.78	13.92	7.05	9.01	16.81	19.52					
Fe ₂ O ₃	13.96	13.34	10.60	8.57	10.02	11.28	11.91	7.09	9.80	7.88	10.15	7.91	6.56	5.89	4.31	10.51	15.02	9.65	10.22	5.09	5.11	7.56	5.96	4.05	7.99					
MnO	0.22	0.11	0.13	0.11	0.15	0.16	0.19	0.02	0.01	0.02	0.10	0.09	0.13	0.02	0.01	0.01	0.01	0.16	0.01	0.01	0.01	0.01	0.01	0.00	0.01					
MgO	4.93	2.19	2.11	2.31	2.86	3.26	3.67	3.78	2.59	4.69	1.87	1.81	2.42	5.11	0.23	0.10	0.08	4.05	0.13	0.10	0.37	0.16	0.09	0.31	0.12					
CaO	9.90	5.44	4.96	5.75	7.15	6.55	9.31	3.42	2.18	4.17	6.05	5.74	7.49	4.56	0.39	0.09	0.08	8.98	0.13	1.30	1.35	0.81	3.28	0.83	2.56					
Na ₂ O	2.38	2.35	2.53	2.18	2.14	1.61	2.25	2.66	2.74	2.56	3.56	3.32	2.59	2.18	2.60	3.19	2.82	2.05	2.66	2.70	2.25	2.13	2.39	1.77	2.73					
K ₂ O	0.18	0.30	0.33	0.51	0.45	0.25	0.56	0.10	0.22	0.07	0.66	0.65	0.86	0.13	0.66	0.19	0.19	0.81	0.29	0.99	0.78	0.80	1.37	1.28	1.30					
P ₂ O ₅	0.09	0.06	0.09	0.05	0.06	0.22	0.12	0.04	0.06	0.06	0.08	0.08	0.06	0.04	0.10	0.04	0.05	0.06	0.04	0.04	0.04	0.05	0.03	0.03	0.09					
S _T	0.02	6.24	3.04	4.39	2.35	1.40	0.04	2.90	5.15	2.28	3.88	3.26	1.69	2.02	9.22	11.78	14.43	0.07	14.96	1.13	3.18	4.12	1.04	3.32	1.01					
Total	100.15	38.61	31.37	35.22	36.28	99.97	99.98	28.71	29.73	31.92	37.32	33.41	33.21	32.53	100.16	32.92	40.14	44.80	38.34	21.03	27.92	23.53	24.26	29.60	100.01					
LOI	0.35	nd	nd	nd	nd	7.00	0.05	nd	nd	nd	nd	nd	nd	nd	24.82	nd	nd	nd	nd	nd	nd	nd	nd	nd	2.29					
Ba (ppm)	98	130	150	150	200	95	158	80	100	80	400	220	160	100	152	<50	<50	200	100	220	300	190	200	170	237					
Sr	223	381	422	454	383	190	183	72	54	86	244	246	247	88	289	43	64	152	89	264	360	240	318	383	410					
Rb	2.65	<15	<15	<15	<15	5.62	7	<15	<15	<15	36	<15	<15	<15	4	<15	<15	<15	<15	<15	<15	<15	<15	<15	4.5					
Cs	0.11	<1	2.00	<1	<1	0.32	0.5	<1	<1	<1	<1	<1	<1	<1	0.3	<1	1	<1	<1	<1	<1	<1	<1	1.0	0.40					
Be	<1	<1	<1	<1	<1	<1	<1	<1	<1	<1	<1	<1	<1	<1	<1	<1	<1	<1	<1	<1	<1	<1	<1	<1	<1					
Br	6.0	8.8	15	9.4	11	8.1	10.5	7.5	10.9	8.9	33.6	31.2	14.6	7.5	37.5	24	14	4.9	16	4.0	13	10	3.4	9.4	2.7					
Cr	10	13	8.0	5.0	5.0	<5	12	7	14	9	9	16	10	10	15	27	28	16	23	33	21	24	25	21	42					
V	468	381	439	437	480	310	426	302	258	325	323	326	412	334	376	359	382	351	417	277	210	274	377	218	371					
Sc	46	39	38	38	40	29	41.2	26.1	26	27.6	40	34.3	37.2	26.3	31.7	38	38	37	35	12	10	8.7	9.0	8.3	15					
Sn	<1	na	na	1.6	<1	1.0	1	<1	<1	<1	<1	<1	<1	5	<1	<1	<1	<1	<1	<1	<1	<1	<1	1.9	<1					
U	0.12	<0.5	1.1	1.2	<0.5	1.9	0.22	<0.5	<0.5	1.4	<0.5	<0.5	1.1	1.0	<1	<0.5	<0.5	<0.5	<0.5	<0.5	<0.5	2.5	<0.5	1	1.7					
Th	0.17	<0.2	<0.2	<0.2	<0.2	0.46	0.27	<0.2	<0.2	<0.2	<0.2	<0.2	<0.2	0.40	0.26	<0.2	<0.2	<0.2	0.3	<0.2	<0.2	<0.2	<0.2	<0.2	0.19					
Nb	0.29	na	na	na	na	0.91	0.60	na	na	na	na	na	na	na	1.0	na	na	na	na	na	na	na	na	na	0.64					
Zr	33	na	na	na	na	63	27.00	na	na	na	na	na	na	na	33	na	na	na	na	na	na	na	na	na	23					
Y	19	9.3	10	10	13	28	19	3.0	5.1	9.1	11	9.3	12	12	2.3	1.9	23	3.5	<1	3.3	<1	1.3	<1	2.2	4.2					
Hf	1.1	<1	<1	<1	<1	2.1	1.1	<1	<1	<1	<1	<1	1.0	<1	1.2	<1	<1	<1	<1	<1	<1	<1	<1	<1	1.0					
Ta	<0.01	<0.5	<0.5	<0.5	<0.5	0.05	0.03	<0.5	<0.5	<0.5	<0.5	<0.5	0.70	<0.5	<0.01	<0.5	<0.5	<0.5	<0.5	<0.5	<0.5	<0.5	<0.5	<0.5	0.02					
W	<0.5	<1	<1	<1	<1	<0.5	<1	<1	<1	<1	<1	<1	<1	<1	<1	<1	<1	<1	<1	<1	<1	<1	<1	<1	<0.5					
Cu	142	209	176	213	185	45	164	61	108	48	213	201	144	37	250	265	349	84	368	60	63	135	89	74	142					
Zn	108	65	64	55	70	89	113	31	28	31	55	51	58	23	14	33	30	73	23	24	23	28	20	13	28					
Pb	3.9	<3	10	11	5.2	15	12	<3	<3	<3	3.7	<3	4.5	<3	8.0	4.2	<3	<3	3.8	<3	<3	3.5	<3	<3	8.0					
Ag	<0.3	<0.3	<0.3	<0.3	<0.3	<0.3	<0.3	<0.3	<0.3	<0.3	<0.3	<0.3	<0.3	<0.3	<0.3	<0.3	<0.3	<0.3	<0.3	<0.3	<0.3	<0.3	<0.3	<0.3	<0.3					
Au (ppb)	1	10	2	2	2	2	1	26	60	23	59	107	150	16	5	6	6	4	2	6	4	2	5	5	2					
As	2.2	2.1	12	2.5	4.3	3.9	6.0	106	295	92	3.2	5.7	3.4	46	8.4	20	26	<0.5	13	8.4	14	7.0	6.3	9.6	7.9					
Sb	0.40	<0.1	0.40	0.20	0.30	<0.1	0.3	<0.1	1	<0.1	<0.1	0.3	<0.1	<0.1	<0.1	<0.1	<0.1	<0.1	<0.1	0.40	0.20	0.20	0.30	0.40	0.50					
Bi	<2	<0.1	<0.1	<0.1	<0.1	<2	<2	0.14	0.28	0.12	0.30	0.29	0.14	0.10	<2	0.16	0.20	<0.1	0.20	<0.1	<0.1	<0.1	<0.1	<0.1	<2					
Cd	0.69	<0.3	<0.3	<0.3	<0.3	0.65	<0.3	<0.3	<0.3	<0.3	<0.3	0.63	<0.3	<0.3	0.91	<0.3	<0.3	<0.3	1.09	<0.3	<0.3	<0.3	<0.3	<0.3	<0.3					
Hg (ppb)	na	24	35	15	7.4	<5	na	23	19	107	196	103	12	8.3	73	294	325	<1	327	12	48	87	9.0	61	6.2					
Mn	1727	813	984	817	1183	1262	1433	119	84	139	756	736	1026	139	93	37	41	1265	42	46	39	51	71	33	70					
In	<0.1	<0.2	<0.2	<0.2	<0.2	<0.1	<0.2	<0.2	<0.2	<0.2	<0.2	<0.2	<0.2	<0.2	<0.1	<0.2	<0.2	<0.2	<0.2	<0.2	<0.2	<0.2	<0.2	<0.2	<0.1					
Tl	0.07	0.19	<0.1	<0.1	<0.1	0.07	0.10	<0.1	<0.1	<0.1	0.57	0.58	0.36	<0.1	1.7	0.15	0.18	<0.1	0.15	0.16	0.13	0.15	0.17	0.15	0.20					
Ge	1.7	0.15	0.12	0.15	0.14	1.1	1.8	<0.1	<0.1	<0.1	0.16	0.12	1.1	<0.1	0.70	0.38	0.29	0.22	0.55	0.10	0.14	0.14	0.11	0.11	1.00					
Ga	17	na	na	na	na	16	15	na	na	na	na	na	na	na	13	na	na	na	na	na	na	na	na	na	15					
Co	41	52	33	34	32	31	33	27	45	29	33	25	22	21	26	37	38	28	44	21	17	52	20	16	51					
Ni	13	17	14	28	11	4.2	18	12	15	11	15	13	17	10	24	27	29	16	41	8.5	10	21	13	12	21					
Se	<3	18	13	27	3.1	<3	<3	1.4	4.6	2.5	21.11	18.83	7.50	<0.1	26	16	24	0.35	26	4.6	16	15	<0.1	12	5.0					
Mo	<2	1.3	4.8	<1	<1	3.03	<2	8.9	6.4	10	3.2	3.6	8.2	<1	7.6	12	13	3.3	8.2	4.5	8.1	3.2	4.0	8.2	<2					
Te	na	2.0	1.4	1.1	0.82	na	na	3.1	5.6	3.2	1.4	2.0	0.80	1.8	na	1.1	1.5	0.29	2.7	1.3	6.1	4.8	0.55	5.0	na					
La	1.5	2.0	3.0	1.6	2.1	3.1	1.7	1.8	2.6	2.0	2.1	1.7	1.5	1.4	0.9	1.7	1.7	1.9	1.3	1.0	0.90	1.0	0.80	0.60	0.89					
Ce	4.4	7.0	7.0	<3	6.0	8.2	4.4	4.0	7.0	6.0	7.0	6.																		

Table 3. Mineralogy of Altered and Mineralized Volcanic Rocks (volcanoes 1 & 19) from the Southern Tonga Island Arc (tr. = traces).

Ore minerals:	Other:
pyrite	quartz
chalcopyrite	crystalobalite ± tridymite
marcasite	natroalunite
magnetite	barite
hematite	anhydrite
tr. pyrrhotite	amorphous silica
arsenopyrite	native sulfur
realgar	illite-smectite
stibnite	tr. kaolinite
rutile	chlorite
intermediate solid solution	tr. adularia
native gold	tr. calcite
	mullite
	tr. atacamite

Table 4. Summary of Microprobe Analyses (in wt. %) of Selected Ore Minerals from the Efuefu and Uli'uli Vent Sites, Southern Tonga Island Arc, SW-Pacific.

Mineral	(N)	Fe	Cu	Zn	Sb	As	Co	Se	Bi	Ni	Tl	Hg	Ag	Au	S	Total												
Efuefu																												
Pyrite	Efuefu I	187	46.17	0.04	[0.86]	0.01	[0.11]	<0.01	[0.07]	0.24	[1.82]	0.03	[0.42]	0.01	[0.04]	0.01	[0.1]	0.02	[0.19]	nd	na	0.01	[0.11]	<0.01	[0.07]	53.42	99.97	
Pyrite	Efuefu II	115	45.61	0.19	[1.61]	0.01	[0.14]	<0.01	[0.05]	0.04	[0.38]	0.05	[1.47]	<0.01	[0.02]	0.01	[0.07]	0.02	[0.30]	<0.01	[0.09]	na	0.01	[0.11]	<0.01	[0.06]	52.97	98.95
Pyrite	Efuefu III	112	46.30	0.02	[0.59]	0.02	[0.17]	<0.01	[0.06]	<0.01	[0.07]	<0.01	[0.08]	0.02	[0.14]	0.01	[0.07]	<0.01	[0.04]	nd	<0.01	[0.09]	<0.01	[0.05]	<0.01	[0.05]	54.43	100.85
Pyrrhotite	Efuefu II	3	59.69	0.98	[1.07]	0.02		<0.01	[0.02]	nd		0.25	[0.29]	0.08	[0.12]	<0.02	[0.03]	0.16	[0.20]	nd	na	<0.01	[0.02]	nd		38.68	99.87	
Marcasite	Efuefu I	42	45.56	0.15	[0.77]	<0.01	[0.04]	<0.01	[0.03]	nd	[0.02]	<0.01	[0.06]	0.05	[0.17]	nd	[0.04]	0.01	[0.04]	nd	na	<0.01	[0.05]	<0.01	[0.05]	53.42	99.31	
Marcasite	Efuefu II	4	45.99	<0.02	[0.05]	<0.01	[0.03]	<0.01	[0.02]	<0.01	[0.02]	<0.01	[0.02]	<0.01	[0.03]	0.02	[0.06]	<0.01	[0.01]	nd	na	nd	[0.01]	<0.01	[0.01]	53.55	99.63	
Marcasite	Efuefu III	52	46.70	<0.01	[0.11]	<0.01	[0.06]	<0.01	[0.05]	<0.01	[0.02]	<0.01	[0.04]	0.01	[0.05]	0.01	[0.07]	<0.01	[0.03]	nd	<0.01	[0.08]	<0.01	[0.05]	<0.01	[0.08]	54.52	101.32
Chalcopyrite	Efuefu I	36	30.07	34.42		nd	[0.02]	<0.01	[0.05]	0.03	[0.44]	<0.01	[0.21]	0.01	[0.04]	0.01	[0.07]	<0.01	[0.04]	nd	na	0.05	[0.15]	0.01	[0.09]	34.75	99.06	
Chalcopyrite	Efuefu II	1	31.05	30.04		0.07		nd		nd		nd		0.04		nd			nd	na	nd		nd		36.88	98.09		
ISS	Efuefu I	5	33.92	2.96	[6.82]	16.78	[36.86]	<0.01	[0.05]	0.14	[0.30]	nd		nd		nd			nd	na	<0.01		nd		47.34	101.17		
Arsenopyrite	Efuefu II	6	35.53	<0.01	[0.02]	<0.02	[0.05]	0.02	[0.04]	44.00		0.05	[0.07]	0.19	[0.23]	<0.01	[0.02]	<0.02	[0.05]	nd	na	<0.01	[0.03]	<0.01	[0.04]	22.28	101.53	
		(N)	Fe ₂ O ₃	TiO ₂	V ₂ O ₃	MgO	MnO	Al ₂ O ₃	SiO ₂	NiO	CoO	Total																
Hematite	Efuefu I	19	92.18	3.87	[19.43]	0.73	[2.32]	0.08	[0.29]	0.02	[0.06]	0.28	[0.72]	0.27	[7.22]	0.01	[0.08]	0.01	[0.06]	98.75								
		(N)	Fe ₃ O ₄	TiO ₂	V ₂ O ₃	MgO	MnO	Al ₂ O ₃	SiO ₂	NiO	CoO	Total																
Magnetite	Efuefu II	31	89.43	4.89	[10.69]	0.32	[4.62]	1.35	[3.11]	0.34	[0.54]	1.62	[2.51]	0.92	[6.30]	0.03	[0.09]	0.04	[0.09]	98.93								
		(N)	Fe	Cu	Zn	Sb	As	Co	Se	Bi	Ni	Tl	Hg	Ag	Au	S	Total											
Uli'uli																												
Pyrite		104	45.53	0.73	[7.14]	0.01	[0.30]	<0.01	[0.06]	0.02	[0.09]	0.03	[0.30]	0.02	[0.05]	0.01	[0.07]	<0.01	[0.06]	nd	0.02	[0.10]	0.01	[0.11]	<0.01	[0.05]	53.71	100.09
Marcasite		102	46.46	0.03	[0.32]	<0.01	[0.04]	<0.01	[0.06]	0.02	[0.08]	<0.01	[0.03]	0.03	[0.08]	0.01	[0.08]	<0.01	[0.04]	nd	0.01	[0.08]	0.01	[0.08]	<0.01	[0.06]	53.91	100.49

Note: Average values in wt.%; numbers in parentheses are maximum reported concentrations

Abbreviations: nd = not detected, na = not analyzed

Table 5. Calculated composition (averages and ranges) of the Uli'uli and Efuefu hydrothermal precipitates, Southern Tonga Island Arc, normalized to ideal massive pyrite composition (46.55 wt.% Fe, 53.45 wt.% S).

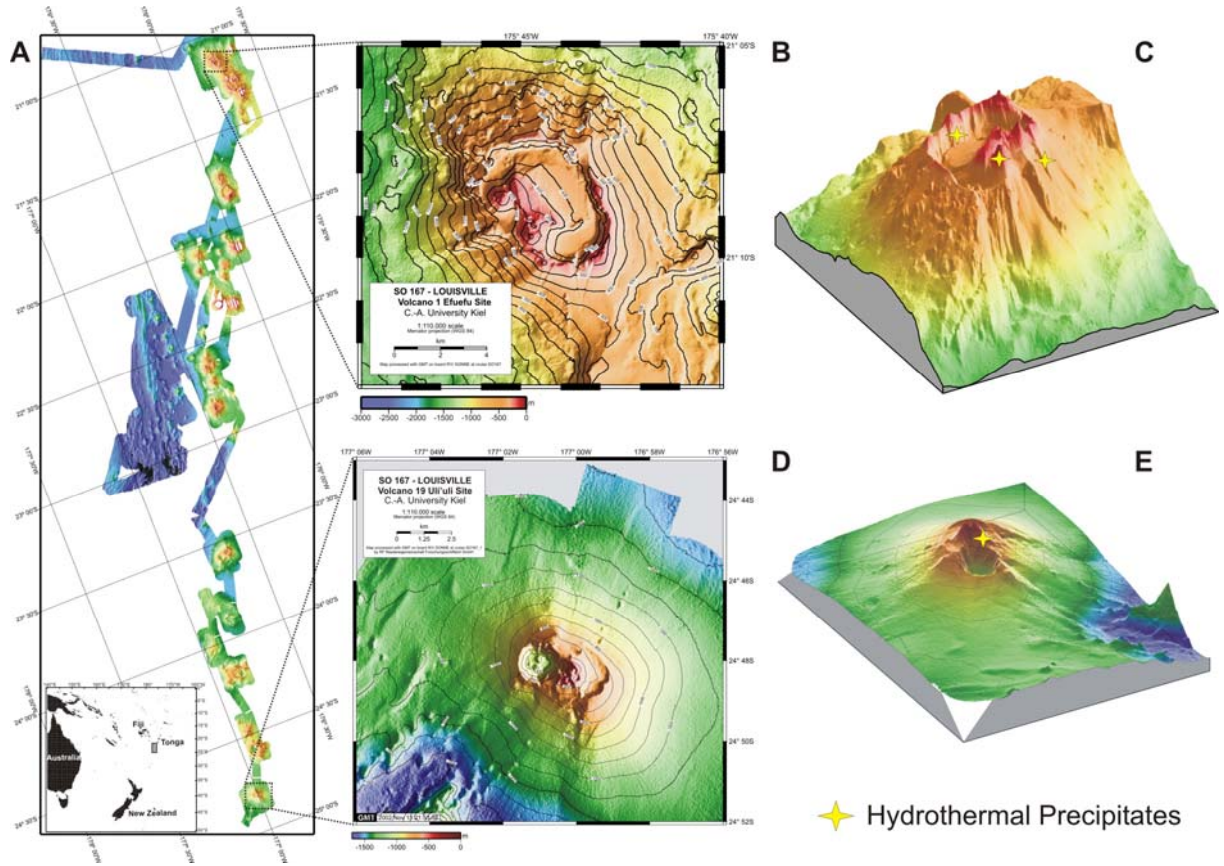
	Uli'uli				Efuefu			
	average	range			average	range		
Cu (wt. %)	0.27	0.17	-	0.42	0.59	0.10	-	6.7
Pb (ppm)	251	119	-	571	135	14	-	422
Au	0.09				0.89	0.02	-	4.8
As	101	18	-	211	620	44	-	3062
Sb	5	2	-	7	11	3	-	26
Hg	0.29	0.17	-	0.61	0.97	0.20	-	2.7
Tl	2	2	-	3	6	1	-	11
Se	197	70	-	331	175	26	-	308
Te	18	14	-	24	56	5	-	228

Table 6. Sulfur Isotope Ratios of Sulfides and Sulfates from the Efuefu and Uli'uli hydrothermal systems, Southern Tonga Island Arc (py = pyrite, cp = chalcopyrite, mc = marcasite, al = alunite, anh = anhydrite, ba = barite)

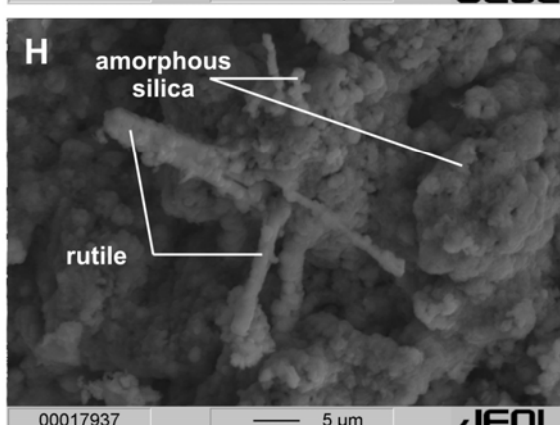
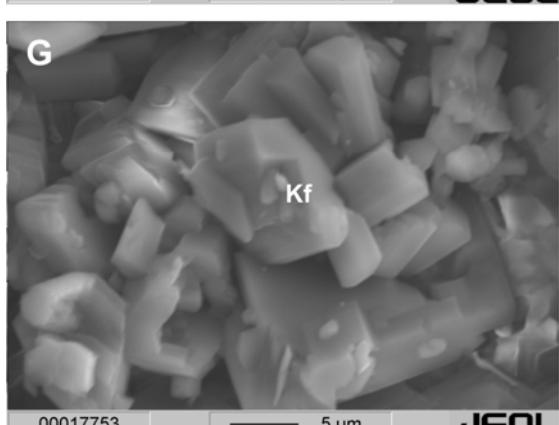
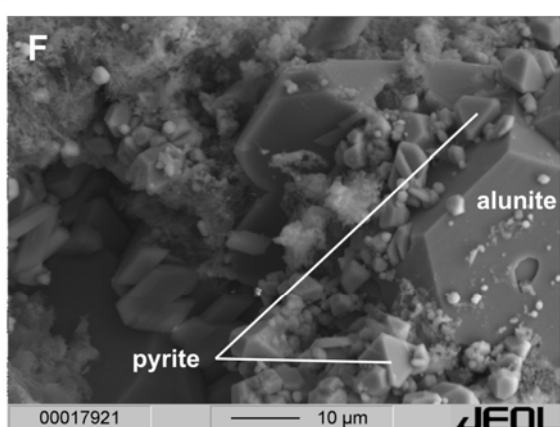
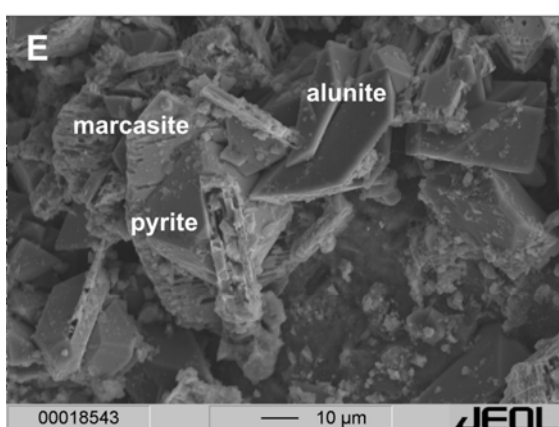
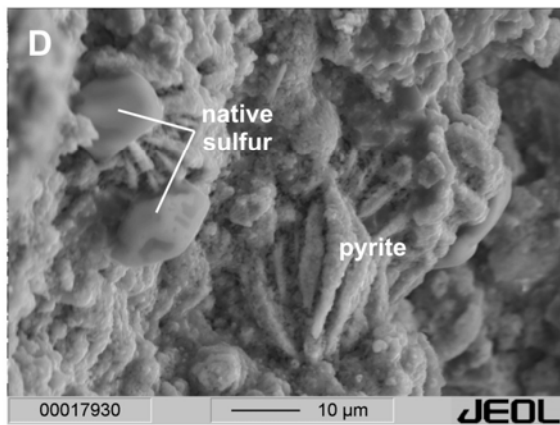
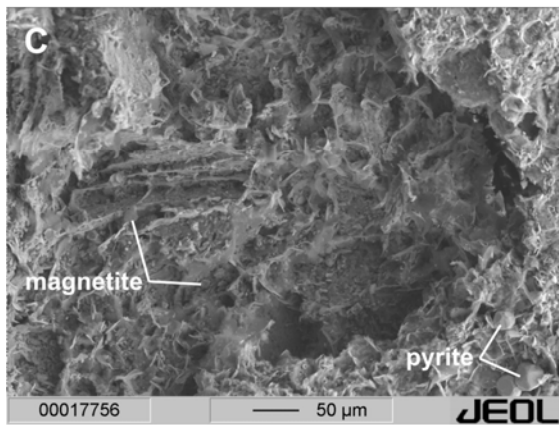
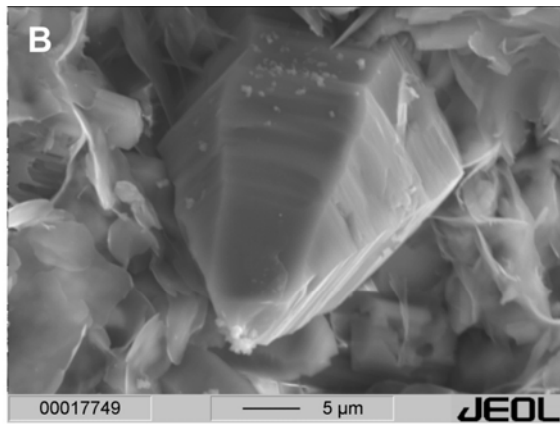
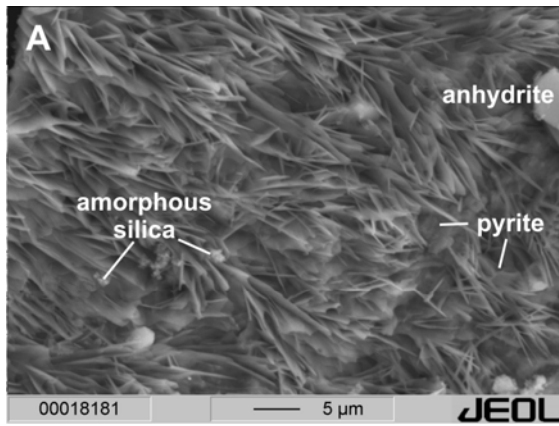
Sample no.	Sulfides		Sulfates	
	Mineralogy	$\delta^{34}\text{S}\text{‰}$	Mineralogy	$\delta^{34}\text{S}\text{‰}$
Efuefu I				
167-04DR-9	py-(cp)	-2.7		
167-04DR-9	py-(cp)	-2.9		
167-04DR-10E	cp-py	-0.2		
167-04DR-10E	cp-py	-0.2		
167-04-DR-10E	cp-py	-0.6	al-(ba-anh)	6.0
167-04DR-10F	py	2.0		
Efuefu II				
167-05DR-17	py-(cp)	-2.9		
167-05DR-20	py	-2.0		
167-05DR-20a	py	-8.8		
167-05DR-20b	py	-6.3		
167-05-DR-20	py	-9.8	al	9.9
Efuefu III				
167-09DR-Ai	py-mc	-7.2		
167-09DR-Aii	py-mc	-12.3		
167-09-DR-Aiii	py-mc	-12.1	al-anh-(ba)	0.5
167-09DR-Bi	py-mc	-5.4	al-anh-(ba)	18.5
167-09-DR-11	py-mc	-17.5	al-anh-(ba)	15.5
Uli'uli				
167-100DR-1	mc-py	-1.1		
167-100DR-2	mc-py	-0.2	al-(anh)	18.9
167-100-DR-C1	mc-py	-4.9	al-(anh)	11.9
167-100-DR-C2	mc-py	-5.1	al-(anh)	15.8

Table 7. Sulfur Isotope Fractionations (after Ohmoto and Rye, 1979) and Assumed Sulfate-Sulfide Equilibrium Temperatures for the Efuefu and Uli'uli Hydrothermal Systems, Southern Tonga Island Arc.

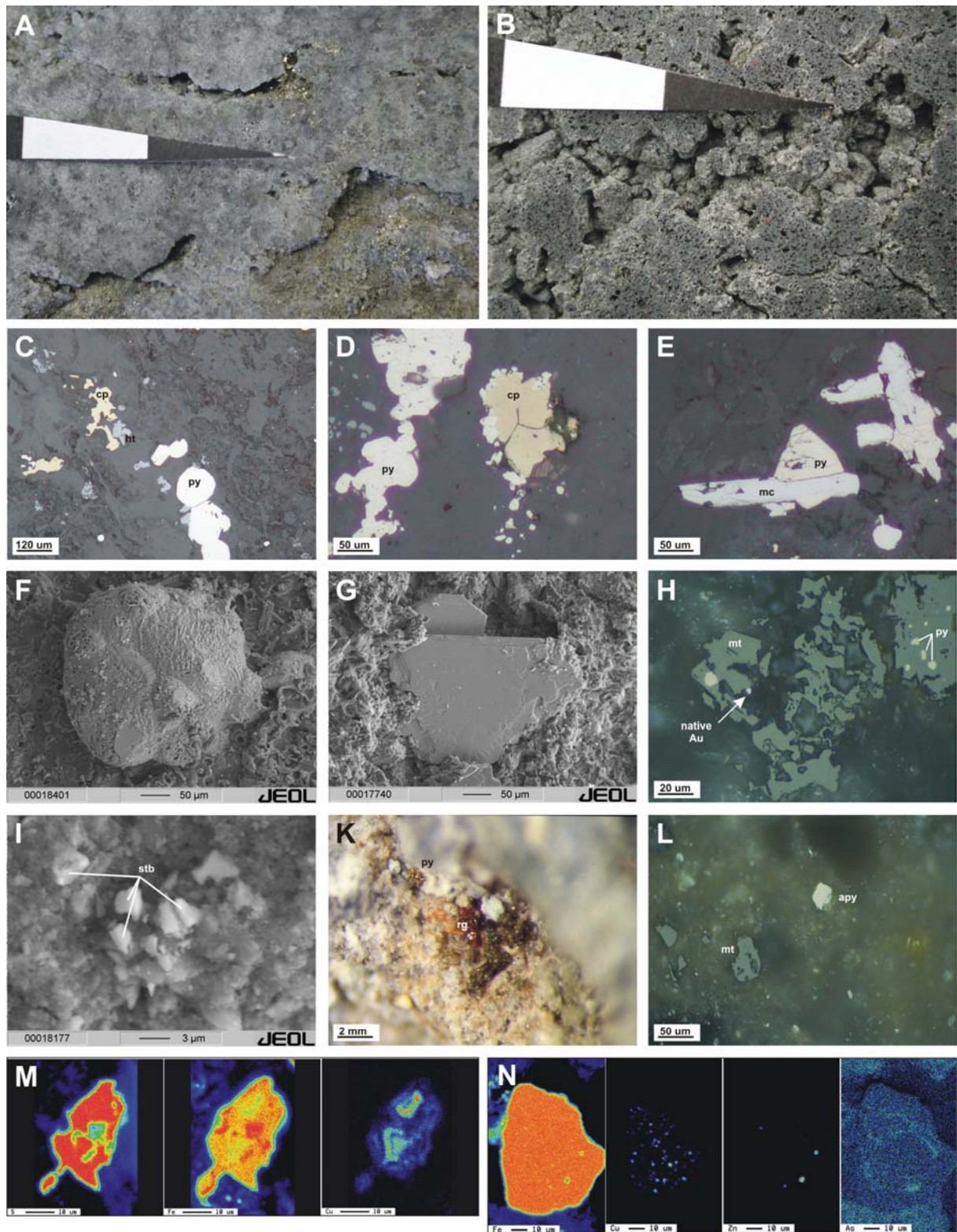
Sample no.	Sulfides	Sulfates	T(°C) (Ohmoto & Rye, 1979)
	$\delta^{34}\text{S}_{\text{‰}}$	$\delta^{34}\text{S}_{\text{‰}}$	
Efuefu I			
167-04-DR-10E	-0.6	6.0	2573
Efuefu II			
167-05-DR-20	-9.8	9.9	322
Efuefu III			
167-09-DR-Aiii	-12.1	0.5	585
167-09DR-Bi	-5.4	18.5	248
167-09-DR-11	-17.5	15.5	151
Uli'uli			
167-100DR-2	-0.2	18.9	336
167-100-DR-C1	-4.9	11.9	398
167-100-DR-C2	-5.1	15.8	298



Schwarz-Schampera et al., Figure 1



Schwarz-Schampera et al., Figure 2



Schwarz-Schampera et al., Figure 3

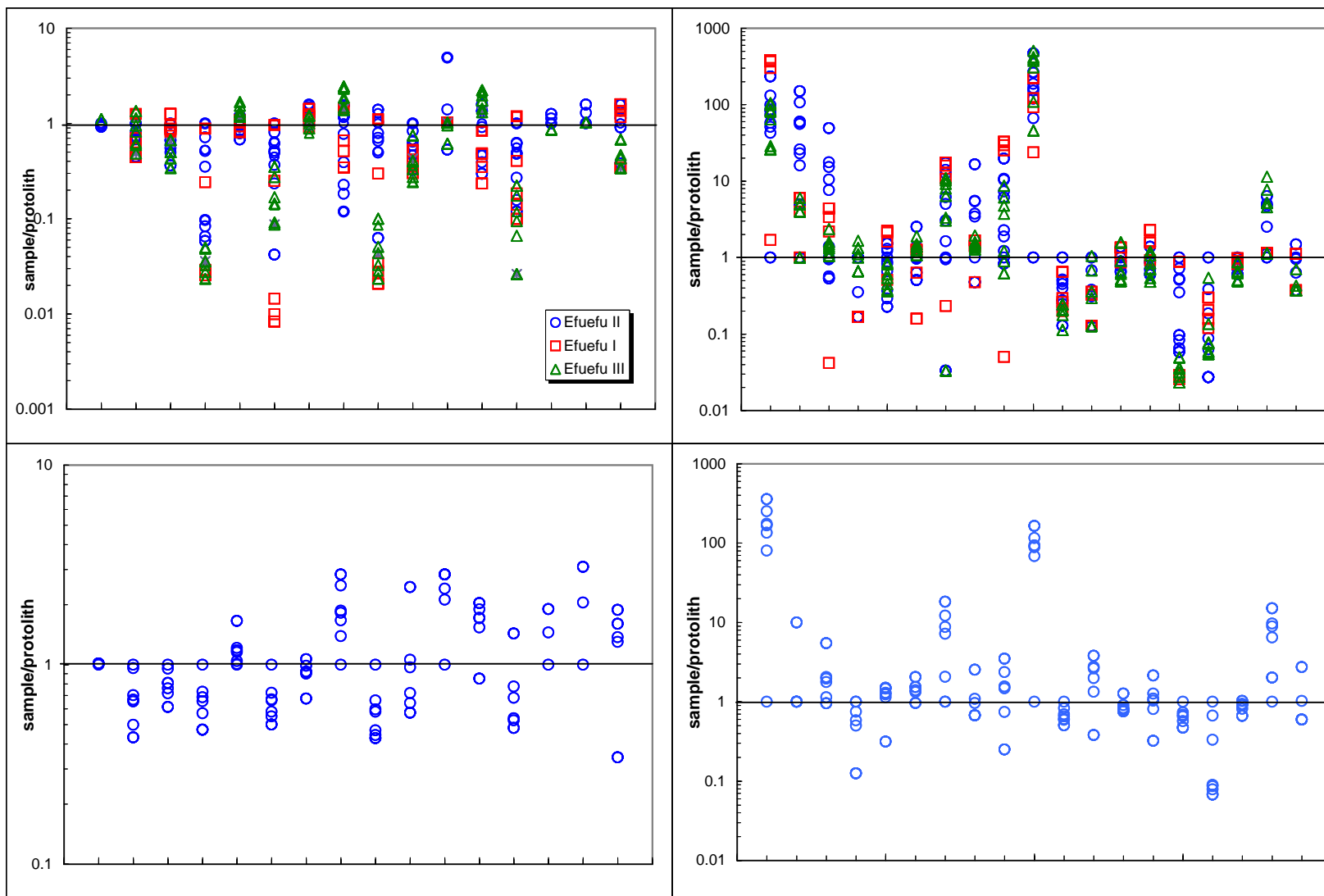


Figure 4. Mass balance calculations based on the normalization of mineralized samples at Eufefu (A) and Uli'uli (B) to the least altered basaltic andesites at volcanoes 1 and 19, respectively. Enrichments are represented by elements which are regarded typical in geothermal environments (e.g., Au, As, Se, Hg, Te).

Hydrothermal activity and magma genesis along a propagating back-arc basin: the Valu Fa Ridge (Southern Lau Basin)

S. Fretzdorff^{1*}, U. Schwarz-Schampera², H. Gibson³, C.-D. Garbe-Schönberg¹, F. Hauff⁴, P. Stoffers¹

¹ Institut für Geowissenschaften, Abteilung Geochemie, Christian-Albrechts-Universität zu Kiel, Olshausenstrasse 40, 24118 Kiel, Germany

² Bundesanstalt für Geowissenschaften und Rohstoffe (BGR), Alfred-Bentz-Haus Stilleweg 2, 30655 Hannover, Germany

³ Department of Earth Sciences, Laurentian University, Sudbury, Ontario, P3E 2C6, Canada

⁴ IFM-Geomar, Dienstgebäude Ostufer, Forschungsbereich 4, Wischhofstr. 1-3, 24148 Kiel, Germany

* Corresponding author-

Dr. Susanne Fretzdorff

e-mail: sf@gpi.uni-kiel.de

tel: +49-431-880 2085

fax: +49-431-880 4376

Submitted to-

J. Geophys. Res.

Version of-

18 July 2005

Word counts-

Abstract: 211

Main text: 5955

References-

70

Tables-

2

Figures-

7

Electronic Supplement-

1

Hydrothermal activity and magma genesis along a propagating back-arc basin: the Valu Fa Ridge (Southern Lau Basin)

S. Fretzdorff¹, U. Schwarz-Schampera², H. Gibson³, C.-D. Garbe-Schönberg¹, F. Hauff⁴, P. Stoffers¹

¹ Institut für Geowissenschaften, Abteilung Geochemie, Christian-Albrechts-Universität zu Kiel, Olshausenstrasse 40, 24118 Kiel, Germany

² Bundesanstalt für Geowissenschaften und Rohstoffe (BGR), Alfred-Bentz-Haus, Stilleweg 2, 30655 Hannover, Germany

³ Department of Earth Sciences, Laurentian University, Sudbury, Ontario, P3E 2C6, Canada

⁴ IFM-Geomar, Dienstgebäude Ostufer, Forschungsbereich 4, Wischhofstr. 1-3, 24148 Kiel, Germany

Abstract

Valu Fa Ridge is an intraoceanic back-arc spreading center located at the southern prolongation of the Lau basin. Bathymetric observations as well as detailed sampling has been carried out along the spreading axis in order to trace hydrothermal and volcanic activity and to study magma generation processes. The survey shows that widespread lava flows from recent volcanic eruptions covered most of the Vai Lili hydrothermal vent field, only diffuse low-temperature discharge and the formation of thin layers of siliceous precipitates have been observed. Evidence of present day hydrothermal activity at the Hine Hina site is indicated by a thermal anomaly in the overlying water column. Our studies did not reveal any signs of hydrothermal activity neither above the seismically imaged magma chamber at 22°25'S nor across the southern rift fault zone (22°51'S). Lavas recovered along the Valu Fa Ridge range from basaltic andesites to rhyolites with SiO₂ contents higher than reported from any other intraoceanic back-arc basin. Based on the highly variable degrees of crystal fractionation along axis, the development of small disconnected magma bodies is suggested. In addition, the geochemical character of the volcanic rocks shows that the transition zone from oceanic spreading to propagating rifting is located south of the Hine Hina vent field in the vicinity of 22°35'S.

1. Introduction

Propagating spreading centres are bounded by pseudofaults with a V-shaped appearance pointing towards the migration of the spreading axis [e.g. Hey, 1977; Hey et al., 1989]. It has been recently suggested that magma generation beneath propagating spreading centers works independent of its location at mid-ocean ridges or back-arc basins [Fleutelot et al., 2005]. This paper presents new bathymetric and geochemical data from the Valu Fa Ridge; a back-arc spreading center located at the southern prolongation of the Lau basin. The studied region

is characterized by intense tectonic and magmatic activity and represents an excellent example to study magma generation processes from the segment center to the propagating ridge tip. Highly differentiated lava have been erupted at Valu Fa Ridge [e.g. *Vallier et al.*, 1991], with SiO₂ contents higher than reported from any other oceanic back-arc basin or mid-ocean ridge. Several authors [e.g., *Fouquet et al.*, 1993; *Perfit et al.*, 1999] suggest that the development of hydrothermal systems is often associated with the emplacement of silica-rich volcanic rocks, and propose a genetic relationship between magmatism, tectonism and hydrothermal activity along oceanic spreading ridges. In November 2002, the R/V Sonne (cruise SO167) surveyed the area between 22°S and 23°S with high resolution swath bathymetry (Fig. 1a), back-scattered imaging and video observation to locate recent tectonic, magmatic, and hydrothermal activity and to investigate the onset of coeval magma-induced hydrothermal activity. Furthermore, the rift and seamount structures south of the Valu Fa Ridge were studied in detail to identify tectonic propagators and to explore a possible relation between hydrothermalism and evolving propagating rift tips.

Fresh volcanic rocks were sampled at the spreading segments, the southern propagating rift tip and at bathymetric highs south of the Valu Fa spreading axis (Fig. 1a). The bathymetry and structural interpretations for the southern Valu Fa Ridge are presented here along with geochemical data of the lavas. These data are used to evaluate the extend of subduction processes influencing magma generation beneath the propagating Valu Fa Ridge and to explore rift tectonic processes and related volcanism.

2. Tectonic setting

The triangular shaped Lau Basin is composed of three major, active spreading ridges, the Central Lau Spreading Center (CLSC), the Eastern Lau Spreading Center (ELSC), and the southernmost part south of 21°20'S, which is referred to as the Valu Fa Ridge [*Jenner et al.*, 1987a; *Vallier et al.*, 1991]. Over the past 5–5.5 Ma, the Lau Basin back-arc opened by successive southward propagation of seafloor spreading centers [*Hawkins*, 1995a; *Hawkins*, 1995b]. It is one of the fastest spreading back-arc centre in the world with full rates between 90 mm/a at 18°S and 65 mm/a at 21°S [*Taylor et al.*, 1996]. Subduction rates of the 100 to 140 Ma old Pacific plate along the Tonga trench varies between 240 mm/a in the north and 165 mm/a in the south [*Bevis et al.*, 1995]. The Valu Fa spreading ridge extends for at least 165 km, is 5 to 6 kilometers wide with ridge flanks rising about 600 m above the surrounding seafloor and is propagating southward into Miocene island arc crust at about 22°45'S [*Wiedicke and Collier*, 1993, *Taylor et al.*, 1996]. The close proximity to the Tofua island arc,

about 40 km to the west, makes this back-arc region in particular interesting for studying interactions between the mantle wedge and the subducting slab. Geophysical studies [e.g. *Stackelberg et al.*, 1988] suggest that the Valu Fa Ridge is divided into three ridge sections, i.e. the southern, central and northern Valu Fa Ridge (SVFR, CVFR, NVFR). However, *Wiedicke and Collier* [1993] interpreted a much more differentiated ridge segmentation and recognized 11 volcanic ridge edifices (nos. 3 to 14; segments nos. 3 to 6 belong to the SVFR, nos. 7 to 9 to the CVFR, and nos. 10 to 14 to the NVFR; Fig. 1). Apart from the three main overlapping spreading segments, the offsets between the individual segments are generally in the order of 0.4 – 2.3 km and affect only the neovolcanic zone at the ridge crest [*Wiedicke and Collier*, 1993]. From the detailed bathymetric map recorded during SO167 it is clear that, besides the active ridge axis, several seamounts of unknown origin occur south of the ridge tip and possibly mark juvenile magmatic activity as a precursor to the evolving rift.

Seismic data indicate that the central Valu Fa Ridge is underlain by a steady axial magma chamber [*Collier and Sinha*, 1990, *Collier and Sinha*, 1992; 1996; *Day et al.*, 2001; Fig. 1a]. The reflection is continuous for at least 10 km, and may extend to 20 km on a profile recorded along the entire axis of the Valu Fa Ridge from 22°10 to 22°30 [Fig. 1a; e.g. *Collier and Sinha*, 1992]. The top of the magma reservoir is interpreted to be 2-3 km wide and located 3.2 km below the sea floor which is relatively deep compared to those found along mid-ocean ridges [e.g. 1.2 – 2.4 km beneath the East Pacific Rise; *Detrick et al.*, 1987]. The well-defined seismic reflectors, and a large reflective coefficient, as well as the flattened top are most likely related to a low-density, highly viscous siliceous melt. A discontinuity in the seismic record towards the CVFR probably reflects thinning of the crystal mush zone and would imply that the overlapping spreading centre between CVFR and NVFR (between V10 and V9 on Fig. 1a) is currently the side of enhanced magmatism [*Turner et al.*, 1999; *Day et al.*, 2001].

3. Bathymetric observation: morphology, hydrothermal and volcanic activity

Bathymetric profiles and video observation across the Valu Fa Ridge spreading axis have been recorded in order to trace hydrothermal and volcanic activity. From north to south there is a systematic eastward shift in the propagation of the ridge axis and an echelon orientation of the ridge segments (Fig. 1). The topography of the Valu Fa Ridge is rather flat, comparable to fast-spreading mid-ocean ridges (Fig. 1b). To the south, the Valu Fa Ridge evolves into a system of tectonic halfgraben and graben.

The Vai Lili and Hine Hina hydrothermal fields are located at overlapping ridge segments on topographical highs (Fig. 1b). Below follows a brief overview of the segments from north (no. V9) to south (no. V5).

3.1. The Vai Lili Segment (No. V9)

In 1989, the French submersible *Nautile* discovered the Vai Lili hydrothermal field and found high-temperature black and white smokers [Fouquet *et al.*, 1989; 1991; 1993]. Apart from the hydrothermal deposits, they identified brecciated lava forming eruptional cones and black rippled volcanoclastic debris in the Vai Lili area. Fouquet *et al.* [1993] have suggested that Vai Lili is in a volcanic / tectonic stage. During SO167, our survey showed significant interim changes of the Vai Lili hydrothermal vent field. We observe the coverage of the Vai Lili area by sediment-free, glassy 'aa-type' aphyric lava flows that were mapped over an area of 850 m x 400 m. Since the flows were not noticed during previous surveys [cf. Fouquet *et al.*, 1989; 1993] a revival of volcanism is suggested. This is in accordance with geophysical observations which locate the greatest crustal thickness beneath this overlapping spreading center and has been interpreted to focus upwelling melt and thereby enhance magmatism [Turner *et al.*, 1999; Day *et al.*, 2001].

Sampling of the recent lava flows by dredging and TV-guided grab revealed neither hydrothermal alteration nor a massive sulfide-forming system. Beside the 'aa-type' flows, pillow lavas are observed (250m x 150m) along a north-south bounded elongated horst-like structure. Assuming the pillow lava flow is younger than the 'aa-type' lavas, the occurrence of white, hydrothermally altered basalt xenoliths in unaltered 'aa' lava indicates that the 'aa-type' flow was erupted after or during an earlier mineralization event. The active chimneys identified during the NAUTILAU cruise [Fouquet *et al.*, 1989; 1991; 1993] were not observed during our survey. As both our OFOS and TV-guided grab positioning was well-constrained during the tracks, we suggest that recent volcanic eruptions covered most of the hydrothermal Vai Lili vent field. Ongoing hydrothermal activity at the former Vai Lili site was recorded by diffuse low-temperature discharge, the formation of thin layers of siliceous precipitates on glassy lavas, and slightly elevated water temperatures.

3.2. Central Valu Fa Ridge (Segment No. V7)

The small distance (2–3 km) between two lines of volcanic edifices and the lack of off-ridge structures were interpreted in terms of rapid and fairly recent southward extension of this segment [Wiedicke and Collier, 1993]. A strong temperature anomaly (between 5 to 15°C) was reported close to the ridge axis at the southern tip at approximately 22°26.0'S and

176°42.5'W in water depths between 1800 and 2000 m based on XBT profiles [Peirce *et al.*, 1996]. Our SIMRAD mapping showed small-scale ridge axis discontinuities up to 250 m marked by volcanic edifices that are about 120–200 m high in water depths between 2000 m and 1940 m. The whole ridge segment has an asymmetric shape, with steeper slopes on the eastern side to water depths of about 2200 m and shallow slopes towards the west (2100 m). Video observations verified that this ridge segment is in a tectonic stage that lacks any evidence of recent volcanic activity. The top of the ridge is dominated by lobate and minor pillow lava flows that are partially covered by grey pelagic sediment. The occurrence of numerous fissures and no evidence of recent (i.e., non-sedimented) volcanic rocks or volcanoclastic sediments suggests that this ridge segment has been volcanically inactive for some time. Still this segment appears tectonically active as a result of continued extension and associated spreading. Our survey did not reveal any signs of ongoing hydrothermal activity (i.e., hydrothermal crust or vent fauna associated with hydrothermal activity) or thermal anomalies in the overlying water column due to diffuse low-temperature discharge. The reported temperature anomaly in the southern part of the segment could not be verified. Single outcrops displayed reddish to yellowish staining which is probably related to cold seawater alteration. Sampling was carried out during three dredges on bathymetric highs of single volcanic edifices in water depths between 2120 m and 1900 m, above the magma chamber (Fig. 1a).

3.3. The Hine Hina Segment (No. V5)

Prior to SO 167 the Hine Hina hydrothermal field was surveyed in 1989 [Fouquet *et al.*, 1989; 1991; 1993]. Important observations were that Hine Hina is in a volcanic stage and that the hydrothermal system is divided into two topographically distinct parts [e.g. Fouquet *et al.*, 1993]. The deeper part is hosted by massive lava flows and has a focused discharge along faults while the upper parts are characterized by volcanoclastic material and diffuse low-temperature venting. In contrast to the significant changes observed at the Vai Lili site, the morphology, tectonic fabric, and volcanological features at this ridge segment have not changed significantly since the last survey in 1989. We suggest that extensive low-temperature hydrothermal discharge at the Hine Hina site is a product of a volcanic environment which is markedly different from that of the Vai Lili segment. Deposits of black volcanoclastic sand are extensive and occur for more than 1000 m along the entire length of the mapped ridge segment. Mapping and TV-guided sampling indicate that the black–grey volcanic sand underlies a hydrothermal Fe-Mn oxyhydroxide crust where it may attain

thicknesses of several meters. Locally, up to 35 cm sized volcanic bombs with thick glass crusts were observed. The morphology of the sand grains, the occurrence of bombs and the volume of sand are consistent with an origin from several small explosive magmatic and hydrovolcanic eruptions during submarine fire-fountaining. The thin (<5–7cm thick) but extensive Fe-Mn oxyhydroxide crust covers much of the upper part of the ridge. It may be a product of unfocussed, diffuse low temperature hydrothermal discharge, facilitated by the permeability of the underlying porous volcanic sand. Hydrothermal activity probably continued after fire-fountain eruptions, as suggested by altered and mineralized clasts in the volcanic sand and the development of Fe-Mn oxyhydroxide crusts on the surface of some lava fragments. Evidence of present day hydrothermal activity is indicated by a thermal anomaly in the overlying water column, shimmering water and white–yellow biological mats.

3.4. The Southern Rift Fault Zone (22°51'S)

The Valu Fa spreading ridge ends at 22°45'S, while two large seamounts immediately south of the ridge tip may represent the initial stage of southward ridge propagation [*Wiedicke and Collier, 1993*]. Structures south of the ridge tip indicate distinct faults that parallel the regional strike of the VFR (N20°E) and its eastward offset (Fig. 1b). Bathymetric highs of inferred sedimented island arc crust SE of the southernmost Valu Fa Ridge segment are bounded by one of the largest fault zones [*Wiedicke and Collier, 1993*]. During SO167, we surveyed a segment of old island arc crust along the SE extension of the southern Valu Fa Ridge tip at 22°51.40'S, 176°44.40'W. The large-scale westward-facing fault-zone indicates the eastern limit of a neovolcanic zone and may represent one of the major structures for recent volcanic eruptions (Fig. 1b). The objectives of our work in this area were to define and map structures that may represent the southern rift propagator, and to locate any sites of recent rift-related volcanism and/or hydrothermal activity. An east–west orientated, 1 km-long, video observation traverse showed that most of the ocean floor in this area is represented by older ocean floor and volcanic edifices covered by a relatively thick (centimeters to decimeters) light grey sediment blanket. Ridges of lobate flows and talus are interpreted to trace faults within the relatively smooth, flat sediment-covered ocean floor. A prominent, 100 m wide and almost 50 m deep rift graben subparallel to the strike of the Valu Fa Ridge may represent the volcanically and tectonically active southern propagator. The graben is characterized by vertical walls with blocky talus and young lobate and tubular flows covering the graben floor. The location of the graben on a topographic high may be related to magmatic doming as well as high-level magma emplacement and would suggest that this fault

is part of the actively southward propagating Valu Fa rift system close to the Tonga island arc 40 km east of the ridge.

4. Sampling

The central Valu Fa Ridge at segment V9 (22°13'S) hosting the Vai Lili hydrothermal vent field, the southward propagating segment V7 (22°25'S), the segments V5 (22°32'S) hosting the Hine Hina hydrothermal field and V3 (22°40'S) at the ridge tip, and the propagating rift in the southward extension of the spreading axis (22°51'S) have been mapped and sampled with dredges and a TV-guided grab (Fig. 1a). In addition, a series of rock samples from seamounts south of the Valu Fa Ridge, recovered during R/V Sonne cruise SO67 in 1990 [Fig. 1a; *Mihe*, 1994], were included in order to more fully constrain magma generation south of the propagating rift.

Samples from the Vai Lili site are mostly fresh aphyric lava covered with glassy rims, similar to segment V7 and V5 (Hine Hina vent field) where fresh glassy aphyric pillow fragments were obtained. At Hine Hina black volcanic sand, Fe-Mn crusts, altered and sulphide mineralized rock fragments have been also recovered. The southernmost segment provided fresh glassy plagioclase-phyric lava, aphyric pillow fragments, but also black aphyric volcanic sand and Fe-Mn crusts that are comparable to those found at Hine Hina. A variety of rock types including fresh glassy aphyric lava fragments, olivine basalt and plagioclase phyric lava locally covered with Fe-oxyhydroxide patches were recovered from the southern rift fault zone.

5. Geochemistry

5.1. Major and trace elements

Major and trace element analyses are presented in Table 1. The Valu Fa Ridge samples range from basaltic andesite to rhyolite and are members of the low-K series, with a few seamount lavas south of the ridge tip showing medium-K basaltic composition (Fig. 2). Interestingly, volcanics from segment V7 have SiO₂ contents up to 72 wt.%, higher than reported from any other intra-oceanic back-arc basin, and are likely to reflect extensive crystal fractionation. Although the seismically imaged magma chamber underlies the ridge from 22°10'S to 22°30'S [e.g. *Collier and Sinha*, 1992; Fig. 1a], dacites and rhyolites have only been erupted at the southern end of the magma chamber. Lavas from the southern tip and seamounts south of the spreading ridge are enriched in K₂O (wt.%) and lie within the geochemical field of the central Tonga Island arc (Fig. 2). Generally, the Tonga Island arc is

characterized by higher K_2O at similar SiO_2 concentrations, compared to the Valu Fa Ridge and Lau Basin lavas, while latter have distinct lower K_2O values (Fig. 2).

According to experimental data incompatible elements such as Na_2O are diluted in the melt as the degree of melting increases [e.g. *Falloon et al.*, 1988; *Hirose and Kushiro*, 1993; *Hirose and Kawamoto*, 1995]. In order to evaluate the melting processes beneath the Valu Fa Ridge, the geochemistry is corrected for the effects of crystal fractionation by calculating the Na_2O contents to a common 8% MgO after *Plank and Langmuir* [1992b]. In order to limit possible errors, only samples with $>2\%$ MgO were selected. There is a slight decrease in Na_8 values of the samples from north to south (Fig. 3). The Vai Lili region shows highest Na_8 composition and is also characterized by a broad range of Na_8 values. Lowest Na_8 lavas occur at a seamount located in the prolongation of the V3 segment (see location in Fig. 1; Fig. 3). Generally, Na_8 values at the southern tip of the ridge are lower than those calculated for Ata Island lavas (ca. 40 km east of the ridge).

Chondrite-normalized REE patterns are shown in Figure 4. All samples of the active Valu Fa spreading axis and most of the seamount lavas have $(La/Lu)_N$ ratios between 0.7 and 0.9; except some seamounts south of the ridge with $(La/Lu)_N = 1.0 - 1.2$. The majority of the patterns run parallel to N-MORB (Fig. 4). For comparison, REE patterns of Ata Island lavas are also shown in Figure 4. They are enriched in LREE and depleted in HREE with $(La/Lu)_N$ ratios up to 1.7. The REE patterns of the high-silica rocks sampled at $22^\circ 25'S$ are characterized by a negative Eu anomaly suggesting plagioclase fractionation prior to eruption.

Incompatible trace element ratios, e.g. Zr/Nb and Nb/Yb (Fig. 5a) are almost constant along the spreading axis of the Valu Fa Ridge. The rhyolites at $22^\circ 25'S$ show slightly higher Zr/Nb ratios which may be attributed to fractional crystallization processes [e.g. *Kamber and Collerson*, 2000] and lavas from the southern tip are characterized by lower Nb/Yb ratios (see discussion below). The lavas south of the ridge are very heterogeneous covering a wide range of e.g. Zr/Nb (30 – 100) and Nb/Yb (0.1 – 0.7; Fig. 5a). Nb/U ratios of the Valu Fa Ridge lava series vary between 2 and 10 with a slight decrease from north to south indicating variable enrichment of U relative to N-MORB [*Hofmann*, 1988; Nb/U: 49]. Similarly, the Ce/Pb ratios of the Valu Fa lavas are lower than those of N-MORB [*Hofmann*, 1988; Ce/Pb: 25] and show a clear decrease from 12 to 2 from the Vai Lili field to the seamounts at the southern prolongation of the ridge (Fig. 5b). Th/Nb ratios lie within 0.2 and 1.1, thus are clearly higher than those of N-MORB [*Hofmann*, 1988; Th/Nb: 0.05]. They are almost constant along the ridge up to the southern tip where elevated ratios are observed. The southern prolongation shows a wide range of Th/Nb between 0.2 and 1.1 (Fig. 5c).

5.2. Radiogenic isotope data

Both, Sr and Nd isotope ratios of the Valu Fa Ridge and seamount lavas lie within a restricted range between $^{87}\text{Sr}/^{86}\text{Sr} = 0.7032 - 0.7034$ and $^{143}\text{Nd}/^{144}\text{Nd} = 0.51301 - 0.51309$ with no recognizable latitudinal ($^{\circ}\text{S}$) variations (Fig. 5d,e). The range in Pb isotopic composition is somewhat broader and a distinct decrease of Pb isotope ratios along the ridge is apparent, e.g. $^{208}\text{Pb}/^{204}\text{Pb}$ decrease from 38.4 in the north to 38.2 at the southern prolongation of the spreading axis (Fig. 5f). Notably, the Pb composition of the recently sampled Vali Lili lava is slightly less radiogenic than the lava sampled in 1990 in very close vicinity [Bach et al., 1998; Fig. 5f]. On a $^{208}\text{Pb}/^{204}\text{Pb}$ versus $^{206}\text{Pb}/^{204}\text{Pb}$ isotope correlation diagram our new data plot in the field of the southern-central Tonga Island arc and overlap with lavas from ODP Sites 834 and 839 [Ewart et al., 1994; Hergt and Hawkesworth, 1994; Fig. 6]. We also note, that new data plots within the Pacific rather the Indian MORB field (Fig. 6b).

6. Degree of melting and subduction influence

The range of major and trace element compositions covered by the Valu Fa Ridge lavas can be explained as the product of crystal fractionation processes. However, some geochemical heterogeneity along the ridge and southern prolongation suggests differences in partial melting and variable subduction influence.

Nb and Yb concentrations are nearly independent of source composition, but vary with the degree of melting; hence Nb/Yb ratios are potential indicators for varying degrees of melting of the mantle wedge [e.g. Pearce and Peate, 1995]. Together with the calculated Na_8 values, which are inversely related with the degree of mantle melting [Klein and Langmuir, 1987], it is possible to derive assumptions about the melting processes beneath the Valu Fa Ridge, the southern prolongation, and Ata Island (representative for the central Tonga arc). The Nb/Yb ratios along the ridge are nearly constant, but generally lower than N-MORB [0.9: Hofmann, 1988; Fig. 5a]. Assuming that N-MORB is produced by 10% batch melting of a depleted mantle peridotite, we suggest that the Valu Fa lava serie is generated at higher degrees of melting above 10%, based on the much lower Nb/Yb ratios. This is in good agreement with the degree of melting estimated for back-arc basins influenced by fluid flux from the slab [Davies and Bickle, 1991; Pfänder et al., 2002]. The region south of Hine Hina is characterized by slightly lower Nb/Yb ratios, thus, lavas are probably generated at even higher degrees of melting. The seamount lavas in the prolongation of the Valu Fa Ridge show a wide range of Nb/Yb ratios as well as of Na_8 values which probably reflects varying degrees

of mantle melting (Fig. 3, 5a). Earlier studies on a small sample set of Valu Fa Ridge and Ata Island lava suggested large degrees of melting between 15 and 25% beneath the spreading axis and greater than 25% for the central Tonga Island arc [Peate *et al.*, 2001]. Taking into account the variation of Na_8 values along the ridge and compare those to Ata Island lavas, their degrees of melting should be slightly higher than those of the Valu Fa spreading ridge (Fig. 3). The ridge tip south of Hine Hina, however, is characterized by distinctly lower Nb/Yb ratios and low Na_8 compositions implying even higher degrees of melting (Figs. 3 and 5a). The most obvious explanation for such lava compositions is that fluids from the subducted slab increased the degree of melting by lowering the mantle solidus.

Positive correlations between H_2O and U have been observed in glasses from the Mariana, East Scotia Ridge, and Lau Basin [Stolper and Newman, 1994; Peate *et al.*, 2001; Fretzdorff *et al.*, 2002]. These studies show, that U can serve as a proxy for fluid addition from the subducting slab to the magma source taking into account the potential H_2O degassing in highly evolved rocks. The behaviour of Yb in subduction zone environments is generally considered “conservative”, because a significant slab contribution of this element to the magma source is mostly not detected [e.g. Pearce and Peate, 1995]. In the diagram U versus Yb (Fig. 7), the Valu Fa Ridge and the Tonga Island arc lava suites display clear positive trends parallel to each other. These within-suite correlations reflect individual crystal fractionation trends with relatively primitive rocks plotting at the low ends and evolved rocks at the high ends of the arrays. The shift towards higher U for a given Yb concentration suggests variable contributions from a fluid component, with Lau Basin samples showing the lowest and Tonga Island arc rocks the highest influence (Fig. 7). Volcanic rocks from the southern tip and the southern prolongation of the Valu Fa spreading axis show elevated U concentrations indicating higher fluid contribution from the subducting slab compared to the rest of the Valu Fa lava suite (Fig. 7). Similarly, these lavas have high Ce/Pb ratios (Fig. 5b), since Pb is highly mobile in fluids relative to Ce [e.g. Miller *et al.*, 1994], this supports our assumption of a high fluid flux beneath the southern ridge tip, hence higher degrees of partial melting at the southern tip of the spreading axis due to fluid contributions from the subducting slab. The distinct decrease in Ce/Pb ratios along the Valu Fa Ridge spreading axis from north to south indicates the preferential addition of Pb towards the south. Such a slab-derived fluid may also consist of variable components, derived from dehydration of basaltic crust and from dewatering of sediments [Ishikawa and Tera, 1999; Class *et al.*, 2000]. Surprisingly, this distinct trend along the back-arc ridge is neither correlated with incompatible trace element ratios indicating varying degrees of partial melting nor with the Na_8 compositions. Since Pb is

extremely soluble in hydrous fluids [Keppler, 1996], a possible explanation for the observed discrepancy is, that the added amount of a fluid component is too low to influence the mantle solidus, but has a visible effect on the Pb concentrations and Pb isotope ratios (see also Figs. 5b, 6). Another explanation is the input of Pb by a sediment melt which does not lead to significantly higher degrees of partial melting [e.g. Class et al., 2000]. Sediment input should lower, for example, the $^{144}\text{Nd}/^{143}\text{Nd}$ ratios [e.g. average south Pacific sediment from DSDP 204: 0.51265; Ewart et al., 1998]. However, there is no evidence for a sediment “fingerprint” in the Nd-isotopic composition of the Valu Fa and Ata Island lavas (Fig. 5e), thus the Pb component was most likely not carried with a sediment melt. A third explanation for the Pb-along axis variation is the presence of a heterogeneous mantle source beneath the Valu Fa Ridge which will be discussed below (see chapter 8).

7. Comparison with other propagating rifts, i.e. the North Fiji Basin

The tip of the propagating North Fiji back-arc basin is characterized by relatively low degrees of melting (ca.16%), whereas in the central part of the basin the melting starts deeper and reaches a higher rate (up to 22%), based on dynamic partial melting of a thermally heterogeneous rising mantle at different depths [Fleutelot, 2005]. This is in agreement with petrogenetic processes at propagating mid-ocean ridge spreading centres such as at Galapagos and Juan de Fuca. Thus, Fleutelot et al. [2005] suggest that magmatic processes along propagating back-arc and mid-ocean ridge spreading centers are comparable. However, our studies show high degrees of mantle melting beneath the propagating ridge tip whereas the lavas erupted at the center of the Valu Fa Ridge have been generated at considerably lower degrees. Consequently, the observation of Fleutelot et al. [2005] seems not valid for all oceanic back-arc basins. Hence, it has to be distinguished between the tectonic and geological settings of propagating back-arc basins with respect to the influence of subduction, and the vicinity to the island arc front. However, similarities between other propagating ocean ridges and the Valu Fa Ridge include the occurrence of extensive crystal fractionation processes about 30 km behind the rift tip. This is in accordance with the observation of [Sinton et al., 1983] suggesting that the maximum of differentiation proceeds within 50 km behind propagating ridge tips and the eruption of the most differentiated lavas some 20 km behind the propagating North Fiji rift tip [Fleutelot, 2005]. Interestingly, the Valu Fa Ridge lavas are characterized by highly variable degrees of differentiation (between 50 and 70 SiO₂ wt.%), even along the seismically imaged magma chamber area. It has been suggested that differentiation variations along ocean ridges may be related to the presence of pseudo-faults.

These systems may represent cold walls, which stop the along-axis magma migration and lead to the development of small disconnected magma bodies [Caroff and Fleutelot, 2003]. Magmas may become more fractionated in larger than in smaller magma bodies due to prolonged residence times [e.g. Sinton et al., 1983]. Based on the highly variable degrees of crystal fractionation, this structural conditions could be apply to the studied area of the Valu Fa Ridge. Thus, there is probably a magma body beneath segment V7 at 22°25'S which is larger than those beneath the adjacent ridge segments. Furthermore, the strong fractionation (Fig. 2), the highly structured and tectonically active state at segment V7 strongly suggest a large potential for hydrothermal circulation. The sampled area, however, does not show any indication for recent hydrothermal activity.

8. Mantle Source – Mantle flow

Hergt and Hawkesworth [1994] suggested a southward displacement of an Indian Ocean MORB by Pacific-type mantle as a result of slab rollback, accompanied by the southward migration of the Valu Fa Ridge into island arc crust. Furthermore, lavas erupted along the Havre Trough between 24° - 29°S reflect Pacific MORB isotopic character and support the model in which Indian-type replaces Pacific-type mantle in the region north of Havre Trough [Haase et al., 2002]. Indeed, isotopic composition of the central and eastern Lau Basin implies that the magma source is very similar to Indian Ocean MORB-type, whereas the mantle source beneath Valu Fa Ridge is characterized by a Pacific-type signature [e.g. *Loock et al.*, 1990; *Peate et al.*, 2001; Fig. 6a]. In contrast, Pb isotope signatures of samples from the northern part of the Valu Fa Ridge are clearly associated with the Indian Ocean MORB field (Fig. 6b). *Haase et al.* [2002] studied the magma generation processes and mantle dynamics along the Kermadec Arc – Havre Trough comparing them to those of the Tonga Island arc and Lau Basin. Based on end-member composition modelling, they have calculated a possible fluid composition from the altered oceanic crust with elevated $^{208}\text{Pb}/^{204}\text{Pb}$ ratios of 38.4 (Fig. 6b). Addition of such a fluid probably have influenced the northern Valu Fa Ridge samples and “push” them into the Indian Ocean MORB field, i.e. overprint their Pacific MORB signature. This is in accordance with mass balance calculations of *Bach et al.* [1998] suggesting that the northern Valu Fa lavas are influenced by a significant addition of subducted altered oceanic crust and subordinate by sediment melt. Our samples have relatively unradiogenic $^{208}\text{Pb}/^{204}\text{Pb}$ ratios that plot well within the Pacific MORB field (Fig. 6b). Both, trace element ratios and isotopic composition from the southern part of the Valu Fa Ridge and southern seamounts resemble very closely those of the volcanic rocks from ODP

Site 839, located west of the Eastern Lau Basin [Ewart *et al.*, 1994; Fig. 6]. This lava sequence is interpreted to reflect an older remnant of a “proto-central Tonga arc” crust and is compositionally very similar to the active central and southern Tonga island arc [Ewart *et al.*, 1994; Fig. 6]. The Pb isotopic composition of lavas from the southern part of the Valu Fa Ridge implies that this part is underlain by the same Pacific-type mantle wedge source generating the basalts from the ODP site 839 and feeding the central and southern Tonga arc volcanoes. The latter are dominated by partial melting of the mantle wedge with addition of fluids from the dehydrating altered oceanic crust and minor contributions from the subducted sediments [Turner and Hawkesworth, 1997; Turner *et al.*, 1997]. The sediment addition is less than 0.5% and takes place as small degree partial melts in equilibrium with ilmenite and rutile, based on the very low concentrations of Ta and Nb [Turner *et al.*, 1997].

Our results show, that the transition from spreading to propagating rifting, hence the compositional change of the mantle wedge, is most likely located south of the Hine Hina field, in the vicinity of 22°35'S, evidenced by, e.g. the decrease in Ce/Pb, increase of Th/Nb ratios, and elevated U ppm concentration (Fig. 5c, 6a, 7). Notably, lavas erupted at Vai Lili show “bimodal” compositions for their $^{87}\text{Sr}/^{86}\text{Sr}$, $^{208}\text{Pb}/^{204}\text{Pb}$ and Ce/Pb ratios, probably due to different eruption ages. The younger lavas that cover most of the Vai Lili vent field (see chapter 3.1), show high $^{208}\text{Pb}/^{204}\text{Pb}$ and therefore represent the active spreading phase. The rocks that are similar in composition to the Tonga island arc likely reflect an older rifting phase.

9. Conclusions

1. Detailed bathymetric maps of the central and southern Valu Fa Ridge show a rather flat topography, comparable to fast-spreading mid-ocean ridges. To the south, the ridge evolves into a system of tectonic halfgraben and graben.

2. Vai Lili field is characterized by a revival of volcanism with lava flows erupted after 1993 covering most of the hydrothermal vent field. Ongoing hydrothermal activity at the former Vai Lili site was only recorded by diffuse low-temperature discharge.

3. Several small explosive eruptions during a phase of submarine fire-fountaining took place at the Hine Hina vent field. Hydrothermal activity continued after fire-fountain eruptions evidenced by a thermal anomaly in the overlying water column, shimmering water and white–yellow biological mats found during our survey.

4. The striking topographic high with a deep graben structure observed at the southern rift fault zone at 22°51'S may be related to magmatic doming which would suggest that this structure is the actively southward propagating Valu Fa rift system close to the Tonga island arc.

5. Valu Fa Ridge samples range from basaltic andesite to rhyolite with SiO₂ contents up to 72 wt.%. Although the seismically imaged magma chamber underlies the ridge from 22°10'S to 22°30'S, dacites and rhyolites have only been erupted at their southern end. We suggest that the magma chamber is divided into several small disconnected magma bodies and that the evolved magma generated in a large magma body due to prolonged residence time. The maximum of differentiation proceeds about 30 km behind the propagating Valu Fa ridge tip, hence fits into the general models of crystal fractionation processes along propagating spreading ridges.

6. Although the eruption of highly fractionated lavas at 25°25'S points to a site of ongoing hydrothermal activity as it is the case for other of hydrothermal fields [*Perfit et al., 1999*], our survey did not reveal any signs of ongoing hydrothermal activity or thermal anomalies in the overlying water column. The highly structured and tectonically active state at segment V7, however, strongly suggest a large potential for hydrothermal circulation.

7. The degrees of melting beneath the studied area are 5 to 10% higher than reported for N-MORB, volcanic rocks from the southern tip of the ridge show degrees of melting above 25%. The seamounts at the southern prolongation of the ridge are characterized by variable degrees of melting, probably in the range of 15 to 25%.

8. The striking topographic high with a deep graben structure observed at the southern rift fault zone at 22°51'S may be related to magmatic doming which would suggest that this structure is the actively southward propagating Valu Fa rift system close to the Tonga island arc.

9. Radiogenic isotope ratios of lava erupted south of the Hine Hina field are similar to those of the ODP Site 839, located west of the Eastern Lau Basin representing old island arc crust. Thus we suggest that the transition from spreading to propagating rifting, i.e. the compositional change of the mantle wedge is located in the vicinity of 22°35'S.

Acknowledgements

We thank Captain Kull, crew and shipboard scientific party of RV *SONNE* cruise SO167 for their expertise and help during the sampling program. Many thanks to P. Appel, B. Mader and

A. Weinkauff for assistance with the major element analyses. This work was funded by the Bundesministerium für Bildung und Forschung (BMBF grant 03GO167A and B).

Appendix

Analytical Techniques

Where possible, fresh glass chips were separated from lava blocks, washed several times with deionized water and picked under a binocular microscope. The major element compositions of the glasses were determined on a JEOL JXA 8900R electron microprobe at Kiel University. This instrument operates with a 10 μm defocused beam, a 10 nA beam current, a 15 kV acceleration voltage and is calibrated against natural glass standards. Precision and accuracy relative to VG-2 were both better than 1 % [2σ] for all major elements. Subsets of glass fragments were ground to powder in an agate mortar and used for trace element and isotope analyses. Cores of the freshest whole rock material were cut, coarse crushed, thoroughly washed in deionized water, and then milled to a fine powder in an agate mortar. For major element determinations, 0.6 grams of powder was mixed with lithium tetraborate and ammonium nitrate, fused to a homogeneous glass bead, and analyzed using a Philips PW1400 XRF spectrometer (Universität Kiel) equipped with a Rh tube and calibrated against international rock standards (Table 1). Precision (2σ) for most major elements was better than 1 %, with exceptions being TiO_2 , Na_2O and P_2O_5 (~ 5 %), and accuracy relative to VG-2 was better than 1 % (Table 1). Loss on ignition was determined by weight loss of 3 g of powder heated to 1000 °C for 2 hours in a silica crucible.

Concentrations of 33 trace elements were determined by ICP mass spectrometry after pressurized HF-aqua regia digestion of approx. 100 mg pulverized sample, made up to a solution with < 0.1 % total dissolved solids in subboiled 2 % (v/v) nitric acid. Prior to analysis, sample digest solutions were 10fold diluted and spiked with 5 ng/ml indium (In) and rhenium (Re) for internal standardisation. The instrument was calibrated using aqueous multi-element calibration standards without further matrix matching. All measurements were done using an Agilent 7500c ICP-MS instrument under standard operating conditions with plasma shield on, but no gas in the octopole reaction cell. Sample solution was introduced using a self-aspirating PFA micro-nebulizer (100 $\mu\text{l}/\text{min}$ sample uptake) in combination with a standard Scott-type spray chamber maintained at 4 °C. The analytical results represent averages of 3 replicate measurements after subtraction of a laboratory reagent blank. For analytical quality control procedural blanks (“Blank”) and international reference standards were prepared and analysed along with the sample series. Results for the international rock standards BIR and BHVO-1 [both from US Geol. Survey; see suggested values of *Jenner et al., 1990; Govindaraju, 1994*] are reported in Table 1. Standards and 3 samples were digested in duplicate yielding differences of the results well below 1-3 % rel. for all elements. Instrument stability was monitored by re-analysing one sample every 11 samples, and precision as calculated from 6 replicate analyses covering 27 hours was < 1-2 % RSD for all elements. Further details of the sample preparation procedure and instrument calibration strategy can be found in *Garbe-Schönberg [1993]*.

Sr, Nd, Pb isotopic compositions are shown in Table 2 and were determined in static mode on the TRITON and MAT 262 RPQ²⁺ thermal ionization mass spectrometers (TIMS) at IFM-GEOMAR. Prior to dissolution, samples were leached for 1 hour in hot 6N HCl (powders) and 3N HCl (glass chips) and thereafter repeatedly rinsed with 18.2M Ω water. Sample chromatography followed *Hoernle and Tilton [1991]*. Applied isotope fractionation corrections are $^{86}\text{Sr}/^{88}\text{Sr} = 0.1194$ and $^{146}\text{Nd}/^{144}\text{Nd} = 0.7219$, with all errors reported as 2σ standard errors of the mean. Analyses of NBS 987 over the course of this study yielded $^{87}\text{Sr}/^{86}\text{Sr} = 0.710261 \pm 10$ (n = 5) and sample values are reported relative to $^{87}\text{Sr}/^{86}\text{Sr} = 0.71025$ for NBS 987. The in-house Nd monitor SPEX gave $^{143}\text{Nd}/^{144}\text{Nd} = 0.511714 \pm 4$ [n = 3] and has been previously calibrated with $^{143}\text{Nd}/^{144}\text{Nd} = 0.511706 \pm 12$ (n = 10) against La

Jolla at $^{143}\text{Nd}/^{144}\text{Nd} = 0.511848 \pm 8$ ($n = 10$). A mass bias correction of $\sim 0.11\%$ /amu is applied to the Pb isotope data based on repeated measurements of NBS 981 [$n = 6$; $^{206}\text{Pb}/^{204}\text{Pb} = 16.904 \pm 9$, $^{207}\text{Pb}/^{204}\text{Pb} = 15.443 \pm 11$, $^{208}\text{Pb}/^{204}\text{Pb} = 36.545 \pm 36$] and normalization to the NBS 981 values reported in *Todt et al.* [1996]. Total chemistry Pb blanks were typically below 100pg and thus considered negligible.

References

- Bach, W., J. Erzinger, L. Dosso, J. Bollinger, H. Bougault, J. Etoubleau, and J. Sauerwein (1996), Unusually large Nb-Ta depletions in North Chile ridge basalts at $36^{\circ}50'$ to $38^{\circ}56'S$: major element, trace element, and isotopic data, *Earth Planet. Sci. Letts.*, *142*, 223-240.
- Bach, W., E. Hegner, and J. Erzinger (1998), Chemical fluxes in the Tonga subduction zone: Evidence from the southern Lau Basin, *Geophys. Res. Letts.*, *25*, 1467-1470.
- Bevis, M., F.W. Taylor, B.E. Schutz, J. Recy, B.L. Isacks, S. Helu, R. Singh, E. Kendrick, J. Stowell, B. Taylor, and S. Calmant (1995), Geodetic observations of very rapid convergence and back-arc extension at the Tonga Arc, *Nature*, *374*, 249-251.
- Boespflug, X., L. Dosso, and H. Bougart (1990), Trace element and isotopic (Sr, Nd) geochemistry of volcanic rocks from the Lau Basin, *Geol. Jahrbuch*, *D92*, 503-516.
- Caroff, M., and C. Fleutelot (2003), The north-south propagating spreading center of the North Fiji Basin. Modeling of the geochemical evolution in periodically replenished and tapped magma chambers, *Minerology and Petrology*, *79*, 203-224.
- Class, C., D.M. Miller, S.L. Goldstein, and C.H. Langmuir (2000), Distinguishing melt and fluid subduction components in Umnak volcanics, Aleutian Arc, *G3*, *1*, 1999GC000010.
- Collier, J., and M. Sinah (1990), Seismic images of a magma chamber beneath the Lau Basin back-arc spreading centre, *Nature*, *346*, 646-648.
- Collier, J.S., and M.C. Sinha (1992), Seismic mapping of a magma chamber beneath the Valu Fa Ridge, Lau Basin, *J. Geophys. Res.*, *97* (B10), 14,031-14,053.
- Davies, J.H., and M.J. Bickle (1991), A physical model for the volume and composition of melt produced by hydrous fluxing above subduction zones, *Phil. Trans. Royal Soc. London*, *335*, 355-364.
- Day, A.J., C. Peirce, and M.C. Sinha (2001), Three-dimensional crustal structure and magma chamber geometry at the intermediate-spreading, back-arc Valu Fa Ridge, Lau Basin; results of a wide-angle seismic tomographic inversion, *Geophys. J. Int.*, *146*, 31-52.
- Detrick, R.S., P. Buhl, E.E. Vera, J.C. Mutter, J.A. Orcutt, J.A. Madsen, and T.M. Brocher (1987), Multi-channel seismic imaging of a crustal magma chamber along the East Pacific Rise, *Nature*, *326*, 35-41.
- Ewart, A., K.D. Collerson, M. Regelous, J.I. Wendt, and Y. Niu (1998), Geochemical evolution within the Tonga-Kermadec-Lau Arc-Back-arc systems: the role of varying mantle wedge composition in space and time, *J. Petrol.*, *39*, 331-368.
- Ewart, A., J.M. Hergt, and J.W. Hawkins (1994), Major element, trace element, and isotope (Pb, Sr, and Nd) geochemistry of Site 839 basalts and basaltic andesites; implications for arc volcanism, in *Proceedings of the Ocean Drilling Program, scientific results, Lau Basin; covering Leg 135 of the cruises of the drilling vessel JOIDES Resolution, Suva Harbor, Fiji, to Honolulu, Hawaii, sites 834-841, 17 December 1990-28 February 1991.*, edited by W.e.a. Hawkins James, pp. 519-531, Texas A & M University, Ocean Drilling Program, College Station, TX, United States.
- Falloon, T.J., D.H. Green, C.J. Hatton, and K.L. Harris (1988), Anhydrous partial melting of a fertile and depleted peridotite from 2 to 30 Kb and application to basalt petrogenesis, *J. Petrol.*, *29*, 1257-1282.
- Fleutelot, C., J.-P. Eissen, L. Dosso, T. Juteau, P. Launeau, C. Bollinger, J. Cotten, L.V. Danyushevsky, and L. Savoyant (2005), Petrogenetic variability along the North-South Propagating Spreading Center of the North Fiji Basin, *Minerology and Petrology*, *83*, 55-86.
- Fouquet, Y., U.v. Stackelberg, and R.K. Muhe (1989), Intense Hydrothermal Activity in a Back Arc Environment: Lau Basin SW Pacific: Results from French-German Cruise With Nautile., *EOS*, *70* (No. 43), 1383.

- Fouquet, Y., U. v. Stackelberg, J.L. Charlou, J.P. Donval, J. Erzinger, J.P. Foucher, P. Herzig, R.K. Mühe, S. Soakai, M. Wiedicke, and H. Whitechurch (1991), Hydrothermal activity and metallogenesis in the Lau back-arc basin, *Nature*, 349, 778-781.
- Fouquet, Y., U.v. Stackelberg, J.L. Charlou, J. Erzinger, P. Herzig, R. Mühe, and M. Wiedicke (1993), Metallogenesis in back arc environments. The Lau Basin example., *Econ. Geol.*, 88, 2154-2181.
- Frenzel, G., R. Mühe, and P. Stoffers (1990), Petrology of the volcanic rocks from the Lau Basin, southwest Pacific, *Geol. Jahrbuch*, D92, 395-479.
- Fretzdorff, S., R.A. Livermoe, C.W. Devey, P.T. Leat, and P. Stoffers (2002), Petrogenesis of the back-arc East Scotia Ridge, South Atlantic Ocean, *J. Petrol.*, 43, 1435-1467.
- Garbe-Schönberg, C.-D. (1993), Simultaneous determination of thirty-seven trace elements in twenty-eight international rock standards by ICP-MS, *Geostand. Newslett.*, 17, 81-97.
- Govindaraju, K. (1994), Compilation of working values and sample-description for 383 geostandards, *Geostand. Newslett.*, 13, 1-158.
- Haase, K.M., T.J. Worthington, P. Stoffers, C.-D. Garbe-Schoenberg, and I.C. Wright (2002), Mantle dynamics, element recycling, and magma genesis beneath the Kermadec Arc-Havre Trough, *G3*, 3, DOI 10.1029/2002GC000335.
- Hawkins, J.W. (1995a), Evolution of the Lau Basin; insights from ODP Leg 135, in *Active margins and marginal basins of the western Pacific.*, edited by B. Taylor, and J. Natland, American Geophysical Union, Washington, DC, United States, 125-173.
- Hawkins, J.W. (1995b), The geology of the Lau Basin, in *Backarc Basins - Tectonics and Magmatism*, edited by B. Taylor, Plenum Press, New York, 63-138.
- Hawkins, J.W., and J.T. Melchior (1985), Petrology of Mariana Trough and Lau Basin Basalts, *J. Geophys. Res.*, 90, 11,431-11,468.
- Hergt, J.M., and K.N. Farley (1994), Major element, trace element, and isotope (Pb, Sr, and Nd) variations in Stie 834 basalts: Implications for the initiation of backarc opening, *In: Hawkins; J., Parson, L., Allan, J. (eds.) Proc. ODP Sci. Res. College Station TX (Ocean Drilling Program)*, 135, 471-485.
- Hergt, J.M., and C.J. Hawkesworth (1994), Pb-, Sr-, and Nd-isotope evolution of the Lau Basin: Implications for mantle dynamics during backarc opening, *In: Hawkins; J., Parson, L., Allan, J. (eds.) Proc. ODP Scientific Results College Station TX (Ocean Drilling Program)*, 135, 505-517.
- Hey, R. (1977), Tectonic evolution of the Cocos-Nazca spreading center, *Geol. Soc. Am. Bull.*, 88, 1404-1420.
- Hey, R.N., J.M. Sinton, and F.K. Duenebier (1989), Propagating rifts and spreading centers, in *The Eastern Pacific Ocean and Hawaii*, edited by E.L. Winterer, D.M. Hussong, and R.W. Decker, Geological Society of America, Boulder, CO, 161-176.
- Hirose, K., and T. Kawamoto (1995), Hydrous partial melting of lherzolite at 1 GPa; the effect of H₂O on the genesis of basaltic magmas, *Earth Planet. Sci. Letts.*, 133, 463-473.
- Hirose, K., and I. Kushiro (1993), Partial melting of dry peridotites at high pressures: Determination of compositions of melts segregated from peridotite using aggregates of diamond, *Earth Planet. Sci. Letts.*, 114, 477-489.
- Hoernle, K.A., and G.R. Tilton (1991), Sr-Nd-Pb isotope data for Fuerteventura (Canary Islands) basal complex and subaerial volcanics: applications to magma genesis and evolution, *Schweizerische Mineralogische und Petrographische Mitteilungen*, 71, 3-18.
- Hofmann, A.W. (1988), Chemical Differentiation of the Earth: the Relationship between Mantle, Continental Crust, and Oceanic Crust, *Earth Planet. Sci. Letts.*, 90, 297-314.
- Ishikawa, T., and F. Tera (1999), Two isotopically distinct fluid components involved in the Mariana arc: Evidence from Nb/B ratios and B, Sr, Nd, and Pb isotope systematics, *Geology*, 27, 83-86.
- Ito, E., W.M. White, and C. Göpel (1987), The O, Sr, Nd and Pb isotope geochemistry of MORB, *Chem. Geol.*, 62, 157-176.
- Jenner, G.A., P.A. Cawwood, M. Rautenschlein, and W.M. White (1987), Composition of back-arc basin volcanics, Valu Fa Ridge, Lau Basin: evidence for a slab-derived component in their mantle source, *J. Volcanol. Geotherm. Res.*, 32, 209-222.
- Jenner, G.A., H.P. Longerich, S.E. Jackson, and B.J. Fryer (1990), A powerful tool for high-precision trace element analysis in earth sciences: evidence from analysis of selected U.S.G.S. reference samples, *Chem. Geol.*, 83, 133-148.

- Kamber, B.S., and K.D. Collerson (2000), Zr/Nb systematic of ocean island basalts reassessed - the case for binary mixing, *J. Petrology*, 41, 1007-1021.
- Keppeler, H. (1996), Constraints from partitioning experiments on the composition of subduction-zone fluids, *Nature*, 380, 237-240.
- Klein, E.M., and C.H. Langmuir (1987), Global Correlation of Ocean Ridge Basalt Chemistry with Axial Depth and Crustal Thickness, *J. Geophys. Res.*, 92 (B8), 8089-8115.
- Loock, G., W.F. McDonough, S.L. Goldstein, and A.W. Hofmann (1990), Isotopic compositions of volcanic glasses from the Lau Basin., *Marine Mining*, 9, 235-245.
- Mahoney, J.J., J.H. Natland, W.M. White, S.H. Poreda, S.H. Bloomer, R.L. Fisher, and A.N. Baxter (1989), Isotopic and geochemical provinces of the western Indian Ocean spreading centers, *J. Geophys. Res.*, 94, 4033-4052.
- Mahoney, J.J., J.M. Sinton, M.D. Kurz, J.D. Macdougall, K.J. Spencer, and G.W. Lugmair (1994), Isotope and Trace Element Characteristics of a Super-Fast Spreading Ridge: East Pacific Rise, 13-23°S, *Earth Planet. Sci. Letts.*, 121, 173-193.
- Miller, D., S.L. Goldstein, and C.H. Langmuir (1994), Cerium/lead and lead isotope ratios in arc magmas and the enrichment of lead in the continents, *Nature*, 368, 514-520.
- Mühe, R. (1994), Zur Petrographie, Geochemie und tektonischen Stellung der Vulkanite des Valu Fa Rückens, Lau Becken (SW-Pazifik), unter besonderer Berücksichtigung der Rückendiskontinuitäten, *Habilitationsschrift an der CAU zu Kiel (Germany)*, 126pp.
- Pearce, J.A., M. Ernewein, S.H. Bloomer, L.M. Parson, B.J. Murton, and L.E. Johnson (1995), Geochemistry of Lau basin volcanic rocks: influence of ridge segmentation and arc proximity, *Volcanism associated with extension of consuming plate margins*. In: J.L. Smellie (ed.). *Geol. Soc. Spec. Publ.*, 81, 53-75.
- Pearce, J.A., and D.W. Peate (1995), Tectonic implications of the composition of volcanic arc magmas, *Annu. Rev. Earth Planet. Sci. Letts.*, 23, 251-285.
- Peate, D.W., T.F. Kokfelt, C.J. Hawkesworth, P.W. van Calsteren, J.M. Hergt, and J.A. Pearce (2001), U-series Isotope Data on Lau Basin Glasses: the Role of Subduction-related Fluids during Melt Generation in Back-arc Basins, *J. Petrol.*, 42, 1449-1470.
- Peccerillo, A., and S.R. Taylor (1976), Geochemistry of Eocene calc-alkaline volcanic rocks from the Kastamonu area, northern Turkey, *Contrib. Mineral. Petrol.*, 58, 63-81.
- Peirce, C., and E.S. Party (1996), RV Maurice Ewing cruise 9512; geophysical investigation of melt bodies beneath the Valu Fa Ridge, Lau Basin (SW Pacific), *InterRidge News*, 5, 3-8.
- Perfit, M.R., W.I. Ridley, and I.R. Jonasson (1999), Geologic, petrologic, and geochemical relationships between magmatism and massive sulfide mineralization along the eastern Galapagos spreading center, in *Volcanic-associated massive sulfide deposits; processes and examples in modern and ancient settings.*, edited by C.T. Barrie, and D. Hannington Mark, 75-100.
- Pfänder, J.A., K.P. Jochum, I. Kozakov, A. Kröner, and W. Todt (2002), Coupled evolution of back-arc and island arc-like mafic crust in the late-Neoproterozoic Agardagh Tes-Chem Ophiolite, Central Asia; evidence from trace element and Sr-Nd-Pb isotope data, *Contrib. Mineral. Petrol.*, 143, 154-174.
- Plank, T., and C.H. Langmuir (1992), Effects of melting regime on the composition of the oceanic crust, *J. Geophys. Res.*, 97, 19,749-19,770.
- Prinzhofer, A., E. Lewin, and C.J. Allegre (1989), Stochastic melting of the marble cake mantle: evidence from local study of the East Pacific Rise at 12° 50'N, *Earth Planet. Sci. Letts.*, 92, 189-206.
- Sims, K.W.W., and D.J. DePaolo (1997), Inferences about mantle magma sources from incompatible element concentration ratios in oceanic basalts, *Geochim. Cosmochim. Acta*, 61, 765-784.
- Sinton, J.M., D.S. Wilson, D.C. Christie, R.N. Hey, and J.R. Delaney (1983), Petrologic consequences of rift propagation on oceanic spreading ridges, *Earth Planet. Sci. Letts.*, 62, 193-207.
- Stackelberg, v., U., and a.S.S. Party (1988), Active Hydrothermalism in the Lau Back-Arc Basin (SW-Pacific): First Results from the SONNE 48 Cruise (1987), *Marine Mining*, 7, 431-442.
- Stolper, E., and S. Newman (1994), The role of water in the petrogenesis of Mariana trough magmas, *Earth Planet. Sci. Letts.*, 121, 293-325.
- Sun, S.-S., and W.F. McDonough (1989), Chemical and isotopic systematics of oceanic basalts: implications for mantle composition and processes, *Magmatism in the Ocean Basins, Geological Society Special Publication*, 42, 313-345.

- Sunkel, G. (1990), Origin of petrological and geochemical variations of Lau Basin lavas (SW Pacific), in *Hydrothermal mineralization of the Lau Basin; results of the Sonne Cruise SO48.*, edited by J.R. Moore, and U. von Stackelberg, pp. 205-234, Taylor & Francis, London, United States.
- Taylor, B., K. Zellmer, F. Martinez, and A.M. Goodliffe (1996), Sea-floor spreading in the Lau back-arc basin, *Earth Planet. Sci. Letts.*, *144*, 35-40.
- Todt, W., R.A. Cliff, A. Hanser, and A.W. Hofmann (1996), Evaluation of a ^{202}Pb - ^{205}Pb double spike for high precision lead isotope analyses. In: Basu, A. & Hart, S. (eds.), *Earth Processes: Reading the Isotopic Code*, *Geophys. Monograph*, *95*, AGU, Washington, DC 429-437.
- Turner, I.M., C. Peirce, and M.C. Sinha (1999), Seismic imaging of the axial region of the Valu Fa Ridge, Lau Basin; the accretionary processes of an intermediate back-arc spreading ridge, *Geophys. J. Internat.*, *138*, 495-519.
- Turner, S., and C. Hawkesworth (1997), Constraints on flux rates and mantle dynamics beneath island arcs from Tonga-Kermadec lava geochemistry, *Nature*, *389*, 568-573.
- Turner, S., N.R. Hawkesworth, J. Bartlett, T. Worthington, J. Hergt, J. Pearce, and I. Smith (1997), ^{238}U - ^{230}Th disequilibria, magma petrogenesis, and flux rates beneath the depleted Tonga-Kermadec island arc, *Geochim. Cosmochim. Acta*, *61*, 4855-4884.
- Vallier, F.T.L., G.A. Jenner, F.A. Frey, J.B. Gill, A.S. Davis, A.M. Volpe, J.W. Hawkins, J.D. Morris, P.A. Cawood, J.L. Morton, D.W. Scholl, M. Rautenschlein, W.M. White, R.W. Williams, A.J. Stevenson, and L.D. White (1991), Subalkaline andesite from Valu Fa Ridge, a back-arc spreading center in southern Lau Basin: petrogenesis, comparative chemistry, and tectonic implications, *Chem. Geol.*, *91*, 227-256.
- Vlastelic, I., D. Aslanian, L. Dosso, H. Bougault, J.L. Olivet, and L. Geli (1999), Large-scale chemical and thermal division of the Pacific mantle, *Nature*, *399*, 345-350.
- Volpe, A.M., J.D. Macdougall, and J.W. Hawkins (1988), Lau Basin basalts (LBB): trace elements and Sr-Nd isotopic evidence for heterogeneity in backarc basin mantle, *Earth Planet. Sci. Letts.*, *90*, 174-186.
- Wiedicke, M., and J.S. Collier (1993), Morphology of the Valu Fa spreading ridge in the southern Lau Basin, *J. Geophys. Res.*, *98* (B7), 11,769-11,782.

Figure caption

Figure 1: a) Seafloor bathymetry of the central and southern Valu Fa Ridge, as recorded and processed by the multichannel SIMRAD EM 120 system during SO167. Sample locations of SO167 are indicated with a black circle and additional stations from an earlier cruise SO67 in 1990 are marked with a red circle. *Wiedicke and Collier* [1993] divided Valu Fa Ridge into 11 volcanic ridge segments (nos. 3 to 14; Segments nos. 3 to 6 belong to the SVFR, nos. 7 to 9 to the CVFR, and nos. 10 to 14 to the NVFR). Seismic data indicate a steady axial magma chamber [highlighted in red after *Day et al.*, 2001]. a) Morphology of the central and southern Valu Fa Ridge. The five profiles show a rather flat and smooth topography comparable with fast-spreading mid-ocean ridges. Despite the extrusion of higher differentiated, silica-rich volcanic flows, the ridge does not represent a significant morphological axial high. To the South, the Valu Fa Ridge develops into a system of halfgrabens.

Figure 2: K₂O vs SiO₂ diagram showing Valu Fa Ridge lavas and seamounts in the southern prolongation of the ridge tip (this study). Data sources with additional Valu Fa Ridge samples, Lau Basin, and Central Tonga Island arc: *Hawkins and Melchior* [1985], *Jenner et al.* [1987b], *Volpe et al.*, [1988], *Boespflug et al.* [1990], *Frenzel et al.* [1990], *Sunkel*, [1990], *Vallier et al.* [1991], *Pearce et al.* [1995], *Turner et al.* [1997], *Bach et al.* [1998], *Peate et al.* [2001]. Series boundaries and nomenclature from *Peccerillo and Taylor* [1976].

Figure 3: Na₈ values calculated after *Plank and Langmuir* [1992] along the central and southern Valu Fa Ridge and for comparison of Ata Island. Samples with MgO wt% contents below 2% have are not shown. Decreasing Na₈ values indicating increasing degrees of mantle melting [e.g. *Klein and Langmuir*, 1987]. Data sources as in Figure 2.

Figure 4: Chondrite normalized [*Sun and McDonough*, 1989] rare earth element (REE) patterns of the Valu Fa Ridge lavas, N-MORB [*Hofmann*, 1988], and for comparison of Ata Island volcanic rocks [*Turner et al.*, 1997].

Figure 5: a) Nb/Yb ; b) Ce/Pb ; c) Th/Nb d) ⁸⁷Sr/⁸⁶Sr, e) ¹⁴³Nd/¹⁴⁴Nd, f) ²⁰⁸Pb/²⁰⁴Pb variations along the central and southern Valu Fa Ridge. The extension of the magma chamber is estimated after *Day et al.* [2001]. For comparison compositions of volcanic

rocks from Ata Island, which is located approx. 40 km west of the back-arc basin, are also plotted [Turner *et al.*, 1997]. In c) N-MORB composition is taken from Hofmann [1988]. Errors [2σ] of the radiogenic isotope ratios lie within the symbol size. Data sources: this study, Boesflug *et al.* [1990], Look *et al.* [1990], Turner *et al.* [1997], Bach *et al.* [1998], Peate *et al.* [2001].

Figure 6: a) $^{208}\text{Pb}/^{204}\text{Pb}$ versus Ce/Pb and b) $^{208}\text{Pb}/^{204}\text{Pb}$ versus $^{206}\text{Pb}/^{204}\text{Pb}$ for volcanic rocks of Valu Fa Ridge and southern prolongation, the Lau Basin, Tonga Island arc, ODP Sites 834 and 839. Pacific sediment and altered oceanic crust fluid composition after Haase *et al.* [2002] and Peate *et al.* [2001] is also plotted in both digrams. In a) average compositions of Indian Ocean and Pacific MORB are from Sims and DePaolo [1997, Ce/Pb ratios] and Hergt and Hawkesworth [1994, $^{208}\text{Pb}/^{204}\text{Pb}$]. Errors (2σ) lie within the symbol size. Data Sources as in Figure 5 and Pacific Sediment: Ewart *et al.* [1998], Indian Ocean and Pacific MORB: Ito *et al.* [1987], Mahoney *et al.* [1989], Prinzhofer *et al.* [1989], Ewart *et al.* [1994], Mahoney *et al.* [1994], Bach *et al.* [1996], Vlastelic *et al.* [1999]; ODP sites: Hergt and Farley [1994], Ewart *et al.* [1994].

Figure 7: U (ppm) versus Yb (ppm) concentrations of the Valu Fa Ridge lavas and seamounts in the southern prolongation of the ridge tip (this study). For comparison Lau Basin and Tonga Island arc volcanic rocks are also shown (data sources as in Figure 2).

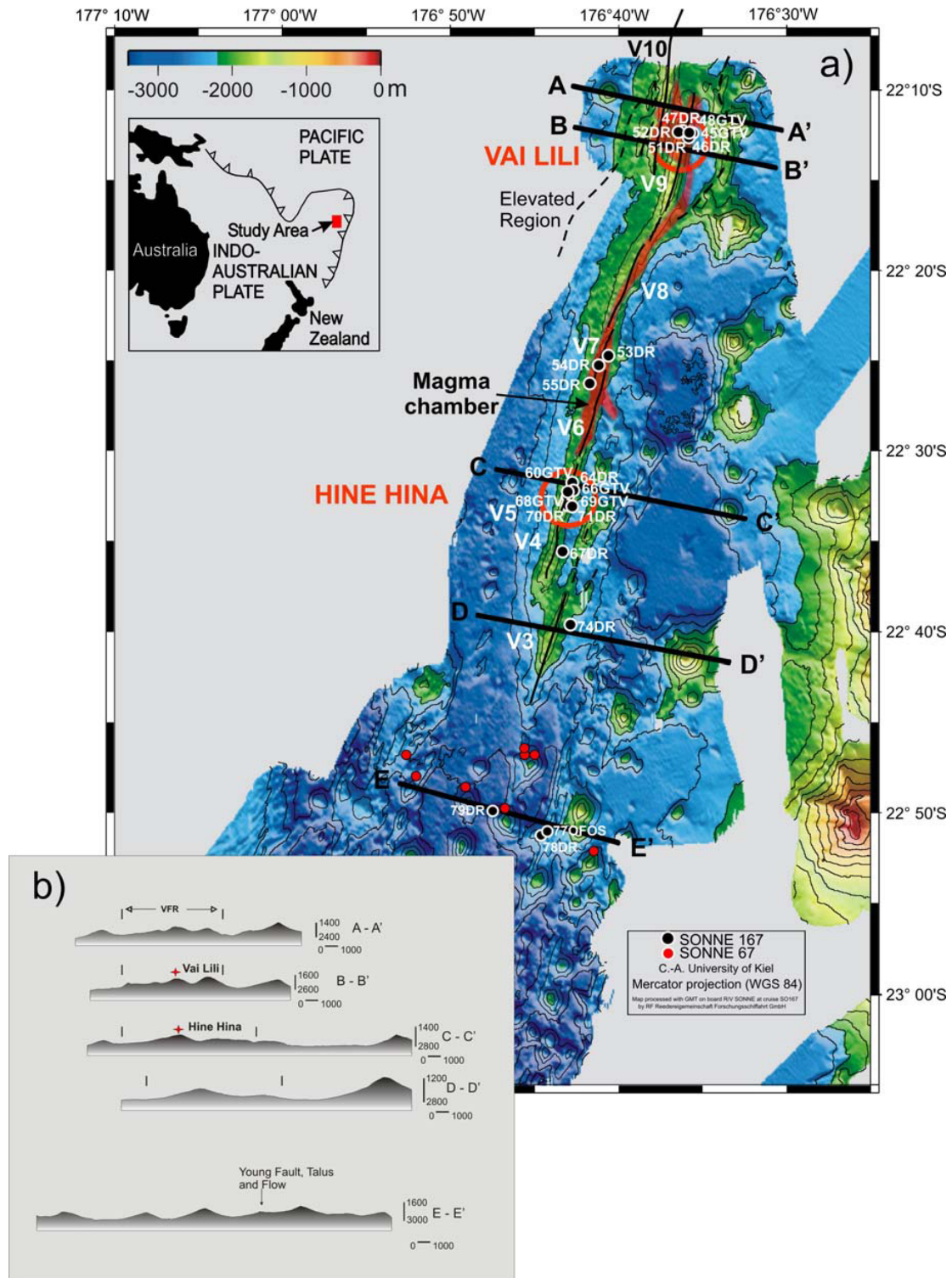


Figure 1

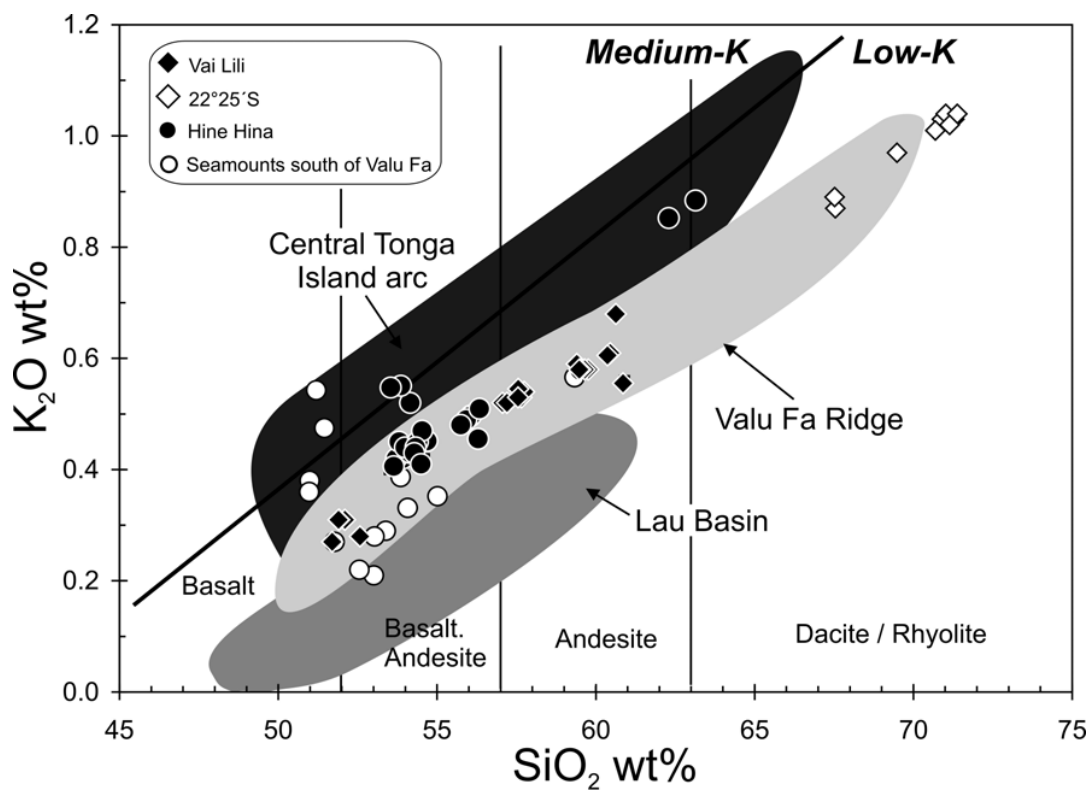


Figure 2

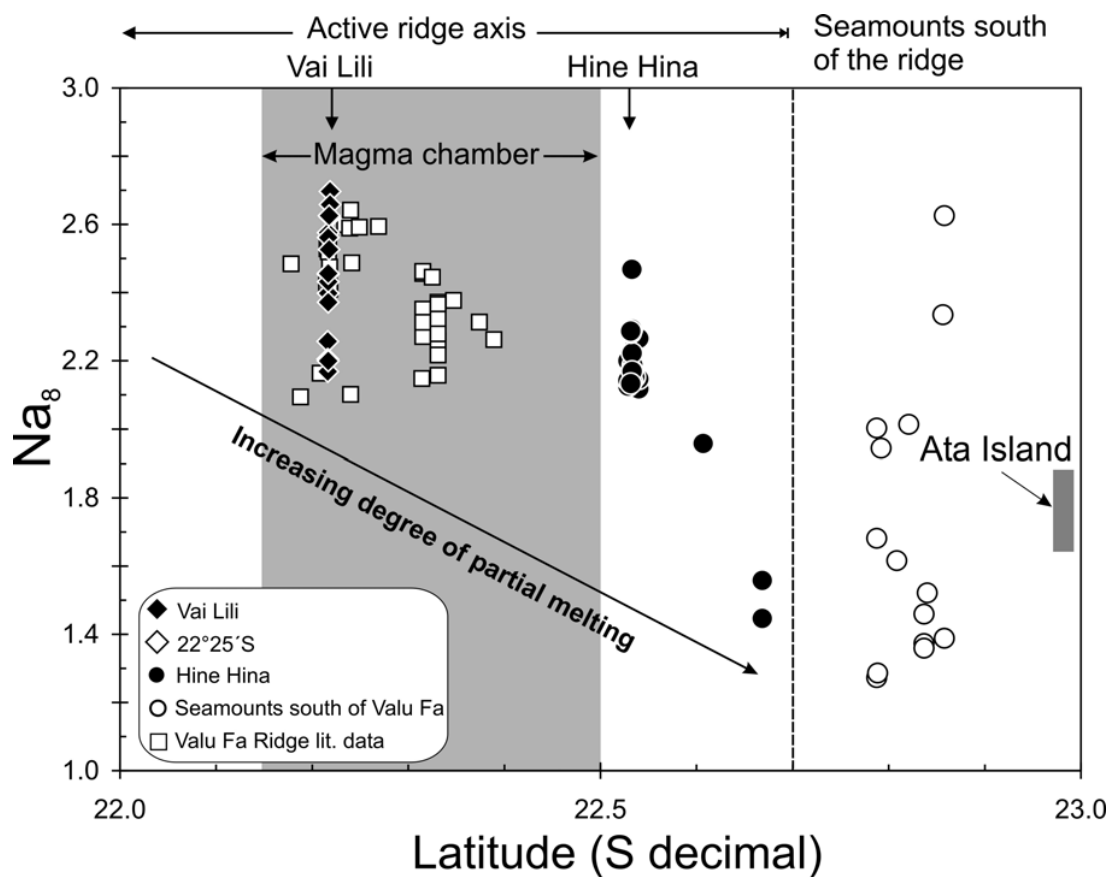


Figure 3

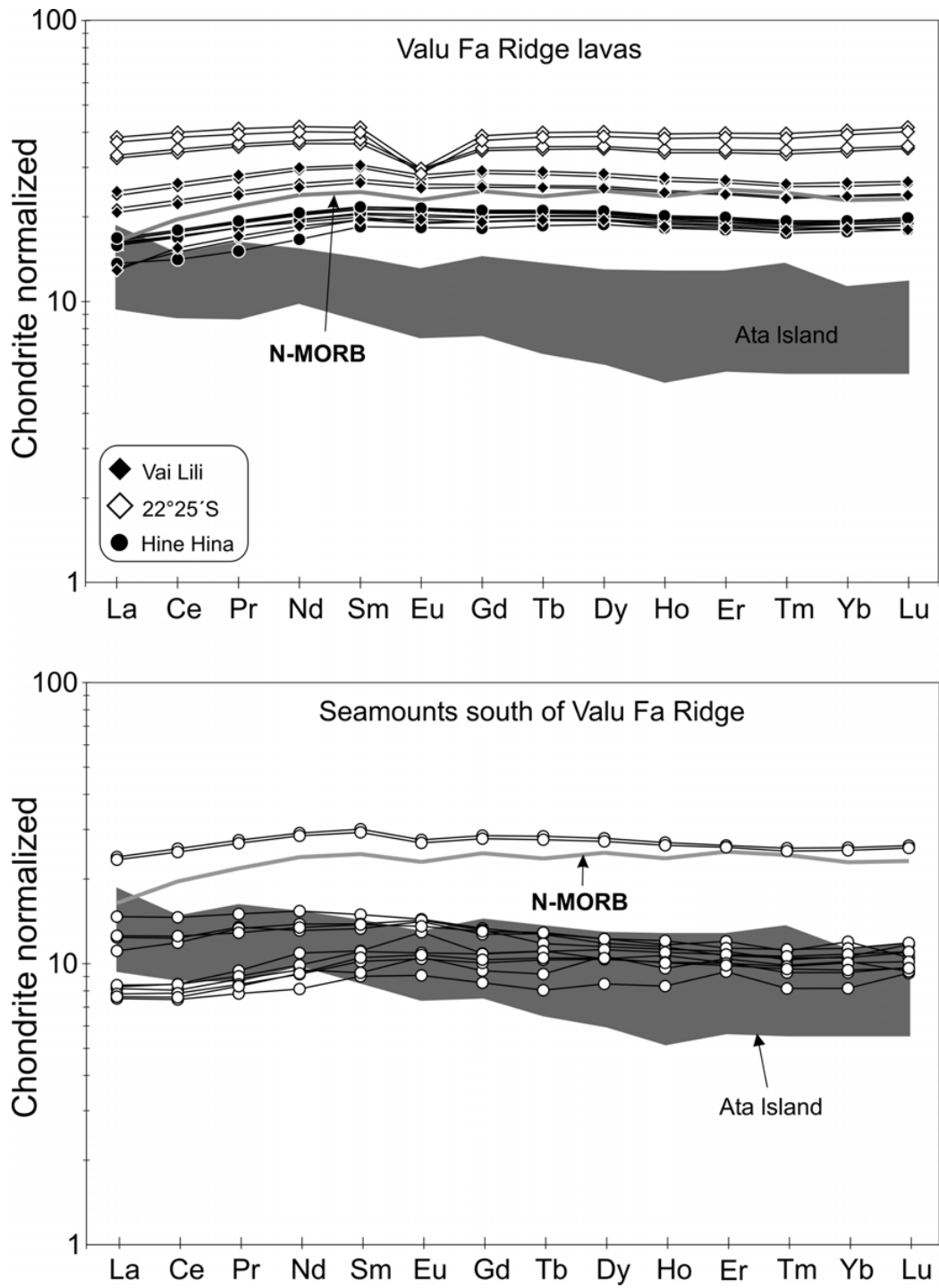


Figure 4

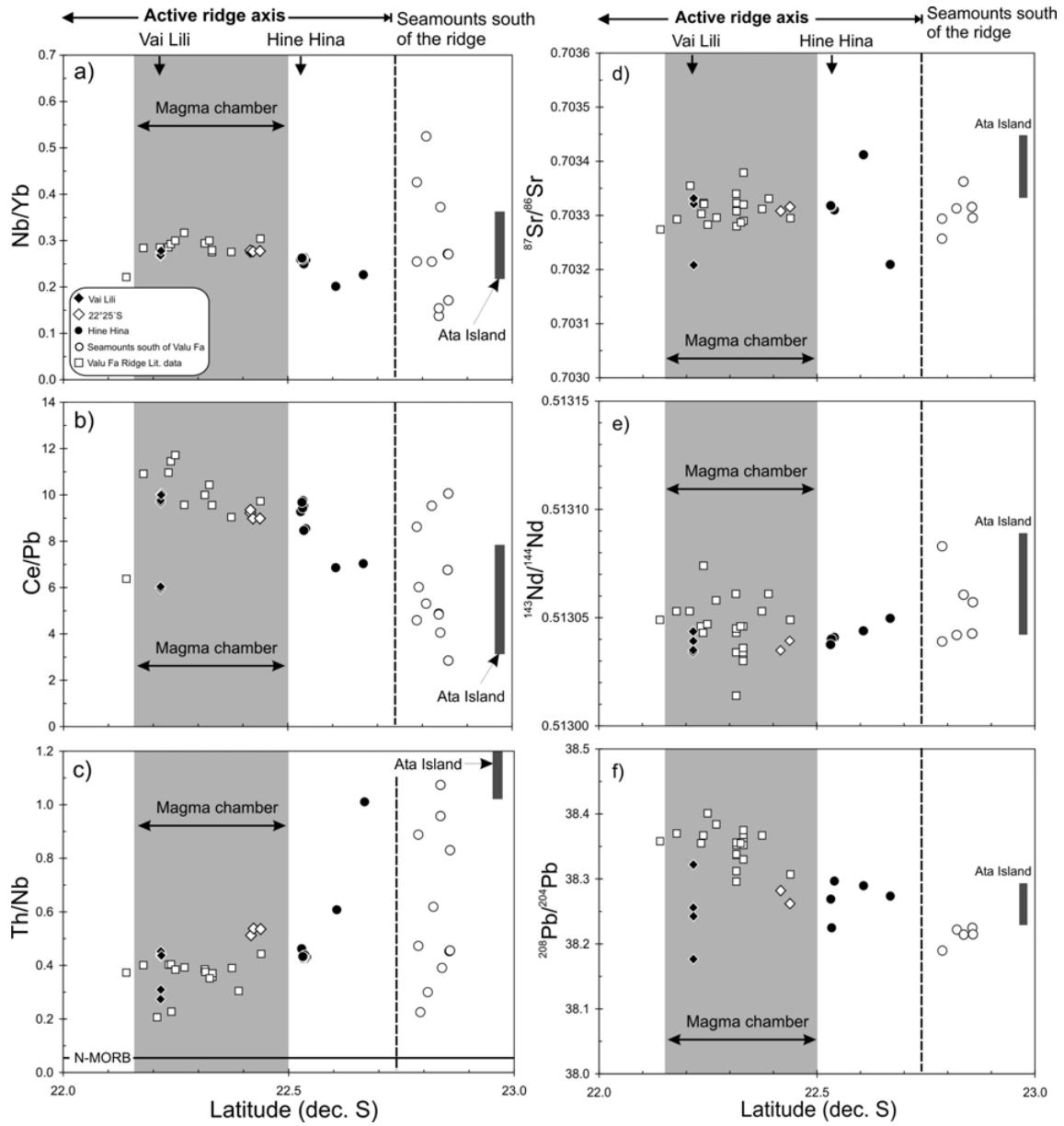


Figure 5

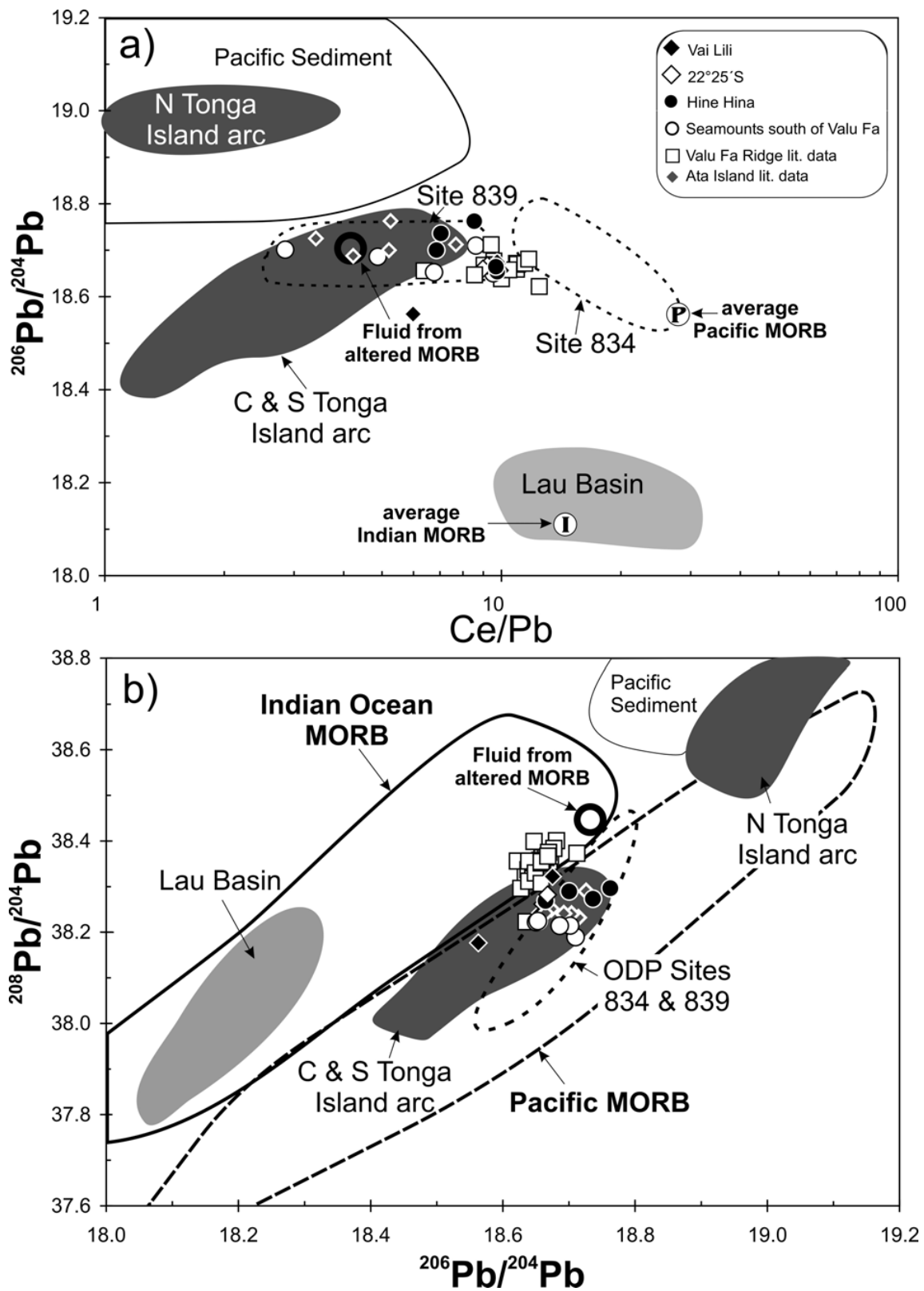


Figure 6

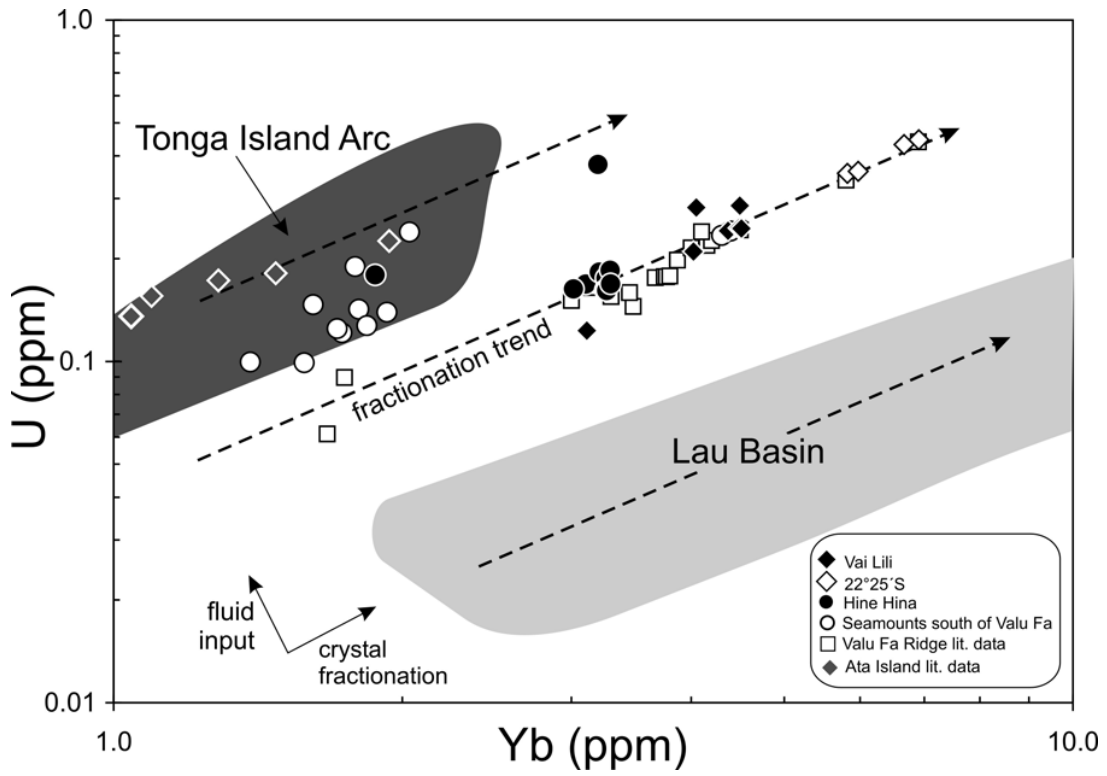


Figure 7

Table 1: Location, water depth and selected geochemical analyses of the Valu Fa Ridge lavas

Location Sample	22°25' S										Hine Hina				
	45 GTV-1	45 GTV-3gl	46 DR-1	47DR-1gl	48 GTV-3	51 DR-1	51 DR-2	52 DR-1	53 DR-1	53 DR-3	54 DR-1	55 DR-1	60GTV-1gl	64 DR-1	66GTV-2gl
Lat. (S)	176°36.5'	176°36.5'	176°36.5'	176°36.6'	176°36.5'	176°36.6'	176°36.6'	176°36.6'	176°40.5'	176°40.5'	176°41.0'	176°41.4'	176°43.0'	176°43.0'	176°42.3'
Long. (W)	22°12.9'	22°12.9'	22°13.1'	22°13.0'	22°13.0'	22°13.0'	22°13.1'	22°13.1'	22°25.0'	22°25.0'	22°25.3'	22°26.3'	22°32.4'	22°31.7'	22°32.2'
Depth (m)	1713	1713	1698	1783	1733	1772	1772	1794	2134	2134	2006	2117	1803	1932	1831
SiO ₂	52.10	60.63	59.76	60.46	52.57	57.56	57.20	59.52	67.54	67.52	70.90	71.02	54.69	54.16	53.64
TiO ₂	1.25	1.59	1.34	1.44	1.23	1.56	1.44	1.34	0.62	0.60	0.37	0.37	1.70	1.42	1.81
Al ₂ O ₃	15.54	13.56	14.79	14.33	15.49	14.81	14.91	14.75	13.54	13.45	12.68	12.66	14.40	14.90	14.54
Fe ₂ O ₃ ^t	11.49		10.24		11.91	10.96	11.12	10.13	7.15	7.01	5.46	5.50		13.13	
FeO ^c		9.43		9.43									12.21		12.00
MnO	0.19	0.20	0.20	0.19	0.24	0.20	0.20	0.20	0.17	0.17	0.14	0.14	0.20	0.19	0.19
MgO	5.12	1.57	2.19	1.97	5.18	2.93	2.09	2.09	0.74	0.69	0.33	0.33	3.52	3.98	3.62
CaO	10.27	5.48	6.27	6.02	10.00	6.84	7.30	6.25	3.93	3.86	2.94	2.91	7.90	8.55	7.91
Na ₂ O	2.79	3.54	3.98	3.63	2.70	3.61	3.73	4.01	4.49	4.35	4.63	4.65	2.86	2.80	2.90
K ₂ O	0.31	0.68	0.58	0.61	0.28	0.55	0.52	0.58	0.87	0.89	1.03	1.04	0.45	0.43	0.41
P ₂ O ₅	0.15	0.49	0.35	0.45	0.15	0.34	0.27	0.35	0.18	0.18	0.09	0.08	0.26	0.16	0.29
LOI	0.17	0.00	1.19		0.05	0.80	0.64	0.96	1.03	1.01	1.26	1.33	0.00	0.00	
Total	99.38	97.16	100.89	98.53	99.80	99.79	100.26	100.18	100.24	99.73	99.78	100.03	98.20	99.72	97.31
Sc	46.2	21.4	21.0	20.9	31.8	23.6	25.3	21.3	14.4	14.5	12.5	11.9	30.4	30.5	31.3
Cr	12.6	1.09	0.930	0.971	11.2	0.801	7.40	1.09	0.795	0.781	0.772	0.652	0.596	4.90	1.71
Co	37.5	15.6	15.2	15.4	35.4	18.7	21.5	15.5	4.38	4.36	2.23	1.96	31.1	32.3	31.2
Ni	22.3	1.21	1.24	1.20	19.0	1.16	4.70	1.23	0.493	0.495	0.376	0.318	2.25	10.8	7.48
Cu	74.1	49.9	22.9	23.1	75.0	18.7	31.4	23.6	11.0	11.2	13.0	12.7	48.4	117	58.1
Zn	107	155	97.4	98.2	98.6	100	99.6	100	94.4	94.9	91.9	87.7	91.3	88.9	94.6
Rb	5.25	10.2	9.75	10.0	4.56	8.88	8.48	10.0	15.3	15.8	19.2	18.5	6.85	7.43	6.94
Sr	162	181	175	181	160	179	141	181	144	144	123	117	174	172	181
Y	29.8	41.6	40.3	41.2	28.4	37.0	36.5	41.4	51.4	52.7	60.2	57.9	28.9	28.1	29.9
Zr	64.5	92.9	90.1	92.1	63.2	81.6	80.5	92.4	133	137	178	173	62.0	60.9	63.4
Nb	0.851	1.24	1.21	1.21	0.831	1.12	1.08	1.25	1.59	1.64	1.91	1.85	0.826	0.805	0.861
Cs	0.169	0.254	0.244	0.252	0.100	0.220	0.212	0.254	0.365	0.379	0.457	0.440	0.169	0.178	0.175
Ba	59.5	174	135	139	100	127	125	141	196	204	237	230	93.5	97.5	97.7
La	3.06	5.84	5.65	5.82	3.13	5.08	4.91	5.85	7.67	7.86	9.11	8.76	3.80	3.85	3.92
Ce	9.49	16.2	15.6	16.1	9.17	14.0	13.6	16.2	20.8	21.3	24.5	23.5	10.4	10.5	10.8
Pr	1.62	2.69	2.60	2.67	1.57	2.34	2.27	2.68	3.37	3.46	3.92	3.74	1.74	1.73	1.82
Nd	8.65	14.0	13.7	14.0	8.41	12.3	11.9	14.0	17.0	17.4	19.6	18.8	9.10	8.95	9.56
Sm	2.99	4.73	4.58	4.69	2.99	4.17	4.04	4.68	5.57	5.78	6.37	6.12	3.12	3.05	3.31
Eu	1.14	1.65	1.59	1.63	1.10	1.52	1.47	1.64	1.70	1.72	1.72	1.65	1.16	1.11	1.25
Gd	3.94	5.99	5.88	6.01	3.96	5.35	5.24	6.01	7.08	7.23	8.00	7.68	4.08	3.96	4.28
Tb	0.729	1.09	1.06	1.08	0.733	0.966	0.952	1.09	1.30	1.33	1.49	1.44	0.750	0.726	0.778
Dy	4.95	7.28	7.07	7.25	4.97	7.26	6.43	7.26	8.88	9.05	10.2	9.82	5.09	4.93	5.25
Ho	1.05	1.57	1.52	1.56	1.08	1.40	1.38	1.57	1.92	1.96	2.24	2.15	1.09	1.06	1.14
Er	3.03	4.50	4.38	4.48	3.11	4.03	3.98	4.48	5.61	5.73	6.58	6.34	3.16	3.07	3.26
Tm	0.456	0.666	0.654	0.668	0.466	0.601	0.592	0.670	0.854	0.879	1.01	0.971	0.471	0.458	0.486
Yb	3.09	4.49	4.37	4.48	3.11	4.05	4.02	4.51	5.82	5.97	6.91	6.67	3.20	3.10	3.26
Lu	0.457	0.681	0.665	0.682	0.473	0.614	0.607	0.679	0.890	0.908	1.06	1.02	0.484	0.473	0.494
Hf	1.86	2.82	2.76	2.84	1.92	2.53	2.49	2.84	4.04	4.18	5.03	4.87	1.93	1.89	1.95
Ta	0.056	0.087	0.084	0.087	0.059	0.079	0.075	0.088	0.109	0.113	0.133	0.128	0.058	0.058	0.062
Ti	0.639	0.219	0.062	0.065	0.082	0.063	0.063	0.064	0.090	0.094	0.116	0.110	0.055	0.046	0.044
Pb	1.60	-	1.55	1.61	1.53	1.62	1.39	1.62	2.25	2.28	2.73	2.62	1.22	1.13	1.14
Th	0.233	0.548	0.534	0.556	0.257	0.487	0.468	0.548	0.820	0.839	1.027	0.991	0.356	0.372	0.366
U	-	0.286	0.241	0.246	0.123	0.282	0.210	0.245	0.356	0.361	0.446	0.432	0.168	0.168	0.175

major elements analyzed by XRF and reported in wt% with total Fe as Fe₂O₃, except for those with suffix gl - glasses analyzed by electron microprobe which are average data of 10 analyses, respectively.
Trace elements analyzed by ICP-MS and reported in ppm.

Table 1:

Location Sample	Hine Hina										south of Valu Fa Ridge										Standards	
	67DR-1gl	68 GTV-1	69DR-1gl	70DR-1gl	71DR-1gl	74DR-1gl	77OFOS gl	78 DR-3	78 DR-4	79DR-1gl	79 DR-2	VG-2 (glass)	BHVO-1									
Lat. (S)	176°43.9'	176°43.1'	176°43.0'	176°43.2'	176°43.2'	176°43.6'	176°44.4'	176°44.5'	176°44.5'	176°47.1'	176°47.1'	n=25	BHVO-1									
Long. (W)	22°36.4'	22°32.0'	22°32.0'	22°32.0'	22°31.9'	22°40.1'	22°51.4'	22°51.5'	22°51.5'	22°50.2'	22°50.2'	n=15	BHVO-1									
Depth (m)	1915	1893	1912	1928	1895	2022	2213	2247	2247	2376	2376	Trace elements:										
SiO ₂	56.29	54.39	56.07	55.92	55.74	53.86	59.33	59.53	51.77	54.07	53.38	50.98	49.61									
TiO ₂	1.49	1.60	1.99	2.02	1.97	0.92	1.39	1.34	0.66	0.79	0.65	1.88	2.77									
Al ₂ O ₃	14.31	14.81	13.33	13.36	13.38	14.65	14.58	14.69	15.82	14.50	16.53	14.08	13.55									
Fe ₂ O ₃ ^t	12.70							10.18	9.98		10.28		12.23									
FeO ^c	11.72		12.49	12.85	12.26	10.56	9.07			10.48		11.79										
MnO	0.21	0.20	0.19	0.20	0.20	0.18	0.19	0.20	0.17	0.18	0.17	0.20	0.17									
MgO	3.20	3.82	2.99	2.91	2.91	5.04	2.04	2.09	6.83	5.08	5.68	6.75	7.18									
CaO	7.71	8.23	7.51	7.25	7.45	9.76	5.99	6.23	12.65	10.04	11.17	11.20	11.48									
Na ₂ O	2.66	3.36	3.06	3.06	2.99	1.68	3.50	4.01	1.47	1.69	1.53	2.66	2.20									
K ₂ O	0.46	0.45	0.50	0.49	0.48	0.55	0.57	0.58	0.27	0.33	0.29	0.19	0.52									
P ₂ O ₅	0.24	0.22	0.36	0.35	0.35	0.25	0.42	0.35	0.09	0.15	0.09	0.30	0.28									
LOI	0.47		0.00			0.00		0.45	0.15	0.37												
Total	98.28	100.25	98.50	98.10	97.73	97.45	97.08	99.65	99.86	97.32	100.14	100.01	99.99									
Sc	31.6	29.2	29.8	29.4	29.8	34.4	19.9	36.6	36.8	36.8	34.5	39.6	28.6									
Cr	2.22	2.41	2.14	2.19	2.01	22.0	0.810	1.15	77.7	44.9	51.5	403	292									
Co	28.4	28.8	29.3	29.3	29.3	30.3	14.5	14.5	34.3	34.9	32.2	50.6	43.3									
Ni	9.13	7.32	7.18	7.51	7.32	20.1	1.06	1.32	38.7	29.2	27.4	156	108									
Cu	77.4	55.1	54.2	52.8	53.8	110	20.8	21.7	70.4	140	121	117	141									
Zn	94.1	91.3	92.5	91.5	92.2	66.5	92.2	90.5	62.2	70.1	65.5	68.2	104									
Rb	6.34	7.17	7.00	6.89	6.96	7.52	9.72	9.48	4.58	3.96	3.71	0.202	9.43									
Sr	161	175	177	174	177	224	175	172	158	156	161	108	396									
Y	27.1	29.6	30.1	29.6	30.1	16.7	40.0	38.9	14.6	16.1	14.8	14.5	24.6									
Zr	47.5	63.4	63.9	63.2	64.2	29.1	89.1	87.0	22.1	25.7	23.7	13.9	178									
Nb	0.607	0.856	0.862	0.846	0.865	0.424	1.19	1.17	0.276	0.253	0.263	0.498	17.4									
Cs	0.230	0.174	0.175	0.175	0.177	0.195	0.247	0.242	0.211	0.189	0.174	0.006	0.098									
Ba	117	99.1	98.9	96.6	98.3	101	137	133	82.9	94.7	88.0	6.47	136									
La	3.24	3.92	3.97	3.90	3.99	3.25	5.68	5.55	1.81	1.99	1.85	0.592	14.9									
Ce	8.63	10.8	11.0	10.8	11.0	7.95	15.7	15.3	4.64	5.16	4.81	1.83	36.9									
Pr	1.44	1.80	1.84	1.80	1.84	1.25	2.61	2.55	0.789	0.856	0.802	0.365	5.27									
Nd	7.76	9.46	9.66	9.47	9.67	6.38	13.62	13.30	4.31	4.61	4.28	2.28	24.0									
Sm	2.83	3.25	3.33	3.26	3.32	2.07	4.60	4.49	1.61	1.69	1.56	1.07	6.08									
Eu	1.06	1.22	1.24	1.23	1.25	0.76	1.60	1.56	0.62	0.63	0.60	0.510	2.04									
Gd	3.74	4.24	4.32	4.25	4.34	2.56	5.86	5.72	2.12	2.22	2.07	1.72	6.30									
Tb	0.697	0.771	0.787	0.773	0.79	0.45	1.06	1.03	0.39	0.41	0.39	0.354	0.943									
Dy	4.78	5.20	5.30	5.23	5.34	3.00	7.09	6.92	2.66	2.85	2.63	2.53	5.30									
Ho	1.03	1.12	1.14	1.13	1.14	0.64	1.53	1.49	0.57	0.62	0.57	0.563	0.977									
Er	2.98	3.23	3.28	3.23	3.30	1.86	4.36	4.29	1.63	1.79	1.66	1.63	2.47									
Tm	0.447	0.482	0.492	0.484	0.49	0.28	0.66	0.64	0.24	0.27	0.25	0.244	0.324									
Yb	3.02	3.25	3.29	3.26	3.30	1.87	4.40	4.30	1.61	1.84	1.71	1.62	1.99									
Lu	0.457	0.492	0.504	0.496	0.504	0.286	0.668	0.655	0.245	0.280	0.258	0.247	0.277									
Hf	1.64	1.97	1.99	1.97	2.02	1.03	2.77	2.71	0.851	0.955	0.880	0.572	4.36									
Ta	0.043	0.060	0.062	0.061	0.062	0.028	0.084	0.084	0.018	0.018	0.019	0.037	1.08									
Tl	0.043	0.042	0.044	0.044	0.045	0.050	0.063	0.061	0.039	0.033	0.031	0.004	0.044									
Pb	1.26	1.11	1.12	1.14	1.13	1.13	2.32	1.52	1.63	1.06	0.993	3.02	2.07									
Th	0.369	0.365	0.371	0.365	0.375	0.429	0.541	0.531	0.230	0.272	0.252	0.029	1.23									
U	0.163	0.162	0.185	0.161	0.169	0.179	0.241	0.234	0.147	0.127	0.125	0.011	0.431									

Table 2: Sr-Nd-Pb isotope ratios of selected Valu Fa Ridge lavas

Sample	$^{87}\text{Sr}/^{86}\text{Sr}^a$	2 σ	$^{143}\text{Nd}/^{144}\text{Nd}$	2 σ	$^{206}\text{Pb}/^{204}\text{Pb}$	2 σ	$^{207}\text{Pb}/^{204}\text{Pb}$	2 σ	$^{208}\text{Pb}/^{204}\text{Pb}$	2 σ
Vai Lili										
45GTV-3gl	0.703329	3	0.513034	3	18.667	0.003	15.529	0.003	38.256	0.007
47DR-1gl	0.703321	3	0.513039	2	18.657	0.001	15.527	0.000	38.242	0.001
48GTV-3	0.703208	3	0.513035	2	18.563	0.001	15.520	0.001	38.177	0.004
51DR-2	0.703330	3	0.513044	2	18.675	0.002	15.551	0.002	38.322	0.007
22°25'S										
53DR-1gl	0.703308	2	0.513035	2	18.668	0.001	15.538	0.001	38.282	0.002
55DR-1	0.703316	2	0.513039	2	18.660	0.001	15.532	0.001	38.262	0.002
Hine Hina										
60GTV-1gl	0.703310	2	0.513041	3	18.762	0.003	15.529	0.002	38.297	0.006
67DR-1gl	0.703412	2	0.513044	3	18.700	0.002	15.538	0.002	38.290	0.005
69DR-1gl	0.703317	2	0.513040	2	18.654	0.001	15.521	0.001	38.225	0.002
71DR-1gl	0.703318	2	0.513038	3	18.665	0.001	15.534	0.001	38.269	0.004
74DR-1gl	0.703209	2	0.513050	2	18.736	0.001	15.532	0.001	38.274	0.002
South of Valu Fa Ridge										
77OFOS gl	0.703316	2	0.513043	3	18.653	0.001	15.522	0.001	38.225	0.002
78DR-4	0.703296	3	0.513057	2	18.701	0.001	15.528	0.001	38.215	0.002
79DR-1gl	0.703362	3	0.513061	2	18.686	0.001	15.532	0.001	38.214	0.002

^a Isotope ratios for Sr normalized to NBS 987 ($^{87}\text{Sr}/^{86}\text{Sr} = 0.71025$) and for Pb to NBS 981 [Todt et al., 1996]. Errors are 2 σ standard errors of the mean and refer to in-run statistics.

Osborn Trough: Structure, Geochemistry and Implications of a mid - Cretaceous Paleosspreading Center in the South Pacific

Tim J. Worthington^{a,*}, Roger Hekinian^b, Peter Stoffers^a, Thomas Kuhn^c, Folkmar Hauff^c

^aInstitut für Geowissenschaften, Universität Kiel, Olshausenstr. 40, 24098 Kiel, Germany

^bKeryunan, 29290 Saint Renan, France

^cIFM-GEOMAR, Leibniz Institut für Meereswissenschaften, Wischhofstr. 1–3, 24148 Kiel, Germany

* Corresponding author-

Dr. Tim J. Worthington

e-mail: tw@gpi.uni-kiel.de

tel: +49-431-8802852

fax: +49-431-8804376

Submitted to-

Earth and Planetary Science Letters

Version of-

19 September 2005

Word counts-

Abstract: 250

Main text: 5512

References-

66

Tables-

4

Figures-

10

Abstract

Bathymetric mapping of a 145 km-wide swath across the ~900 km-long Osbourn Trough revealed three segments offset by 23–35 km-long basins that strike perpendicular to the trough axis. Each segment comprises a 10–15 km-wide axial valley bounded by 300–500 m-high ridge mountains, has inside corner highs at its NW and SE margins that rise 1000–1200 m above the axial valley, and has a flanking set of subparallel abyssal hills. Dredging on steep escarpments successfully penetrated thick sediments and recovered Fe-Mn oxyhydroxide-encrusted volcanoclastic breccias. Lava clasts within the breccias have undergone variable degrees of marine weathering, leading to strong enrichment in most alkali elements and the light REE (except Ce). Nevertheless, their immobile element concentrations are consistently MORB-like and they plot within the MORB fields of tectonic discrimination diagrams. Isotope analyses indicate an affinity with Pacific MORB-source mantle.

Both the morphology of Osbourn Trough and geochemistry of its lavas establish that it was a mid-Cretaceous spreading ridge. The trough is nearly equidistant (1750 km versus 1550 km) from the Manihiki and Hikurangi Plateaus, which we interpret as remnants of a formerly contiguous large igneous province. Inception of the Osbourn spreading ridge was coincident with the demise of the former Pacific–Phoenix spreading ridge (Nova-Canton Trough) and fragmentation of the Manihiki Plateau at ~118 Ma. Spreading across Osbourn Trough ceased when the Hikurangi Plateau collided with and blocked a southward-dipping subduction system developed along the Chatham Rise (eastern New Zealand) sector of the Gondwana margin at ~86 Ma.

Keywords: Osbourn Trough; tectonic history; Pacific; Cretaceous; marine weathering

1. Introduction

The Mesozoic–Cenozoic history of the central–southern Pacific Basin is dominated by the interplay of at least three large oceanic plates: the Pacific, Phoenix, and Farallon Plates [1–5]. However, reconstructions of the paleo-Pacific are complicated by a series of tectonic processes that include the repeated development of ephemeral microplates (e.g., the active Juan Fernandez and Easter microplates [6] and the now defunct Selkirk and Magellan microplates [2,7]), jumping accretionary ridges (e.g., Galapagos Rise [8]), fracturing to generate new plates (e.g., the Farallon Plate splitting along the Cocos–Nazca Ridge [9]), and the continual re-organization of migrating triple junctions (e.g., the Tongareva triple junction at the Pacific–Phoenix–Farallon boundary [5]). Much important evidence has been lost by subduction beneath the convergent margins rimming the Pacific, and many key areas are devoid of magnetic lineations because the seafloor was generated during the mid-Cretaceous interval of constant magnetic polarity (84–121 Ma).

Nevertheless, an understanding of the mid-Cretaceous Pacific is important not just for pre-Tertiary plate reconstructions. At least three large igneous provinces (the Ontong Java, Manihiki, and Hikurangi Plateaus), which combined cover ~1 % of the Earth's surface and represent a volume of ~100 million km³ of degassed basaltic magma, were emplaced in the central–southern Pacific at ~120 Ma. The origins of this immense magmatic outburst, its possible link to one or more mantle plumes or bolide impacts, and the spatial relationships of the three large igneous provinces to each other at their time of formation remain controversial [10–15]. In a different research field, models of subduction-related magma genesis typically envisage mantle melting in response to the transfer of an aqueous fluid and/or a partial melt from the subducting slab [16,17]. Constraining mass balance in such models requires knowledge of the subducting oceanic crust composition, yet in many Pacific rim subduction zones it remains unclear whether this crust was always part of the Pacific Plate or shares the geochemical characteristics of crust generated at the East Pacific Rise (EPR) and its eastern Pacific predecessors.

A key area of oceanic crust relevant to these problems is that separating the Manihiki and Hikurangi Plateaus, bounded to the west by the Tonga–Kermadec Trench and to the east by the Wishbone–East Manihiki Scarp (Fig. 1). Magnetic lineations have not been detected in this area [19]. The publication of satellite-derived altimetry first drew attention to the ~900 km-long east–west trending Osbourn Trough, which extends from the Tonga–Kermadec Trench near 25.5°S to the Wishbone–East Manihiki Scarp. This feature has been variously

interpreted as a spreading ridge abandoned at ~105 Ma [20] or a tear in the Pacific Plate resulting from stress imposed by subduction of the Louisville Ridge at the Tonga Trench [21]. A detailed geophysical survey covering a 36 km-wide swath across Osbourn Trough revealed a 200–500 m-deep steep-sided axial valley flanked by several parallel ridges and valleys, including a prominent inside corner high and other features characteristic of slow-spreading ridges [22]. Modeling of subtle magnetic anomalies near the trough suggested spreading may have ceased as recently as 71 Ma. However, a more recent survey crossing the trough further to the east found that these anomalies do not represent reversals in the magnetic field and that the cessation of spreading must have been prior to ~84 Ma [23]. Radiolarian faunas from the nearby DSDP Sites 595 and 596 yielded minimum basement ages of 132–144 Ma and 94–99 Ma respectively [3], but these sites are in close proximity to the East Manihiki Scarp and it is unclear to which side of the scarp they belong.

Despite the recent geophysical surveys, only ~5 % of Osbourn Trough had been mapped and no lavas had been recovered. Here, we report the results of our multi-beam bathymetric survey across a 145 km-wide section of the trough adjacent to the 36 km-wide swath mapped by Billen and Stock [22]. We also dredged lavas from 6 stations located along the steep inner walls of the trough. Our bathymetric survey provides further strong morphological evidence that Osbourn Trough was indeed a paleo-spreading ridge, and geochemical analyses of the recovered lavas confirm that they are weathered MORB with the isotopic characteristics of Pacific-type MORB.

2. Bathymetry and structure of Osbourn Trough

Our Osbourn Trough bathymetric survey utilized the SIMRAD EM120 multi-beam system on the FS *SONNE*. A 12 kHz acoustic signal with a beam width of 150° across- and 2° along-track was emitted, and echoes were received as 191 beams with an accuracy of 0.2 % of water-depth. Real-time beam steering was used to compensate for roll, pitch and yaw of the ship, the beam data was merged with the data from the ship's navigational system (GPS), and the dataset was cleaned using NEPTUNE software. Calibration of the seawater acoustic profile was achieved by deploying a CTD at the start of the survey. Post-cruise, the data were further cleaned and re-gridded using a 50 m cell size.

Our swath reveals three linear segments with well-defined, flat-floored, axial valleys that trend 095° (Fig. 2). Each segment is offset from the next by a short valley or basin

oriented nearly perpendicular (trending 358°) to the axial valleys. All segment offsets are dextral. Inside corner highs rise 600–800 m above the mean height of the ridge mountains bounding the axial valleys, and are developed at the SW and NE margins of each segment. A series of abyssal hills, occasionally curved near the segment terminations, flank each segment and progressively diminish in relief with distance from the axial valley. A general upward slope to the west of all features throughout the surveyed area reflects the approaching outer flexural high of the Tonga–Kermadec Trench. We have labelled the three segments from west to east; thus our survey covers the eastern margin of Segment 1, all of the adjacent Segment 2, and the western part of Segment 3.

2.1. Segment 1

The axial valley defined by Billen and Stock [22] terminates near 173°30'W at the western margin of our surveyed area. In this region, the flat axial valley is 13 km-wide at 5330–5380 mbsl and 200–500 m below the bounding ridge mountains. Our survey confirms the presence of a lens-shaped, 10 km-long by 4 km-wide, inside corner high at the SE margin of the segment. This inside corner high rises abruptly from the valley floor to a maximum elevation of 4290 mbsl. Its summit slopes gently downwards to the SW, and consists of a series of peaks separated by ~100 m-deep valleys interpreted as sector collapse scars.

2.2. Segment 2

Segment 2 is 58 km-long and offset 23 km to the south of Segment 1. The axial valley is 9–13 km-wide at 5390–5630 mbsl, with a gentle eastward-facing slope. Narrow ridges 7–10 km-long and 2 km-wide rise up to 200 m above the surrounding seafloor in the center of the axial valley and near its western margin. However, the true dimensions and character of these features are obscured by their nearly complete sediment burial. Ridge mountains bounding the axial valley rise 300–600 m above the valley floor, with the southern wall consistently having greater elevation. Inside corner highs are developed at both the NW and SE segment margins; these have diameters of 10–15 km, precipitous axial valley-facing walls but gently-dipping outward-facing slopes, and summits at 4380 mbsl and 4250 mbsl respectively.

Further from the axial valley are a series of parallel semi-regularly spaced abyssal hills separated by troughs. The hills are spaced 15–20 km apart and rise 200–400 m above their adjacent troughs. The bounding wall of each hill facing towards the Segment 2 axial valley is

typically precipitous, whereas the opposite bounding wall has a gentler slope. Some abyssal hills display a marked bending at their eastern or western margins. These hills and troughs become progressively deeper and more subdued in relief with distance from the axial valley. Nearly identical constructs, including such details as precipitous inward-facing and less dramatic outward facing scarps, are observed on slow spreading segments of the Mid-Atlantic Ridge [24,25]. In the SW part of the surveyed area, south of 26°S, the abyssal hills are progressively buried by sediment derived from sector collapses on the nearby Louisville Ridge seamounts.

2.3. Segment 3

Segment 3 is offset 35 km to the south of Segment 2. Only the westernmost 45 km of this segment was mapped; the satellite-derived bathymetry suggests Segment 3 may be continuous for several hundred km to the east (Fig. 1). The general morphology and structure of Segment 3 resembles that of Segment 2. It has a flat axial valley 12–15 km wide at 5700–5760 mbsl, the bounding ridge mountains rise 400–600 m above the valley floor, and a series of parallel abyssal hills flank the axial valley. However, two inside corner highs are developed near the NW margin of Segment 3. The first is offset 28 km east from the NW axial valley margin and rises to 4500 mbsl, whereas the second is developed at the NW margin of the first flanking ridge north of the segment axis and rises to 4470 mbsl. The nature of the Segment 2–3 boundary is also more complex. Two partly buried curved ridges, 10–20 km in length, rise up to 300 m above the seafloor and extend from the SE margin of Segment 2 towards Segment 3. Further north, two deep rectilinear basins bounded by normal faults are incised into the western margin of Segment 3. These faults trend 110–120° and are oblique to all other structures in the Osbourn area, although they parallel the present-day motion of the Pacific Plate as indicated by seamount chains. We suggest they may be recently active pull-apart structures related to stresses within the Pacific Plate.

3. Osbourn samples

Ten dredge stations in and around Osbourn Trough were positioned on the steep, inward-facing, flanks of the inside corner highs in an attempt to penetrate the thick sediment cover. Lava fragments of sufficient size for analytical work were extracted from Fe-Mn

oxyhydroxide encrusted volcanic breccias recovered by six of these dredges (Table 1, Fig. 2). These breccias were commonly cored by one or more angular weathered lava fragments set in a matrix of deeply weathered lava granules and pale yellow palagonitic clay (Fig. 3). A sharp discontinuity usually separated this core from an overlying layer of yellow-brown sediment that bears black Fe-Mn oxyhydroxide discontinuous relict growth surfaces. The proportion of Fe-Mn oxyhydroxide increases rapidly with distance from the block core, and the outermost ~8 cm of most blocks was composed of alternating dense submetallic-black and porous dull-black Fe-Mn oxyhydroxide layers with minimal sediment. Multiple generations of Fe-Mn oxyhydroxide crusts were often observed, and probably formed by detached blocks rolling downslope, fracturing, and being overgrown by further Fe-Mn oxyhydroxide layers.

Lava fragments in the breccias are typically surrounded by dark brown oxidation haloes up to several mm thick (Fig. 3). Most fragments are non-vesicular aphanitic basalt in which much of the groundmass has been replaced by a mixture of celadonite, nontronite, saponite, Fe-oxyhydroxides, and other clay minerals. They range from brownish grey clasts with inner light grey domains, where replacement of the primary groundmass assemblage is only partial, to pale brownish yellow clasts in which there is near total replacement of the groundmass. Some fragments contain relict microphenocrysts, and in these the former olivine crystals are completely pseudomorphed by the secondary minerals whereas plagioclase is only altered along internal fractures. The secondary mineral assemblage of the lava fragments is typical of that observed elsewhere in marine weathered MORB and attributed to low-temperature alteration in a predominantly oxidising, high water/rock ratio, environment [26]. Many of the breccias contain fragments with different protoliths (e.g., aphyric basalt, olivine basalt, serpentinite) or different degrees of alteration, indicating widespread mass wasting occurred prior to burial of the fragments by sediment and the Fe-Mn oxyhydroxide crusts.

4. Fe-Mn oxyhydroxide crusts

A compositional profile through the ~65 mm thick Fe-Mn oxyhydroxide crust of sample 121-1 was generated to investigate the origin of the crust, its growth rate and changes in composition with time. The crust was subsampled at five intervals from its surface to the underlying contact with the sediment-hydroxide mix that overlies and encloses an angular basalt clast (Table 2). Low Fe/Mn ratios (0.62–1.49), high transition metal and REE contents (e.g., Co 2530–4570 ppm, La 173–278 ppm), and a strong positive Ce anomaly (Fig. 4;

$(\text{Ce}/\text{Ce}^*)_{\text{N}} = 5\text{--}8$ with Ce^* estimated by interpolation between chondrite-normalized La and Nd) throughout the crust are indicative of a hydrogenetic origin and a negligible hydrothermal component [31]. The positive Ce anomaly reflects preferential scavenging of Ce from seawater relative to the other REE, and is indicative of oxidising conditions with $\text{pH} > 4.8$ [32]. Phosphorus contents remain low across the profile (0.13–0.23 wt.%), and suggest the two Tertiary phosphogenic events recognized on central Pacific seamounts did not affect the deep south Pacific seafloor [33].

Growth rates for the crust based on the Co formula are in the range 1.2–3.7 mm/Ma [34], and show a general increase towards the present day. If these rates are accurate, then the base of the crust at the contact to the sediment–hydroxide mix has a minimum age of ~36 Ma. A variety of factors, including possible cryptic dissolution surfaces and growth pauses in the crust together with the uncertain time interval represented by the sediment–oxyhydroxide mix, suggest this severely underestimates the age of the enclosed Osbourn lava fragment. Element profiles throughout the crust show minor variations, most notably long-term trends of increasing Fe, V, and REE concentrations towards the present-day surface which are mirrored by decreasing Mn, Co, Te and Tl concentrations. Both P and Se show an initial decline in concentration followed by a progressive increase.

5. Analytical techniques

The least weathered 13 lava fragments were selected for geochemical analysis. Cores were cut from these fragments, coarse crushed, hand-picked to ensure removal of all Fe-Mn oxyhydroxides, washed thoroughly in an ultrasonic bath with deionized water to remove sea-salts, and then fine crushed in an agate mortar. For major element determinations, 0.6 grams of rock powder was mixed with lithium tetraborate and ammonium nitrate, fused to a homogenous glass disk, and analyzed using a Philips PW 1480 XRF spectrometer calibrated against international rock standards. Loss on ignition was determined by weight loss of >3 grams of rock powder heated in a furnace at 1000 °C for at least 4 hours. For trace element determinations, ~100 mg of rock powder was dissolved following the HF-HClO₄-aqua regia digestion procedure outlined in Garbe-Schönberg [35]. Sample residues were taken up in 2 % HNO₃, diluted, spiked for calibration, and analyzed using an Agilent 7500c ICP-MS. Accuracy was checked against international rock standards (BHVO-1, AGV-1), and precision (2σ) for duplicate analyses was better than 3 % for all elements (mostly better than 1 %).

Four lavas were analyzed for Sr-Nd-Pb isotopic composition, with both leached and unleached compositions being determined. For the former, ~250 mg of rock powder was leached in ultrapure 6N HCl on a hot plate for 1 hour and further washed with deionized water prior to dissolution in an HF/HNO₃ mix. Standard ion exchange techniques were then used to produce Pb, Sr and Nd separates [36]. Isotopic compositions were determined using the MAT 262 (Sr, Pb) and TRITON (Nd) thermal ionization mass spectrometers at IFM-GEOMAR in Kiel. Applied isotope fractionation corrections for Sr and Nd were $^{86}\text{Sr}/^{88}\text{Sr} = 0.1194$ and $^{146}\text{Nd}/^{144}\text{Nd} = 0.7219$, with all errors reported as 2σ standard errors of the mean. Repeated measurements of NBS 987 completed during the study yielded $^{87}\text{Sr}/^{86}\text{Sr} = 0.710237$ ($n = 13$) and for the in-house SPEX monitor yielded $^{143}\text{Nd}/^{144}\text{Nd} = 0.511718$ ($n = 7$). All reported analyses are normalized to $^{87}\text{Sr}/^{86}\text{Sr} = 0.710250$ for NBS 987 and $^{143}\text{Nd}/^{144}\text{Nd} = 0.511708$ (calibrated against $^{143}\text{Nd}/^{144}\text{Nd} = 0.511848$ for La Jolla). For Pb, the analyses were fractionation-corrected using repeated measurements of NBS 981 conducted under the same loading and run conditions ($n = 11$, $^{206}\text{Pb}/^{204}\text{Pb} = 16.899$, $^{207}\text{Pb}/^{204}\text{Pb} = 15.437$, $^{208}\text{Pb}/^{204}\text{Pb} = 36.525$; mass fractionation = 0.115 % per amu) and normalized to its accepted values [37]. Pb blanks were negligible (<250 pg).

6. Geochemistry of Osbourn lavas

The prime objective of the geochemical program was to establish whether Osbourn lavas have MORB-like compositions or the more alkalic compositions that would suggest an origin by intraplate processes or a relationship to the passage of a nearby mantle plume. Although only the freshest lavas were analyzed, all were severely weathered and their loss on ignition values ranged from 4.2 to 6.9 wt.% (Table 3). On a total alkali (Na₂O+K₂O) versus SiO₂ plot (not presented), the analyses straddle the discriminant line separating fields for alkaline and tholeiitic lavas and cluster around the basalt–trachybasalt boundary. However, anomalously low Mg# for many of these basaltic lavas testify to major loss of Mg during marine weathering and suggest widespread exchange of other elements (e.g., 8 of 13 lavas have Mg# in the range 21–30 despite SiO₂ contents <51.7 wt.%, where $\text{Mg\#} = 100 \cdot (\text{Mg}^{2+} / (\text{Mg}^{2+} + \text{Fe}^{2+}))$ with all Fe as FeO).

Normalization of incompatible elements in the Osbourn lavas to the composition of average MORB provides a useful guide both to the genesis of the lavas and to the extent of chemical exchange during their subsequent weathering (Fig. 5). Large positive anomalies are

evident for most large ion lithophile elements (LILE- e.g., Cs, Tl, Rb, K), whereas near-MORB values are apparent for the high field strength elements (HFSE- e.g., Th, Ta, Nb, Zr, Hf, Ti) and the heavy REE. This results in a spiked pattern when the elements are arranged in order of decreasing incompatibility during mantle melting (Fig. 5a-b). Such a pattern contrasts strongly to the smooth negative trend that would be generated by low degree partial melting of MORB-source mantle, where the MORB-normalized concentration of an element in the melt is proportional to its incompatibility, or to the similar pattern arising from melting of enriched mantle plume sources (e.g., OIB, Louisville). In particular, the MORB-like Th, Ta, Nb and Ce concentrations of Osbourn lavas would require a mantle source depleted in those elements. Re-arranging the element order to that of mobility during marine weathering results in a much improved fit (Fig. 5c-d). Both the order of element enrichment relative to MORB and the magnitude of this enrichment closely match that reported for weathered EPR MORB [40]. The prime difference is that Pb, Ba and Th in our Osbourn lavas are less enriched relative to MORB than in the weathered EPR lavas. Among the analyzed elements, only MgO, CaO and V in Osbourn lavas are consistently lower than the average MORB composition.

Chondrite-normalized REE patterns for Osbourn lavas range from flat and MORB-like to moderately light REE-enriched ($(La/Yb)_N = 0.9-4.4$; Fig. 6). A striking feature of these patterns is the ubiquitous presence of a deep negative Ce anomaly ($Ce/Ce^* = 0.12-0.77$). Nevertheless, Ce concentrations remain much closer to an average MORB composition than those of the other light REE. Values of Ce/Ce^* decrease with increasing loss on ignition, and correlate most strongly with increasing P_2O_5 and La (Fig. 7a-b). Light REE concentrations (excepting Ce) correlate strongly with P_2O_5 , with La increasing by a factor of 15 across the range in P_2O_5 (Fig. 7c). Although some of this increase could be attributed to the incompatibility of both elements during fractional crystallization of Osbourn magmas ascending through the crust, the more incompatible heavy REE (and Ce) increase by a factor of only 2–3. Furthermore, Zr, Nb, Th, and most other elements expected to behave incompatibly during fractional crystallization exhibit minimal correlation with P_2O_5 or La. An exception is U, which correlates strongly with La and P_2O_5 (Fig. 7d).

Instead, we attribute the REE systematics of the Osbourn lavas to the addition of the light REE (except Ce) from seawater during marine weathering. Adsorption of the REE probably occurred on Fe-oxyhydroxide surfaces formed during breakdown of the groundmass in a manner broadly analogous to the later episode of Fe-Mn oxyhydroxide crust formation. Therefore, the chondrite-normalized pattern of the Fe-Mn oxyhydroxide crust should reflect

the pattern of added REE to the Osbourn lavas. Only the La–Sm concentrations of the Fe-Mn oxyhydroxide crusts exceed (or are comparable to) those of the lavas, and it is notable that only these REE are now present at levels significantly above those of MORB in the lavas (Figs. 2, 6). A critical difference between these two phases of REE adsorption occurs for Ce. Within the lavas, Ce is not preferentially scavenged from circulating fluids by Fe-oxyhydroxides and remains in solution as Ce(IV) compounds under alkaline conditions [41]. Therefore, all light REE except Ce are added to Osbourn lavas during marine weathering. Conversely, Ce is preferentially scavenged at $\text{pH} > 4.8$ by the $\delta\text{-MnO}_2$ comprising much of the Fe-Mn oxyhydroxide crusts [32]. We conclude that the original chondrite-normalized REE pattern of the Osbourn lavas is represented by a curve passing through Ce and the REE heavier than Sm.

The immobility of the HFSE and Ce can be used to track the mobility of other elements during the weathering process. All Osbourn lavas have $\text{Nb}/\text{U} < 25$, whereas fresh MORB has $\text{Nb}/\text{U} = 47 \pm 10$ [42]. Thus, if Osbourn lavas were MORB, all have been affected by significant addition of U (Fig. 7e). The behaviour of Pb is more varied, with two lavas having Ce/Pb values within the fresh MORB range of 25 ± 5 but all others showing Pb addition (Fig. 7f).

7. Tectonic discrimination of Osbourn lavas and their mantle source

Elements that are immobile during weathering and alteration processes can provide a powerful means of discriminating between lavas generated in different tectonic settings [43,44]. We have argued that the HFSE and heavy REE (including Ce) systematics of the Osbourn lavas were negligibly affected by marine weathering, and demonstrated that both groups of elements have MORB-like concentrations in these lavas. Here, we use tectonic discrimination diagrams for basaltic lavas to examine whether co-variations among and between these elements remain consistent with classifying Osbourn lavas as weathered MORB.

Osbourn lavas scatter widely on plots of both Zr/Y versus Y and Ti/Y versus Nb/Y (Fig. 8a-b), though most fall within the MORB field and none occupy the within plate or OIB field. Two Osbourn lavas plot outside the MORB field and have anomalously low Zr/Y and Ti/Y values. The most anomalous lava (sample 132-1) has the highest reported P_2O_5 content coupled with high La and Y concentrations but MORB-like Ce (Fig. 5b, 6b); we consider this

lava was probably affected by Y addition during weathering. A tighter clustering and near complete overlap with present-day EPR MORB compositions is observed on plots of Nb/Zr versus Nb and $(\text{Ce}/\text{Yb})_{\text{N}}$ versus $(\text{Ce})_{\text{N}}$ (Fig. 8c-d). All Osbourn lavas have far lower Nb/Zr and $(\text{Ce}/\text{Yb})_{\text{N}}$ than lavas from the nearby Louisville Ridge seamounts and the other south Pacific seamount chains that potentially crossed this region during the Cretaceous–Tertiary (Society, Cook–Austral, Pitcairn). Thus, the tectonic discrimination diagrams designed to identify the paleo-environment of altered and metamorphosed lavas consistently indicate that the Osbourn lavas formed as MORB.

The Sr-Nd-Pb isotope systematics of four Osbourn lavas were investigated as a further check on their mantle source and provenance (Table 4). Both the $^{87}\text{Sr}/^{86}\text{Sr}$ and $^{143}\text{Nd}/^{144}\text{Nd}$ values of the lavas are shifted to less radiogenic compositions after leaching, reflecting the addition of these elements from seawater during marine weathering. Lead isotope compositions can be used to distinguish a variety of mantle domains, including the Pacific MORB-source mantle (PMM) and Indian MORB-source mantle (IMM) reservoirs that are of considerable interest in tracking mantle convection at spreading systems and mass transfer in subduction zones [49–51]. Lead isotopes are also sensitive indicators of other mantle sources that are generally tapped only by OIB [52].

Present-day Pb isotope compositions of Osbourn lavas fall within the PMM field for both unleached and leached aliquots (Fig. 9). Assuming that the lavas have an age of 86 Ma (see below) and have remained closed to U and Pb since shortly after eruption, their initial Pb isotope compositions were close to the PMM–IMM boundary (sample 125-1 plots marginally within the IMM field, the others remain PMM; changes in the MORB fields corrected to 86 Ma are insignificant compared to Pb ingrowth in the Osbourn lavas). However, all Osbourn lavas have gained U during marine weathering and all but two have gained Pb (Figs. 7e-f). Uranium and Pb addition in oceanic crust typically occurs within a few million years of formation while the system remains open to circulating fluids [53,54], but this is not necessarily the case for our Osbourn lavas as some have been fractured during recurrent mass wasting events on the steep axial slopes (Fig. 3). If sample 125-1 gained U more recently than 75 Ma, then this lava would also have an initial Pb isotope composition within the PMM field. We conclude that Osbourn lavas require a PMM source unless they are considerably older than 86 Ma. Their Pb isotope systematics also provide no evidence for any link to the nearby Louisville and Cook–Austral seamount chains, both of which have markedly more radiogenic Pb isotope compositions (Fig. 9).

8. Osbourn spreading ridge and the Cretaceous Pacific

Our bathymetric survey of the western 145 km of Osbourn Trough confirms that the trough has the morphology of a slow to intermediate spreading ridge, replete with a well-developed axial valley, bounding ridge mountains, flanking abyssal hills and small non-transform segment offsets. The total relief between the axial valley and ridge mountains is typically 300–500 m, or 1000–1200 m if the inside corner highs are included. Total relief across the axial valley of spreading ridges is inversely proportional to their spreading rate, and becomes insignificant for spreading rates above 9 cm/year [55]. The observed relief is approximately half that of similar constructs at 28–29°N and 37°N on the Mid-Atlantic Ridge, where the full spreading rate is ~3 cm/year [24,25]. Indeed, Osbourn Trough closely resembles many Mid-Atlantic Ridge segments rotated through 90°.

Given the clear bathymetric evidence that Osbourn Trough was a spreading ridge and the unambiguous geochemical evidence that Osbourn lavas are weathered MORB, we now examine the implications for Cretaceous reconstructions of the Pacific. During the early to mid-Cretaceous, the Pacific–Phoenix–Farallon triple junction was located at the eastern end of the Nova-Canton Trough (Fig. 10a). Seafloor spreading between the Pacific and Phoenix Plates at the Nova-Canton Trough ceased by ~118 Ma, and a more complex spreading system began to evolve near the NE margin of the Manihiki Plateau [2,4,56,57]. The spreading ridge jump was probably triggered by the emplacement of the Manihiki–Hikurangi large igneous province at 119–121 Ma [4,58], with the mechanism being either disturbance to the shallow mantle convection pattern by the rising plume or lithospheric fracturing caused by thermal doming.

Both the northern and eastern margins of the present-day Manihiki Plateau initially developed as the NW and southern arms of the new triple junction [5]. The triple junction rapidly migrated to the SE, with the abyssal hill fabric of the Penrhyn Basin indicating that an east–west oriented spreading ridge linked the triple junction to the East Manihiki Scarp (Fig. 10a) [4,5]. We propose that the Osbourn Trough represents a further segment of this east–west oriented spreading system, extending west from the East Manihiki transform and rifting away the southern section of the Manihiki Plateau as the Hikurangi Plateau (Fig. 10a). Thus, the net effect of the mid-Cretaceous re-alignment was that seafloor spreading centered on the Osbourn Trough replaced that previously centered on the Nova-Canton Trough, and that the Manihiki Plateau remnant (and the area to its west) was transferred from the Phoenix Plate to the Pacific Plate.

The termination of seafloor spreading at Osbourn Trough was probably coincident with the Hikurangi Plateau reaching and blocking a southward-dipping subduction system developed along the Chatham Rise margin of Gondwana (Fig. 10b). Although much of the New Zealand Gondwana margin may not have been under compression since ~105 Ma [59], a series of new studies focussed on the eastern part of this margin closest to the Chatham Rise record unequivocal evidence of later convergence; (1) calc-alkaline volcanism with subduction-related geochemistry persisted in the Canterbury province until at least 89 Ma [60], (2) seaward-migrating thrust systems preserved along the eastern side of the North Island have been dated at 85–89 Ma [61,62], and (3) the dominant metamorphic isograds in the Alpine Schist of the South Island formed at 86 Ma [63]. Thus, we contend that ~86 Ma is the most probable age for the cessation of spreading at Osbourn Trough.

Previous estimates for the cessation of Osbourn spreading have ranged from 71 Ma [22] to 105 Ma [20]. New magnetic profiles across a larger section of Osbourn Trough have demonstrated that the trough has a minimum age of ~84 Ma [23]. In addition, the nearest Louisville Ridge seamount to Osbourn Trough has recently been re-dated as ~77 Ma [64], and the ability of the lithosphere to withstand this load requires a significantly greater age. The older age estimates for Osbourn Trough were based on the apparent absence of convergence along the New Zealand Gondwana margin. In our view, mid-Cretaceous tectonic reconstructions that assume the entire New Zealand Gondwana margin has been under extension since ~105 Ma cannot be sustained [20,65,66]. We do, however, agree that the evidence for extension rapidly evolving to break-up along the New Zealand Gondwana margin after ~84 Ma is overwhelming.

Insufficient bathymetric and geophysical data is available to attempt a rigorous fit of the Manihiki and Hikurangi Plateau margins or to fit either to our Osbourn bathymetry. However, to provide some first order constraints we have selected points on all three at the same distance from the East Manihiki and Wishbone Scarps. Our chosen location is the junction of Osbourn Trough segments 2 and 3, for which the Osbourn–Manihiki distance is ~1750 km and the Osbourn–Hikurangi distance is ~1550 km. Thus, over its inferred 32 Ma lifespan, the average spreading rate across the Osbourn Trough was ~10 cm/year (full rate). This is approximately half that inferred for Pacific–Phoenix spreading across the Nova-Canton Trough [4], yet too great for the morphological features preserved at Osbourn Trough. Most likely, spreading rates at Osbourn Trough were initially ~20 cm/year and decreased as spreading segments further west underwent progressive elimination by collision with the Gondwana margin.

9. Conclusions

Bathymetric mapping of a 120 km by 145 km section of the ~900 km-long Osbourn Trough combined with geochemical analyses of lavas recovered from steep escarpments have resolved the origin of this previously enigmatic feature on the south Pacific seafloor. Our prime conclusions are:

1. Osbourn Trough has the morphology of a slow-spreading ridge. Within the surveyed area we distinguish three segments offset from each other by 23–35 km-long basins that strike perpendicular to the trough axis. Each segment features a 10–15 km-wide flat-floored axial valley bounded by 300–500 m-high ridge mountains, with inside corner highs developed at the NW and SE margins and rising 1000–1200 m from the axial valley floor. The segments are flanked by subparallel abyssal hills that often curve near the segment terminations. Inward-facing fault scarps are well-developed and precipitous, whereas outward-facing scarps are less so. All these features closely match those of the slow-spreading Mid-Atlantic Ridge.
2. Osbourn lavas are weathered MORB. Lava clasts extracted from volcanoclastic breccias have undergone marine weathering, with extensive replacement of their primary mineral assemblage by clays and Fe-oxyhydroxides. They are strongly enriched in most alkali elements and the light REE (except Ce) relative to MORB, and both the order and magnitude of element enrichment is similar to that observed for weathered MORB elsewhere. Elements considered immobile during marine weathering are consistently at MORB-like concentrations. The lavas plot within the MORB fields of tectonic discrimination diagrams and show no evidence for any alkalic or plume components. Isotope analyses indicate an affinity with Pacific MORB-source mantle.
3. Spreading occurred across Osbourn Trough from ~118 Ma to ~86 Ma. Osbourn Trough is nearly equidistant (1750 km versus 1550 km) from the Manihiki and Hikurangi Plateaus. Given the now unequivocal evidence that Osbourn Trough was a spreading ridge, we consider these plateaus are remnants of a formerly contiguous large igneous province emplaced at ~120 Ma. Their emplacement triggered a major re-organization of the Pacific–Phoenix spreading system, with spreading jumping southwards from the Nova-Canton Trough to the margins of the Manihiki–Hikurangi Plateau at ~118 Ma. The plateau was fragmented, and Pacific–Phoenix spreading was re-established at Osbourn Trough. Initial spreading rates across Osbourn Trough were probably similar to that of the former Pacific–Phoenix system (~20 cm/year), but likely declined with time to ~5 cm/year.

Spreading across Osbourn Trough finally ceased when the Hikurangi Plateau collided with and blocked a southward-dipping subduction system developed along the Chatham Rise (eastern New Zealand) sector of the Gondwana margin at ~86 Ma.

Acknowledgements

We thank Captain Martin Kull, his officers and crew, and the other members of the Shipboard Scientific Party for their efforts and professionalism during the SO-167 cruise of the FS *SONNE*. Dieter Garbe-Schönberg, Ulrike Westernströer and Inga Dold provided assistance with the geochemical analyses; Silke Hauff assisted with the isotope work. Funding for the cruise and analytical program was provided by the Bundesministerium für Bildung und Forschung (BMBF grant 03G0167A). RH thanks the Alexander von Humboldt Foundation for their support.

References

- [1] R.L. Larson, C.G. Chase, Late Mesozoic evolution of the western Pacific Ocean, *Geol. Soc. Amer. Bull.* 83 (1972) 3627–3644.
- [2] M. Nakanishi, E.L. Winterer, Tectonic history of the Pacific–Farallon–Phoenix triple junction from late Jurassic to early Cretaceous: an abandoned Mesozoic spreading system in the central Pacific, *J. Geophys. Res.* 103 (1998) 12453–12468.
- [3] R. Sutherland, C. Hollis, Cretaceous demise of the Moa Plate and strike-slip motion at the Gondwana margin, *Geology* 29 (2001) 279–282.
- [4] R.L. Larson, R.A. Pockalny, R.F. Viso, E. Erba, L.J. Abrams, B.P. Luyendyk, J.M. Stock, R.W. Clayton, Mid-Cretaceous tectonic evolution of the Tongareva triple junction in the Southwestern Pacific basin, *Geology* 30 (2002) 67–70.
- [5] R.F. Viso, R.L. Larson, R.A. Pockalny, Tectonic evolution of the Pacific–Phoenix–Farallon triple junction in the South Pacific Ocean, *Earth Planet. Sci. Lett.* 233 (2005) 179–194.
- [6] R.C. Searle, R.T. Bird, R.I. Rusby, D.F. Naar, The development of two oceanic microplates: Easter and Juan Fernandez microplates, East Pacific Rise, *J. Geol. Soc. London* 150 (1993) 965–976.
- [7] A. Blais, P. Gente, M. Maia, D.F. Naar, A history of the Selkirk paleomicroplate, *Tectonophys.* 359 (2002) 157–169.
- [8] J.A. Goff, J.R. Cochran, The Bauer scarp ridge jump; a complex tectonic sequence revealed in satellite altimetry, *Earth Planet. Sci. Lett.* 141 (1996) 21–33.
- [9] P. Lonsdale, Creation of the Nazca and Cocos plates by fission of the Farallon plate, *Tectonophys.* 404 (2005) 237–264.
- [10] M.A. Richards, R.A. Duncan, V. Courtillot, Flood basalts and hotspot tracks: plume heads and tails, *Science* 246 (1989) 193–107.
- [11] J.A. Tarduno, W.V. Sliter, L.W. Kroenke, M. Leckie, H. Mayer, J.J. Mahoney, R. Musgrave, M. Storey, E.L. Winterer, Rapid formation of Ontong Java Plateau by Aptian mantle plume volcanism, *Science* 254 (1991) 399–403.
- [12] R.L. Larson, Superplume and ridge interactions between Ontong Java and Manihiki Plateaus and the Nova-Canton Trough, *Geology* 25 (1997) 779–782.
- [13] S. Ingle, M.F. Coffin, Impact origin for the greater Ontong Java Plateau?, *Earth Planet. Sci. Lett.* 218 (2004) 123–134.

- [14] M. Antretter, P. Riisager, S. Hall, X. Zhao, B. Steinberger, Modeled paleolatitudes for the Louisville hotspot and the Ontong Java Plateau, in: J.G. Mahoney, P.J. Wallace, A.D. Saunders (eds.) *Origin and Evolution of the Ontong Java Plateau*, Geol. Soc. Spec. Publ. 229 (2005) 21–30.
- [15] K. Hoernle, F. Hauff, P. van den Bogaard, R. Werner, N. Mortimer, The Hikurangi oceanic plateau: another large piece of the largest volcanic event on Earth, 15th Annual Goldschmidt Conference abstracts (2005) A96.
- [16] J.A. Pearce, D.W. Peate, Tectonic implications of the composition of volcanic arc magmas, *Annu. Rev. Earth Planet. Sci.* 23 (1995) 251–285.
- [17] C. Hawkesworth, S. Turner, D. Peate, F. McDermott, P. van Calsteren, Elemental U and Th variations in island arc rocks: implications for U-series isotopes, *Chem. Geol.* 139 (1997) 207–221.
- [18] W.H.F. Smith, D.T. Sandwell, Global sea floor topography from satellite altimetry and ship sounding depths, *Science* 277 (1997) 1956–1962.
- [19] A.B. Watts, J.K. Weissel, R.A. Duncan, R.L. Larson, Origin of the Louisville Ridge and its relationship to the Eltanin Fracture Zone system, *J. Geophys. Res.* 93 (1988) 3051–3077.
- [20] P. Lonsdale, An incomplete geologic history of the south-west Pacific basin, *Geol. Soc. Am. Abstr. Programs* 29 (1997) 4574.
- [21] C. Small, D. Abbott, Subduction obstruction and the crack-up of the Pacific Plate, *Geology* 26 (1998) 795–798.
- [22] M.I. Billen, J. Stock, Morphology and origin of the Osbourn Trough, *J. Geophys. Res.* 105 (2000) 13481–13489.
- [23] N. Downey, J.M. Stock, R.W. Clayton, S.C. Cande, The geophysical character of the Osbourn Trough, AGU Western Pacific Geophysics Conference abstracts (2004).
- [24] K.C. Macdonald, B.P. Luyendyk, Deep-tow studies of the structure of the Mid-Atlantic Ridge crest near lat 37°N, *Geol. Soc. Am. Bull.* 88 (1977) 621–636.
- [25] H. Sloan, P. Patriat, Generation of morphotectonic fabric on the mid-Atlantic Ridge flanks, 28° to 29°N: implications for the limits of tectonic deformation and abyssal hill formation, *Geochem. Geophys. Geosyst.* 5 (2004) Q02004, doi:10.1029/2003GC000584.
- [26] E.H. Talbi, J. Honnorez, Low-temperature alteration of Mesozoic oceanic crust, *Ocean Drilling Program Leg 185, Geochem. Geophys. Geosyst.* 4 (2003) 8906, doi:10.1029/2002GC000405.

- [27] F.J. Flanagan, D. Gottfried, USGS Rock Standards, III: Manganese-nodule reference samples USGS-NOD-A-1 and USGS-NOD-P-1, US Geol. Surv. Prof. Paper 1155 (1980).
- [28] T. Kuhn, M. Bau, N. Blum, P. Halbach, Origin of negative Ce anomalies in mixed hydrothermal-hydrogenetic Fe-Mn crusts from the Central Indian Ridge, *Earth Planet. Sci. Lett.* 163 (1998) 207–220.
- [29] S.-S. Sun, W.F. McDonough, Chemical and isotopic systematics of oceanic basalts: implications for mantle composition and processes, in: A.D. Saunders, M.J. Norry, (eds.), *Magmatism in the Ocean Basins*, *Geol. Soc. Spec. Publ.* 42 (1989) 313–345.
- [30] S.M. McLennan, Rare earth elements in sedimentary rocks: influence of provenance and sedimentary processes, in: B.R. Lipkin, G.A. McKay (eds.), *Geochemistry and Mineralogy of Rare Earth Elements*, *Rev. Mineral.* 21 (1989) 169–200.
- [31] J.R. Hein, A. Koschinsky, P. Halbach, F.T. Manheim, M. Bau, J.K. Kang, N. Lubick, Iron and manganese oxide mineralization in the Pacific. In: K. Nicholson, J.R. Hein, B. Bühn, S. Dasgupta (eds.) *Manganese Mineralization: Geochemistry and Mineralogy of Terrestrial and Marine Deposits*, *Geol. Soc. Spec. Publ.* 119 (1997) 123–138.
- [32] A. Ohta, I. Kawabe, REE(III) adsorption onto Mn dioxide (δ -MnO₂) and Fe oxyhydroxide: Ce(III) oxidation by δ -MnO₂, *Geochim. Cosmochim. Acta* (2001) 695–703.
- [33] J.R. Hein, H.W. Yeh, S.H. Gunn, W.H. Sliter, L.M. Benninger, C.-H. Wang, Two major Cenozoic episodes of phosphogenesis recorded in equatorial Pacific seamount deposits, *Paleoceanography* 8 (1993) 293–311.
- [34] F.T. Manheim, C.M. Lane-Bostwick, Cobalt in ferromanganese crusts as a monitor of hydrothermal discharge on the Pacific seafloor, *Nature* 335 (1988) 59–62.
- [35] C.-D. Garbe-Schönberg, Simultaneous determination of thirty-seven trace elements in twenty-eight international rock standards by ICP-MS, *Geostand. Newslett.* 17 (1993) 81–97.
- [36] K.A. Hoernle, G.R. Tilton, Sr-Nd-Pb isotope data for Fuerteventura (Canary Islands) basal complex and subaerial volcanics: applications to magma genesis and evolution, *Schweizerische Mineralogische und Petrographische Mitteilungen* 71 (1991) 3–18.
- [37] W. Todt, R.A. Cliff, A. Hanser, A.W. Hofmann, Evaluation of a ²⁰²Pb–²⁰⁵Pb double spike for high-precision lead isotope analysis, in: G.E. Bebout et al. (eds.), *AGU Geophys. Monogr. Ser.* 95 (1996) 429–437.

- [38] J.A. Pearce, I.J. Parkinson, Trace element models for mantle melting: application to volcanic arc petrogenesis, in: H.M. Pritchard et al. (eds.), *Magmatic Processes and Plate Tectonics*, Geol. Soc. Spec. Publ. 76 (1993) 373–403.
- [39] T.J. Worthington et al. in prep.
- [40] K.P. Jochum, S.P. Verma, Extreme enrichment of Sb, Tl and other trace elements in altered MORB, *Chem. Geol.* 130 (1996) 289–299.
- [41] P. Möller, M. Bau, Rare-earth patterns with positive cerium anomaly in alkaline waters from Lake Van, Turkey, *Earth Planet. Sci. Lett.* 117 (1993) 671–676.
- [42] A.W. Hofmann, K.P. Jochum, M. Seufert, W.M. White, Nb and Pb in oceanic basalts: new constraints on mantle evolution, *Earth Planet. Sci. Lett.* 79 (1986) 33–45.
- [43] J.A. Pearce, J.R. Cann, Ophiolite origin investigated by discriminant analysis using Ti, Zr and Y, *Earth Planet. Sci. Lett.* 12 (1971) 339–349.
- [44] J.A. Pearce, J.R. Cann, Tectonic setting of basic volcanic rocks determined using trace element analyses, *Earth Planet. Sci. Lett.* 19 (1973) 290–300.
- [45] J.A. Pearce, M.J. Norry, Petrogenetic implications of Ti, Zr, Y and Nb variations in volcanic rocks, *Contrib. Mineral. Petrol.* 69 (1979) 33–47.
- [46] J.A. Pearce, Trace element characteristics of lavas from destructive plate boundaries, in: R.S. Thorpe (ed.), *Andesites* (1982), Wiley, Chichester, pp. 525–548.
- [47] Su, Y.J., Mid-ocean ridge basalt trace element systematics: constraints from database management, ICP-MS analyses, global data compilation and petrologic modeling, PhD thesis (2002), Columbia University, 472 pp.
- [48] R. Hekinian, Petrology of young submarine hotspot lava: composition and classification, in: R. Hekinian, P. Stoffers, J.-L. Cheminee (eds.), *Oceanic Hotspots* (2004), Springer, Berlin, pp. 431–459.
- [49] S.R. Hart, A large-scale isotope anomaly in the Southern Hemisphere mantle, *Nature* 309 (1984) 753–757.
- [50] J.A. Pearce, P.D. Kempton, G.M. Nowell, S.R. Noble, Hf-Nd element and isotope perspective on the nature and provenance of mantle and subduction components in western Pacific arc–basin systems, *J. Petrol.* 40 (1999) 1579–1611.
- [51] P.D. Kempton, J.A. Pearce, T.L. Barry, J.G. Fitton, C. Langmuir, D.M. Christie, Sr-Nd-Pb-Hf isotope results from ODP Leg 187: evidence for mantle dynamics of the Australian–Antarctic discordance and origin of the Indian MORB source, *Geochem. Geophys. Geosyst.* 3 (2002) 1074, doi:10.1029/2002GC000320.

- [52] A. Stracke, A.W. Hofmann, S.R. Hart, FOZO, HIMU, and the rest of the mantle zoo, *Geochem. Geophys. Geosyst.* 6 (2005) Q05007, doi:10.1029/2004GC000824.
- [53] F. Hauff, K. Hoernle, G. Tilton, D. Graham, A.C. Kerr, Large volume recycling of oceanic lithosphere: geochemical evidence from the Caribbean large igneous province, *Earth Planet. Sci. Lett.* 174 (2000) 247–263.
- [54] F. Hauff, K. Hoernle, A. Schmidt, Sr-Nd-Pb composition of Mesozoic Pacific oceanic crust (Site 1149 and 801, ODP Leg 185): implications for alteration of ocean crust and the input into the Izu–Bonin–Mariana subduction system, *Geochem. Geophys. Geosyst.* 4 (2003) 8913, doi:10.1029/2002GC000421.
- [55] K.C. Macdonald, The crest of the Mid-Atlantic Ridge: models for crustal generation processes and tectonics, in: P.R. Vogt, B.E. Tucholke (eds.) *The Geology of North America*, vol. M, The Western North Atlantic Region. Geol. Soc. Am, Boulder, Colorado (1986).
- [56] E.L. Winterer, P.F. Lonsdale, J.L. Matthews, B.R. Rosendahl, Structure and acoustic stratigraphy of the Manihiki Plateau, *Deep-sea Res.* 21 (1974) 793–814.
- [57] D. Joseph, B. Taylor, A.N. Shor, The Nova-Canton Trough and the late Cretaceous evolution of the central Pacific, in: M.S. Pringle et al. (eds.) *The Mesozoic Pacific: Geology, Tectonics and Volcanism*, AGU Geophys. Monogr. Ser. 77 (1993) 171–185.
- [58] J.J. Mahoney, M. Storey, R.A. Duncan, K.J. Spencer, M. Pringle, Geochemistry and age of the Ontong Java Plateau, in: M.S. Pringle et al. (eds.) *The Mesozoic Pacific: Geology, Tectonics and Volcanism*, AGU Geophys. Monogr. Ser. 77 (1993) 233–261.
- [59] J.D. Bradshaw, Cretaceous geotectonic patterns in the New Zealand region, *Tectonics* 8 (1989) 803–820.
- [60] T.R. Smith, J.W. Cole, Somers Ignimbrite Formation: Cretaceous high-grade ignimbrites from South Island, New Zealand, *J. Volcanol. Geotherm. Res.* 75 (1997) 39–57.
- [61] P.J.J. Kamp, Tracking crustal processes by FT thermochronology in a forearc high (Hikurangi margin, New Zealand) involving Cretaceous subduction termination and mid-Cenozoic subduction initiation, *Tectonophys.* 307 (1999) 313–343.
- [62] P.J.J. Kamp, Thermochronology of the Torlesse accretionary complex, Wellington region, New Zealand, *J. Geophys. Res.* 105 (2000) 19253–19272.
- [63] J.K. Vry, J. Baker, R. Maas, T.A. Little, R. Grapes, M. Dixon, Zoned (Cretaceous and Cenozoic) garnet and the timing of high grade metamorphism, Southern Alps, New Zealand, *J. Metamorph. Geol.* 22 (2004) 137–157.

- [64] A.A.P. Koppers, R.A. Duncan, B. Steinberger, Implications of a nonlinear $^{40}\text{Ar}/^{39}\text{Ar}$ age progression along the Louisville seamount trail for models of fixed and moving hot spots, *Geochem. Geophys. Geosyst.* 5 (2004) Q06L02, doi:10.1029/2003GC000671.
- [65] R.D. Larter, A.P. Cunningham, P.F. Barker, K. Gohl, F.O. Nitsche, Tectonic evolution of the Pacific margin of Antarctica, 1. Late Cretaceous tectonic reconstructions, *J. Geophys. Res.* 107 (2002) 2345, doi:10.1029/2000JB000052.
- [66] G. Eagles, K. Gohl, R.D. Larter, High-resolution animated tectonic reconstruction of the south Pacific and West Antarctic margin, *Geochem. Geophys. Geosyst.* 5 (2004) Q07002, doi:10.1029/2003GC000657.

Table 1
SO-167 dredge stations around Osbourn Trough^a

Station	Latitude ^b °S	Longitude ^b °W	Depth mbsl	Recovered lithologies ^c
121	25°37.0'	173°32.1'	4716–4376	Aphanitic, ol and plag basalts
125	25°38.5'	173°18.0'	5299–4361	Aphanitic and ol-plag basalts
128	25°47.2'	172°36.4'	5558–4744	Aphanitic, ol-plag and plag basalts
129	25°39.3'	172°35.2'	5994–5198	Aphanitic, ol, ol-plag and plag basalts; srp clasts
130	25°52.3'	172°47.0'	5378–4435	Aphanitic and ol-plag basalts
132	25°59.2'	172°15.0'	5419–4654	Ol-plag and plag basalts; srp clasts

^a Four dredges that only returned Fe-Mn oxyhydroxide crusts are not listed.

^b Co-ordinates are the mid-points of dredge tracks typically 500 m long.

^c These lithologies are the protoliths of weathered clasts within volcanoclastic breccias encrusted by Fe-Mn oxyhydroxides (ol = olivine, plag = plagioclase, srp = serpentinite).

Table 2
Geochemical profile across the Fe-MnOx crust of SO-167-121-1

Element ^a	Method	Interval ^b					Nod-A-1 ^c	Nod-A-1 ^d
		0–15	15–30	30–45	45–55	55–65		
Fe	INAA	17.2	20.9	15.3	12.2	12.0	12.0	10.9
Mn	INAA	18.9	14.1	21.0	19.1	19.4	20.8	17.5
P	ICP-AES	0.174	0.157	0.154	0.135	0.231	0.240	
Fe/Mn		0.91	1.49	0.73	0.64	0.62	0.58	0.62
V	ICP-AES	666	631	618	507	511	495	770
Co	INAA	3330	2530	4380	4200	4570	3240	3100
Se	ICP-MS	6.1	5.6	4.9	4.1	6.7	2.2	
Te	ICP-MS	30.5	20.8	37.8	40.3	48.4	35.7	
La	INAA	273	278	232	173	214	134	112
Ce	INAA	1600	1420	1480	1430	1540	807	745
Nd	INAA	240	229	176	139	210	94	100
Sm	INAA	56.4	60.0	47.0	37.6	48.0	24.8	21.5
Eu	INAA	13.4	13.7	10.3	8.5	10.8	5.2	5.3
Tb	INAA	8.2	9.0	6.0	4.8	6.4	3.1	4.0
Yb	INAA	25.5	27.3	24.0	20.3	27.3	15.4	13.7
Lu	INAA	4.08	4.45	3.78	3.33	4.10	2.27	2.16
Tl	ICP-MS	45.4	44.2	78.6	92.5	130.0	109.0	
Bi	ICP-MS	20.0	11.1	12.7	13.6	13.6	10.5	
Growth rate ^e		2.5	3.7	1.6	1.3	1.2		
Age ^f		6.0	10.1	19.5	27.2	35.5		

^a Fe, Mn and P are reported in wt.%, all others in ppm.

^b Interval in cm beneath the present-day surface from which material was extracted for analysis.

^c Concentration in the Nod-A-1 reference standard measured during this study.

^d Published concentration data for the Nod-A-1 reference standard: Fe, Mn and V from Flanagan and Gottfried [27], REE from Kuhn et al. [28].

^e Growth rate in mm/Ma, calculated from the Co formula of Manheim and Lane-Bostwick [34].

^f Age in Ma at the base of each layer calculated from the growth rate and assuming continual growth.

Table 3
Geochemical analyses of Osbourn lavas

Sample ^a	121-1	125-1	125-3	128-1	128-2	128-4	129-1	130-1	130-2	130-4	132-1	132-2	132-3
SiO ₂	51.09	46.89	46.96	48.75	47.55	46.60	49.33	47.72	47.43	47.91	46.81	47.91	48.61
TiO ₂	2.79	1.69	1.62	1.53	2.01	1.94	1.98	0.93	2.17	1.60	1.33	1.32	1.51
Al ₂ O ₃	14.38	18.77	18.73	17.49	18.32	17.35	17.63	17.58	17.05	18.14	19.26	19.30	18.53
Fe ₂ O ₃	11.61	11.91	11.57	10.16	12.33	13.36	11.09	8.73	13.53	11.14	10.77	11.44	11.94
MnO	0.16	0.16	0.19	0.15	0.14	0.14	0.08	0.13	0.16	0.12	0.14	0.15	0.11
MgO	5.47	2.43	2.48	4.77	1.93	1.86	4.11	7.66	1.83	4.41	1.58	2.13	2.39
CaO	5.32	7.56	7.74	8.46	7.16	6.51	5.91	10.07	5.97	5.58	8.43	6.34	5.74
Na ₂ O	3.96	2.94	2.94	3.03	3.59	2.73	3.15	2.48	3.08	3.16	2.74	2.76	2.94
K ₂ O	0.80	1.54	1.54	1.15	1.42	2.24	1.26	0.73	2.10	1.75	1.68	1.80	2.09
P ₂ O ₅	0.31	0.47	0.59	0.15	0.50	0.82	0.24	0.08	0.49	0.15	1.25	0.23	0.17
LOI	4.24	5.57	5.62	4.47	4.96	6.57	5.46	4.20	5.95	6.35	6.18	6.90	6.28
Total	100.13	99.93	99.98	100.11	99.91	100.12	100.24	100.31	99.76	100.31	100.17	100.28	100.31
Li	36.8	28.8	28.3	97.8	19.2	20.0	38.1	67.4	19.0	50.2	20.0	30.9	25.5
Sc	34.8	42.6	40.8	42.5	37.8	41.9	47.4	35.6	41.5	46.6	41.5	44.3	36.2
V	333	202	175	215	182	200	229	197	196	181	147	122	188
Cr	146	335	298	293	236	298	236	373	219	379	389	491	384
Co	30.0	39.9	40.0	42.1	36.2	34.9	32.3	39.2	41.9	38.6	35.0	38.0	32.4
Ni	147	102	101	72.7	88.3	73.7	103	245	90.0	159	86.7	98.6	83.6
Cu	157	118	218	175	141	156	105	123	164	189	248	162	304
Zn	302	203	196	343	183	207	144	210	147	244	163	155	202
Ga	18.7	19.2	18.4	19.1	18.4	18.3	16.9	15.2	21.2	18.6	17.6	17.2	19.0
Rb	16.9	34.1	33.7	37.7	35.1	42.0	21.1	12.1	53.9	57.4	33.5	39.1	38.5
Sr	84.9	142	143	121	186	127	101	79.2	133	120	133	96.6	97.5
Y	56.3	45.7	48.9	27.4	45.7	52.5	47.9	20.4	43.3	22.4	96.6	53.0	21.0
Zr	218	94.8	91.8	92.6	134	115	107	37.2	134	67.2	65.4	59.3	85.7
Nb	5.77	1.28	1.25	2.10	3.24	4.38	3.31	0.934	2.08	1.15	1.49	1.46	1.74
Cs	1.01	1.48	1.55	3.17	1.67	1.68	0.721	0.663	2.32	4.91	1.36	1.57	1.80
Ba	11.2	46.8	49.6	19.8	67.3	55.9	19.9	8.01	37.5	19.7	49.5	40.4	25.8
La	10.3	11.6	16.8	5.90	15.5	15.0	8.14	2.48	8.87	6.09	37.5	17.7	5.08
Ce	21.6	9.83	9.77	10.4	14.8	13.3	11.6	3.86	14.2	8.56	6.70	6.35	7.77
Pr	4.53	2.69	3.70	2.26	4.39	4.89	2.96	0.952	3.44	2.19	5.29	4.33	1.97
Nd	22.6	13.7	17.5	11.3	20.8	22.7	14.9	5.33	17.0	10.9	23.8	20.2	9.60
Sm	6.99	4.22	4.89	3.56	5.88	6.38	4.88	2.03	5.27	3.34	5.71	5.39	2.99
Eu	2.31	1.62	1.76	1.37	2.03	2.09	1.80	0.842	1.89	1.25	1.94	1.85	1.13
Gd	8.78	5.90	6.59	4.48	7.25	8.01	6.64	2.88	6.61	4.09	8.45	7.42	3.57
Tb	1.56	1.03	1.11	0.787	1.24	1.37	1.20	0.536	1.16	0.703	1.37	1.23	0.630
Dy	10.2	6.90	7.30	5.13	7.89	8.96	8.15	3.62	7.61	4.49	9.36	8.02	4.07
Ho	2.10	1.48	1.54	1.04	1.62	1.85	1.71	0.763	1.56	0.891	2.13	1.69	0.820
Er	5.84	4.16	4.30	2.84	4.44	5.15	4.80	2.13	4.34	2.45	6.21	4.60	2.27
Tm	0.846	0.612	0.624	0.411	0.637	0.745	0.711	0.314	0.636	0.350	0.904	0.643	0.333
Yb	5.46	4.00	4.08	2.69	4.12	4.91	4.65	2.08	4.14	2.32	5.95	4.03	2.21
Lu	0.750	0.593	0.607	0.386	0.611	0.721	0.682	0.299	0.609	0.318	0.921	0.584	0.313
Hf	5.39	2.77	2.71	2.65	3.78	3.33	3.23	1.28	3.86	2.11	2.05	1.96	2.41
Ta	0.378	0.100	0.106	0.150	0.211	0.272	0.214	0.072	0.153	0.088	0.106	0.097	0.118
Tl	0.291	0.257	0.983	0.155	0.402	0.751	0.139	0.108	0.407	0.181	0.705	0.374	0.414
Pb	2.58	0.389	1.09	2.13	3.88	4.65	0.473	0.244	3.25	1.41	3.38	3.09	2.92
Th	0.431	0.082	0.085	0.142	0.243	0.329	0.253	0.070	0.141	0.059	0.111	0.116	0.123
U	0.235	0.451	0.480	0.222	0.694	0.717	0.356	0.101	0.544	0.301	0.652	0.300	0.255

^a All sample numbers are prefixed by SO-167; major elements are reported in wt.% and trace elements in ppm.

Table 4
Sr-Nd-Pb isotope data for Osbourn lavas^a

Sample	⁸⁷ Sr/ ⁸⁶ Sr	¹⁴³ Nd/ ¹⁴⁴ Nd	ϵ_{Nd} ^b	²⁰⁶ Pb/ ²⁰⁴ Pb	²⁰⁷ Pb/ ²⁰⁴ Pb	²⁰⁸ Pb/ ²⁰⁴ Pb
<i>unleached</i>						
121-1	0.704505 ± 5	0.512981 ± 2	6.68	18.649 ± 1	15.566 ± 0	38.347 ± 1
125-1	0.704565 ± 5	0.512927 ± 2	5.63	19.1 ± 1	15.55 ± 8	37.9 ± 2
129-1	0.704661 ± 5	0.512939 ± 2	5.87	19.010 ± 1	15.547 ± 1	38.124 ± 2
130-1	0.704657 ± 5	0.513019 ± 2	7.43	18.913 ± 2	15.585 ± 2	38.457 ± 4
<i>leached</i>						
121-1	0.703689 ± 5	0.513120 ± 2	9.39	18.593 ± 4	15.493 ± 3	37.944 ± 8
125-1	0.702922 ± 5	0.513144 ± 2	9.87	19.095 ± 8	15.528 ± 7	37.78 ± 2
129-1	0.703704 ± 5	0.513101 ± 2	9.04	18.962 ± 3	15.522 ± 2	37.972 ± 6
130-1	0.704109 ± 4	0.513183 ± 3	10.64	18.70 ± 2	15.50 ± 1	37.84 ± 4

^a All errors are 2 σ standard errors of the mean and apply to the last quoted digit of the analyzed ratio.

^b Calculated assuming present-day ϵ_{Nd} for CHUR = 0.512638; 2 σ error in ϵ_{Nd} is $\sim \pm 0.05$.

Figure Captions

- Fig. 1: Location map showing the principal features of the Pacific seafloor east of the Tonga–Kermadec Trench (predicted bathymetry from Smith and Sandwell [18]). The white box encloses the 120 by 145 km area surveyed during this study.
- Fig. 2: Bathymetric map of the surveyed western part of Osbourn Trough and its surrounds. The axial valleys and inferred spreading directions are shown, together with the SO-167 dredge stations from which lavas were recovered. Note the orthogonal segment offsets, presence of inside corner highs at the NW and SE margins of each segment, and the flanking abyssal hills subparallel to the axial valley. Contour interval is 100 m.
- Fig. 3: Cross-section through sample 130-1, showing six angular aphanitic basalt fragments within a volcanoclastic breccia encrusted by Fe-Mn oxyhydroxides. Two generations of oxyhydroxide are evident; (i) a young 2 cm-thick crust seen at the top and right, and (ii) an older 5 cm-thick crust seen at the base of the sample but inferred to have originally overlain the breccia before a mass wasting event. Scale bar intervals are 1 cm.
- Fig. 4: Normalized REE diagram for the profile through the Fe-Mn oxyhydroxide crust enclosing sample 121-1 (chondrite after Sun and McDonough [29]; PAAS after McLennan [30]). Note the positive Ce anomaly.
- Fig. 5: MORB-normalized plots for selected incompatible elements in Osbourn lavas (MORB after Pearce and Parkinson [38]). Panels A–B: the elements are arranged in order of decreasing incompatibility during mantle melting [38], LR is the compositional range of Louisville Ridge lavas for comparison [39]. Panels C–D: the elements are arranged in order of decreasing mobility during marine weathering, the shaded field depicts the range of weathered EPR MORB [40].
- Fig. 6: Chondrite-normalized REE plots for Osbourn lavas (chondrite after Sun and McDonough [29]; MORB after Pearce and Parkinson [38]). Note the deep negative Ce anomalies of the lavas (cf. Fig. 3), and that $(Ce)_N$ approximates MORB

concentrations. LR is the compositional range of Louisville Ridge lavas for comparison [39].

Fig. 7: Selected trace element plots for Osbourn lavas demonstrating correlations between Ce/Ce*, La, U, Nb/U and Ce/Pb with loss on ignition and P₂O₅. MORB field on panels E–F from Hofmann et al. [42].

Fig. 8: Tectonic discrimination diagrams for Osbourn lavas. MORB and within plate basalt fields on panels A–B from Pearce and Norry [45] and Pearce [46] respectively. Compositional fields for the EPR from Su [47], Louisville Ridge from Worthington et al. [39], and the Society, Austral and Pitcairn hotspots from Hekinian [48] and references therein.

Fig. 9: ²⁰⁸Pb/²⁰⁴Pb versus ²⁰⁶Pb/²⁰⁴Pb plot for Osbourn lavas demonstrating their PMM provenance (see text for details). Compositional fields for PMM, IMM and the PMM–IMM boundary from Kempton et al. [51], Louisville Ridge from Worthington et al. [39], and the Cook–Austral chain HIMU and FOZO from Stracke et al. [52]. Dashed PMM–IMM boundary is the boundary recalculated for 86 Ma.

Fig. 10: Tectonic reconstruction of the south Pacific at ~112 Ma and ~86 Ma in the Australian paleomagnetic reference frame following Sutherland and Hollis [3]. Panel A: Spreading at the Nova-Canton Trough has ceased and jumped southwards to the Tongareva Triple Junction (TTJ), which rifts the Manihiki Plateau into three fragments (representation is a simplified version from Viso et al. [5]). Osbourn Trough develops as an extension of the TTJ west arm, offset by the East Manihiki transform, and splits off the Hikurangi Plateau. Panel B: The Hikurangi Plateau is colliding with the subduction system at the Chatham Rise and spreading across Osbourn Trough is about to cease. Location and trace of the Tongareva Triple Junction after Viso et al. [5].

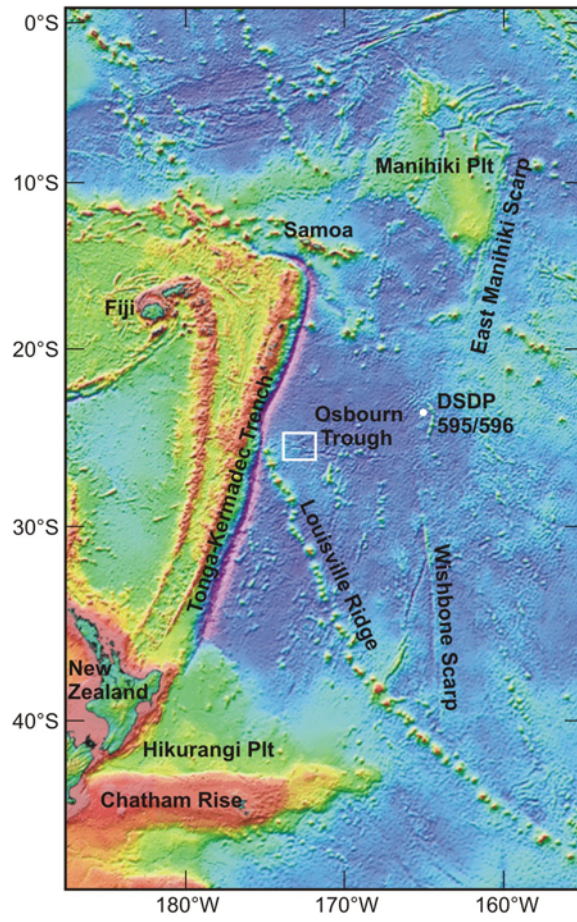


Figure 1

Worthington et al., Osborn Trough

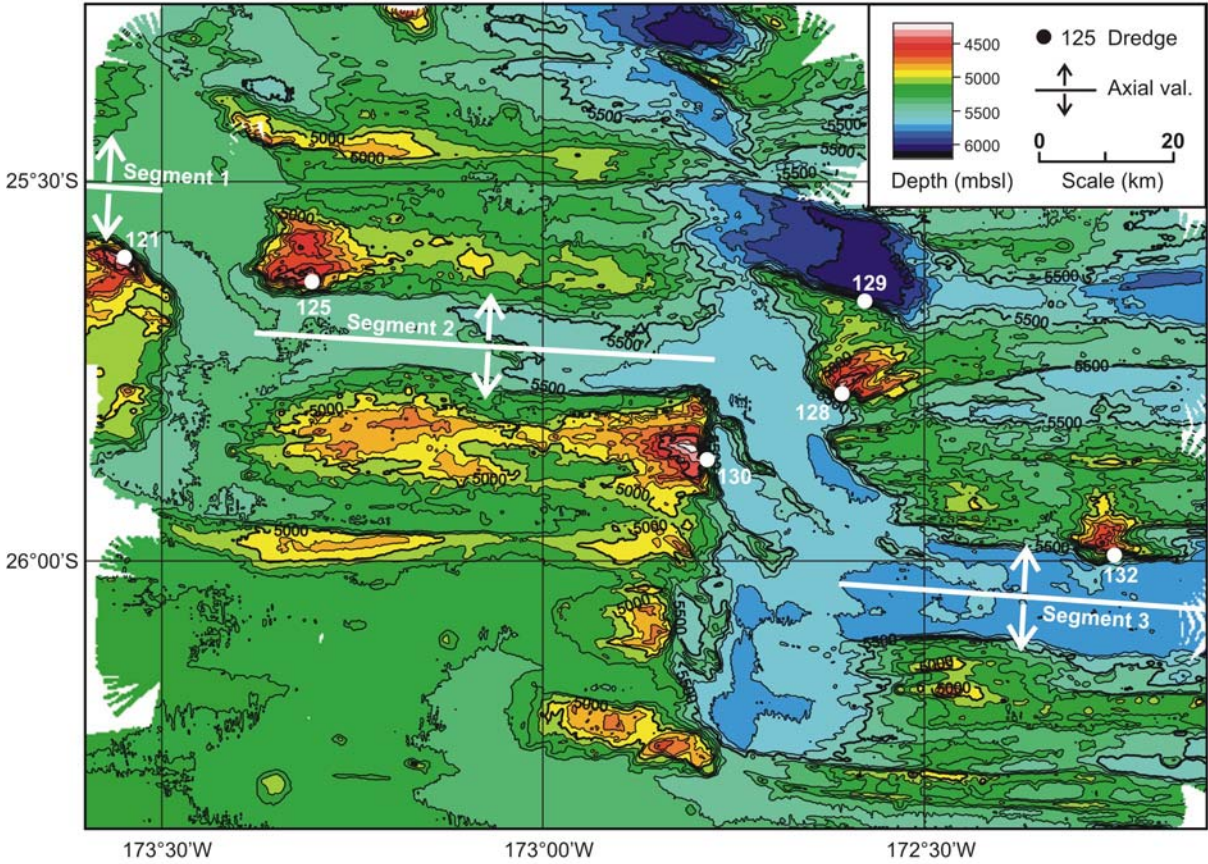


Figure 2

Worthington et al., Osbourn Trough

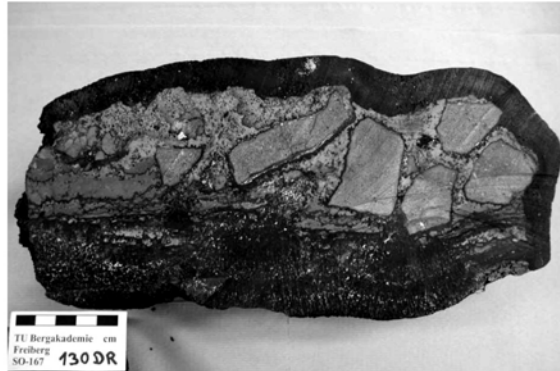


Figure 3

Worthington et al., Osbourn Trough

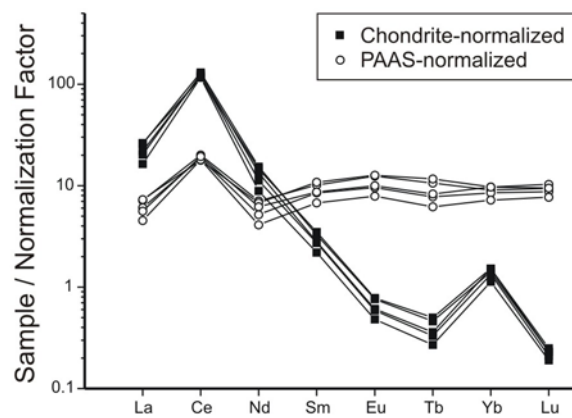


Figure 4

Worthington et al., Osborn Trough

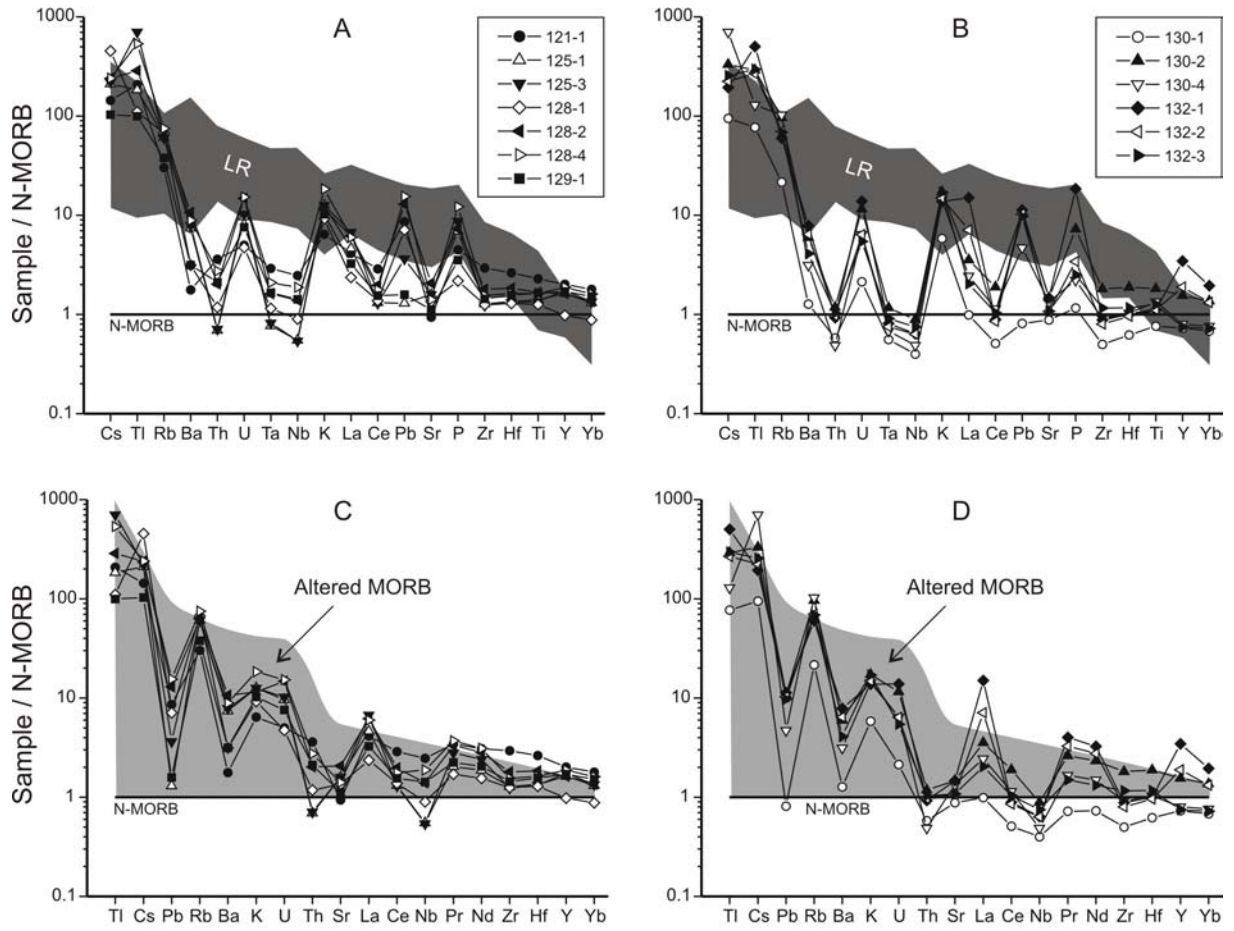


Figure 5

Worthington et al., Osborn Trough

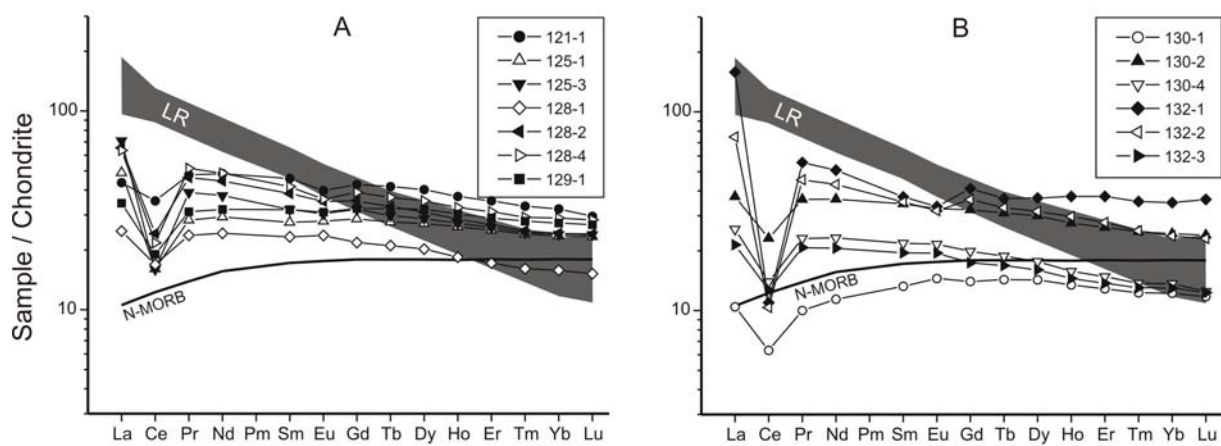


Figure 6

Worthington et al., Osborn Trough

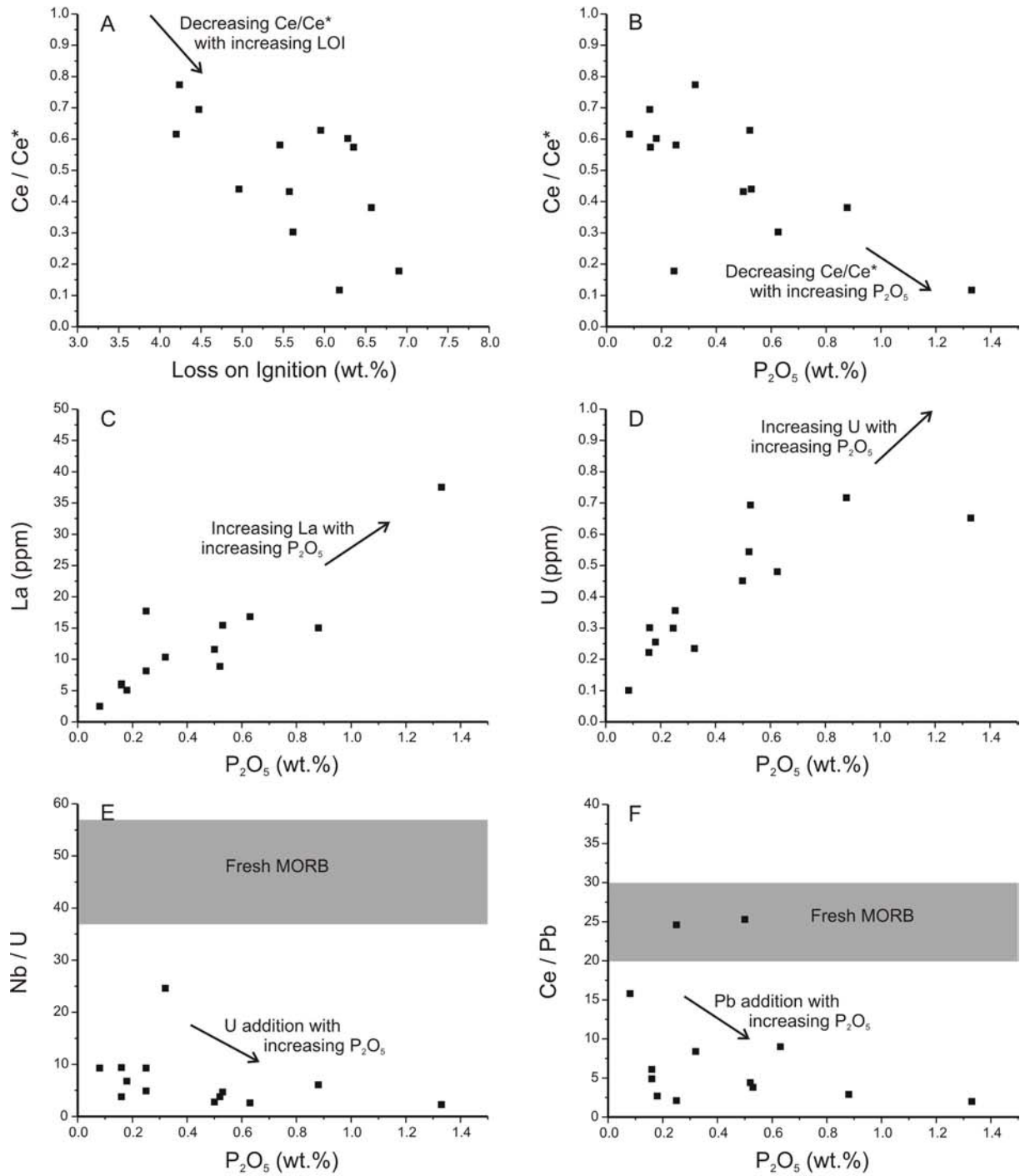


Figure 7

Worthington et al., Osborn Trough

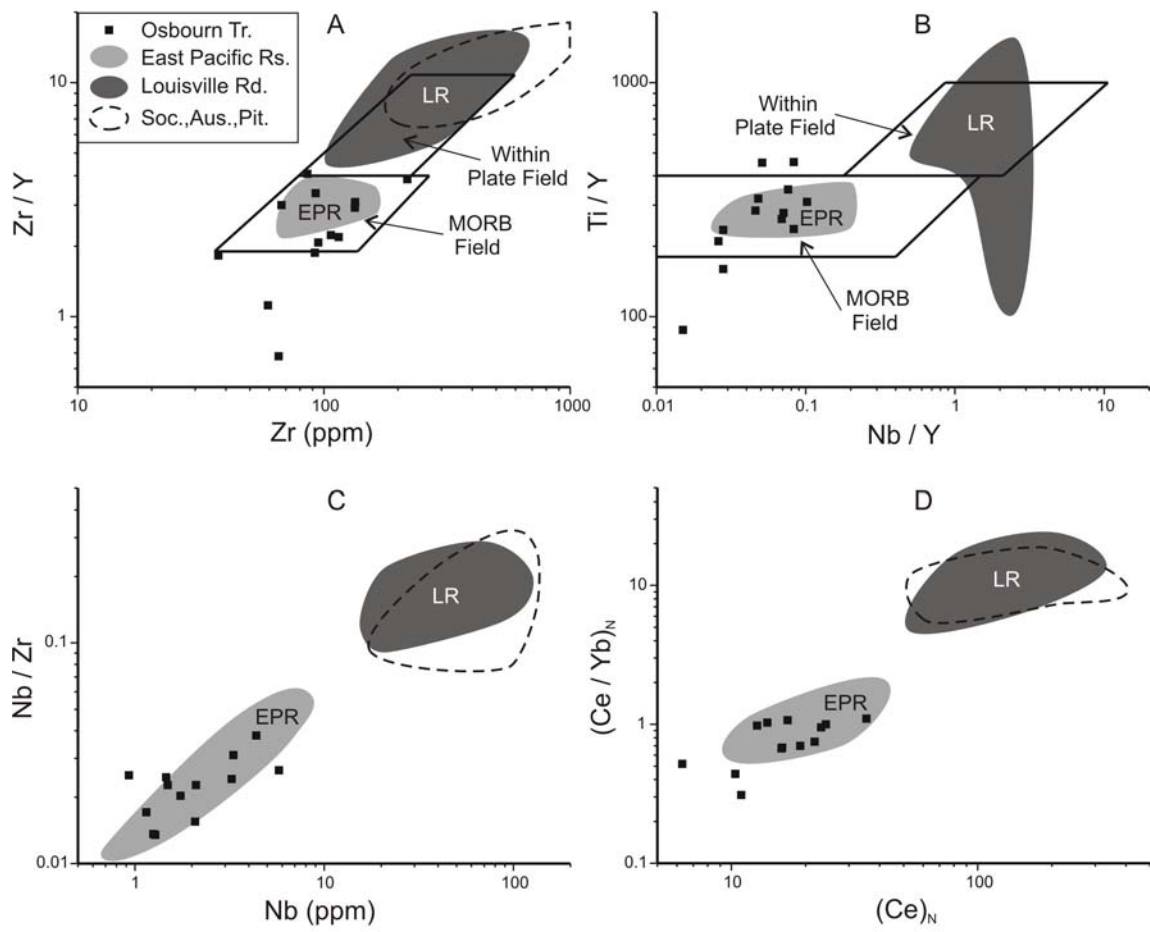


Figure 8

Worthington et al., Osbourn Trough

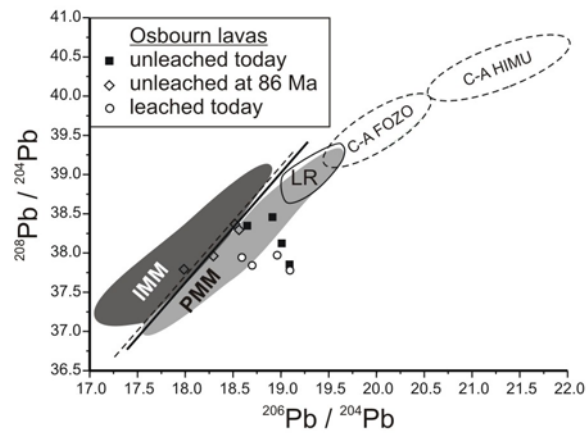


Figure 9

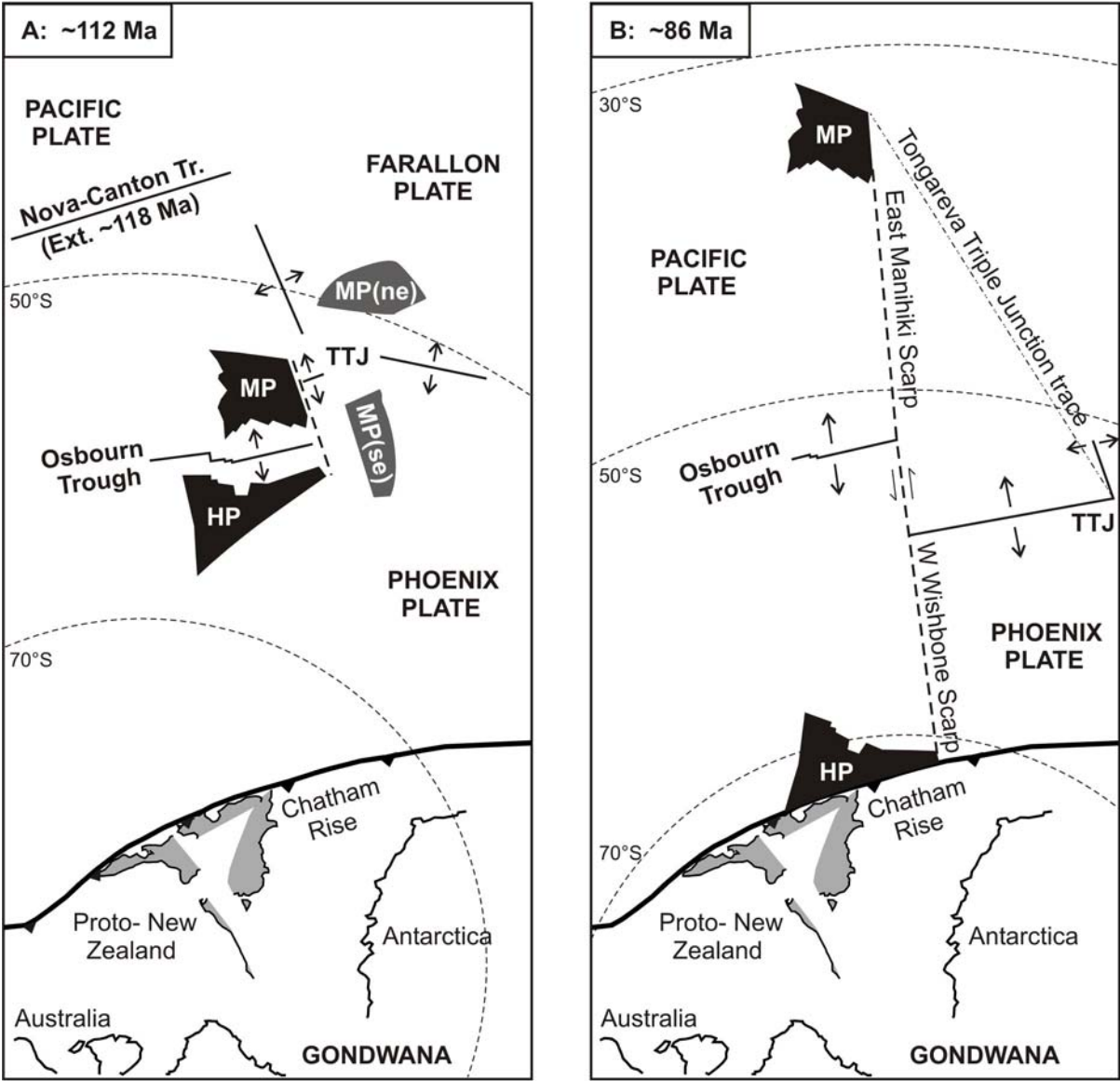


Figure 10

Louisville Ridge: Characterization of Alkaline Lavas from a Mantle Plume and Their Eruption Through Lithosphere of Increasing Age

**Tim J. Worthington^{a,*}, Roger Hekinian^b, Peter Stoffers^a, Dieter Garbe-Schönberg^a,
Folkmar Hauff^c**

^aInstitut für Geowissenschaften, Universität Kiel, Olshausenstr. 40, 24098 Kiel, Germany

^bKeryunan, 29290 Saint Renan, France

^cIFM-GEOMAR, Leibniz Institut für Meereswissenschaften, Wischhofstr. 1–3, 24148 Kiel, Germany

* Corresponding author-

Dr. Tim J. Worthington

e-mail: tw@gpi.uni-kiel.de

tel: +49-431-8802852

fax: +49-431-8804376

In preparation for-

Earth and Planetary Science Letters

Word counts-

Abstract: 250

Main text: 5132

References-

58

Tables-

3

Figures-

9

Abstract

Eleven major seamounts of the Louisville Ridge were dredged, spanning the region between the intersection of the ridge with the Tonga–Kermadec Trench (Osborn seamount; 78 Ma) and a large edifice near 168°W (45 Ma). Recovered lavas were affected by mild marine weathering: olivine and glass are generally replaced by secondary clays, abundant (to 25 vol.%) vesicles are often infilled by calcite, phillipsite and clays, but plagioclase and clinopyroxene remain fresh. Dredge stations were specifically targeted at the headscarps of sector collapse scars 500–1000 m below the break in slope in a deliberate attempt to bias sampling towards the main shield-building phase at each center. Nevertheless, all analyzed lavas are alkaline (foidite to benmoreite) and the majority are classified as basanite or alkali basalt. Thus, we find no evidence of a tholeiitic shield-building phase at these volcanic centers.

Incompatible element ratios define a trend of decreasing partial melting with increasing distance from the Tonga–Kermadec Trench that reflects the increasing age of the lithosphere passing over the Louisville plume (~10 Ma at Osborn seamount, ~55 Ma at 168°W). This change is also reflected by a progressive decrease in $^{87}\text{Sr}/^{86}\text{Sr}$, increase in $^{143}\text{Nd}/^{144}\text{Nd}$ and increase in $^{206}\text{Pb}/^{204}\text{Pb}$ with time, but seamounts younger than ~60 Ma show a wider range of isotopic compositions. In Sr-Nd-Pb isotope space, Louisville lavas are at the radiogenic end of the MORB array adjacent to, but not within, FOZO. All are significantly more radiogenic than the underlying lithosphere. No HIMU, EM-I or EM-II components are evident.

Keywords: Louisville Ridge; mantle plumes; geochemistry; Pacific; hotspot volcanism

1. Introduction

Linear volcanic chains with a well-defined age progression were first attributed to the passage of a moving lithospheric plate over a mantle plume by Morgan (1971). Plumes were originally regarded as fixed in a mantle reference frame, and thus excellent recorders of lithospheric plate motion (Clague and Jarrard, 1973; Duncan, 1981; Müller et al., 1993). More recently, computer modeling of plumes has indicated they should be distorted by mantle flow (Steinberger and O'Connell, 2000). Mismatches between "hotspot" reference frames for different oceans and between apparent changes in plate motion and regional tectonic events are now apparent (Molnar and Stock, 1987; Cande et al., 1995; Norton, 1995; 2000; Raymond et al., 2000), and it has been proposed that the surface track of plumes can move at velocities comparable to those of lithospheric plates (Tarduno et al., 2003; Steinberger et al., 2004).

Geochemical and isotopic studies of linear volcanic chains have provided strong support for unusual sources in the "deep" mantle. Lavas erupted along these chains typically have very high concentrations of elements that behave incompatibly during mantle melting relative to MORB, implying a source less depleted ("melted") than that of normal MORB (Hoffman, 1997; Davies, 1999), they have Sr-Nd-Pb-Hf isotopic ratios that reveal mantle components seldom seen in MORB (e.g., EM-I, EM-II, HIMU; DePaolo and Wasserburg, 1976; Zindler and Hart, 1986; Hoffman, 1988; Hart et al., 1992), and they have high $^3\text{He}/^4\text{He}$ ratios and noble gas contents implying an "undegassed" source (Farley et al., 1992; Davies, 1999). At Hawaii, individual volcanic centers typically evolve through an early phase characterised by eruption of alkalic lavas, a main shield-building phase of tholeiitic lavas, and a late phase of alkalic lavas; such a sequence mimics that expected from low degree melting changing to progressively higher degrees as the plume passes beneath the volcano, and then dwindling again as the plume becomes distal (Clague and Dalrymple, 1987). Lavas from some chains (notably Hawaii and Galapagos) also show distinct spatial and temporal changes in trace element and isotopic ratios that are inferred to reveal zoning, concentric or more complex, within the mantle plume (DePaolo and Stolper, 1996; Hoernle et al., 2000; DePaolo et al., 2001; Harpp and White, 2001; Abouchami et al., 2005).

The advent of more sophisticated geophysical techniques has led to a vigorous debate over whether plumes really exist and their possible relationships to large igneous provinces (LIPS). Vertically continuous velocity anomalies in the upper mantle have been detected beneath only eight of 29 well-defined "hotspots" (Ritsema and Allen, 2003). Some contend that linear volcanic chains may be propagating lithospheric cracks, leaky transforms or other

regions of unusual upper mantle that do not require a deep-seated mantle plume. Others have noted that the age progression is not necessarily monotonic, and that resurgent volcanism may occur up to 7 Ma after the main shield-building phase; both require viable explanations. The relationship between the immense magmatic outbursts represented by LIPS and mantle plumes impinging on the lithosphere, and which plumes may relate to which LIPs, remains controversial (Richards et al., 1989; Tarduno et al., 1991; Larson, 1997; Ingle and Coffin, 2004; Antretter et al., 2004; Hoernle et al., 2005).

The 4300 km-long Louisville Ridge is the second most prominent linear seamount chain in the Pacific Ocean after the Hawaii–Emperor chain (Fig. 1). Early age determinations revealed a progressive decrease in seamount age to the SE, from ~66 Ma at Osbourn Seamount (presently entering the Tonga–Kermadec Trench) to 0.5 Ma near Hollister Ridge adjacent to the Pacific–Antarctic Ridge (Hawkins et al., 1987; Watts et al., 1988; Vlastelic et al., 1998). An apparent bend in the seamount chain near 168°W was considered analogous to the Hawaii–Emperor bend at ~43 Ma Ridge and inferred to represent a change in Pacific Plate motion (Lonsdale, 1988). However, re-dating of these lavas by more sophisticated techniques has significantly increased the age of the NW seamounts (Osbourn is now dated at ~78 Ma) and the bend has been re-interpreted as revealing a change in slant of the Louisville plume within the mantle (Koppers et al., 2004; Steinberger et al., 2004). Published analyses of Louisville lavas are nearly exclusively alkaline basalt with isotopic compositions more radiogenic than MORB, but the significance of this was unclear given the small size of the database and an over-representation of lavas dredged from the NW summit of Osbourn Seamount (Hawkins et al., 1987; Cheng et al., 1987).

Here, we report the petrology and geochemistry of lavas dredged from eleven Louisville Ridge seamounts between Osbourn Seamount (at the Tonga–Kermadec Trench) and a large seamount at 168°W during the SO-167 cruise of the FS *SONNE*. Despite deliberate biasing of dredge stations towards scarps expected to expose the shield-building lavas of each edifice, all analyzed lavas are alkaline. The lavas record a range of partial melting and subsequent fractional crystallization at most centers. The degree of partial melting is highest in the western seamounts near the Osbourn Trough, where the lithospheric thickness was least at the time of seamount construction. In contrast, the most evolved lavas were recovered from the largest seamount at 168°W and testify to a more robust magmatic system. Isotopically, all Louisville lavas are at the radiogenic end of the MORB array and close to FOZO compositions; none show EM-I, EM-II, or HIMU affinities. They are, however, significantly more radiogenic than MORB erupted at the Osbourn paleo-spreading ridge.

2. Bathymetry and structure of Louisville Ridge west of 168°W

Eleven major seamounts along the Louisville Ridge from its intersection with the Tonga–Kermadec Trench to ~168°W were partly surveyed and sampled (Fig. 1). All surveyed seamounts were flat-topped guyots. Their wave-cut summit plateaux testify to volcanic islands that were eroded down to sea-level and have subsequently subsided by as much as 2000 m. The amount of subsidence decreases to the SE as the seamounts become younger. Thick deposits of foram-bearing sandstone bury drowned coral reefs on their summits. The dredging program utilised the ability of the SIMRAD EM120 to provide high resolution bathymetric coverage of a wide swath in real-time. Slump blocks 2–6 km downslope of their headscarps were quickly identified. Dredging targeted the steep headscarps behind these slumps on the upper flanks of the seamounts, typically at 2000–2500 mbsl but still 500–1500 m below the wave-cut break in slope. Thus, by analogy with the Hawaiian Islands, dredging should have sampled the late main shield-building phase of volcanism and avoided any post-erosional stage lavas (the latter being mostly confined to the central summit region). The majority of the slumps occur on the south-facing flanks of the Louisville seamounts, which would have faced into the prevailing southerly storm fronts when the volcanoes were subaerial or at shallow depth.

Full bathymetric coverage was achieved for only two seamounts. LR 34 (Fig. 2a) has the structure of two intergrown volcanic centers, with a combined basal diameter of 22 by 28 km at 3800 mbsl. The break in slope occurs at 1700 mbsl, above which is a 4 km-wide elongate summit plateau capped by twin summit peaks at 1350 mbsl. A series of small pinnacles rising from the SW summit possibly represent resistant dykes or late-stage resurgent volcanism that followed the submergence of the edifice. Prominent ridges extend to the NNW, NNE, SE and SW of the edifice. Klingon (Fig. 2b) consists of two relatively small volcanic centers joined by a flat-topped 6 km-wide, 20 km-long, ridge. Overall, the NW–SE elongate massif has basal dimensions of 30 by 70 km at 4000 mbsl. The NW and SE centers have basal diameters of 30 km, break in slopes at 1250 mbsl, and rise to summit plateaus at 1050 mbsl. Both volcanic centers and their joining ridge were clearly subaerial and have been wave-cut on later subsidence. Prominent ridges extend to the NE and SW of both volcanic centers, and along strike of the massif to the SE.

Our bathymetry confirmed that the Louisville Ridge comprises NW–SE ridge segments that are linked by short NE–SW segments. The largest seamounts are built along the dominant NW–SE segments and are commonly elongated in this direction. However, less voluminous

volcanism has occurred along the NE–SW segments. Both the NE–SW segments, and some flank ridges extending from the larger seamounts, have the same trend as the non-transform discontinuities recognised at Osbourn Trough (Worthington et al., in review). The trend of these ridge segments progressively swings from north–south to NE–SW with increasing distance from the Osbourn Trough. These non-transform discontinuities evidently represent zones of lithospheric weakness that were exploited by the Louisville magmas.

3. Louisville samples

Thirty-one dredge stations on 11 Louisville seamounts recovered lavas, the majority of which were highly vesicular (up to 25 vol.% vesicles) and either olivine-phyric or aphanitic (Table 1). Apart from the near total replacement of olivine phenocrysts by iddingsite pseudomorphs, most lavas were not severely weathered. This probably reflects the success of the dredging strategy in targeting relatively young slump scarps and minimising seawater exposure times. Breccias were recovered from many dredge stations and testify to mass wasting on the slopes. Porous dull brown to black Fe-Mn oxyhydroxide crusts, typically 2–3 cm thick but locally up to 5 cm across, enclose many of the breccias and less commonly grow directly on the lava blocks. Slump blocks of semi-lithified foram ooze were common.

Typical Louisville lavas comprise olivine phenocrysts set in an intersertal groundmass of palagonised glass, plagioclase and clinopyroxene microlites, Ti-magnetite and rarely Cr-spinel. Most olivine phenocrysts, and all groundmass olivines, are completely replaced by a mix of iddingsite and Fe-oxyhydroxide or pale green fibrous clay. Rare relic patches in some lavas (e.g. 168-2) have forsteritic compositions (Fo_{84-90}). Clinopyroxene phenocrysts are salite with occasional small domains of calcite replacement; groundmass clinopyroxenes are Ti-augites with ~3 wt.% TiO_2 . Plagioclase phenocrysts are labradorite (An_{53-71}), and their cores are often replaced by secondary clays or rarely by K-feldspar; groundmass plagioclase is unaltered. The primary oxide phases are mostly replaced by Fe-oxyhydroxides, but unaltered crystals of Ti-magnetite and Cr-spinel are preserved in some lavas.

Vesicles range in size from spheroids <1 mm in diameter to large cavities >3 cm across. Near the lava rim most are completely infilled by coarsely crystalline low-Mg calcite, although commonly they remain open or only partly filled within the block. Phillipsite often separates calcite from the vesicle walls. Red to black oxidation haloes surround the vesicles and grade inwards to pale coloured clays.

Saponite, beidellite, Fe-oxyhydroxides, and less commonly celadonite are the main secondary minerals replacing the groundmass. The relative abundance of saponite to celadonite is unusual, as the strongly oxidising conditions and high water/rock ratios associated with large-volume circulation of seawater favour celadonite over saponite (Talbi and Honnorez, 2003). However, a relatively low water/rock ratio and limited seawater circulation is consistent with the limited replacement of the groundmass in many blocks. Many Louisville lavas were probably sealed from seawater by overlying lavas and impermeable sediment layers shortly after their eruption until exposed by recent slumping on the seamount flanks.

4. Analytical techniques

The least weathered 57 lavas were selected for geochemical analysis. Cores were cut from these fragments specifically avoiding areas of major alteration and vesicle infilling. The cores were then coarse crushed, hand-picked to ensure removal of all Fe-Mn oxyhydroxides and as much calcite, phillipsite and other secondary minerals as possible, washed thoroughly in an ultrasonic bath with deionized water to remove sea-salts, and then fine crushed in an agate mortar. For major element determinations, 0.6 grams of rock powder was mixed with lithium tetraborate and ammonium nitrate, fused to a homogenous glass disk, and analyzed using a Philips PW 1480 XRF spectrometer calibrated against international rock standards. Loss on ignition was determined by weight loss of >3 grams of rock powder heated in a furnace at 1000 °C for at least 4 hours. For trace element determinations, ~100 mg of rock powder was dissolved following the HF-HClO₄-aqua regia digestion procedure outlined in Garbe-Schönberg (1993). Sample residues were taken up in 2 % HNO₃, diluted, spiked for calibration, and analyzed using an Agilent 7500c ICP-MS. Accuracy was checked against international rock standards (BHVO-1, AGV-1), and precision (2σ) for duplicate analyses was better than 3 % for all elements (mostly better than 1 %).

Sixteen lavas were analyzed for Sr-Nd-Pb isotopic composition. For Sr and Nd, ~250 mg of rock powder was leached in ultrapure 6N HCl on a hot plate for 1 hour and further washed with deionized water prior to dissolution in an HF/HNO₃ mix. For Pb, the powder was dissolved in acid without leaching. The Sr-Nd-Pb isotopic compositions of three lavas were determined on both leached and unleached aliquots as a check on this procedure. Standard ion exchange techniques were then used to produce Pb, Sr and Nd separates

(Hoernle and Tilton, 1991). Isotopic compositions were determined using the MAT 262 (Sr, Pb) and TRITON (Nd) thermal ionization mass spectrometers at IFM-GEOMAR in Kiel. Applied isotope fractionation corrections for Sr and Nd were $^{86}\text{Sr}/^{88}\text{Sr} = 0.1194$ and $^{146}\text{Nd}/^{144}\text{Nd} = 0.7219$, with all errors reported as 2σ standard errors of the mean. Repeated measurements of NBS 987 completed during the study yielded $^{87}\text{Sr}/^{86}\text{Sr} = 0.710237$ ($n = 13$) and for the in-house SPEX monitor yielded $^{143}\text{Nd}/^{144}\text{Nd} = 0.511718$ ($n = 7$). All reported analyses are normalized to $^{87}\text{Sr}/^{86}\text{Sr} = 0.710250$ for NBS 987 and $^{143}\text{Nd}/^{144}\text{Nd} = 0.511708$ (calibrated against $^{143}\text{Nd}/^{144}\text{Nd} = 0.511848$ for La Jolla). For Pb, the analyses were fractionation-corrected using repeated measurements of NBS 981 conducted under the same loading and run conditions ($n = 11$, $^{206}\text{Pb}/^{204}\text{Pb} = 16.899$, $^{207}\text{Pb}/^{204}\text{Pb} = 15.437$, $^{208}\text{Pb}/^{204}\text{Pb} = 36.525$; mass fractionation = 0.115 % per amu) and normalized to its accepted values (Todt et al., 1996). Pb blanks were negligible (<250 pg).

5. Geochemistry of Louisville lavas

All Louisville lavas have suffered marine weathering with partial replacement of their groundmass and some phenocryst phases. A group of nine lavas have been strongly phosphatized (3–7 wt.% P_2O_5), and a further nine lavas have anomalous concentrations for specific elements (e.g., Tl, Rb) or element ratios ($(\text{Ce}/\text{Ce})_{\text{N}} < 0.9$) that are far from those of the less unaltered lavas and that correlate with mildly elevated P_2O_5 or a high LOI (Fig. 3). These analyses are regarded as unreliable, especially for the more mobile elements, and no further use is made of them (however, Sr-Nd-Pb isotope analyses are presented for four of these weathered lavas in order to maximise spatial coverage of the seamount chain- for those determinations strong acid leaching has removed the effects of weathering). All lavas from seamount LR "x" and the eastern summit of Klingon are in this category. These were among the most vesicular lavas recovered, with extensive infilling of their vesicles by calcite and phillipsite.

The remaining 39 analyses define an alkalic lava series ranging from foidite to benmoreite (Fig. 4a). Both the range and scatter on this diagram are strong functions of phenocryst content. Most foidites have $\text{MgO} > 6$ wt.% and 10–20 vol.% pseudomorphs after former olivine phenocrysts (Fig. 4b). Similarly, other lavas with abundant olivine pseudomorphs and high-MgO are displaced from their inferred liquid compositions near the axis of the Louisville array towards the tholeiite field (by dilution of their alkali and other

components). Only sample 152-1 from LR 35 plots to the tholeiite side of the alkalic–tholeiitic boundary line of Macdonald and Katsura (1964). This lava has ~25 vol.% pseudomorphs after olivine phenocrysts, and is inferred to represent an alkalic hawaiite magma that was contaminated by abundant cumulus olivine.

Louisville analyses form tightly constrained linear arrays on most element–element plots, particularly for the incompatible elements that are not sensitive to marine weathering (Fig. 5). A consistent feature of all Louisville lavas is that values of more incompatible trace elements over less incompatible elements have significantly higher values than tholeiitic lavas from Hawaii. For example, Louisville lavas have $Nb/Zr > 0.10$ and $(Ce/Yb)_N > 5$ whereas all Mauna Kea tholeiites have $Nb/Zr = 0.09–0.06$ and $(Ce/Yb)_N < 5$ (Figs. 5cd; Yang et al., 2003). These characteristics provide additional evidence that all Louisville lavas are alkalic and that their position on the TAS plot is not a consequence of alkali element mobility during marine weathering. Furthermore, lavas from Osbourn Seamount always plot closest to the tholeiitic field and those from Klingon Seamount always plot furthest into the alkalic realm.

Chondrite-normalized REE patterns for Louisville lavas are strongly light REE-enriched ($La/Yb = 6–26$) and form a spread of sub-parallel lines ranging from $(La)_N = 69–345$ (Fig. 6ab). The more evolved lavas, especially those from LR 40, have mildly positive Eu anomalies ($Eu/Eu^* = 1.0–1.2$) that reflect their plagioclase-phyric nature. Primitive mantle-normalized patterns are convex upward when the elements are arranged in order of increasing incompatibility during mantle melting, which contrasts with the positive slope at far lower values shown by MORB (Fig. 6cd). A steep increase in normalized values occurs from Cs to Ta, after which there is a general decrease. Negative anomalies occur for K, Pb, and occasionally for U; these are typical of OIB from most plumes (Hart et al., 2004). The lack of a negative U anomaly for some lavas probably reflects U addition during marine weathering.

6. Melting of the Louisville plume

Volcanism at the well-exposed Hawaiian volcanoes passes through a series of stages from the initial eruption of low-volume alkalic melts, a voluminous shield-building tholeiitic phase, a return to low-volume alkalic melts, and in many instances a post-erosional phase in which further low-volume alkalic melts are erupted after a significant hiatus in eruptive activity (Clague and Dalrymple, 1987). To a first approximation, both the symmetry in lava geochemistry and production rate are consistent with the lithosphere approaching a mantle

plume, passing over the core of the plume, and then becoming distant from the plume. Hawaiian tholeiitic lavas represent high-degree partial melts (up to 18 %) of a lherzolitic source within the garnet stability field (Sims et al., 1995; Feigenson et al., 1996), whereas alkalic lavas are products of relatively low-degree melting (1–3 %) and may feature a more varied source that includes residues from the main phase of mantle melting (Frey et al., 2000; Lassiter et al., 2000).

All Louisville lavas are alkalic in composition and thus do not simply fit the Hawaiian model. Insufficient stratigraphic control is available to investigate changes in composition with time at any one seamount. However, modeling of incompatible element ratios can place first order constraints upon melting parameters of the Louisville plume. We restrict our modeling to those incompatible elements that are not significantly affected by olivine fractionation rather than adjusting the MgO content of the magma to a set value by adding olivine and/or other phases, in part because the MgO content is sensitive to marine weathering and in part because there are no experimental studies of liquidus conditions for Louisville magmas.

Chondrite-normalized REE patterns of Louisville lavas are strongly light-REE enriched, show a progressive incremental decrease in the level of each element through the series, and are non-crossing (Fig. 6ab). Garnet/melt partition coefficients for the heavy-REE exceed those for the mid-REE (Shimizu and Kushiro, 1975), whereas their clinopyroxene/melt partition coefficients are essentially equivalent (Hart and Dunn, 1993; Johnson, 1998; Green et al., 2000). Thus, the mid- to heavy-REE are particularly sensitive to changes in the source composition. In particular, if garnet is a residual phase during melting then mid-REE/heavy-REE ratios such as Tb/Yb will decrease rapidly as the degree of melting increases. In contrast, no change in mid-REE/heavy-REE values will occur if garnet is absent. We follow Frey et al. (2000) in investigating changes in mid-REE/heavy REE values against Th, as Th is both strongly incompatible during mantle melting and immobile during marine weathering. Increasing Th concentrations are generated by fractional crystallization, decreasing Th by greater degrees of partial melting, and a positive slope is imparted to the array if garnet is present in the residue.

Our Louisville analyses form a positive slope with significant scatter on these plots (Fig. 7a). Osbourn lavas have the lowest Th and low Tb/Yb \sim 0.45, consistent with their representing the highest degree melts. At the opposite end of the array, Klingon lavas have higher Th coupled with high Tb/Yb \sim 0.8 and represent the lowest degree melts. Five analyses with high Th and low Tb/Yb represent the most evolved lavas in our suite and their

compositions reflect extensive fractional crystallization. Assuming that all Louisville lavas are melts of a similar source, we conclude that garnet must be a residual phase during melting. The width of the array indicates considerable variation in the garnet/clinopyroxene ratio of the source generating melts beneath each seamount or in the subsequent pooling of fractional melts, but provides no evidence for a long term change in source composition along the Louisville Ridge.

The degree of source melting can be further constrained by modeling partial melting of a lherzolite source close to the garnet-spinel facies transition at ~30 kbar (Fig. 7b). Our results show that most Louisville lavas can be generated by 2–9 % partial melting of a garnet source, with the highest melt fraction required for Osbourn lavas. Although the Louisville array is centered close to the 30 kbar model for garnet lherzolite melting, some lavas plot between this model trajectory and the 30 kbar spinel lherzolite curve suggesting they represent pooled aggregates of polybaric melts with average depths close to the spinel-garnet transition. A few lavas plot above the 30 kbar garnet trajectory, but these are the more evolved lavas from LR 40 that have been most affected by fractional crystallization. Notably, all Louisville lavas require far higher average pressures than the post-erosional and late-stage alkalic lavas from Hawaii.

7. Effect of increasing age and lithospheric structure

A mid-Cretaceous age for the lithosphere supporting the NW Louisville Ridge has generally been assumed from the lack of magnetic lineations in the seafloor east of the Tonga–Kermadec Trench. Recent work has shown that this lithosphere was generated at the east–west trending Osbourn Trough, which intersects the Tonga–Kermadec Trench at 25.5°S and immediately north of Osbourn Seamount (Fig. 1; Billen and Stock, 2000; Worthington et al., in review). Spreading across Osbourn Trough probably commenced at ~118 Ma and ceased at ~86 Ma, when the Hikurangi Plateau entered and blocked a subduction system developed along the Chatham Rise segment of Gondwana margin. Consequently, the crust beneath Louisville Ridge is expected to increase in age to the south until a major fracture zone, the Wishbone Scarp, is intersected near 168°W (Fig. 1). In addition, the NW Louisville Ridge consists of two segments that are offset along NE–SW trending fractures near 173.5°W and 170°W. These fractures have the same orientation as non-transform offsets developed at

Osborn Trough (Worthington et al., in review), and we infer possible lesser jumps in crustal age across them.

We have investigated whether changes in geochemistry or isotopic composition occur along the NW Louisville Ridge. The ages of the Louisville seamounts were interpolated from the recent Ar/Ar study of Koppers et al. (2004), which substantially improves the precision of earlier results and shifts the age of Osborn Seamount at the Tonga–Kermadec Trench back to ~78 Ma (cf. Watts et al., 1988). Koppers et al. (2004) also evaluate evidence for the movement of the Louisville plume in the mantle reference frame using the model of Steinberger et al. (2004) and relative to that of the Hawaiian plume. They note that the motion of the Louisville plume can be subdivided into three intervals, 78–62 Ma, 62–47 Ma, and 47–0 Ma, with the 62–47 Ma interval representing a period of unexpectedly fast motion relative to the Steinberger et al. (2004) model. This anomalous period is closely bounded by passage of the Louisville plume beneath the 173.5°W and 170°W fractures (Fig. 8).

Incompatible trace element ratios sensitive to the extent of mantle melting consistently show the greatest degrees of melting for Osborn Seamount and the least at Klingon Seamount (Figs. 5, 7). A general decrease in the degree of partial melting with distance from Osborn Seamount is apparent, although in detail there is a possible reversal for the period ~60–47 Ma (Fig. 8a). Lavas erupted as the plume reached the Wishbone Scarp have a wide range of incompatible element values, but all require lower degrees of plume melting than for the Osborn Seamount lavas.

We attribute the overall decline in degree of plume melting to the increasing age and thickness of the lithosphere passing over the plume. Osborn Seamount was emplaced at ~78 Ma (Koppers et al., 2004). Therefore, the age of the lithosphere at the time Osborn Seamount was active was ~8 Ma. As spreading had ceased across Osborn Trough, the NW motion of the Pacific Plate brought progressively older crust over the Louisville plume and at Klingon Seamount (adjacent to the Wishbone Scarp) this crust has an age of ~100 Ma (i.e., ~55 Ma at the time of Klingon Seamount activity). Oceanic lithosphere thickens rapidly and attains close to its full thickness within 20–30 Ma of formation. The increasing thickness of this lithospheric cap would have terminated melting at progressively greater depths when ascending plume material ceased rising and commenced lateral flow beneath the cap, resulting in a decrease in the maximum extent of partial melting with time. This is consistent with the observed geochemistry of the seamounts, which require a decrease in average melting from ~6 to ~2 % (Figs. 5, 7, 8a).

Changes in Sr, Nd and Pb isotope composition of the Louisville lavas mimic those for the incompatible elements. A steady decline in $^{87}\text{Sr}/^{86}\text{Sr}$ occurs from Osbourn Seamount to ~60 Ma, followed by an abrupt reversal to values near those of Osbourn Seamount and a wide variation at Klingon and the eastern end of the chain (Fig. 8b). Values of $^{143}\text{Nd}/^{144}\text{Nd}$ increase at first followed by a decline, and provide a mirror image of those in $^{87}\text{Sr}/^{86}\text{Sr}$ (Fig. 8c). Lead isotopes show a similar pattern to $^{143}\text{Nd}/^{144}\text{Nd}$, with an initial increase in $^{206,207,208}\text{Pb}/^{204}\text{Pb}$ followed by an abrupt decline at ~60 Ma and appreciable scatter at ~47 Ma (Fig. 8d).

We believe these trends and changes in isotopic composition represent real variations along the Louisville Ridge rather than the small size of the dataset because they are consistent for all three investigated isotopic systems, correlate with the changes seen in trace element geochemistry, and occur at structural breaks along the ridge. The abrupt reversal from a trend of increasingly unradiogenic Sr and Nd but more radiogenic Pb with time occurs when the Louisville plume crosses the 173.5°W fracture and begins a period of faster motion within the mantle reference frame at ~60 Ma. The next change, to a wide range of compositions that span much of the total range for each isotopic system, takes place when the plume reaches the major Wishbone Scarp at ~46 Ma and its motion stabilises within the mantle. A significant increase also occurs in the isotopic range of lavas erupted by the Hawaiian plume when that plume crosses major fracture zones, and possibly reflects either more fractured lithospheric conditions allowing less pooling of individual melt batches prior to eruption or the assimilation of crust altered by seawater penetration along the fracture zone (xxxx). We interpret the correlation between degree of partial melting in the plume and the isotopic composition of the melts to indicate that either the plume has a zoned structure, with low degree melts reflecting a higher contribution from the plume core and less from the sheath, or that plume motion within the mantle resulted in changing proportions of plume and adjacent mantle asthenosphere in the source.

8. No Louisville – Ontong Java Plateau link

At least three large igneous provinces (the Ontong Java, Manihiki, and Hikurangi Plateaus), which combined cover ~1 % of the Earth's surface and represent a volume of ~100 million km³ of degassed basaltic magma, were emplaced in the central–southern Pacific at ~120 Ma. The spatial relationships of these LIPs to each other at their time of formation has been controversial, although it is now clear that at least the Manihiki and Hikurangi Plateaus

represent fragments of a formerly contiguous larger plateau and that several more pieces of this plateau may be scattered around the Pacific rim (Viso et al., 2005; Worthington et al., in review). It has been proposed that the Ontong Java Plateau represents a magmatic outburst associated with the Louisville plume head first impinging upon the lithosphere (xxxx), although paleomagnetic evidence is against this. Certainly the Louisville plume was located to the NW of the greater Manihiki Plateau during that time interval, as the plume crossed the Osbourn Trough paleo-spreading center shortly after spreading ceased at ~86 Ma.

All analyzed Louisville lavas have isotope compositions that are considerably more radiogenic than the MORB-like compositions reported for Ontong Java lavas. In addition, Ontong Java lavas are mostly tholeiitic whereas all Louisville lavas are alkalic. Thus, major changes in plume geochemistry would be required between the emplacement of the Ontong Java Plateau at ~120 Ma and the oldest Louisville seamount (Osbourn Seamount dated at 78 Ma). This stands in marked contrast to the relative uniformity of Louisville geochemistry and isotope compositions seen along the entire chain from Osbourn Seamount to the present location of the plume near Hollister Ridge (Hawkins et al., 1987).

9. Conclusions

Lavas dredged from the Louisville Ridge are highly vesicular and mildly weathered, with replacement of primary olivine and glass by secondary minerals. They define an alkalic series ranging in composition from foidite to benmoreite, and tholeiitic lavas are notably absent. Thus, the main shield-building phase of Louisville volcanic centers appears to have been alkalic and not tholeiitic. This is despite deliberate biasing of the dredge program towards sites at the headscarps of sector collapses 500–1000 m below the break in slope in an attempt to obtain only samples of the shield-building phase.

Louisville lavas require 2–9 % partial melting of a plume source, with most of the melting taking place within the garnet stability field at the base of the lithosphere. A progressive decrease in the degree of melting along the chain correlates to an increase in age and lithospheric thickness away from Osbourn Trough. Isotopically, Louisville Ridge lavas plot at the radiogenic end of the MORB array adjacent to, but not within, the FOZO field. There is no evidence for any HIMU, EM-I or EM-II components in these lavas. Changes in isotope values mirror those in partial melting of the source, and show abrupt discontinuities where the plume trail crosses fracture zones at 173.5°W, 170°W and the Wishbone Scarp at

168°W. It is also possible that these discontinuities bound a period of faster plume motion within the mantle and relate to tilting of the ascending plume.

Acknowledgements

We thank Captain Martin Kull, his officers and crew, and the other members of the Shipboard Scientific Party for their efforts and professionalism during the SO-167 cruise of the FS *SONNE*. Laboratory assistance was kindly provided by Peter Appel and Barbara Mader (microprobe analyses), Inga Dold, Ulrike Westernströer and Astrid Weinkopf (geochemical analyses), and Silke Hauff (isotope analyses). Funding for the cruise and analytical program was provided by the Bundesministerium für Bildung und Forschung (BMBF grant 03G0167A). RH thanks the Alexander von Humboldt Foundation for their support.

References

- [1] W.J. Morgan, Convection plumes in the lower mantle, *Nature* 230 (1971) 42–43.
- [2] D.A. Clague, R.D. Jarrard, Tertiary Pacific plate motion deduced from the Hawaiian–Emperor chain, *Geol. Soc. Am. Bull.* 84 (1973) 1135–1154.
- [3] Duncan (1981)
- [4] R.D. Müller, J.-Y. Royer, L.A. Lawver, Revised plate motion relative to the hotspots from combined Atlantic and Indian Ocean hotspot tracks, *Geology* 21 (1993) 275–278.
- [5] B. Steinberger, R.J. O'Connell, Effects of mantle flow on hotspot motion, in: M.A. Richards, R.G. Gordon, R.D. van der Hilst (eds.) *The History and Dynamics of Global Plate Motions*, AGU Geophys. Monogr. Ser. 121 (2000) 377–398.
- [6] P. Molnar, J. Stock, Relative motions of hotspots in the Pacific, Atlantic and Indian Oceans since late Cretaceous time, *Nature* 327 (1987) 587–591.
- [7] S.C. Cande, C.A. Raymond, J. Stock, W.F. Haxby, Geophysics of the Pitman Fracture Zone and Pacific-Antarctic plate motions during the Cenozoic, *Science* 270 (1995) 947–953.
- [8] I.O. Norton, Plate motions in the north Pacific: the 43 Ma non-event, *Tectonics* 14 (1995) 1080–1094.
- [9] I.O. Norton, Global hotspot reference frames and plate motion, in: M.A. Richards, R.G. Gordon, R.D. van der Hilst (eds.) *The History and Dynamics of Global Plate Motions*, AGU Geophys. Monogr. Ser. 121 (2000) 339–357.
- [10] C.A. Raymond, J.M. Stock, S.C. Cande, Fast Paleogene motion of the Pacific hotspots from revised global plate circuit reconstructions, in: M.A. Richards, R.G. Gordon, R.D. van der Hilst (eds.) *The History and Dynamics of Global Plate Motions*, AGU Geophys. Monogr. Ser. 121 (2000) 359–376.
- [11] J.A. Tarduno, et al., The Emperor Seamounts: southward motion of the Hawaiian hotspot plume in Earth's mantle, *Science* 301 (2003) 1064–1069.
- [12] B. Steinberger, R. Sutherland, R.J. O'Connell, Prediction of Emperor–Hawaii seamount locations from a revised model of plate motion and mantle flow, *Nature* 430 (2004) 167–173.
- [13] Hoffman (1997)
- [14] Davies (1999)
- [15] DePaolo and Wasserburg (1976)

- [16] A. Zindler, S.R. Hart, Chemical geodynamics, *Annu. Rev. Earth Planet. Sci.* 14 (1986) 493–571.
- [17] A.W. Hoffman, Nb in Hawaiian magmas: constraints on source composition and evolution, *Chem. Geol.* 57 (1988) 17–30.
- [18] Hart et al. (1992)
- [19] K.A. Farley, J.H. Natland, H. Craig, Binary mixing and enriched and undegassed (primitive?) mantle components (He, Sr, Nd, Pb) in Samoan lavas, *Earth Planet. Sci. Lett.* 111 (1992) 193–199.
- [20] D.A. Clague, G.B. Dalrymple, The Hawaiian–Emperor volcanic chain, I, Geologic evolution, *U.S. Geol. Surv. Prof. Pap.* 1350 (1987) 5–54.
- [21] DePaolo and Stolper, 1987
- [22] Hoernle et al. 2000
- [23] D.J. DePaolo, J.G. Bruce, A. Dodson, D.L. Shuster, B.M. Kennedy, Isotopic evolution of Mauna Loa and the chemical structure of the Hawaiian plume, *Geochem. Geophys. Geosyst.* 2 (2001), doi:10.1029/2000GC000139.
- [24] K.S. Harpp, W.M. White, Tracing a mantle plume; isotopic and trace element variations of Galapagos seamounts, *Geochem. Geophys. Geosyst.* 2 (2001) 46, doi:10.1029/2000GC000137.
- [25] W. Abouchami, A.W. Hofmann, S.J.G. Galer, F.A. Frey, J. Eisele, M. Feigenson, Lead isotopes reveal bilateral asymmetry and vertical continuity in the the Hawaiian mantle plume, *Nature* 434 (2005) 851–856.
- [26] J. Ritsema, R.M. Allen, The elusive mantle plume, *Earth Planet. Sci. Lett.* 207 (2003) 1–12.
- [27] M.A. Richards, R.A. Duncan, V. Courtillot, Flood basalts and hotspot tracks: plume heads and tails, *Science* 246 (1989) 193–107.
- [28] J.A. Tarduno, W.V. Sliter, L.W. Kroenke, M. Leckie, H. Mayer, J.J. Mahoney, R. Musgrave, M. Storey, E.L. Winterer, Rapid formation of Ontong Java Plateau by Aptian mantle plume volcanism, *Science* 254 (1991) 399–403.
- [29] R.L. Larson, Superplume and ridge interactions between Ontong Java and Manihiki Plateaus and the Nova-Canton Trough, *Geology* 25 (1997) 779–782.
- [30] S. Ingle, M.F. Coffin, Impact origin for the greater Ontong Java Plateau?, *Earth Planet. Sci. Lett.* 218 (2004) 123–134.
- [31] M. Antretter, P. Riisager, S. Hall, X. Zhao, B. Steinberger, Modeled paleolatitudes for the Louisville hotspot and the Ontong Java Plateau, in: J.G. Mahoney, P.J. Wallace,

- A.D. Saunders (eds.) Origin and Evolution of the Ontong Java Plateau, Geol. Soc. Spec. Publ. 229 (2005) 21–30.
- [32] K. Hoernle, F. Hauff, P. van den Bogaard, R. Werner, N. Mortimer, The Hikurangi oceanic plateau: another large piece of the largest volcanic event on Earth, 15th Annual Goldschmidt Conference abstracts (2005) A96.
- [33] J.W. Hawkins, P.F. Lonsdale, R. Batiza, Petrologic evolution of the Louisville seamount chain, in: B.H. Keating et al. (eds.) Seamounts, Islands, and Atolls, AGU Geophys. Monogr. Ser. 43 (1987) 235–254.
- [34] A.B. Watts, J.K. Weissel, R.A. Duncan, R.L. Larson, Origin of the Louisville Ridge and its relationship to the Eltanin Fracture Zone system, J. Geophys. Res. 93 (1988) 3051–3077.
- [35] I. Vlastelic, L. Dosso, H. Guillou, H. Bougault, L. Geli, J. Etoubleau, J.L. Joron, Geochemistry of the Hollister Ridge: relation with the Louisville hotspot and the Pacific–Antarctic Ridge, Earth Planet. Sci. Lett. 160 (1998) 777–793.
- [36] P. Lonsdale, Geography and history of the Louisville hotspot chain in the southwest Pacific, J. Geophys. Res. 93 (1988) 3078–3104.
- [37] A.A.P. Koppers, R.A. Duncan, B. Steinberger, Implications of a nonlinear $^{40}\text{Ar}/^{39}\text{Ar}$ age progression along the Louisville seamount trail for models of fixed and moving hot spots, Geochem. Geophys. Geosyst. 5 (2004) Q06L02, doi:10.1029/2003GC000671.
- [38] Q. Cheng, K.-H. Park, J.D. Macdougall, A. Zindler, G.W. Lugmair, H. Staudigel, J. Hawkins, P. Lonsdale, Isotopic evidence for a hotspot origin of the Louisville seamount chain, in: B.H. Keating et al. (eds.) Seamounts, Islands, and Atolls, AGU Geophys. Monogr. Ser. 43 (1987) 283–296.
- [39] T.J. Worthington, R. Hekinian, P. Stoffers, T. Kuhn, F. Hauff, Osbourn Trough: structure. Geochemistry and implications of a mid-Cretaceous paleospreading center in the south Pacific, Earth Planet. Sci. Lett. in review.
- [40] E.H. Talbi, J. Honnorez, Low-temperature alteration of Mesozoic oceanic crust, Ocean Drilling Program Leg 185, Geochem. Geophys. Geosyst. 4 (2003) 8906, doi:10.1029/2002GC000405.
- [41] C.-D. Garbe-Schönberg, Simultaneous determination of thirty-seven trace elements in twenty-eight international rock standards by ICP-MS, Geostand. Newslett. 17 (1993) 81–97.

- [42] K.A. Hoernle, G.R. Tilton, Sr-Nd-Pb isotope data for Fuerteventura (Canary Islands) basal complex and subaerial volcanics: applications to magma genesis and evolution, *Schweizerische Mineralogische und Petrographische Mitteilungen* 71 (1991) 3–18.
- [43] W. Todt, R.A. Cliff, A. Hanser, A.W. Hofmann, Evaluation of a ^{202}Pb – ^{205}Pb double spike for high-precision lead isotope analysis, in: G.E. Bebout et al. (eds.), *AGU Geophys. Monogr. Ser.* 95 (1996) 429–437.
- [44] G.A. Macdonald, T. Katsura, Chemical composition of Hawaiian lavas, *J. Petrol.* 5 (1964) 82–133.
- [45] S.-S. Sun, W.F. McDonough, Chemical and isotopic systematics of oceanic basalts: implications for mantle composition and processes, in: A.D. Saunders, M.J. Norry, (eds.), *Magmatism in the Ocean Basins*, *Geol. Soc. Spec. Publ.* 42 (1989) 313–345.
- [46] J.A. Pearce, I.J. Parkinson, Trace element models for mantle melting: application to volcanic arc petrogenesis, in: H.M. Pritchard et al. (eds.), *Magmatic Processes and Plate Tectonics*, *Geol. Soc. Spec. Publ.* 76 (1993) 373–403.
- [47] K.W.W. Sims, D.J. DePaolo, M.T. Murrell, W.S. Baldrige, S.J. Goldstein, D.A. Clague, Mechanisms of magma generation beneath Hawaii and mid-ocean ridges: uranium/thorium and samarium/neodymium isotopic evidence, *Science* 267 (1995) 508–512.
- [48] M.D. Feigenson, L.C. Patino, M.J. Carr, Constraints on partial melting imposed by rare earth element variations in Mauna Kea basalts, *J. Geophys. Res.* 101 (1996) 11815–11829.
- [49] Frey et al 2000
- [50] Lassiter et al 2000
- [51] N. Shimizu, I. Kushiro, The partitioning of rare earth elements between garnet and liquid at high pressure: preliminary experiments, *Geophys. Res. Lett.* 2 (1975) 413–416.
- [52] S.R. Hart, T. Dunn, Experimental cpx/melt partitioning of 24 elements, *Contrib. Mineral. Petrol.* 113 (1993) 1–8.
- [53] K.T.M. Johnson, Experimental determination of partition coefficients for rare earth and high-field-strength elements between clinopyroxene, garnet, and basaltic melt at high pressures, *Contrib. Mineral. Petrol.* 133 (1998) 60–68.
- [54] T.H. Green, J.D. Blundy, J. Adam, G.M. Yaxley, SIMS determination of trace element partition coefficients between garnet, clinopyroxene and hydrous basaltic liquids at 2–7.5 GPa and 1080–1200°C, *Lithos* 53 (2000) 165–187.

- [55] M.I. Billen, J. Stock, Morphology and origin of the Osbourn Trough, *J. Geophys. Res.* 105 (2000) 13481–13489.
- [56] A. Stracke, A.W. Hofmann, S.R. Hart, FOZO, HIMU, and the rest of the mantle zoo, *Geochem. Geophys. Geosyst.* 6 (2005) Q05007, doi:10.1029/2004GC000824.
- [57] R.F. Viso, R.L. Larson, R.A. Pockalny, Tectonic evolution of the Pacific–Phoenix–Farallon triple junction in the South Pacific Ocean, *Earth Planet. Sci. Lett.* 233 (2005) 179–194.
- [58] W.H.F. Smith, D.T. Sandwell, Global sea floor topography from satellite altimetry and ship sounding depths, *Science* 277 (1997) 1956–1962.

Table 1
SO-167 dredge stations along Louisville Ridge^a

Seamount	Stn	Latitude ^b °S	Longitude ^b °W	Depth mbsl
Osbourn	116	26°03.1'	174°58.7'	3021–2753
	117	26°02.7'	174°57.5'	2693–2599
	119	26°00.6'	174°54.8'	2179–1918
	120	26°02.5'	174°57.5'	2594–2159
LR 32	134	26°25.9'	174°46.4'	2675–2200
	135	26°43.1'	174°37.9'	2345–1804
	137	26°48.5'	174°35.2'	3007–2514
LR 33	139	27°35.0'	174°01.8'	2541–2116
	140	27°36.5'	174°03.2'	2388–1933
	141	27°38.5'	174°04.5'	2320–1797
LR 34	143	28°31.1'	173°22.5'	2203–1920
	145	28°36.7'	173°20.8'	2321–1971
	146	28°37.0'	173°20.8'	2387–2420
	147	28°36.8'	173°19.6'	2363–2177
Louisville	149	31°33.8'	172°06.3'	2560–2043
	150	31°32.4'	172°07.9'	2336–1847
	152	31°29.2'	172°16.1'	2239–1713
LR 36	154	33°44.1'	171°26.0'	1984–1798
Forde	157	35°27.6'	170°24.8'	2165–1921
	158	35°28.5'	170°21.8'	2107–1814
LR X	159	36°04.7'	169°34.5'	2188–1629
LR 38	161	37°01.0'	169°45.6'	1805–1620
	162	37°01.1'	169°46.6'	2221–1673
	163	37°00.8'	169°46.3'	1840–1653
Klingon	164	37°28.1'	169°26.5'	2340–1800
	165	37°32.0'	169°25.1'	2677–2079
	167	37°32.0'	169°18.5'	1950–1982
	168	37°31.9'	169°18.3'	1925–1766
	171	37°37.7'	169°09.7'	2283–1481
	172	37°43.4'	168°55.9'	2333–2205
LR 40	173	38°14.8'	168°08.3'	2192–1906

^a Only dredge stations with recovered lavas are listed.

^b Co-ordinates are the mid-points of dredge tracks typically 500 m long.

Table 2
Geochemical analyses of Louisville lavas

Sample ^a	116-4	117-1	120-34	120-35	134-1	135-1	135-2	135-3	139-1	139-2	139-3	139-4	141-7	147-1	147-2	147-4
SiO ₂	42.09	41.51	45.40	44.44	44.97	48.29	47.12	47.04	45.58	44.85	44.69	43.30	37.68	42.98	37.88	42.56
TiO ₂	3.64	2.29	2.88	3.06	3.02	5.10	5.09	5.20	3.53	3.89	4.16	4.23	5.17	2.71	3.07	3.62
Al ₂ O ₃	19.35	15.83	16.48	16.99	15.46	18.77	18.33	18.42	14.40	15.95	15.45	16.83	16.58	13.84	13.35	15.49
Fe ₂ O ₃	12.90	11.27	13.39	13.86	11.61	8.98	11.16	10.98	13.52	13.06	12.42	12.37	16.34	11.26	10.45	14.22
MnO	0.16	0.09	0.17	0.19	0.12	0.07	0.08	0.09	0.19	0.17	0.16	0.14	0.15	0.10	0.19	0.16
MgO	3.01	9.21	3.26	3.16	4.41	1.23	1.36	1.22	5.25	3.97	3.87	2.63	2.10	6.40	1.94	4.81
CaO	10.30	5.16	9.98	9.82	11.66	5.78	4.87	4.90	10.78	10.54	10.78	9.99	8.14	12.92	14.16	11.37
Na ₂ O	2.52	2.41	2.70	2.98	2.25	4.43	3.83	3.80	3.09	3.03	2.93	3.11	2.72	2.29	3.41	2.29
K ₂ O	0.77	1.61	2.20	1.31	1.49	1.53	1.70	1.84	1.39	1.32	1.26	1.43	1.37	0.98	2.10	0.79
P ₂ O ₅	0.52	0.29	0.71	0.66	0.82	1.01	0.84	0.86	0.67	0.72	0.96	1.83	1.98	0.46	5.66	0.66
LOI	4.36	10.63	1.84	3.31	3.94	4.07	5.30	5.19	0.47	1.23	1.93	2.90	5.85	5.85	6.08	3.18
Total	99.62	100.30	99.01	99.78	99.75	99.26	99.68	99.54	98.87	98.73	98.61	98.76	98.08	99.79	98.29	99.15
Li	27.1	63.9	4.78	6.94	18.1	14.8	11.6	11.5	7.36	8.64	12.6	14.5	25.3	52.7	23.5	20.5
Sc	22.3	41.3	38.9	33.5	34.7	26.2	17.9	17.7	30.7	27.6	29.9	23.7	33.9	29.6	16.3	31.1
V	286	218	403	359	295	252	232	235	352	369	401	358	464	304	182	349
Cr	13.0	413	238	388	151	3.49	3.23	4.11	26.1	44.8	27.2	23.7	43.1	177	2.60	26.2
Co	32.8	45.1	45.1	56.5	40.8	13.8	12.7	13.9	43.7	38.4	35.9	30.1	33.9	39.0	19.3	40.1
Ni	43.5	134	167	167	70.6	9.17	8.63	20.0	45.7	43.6	36.3	41.4	83.3	137	72.8	59.7
Cu	52.7	165	90.1	81.1	110	28.2	22.7	26.1	43.8	64.8	87.6	81.4	135	75.8	55.6	102
Zn	173	102	130	142	174	221	235	255	135	138	153	165	265	179	227	183
Ga	25.9	22.3	26.6	26.0	20.3	30.9	29.6	29.6	25.6	26.3	26.4	26.2	23.2	20.4	20.5	23.2
Rb	10.0	11.8	16.3	15.8	37.2	16.9	13.6	14.8	25.2	16.8	15.5	17.0	14.4	29.5	43.2	12.5
Sr	1126	272	481	569	490	1262	1223	1362	612	740	725	911	2136	412	735	736
Y	33.2	30.8	30.6	29.8	67.9	48.7	22.1	28.0	34.3	32.8	36.5	39.3	238	27.9	128	48.3
Zr	290	148	210	224	214	434	334	347	294	305	320	357	428	213	350	292
Nb	36.1	17.1	20.9	24.8	24.1	62.8	51.8	51.5	42.0	46.5	48.4	46.2	56.1	27.0	40.8	41.2
Cs	0.233	0.140	0.084	0.202	2.24	0.342	0.211	0.240	0.521	0.323	0.351	0.401	0.503	2.30	2.52	0.476
Ba	142	91.4	150	163	119	400	365	373	239	336	351	348	274	146	248	162
La	32.6	20.5	19.5	22.7	45.7	57.1	50.7	57.0	34.1	38.5	41.1	46.3	233	23.9	87.2	42.6
Ce	71.9	42.4	45.7	53.0	48.3	116	101	110	76.7	86.0	91.5	101	113	51.2	97.8	75.9
Pr	10.1	6.41	6.64	7.54	9.88	16.8	14.2	16.1	10.4	11.5	12.3	13.6	34.7	7.14	14.8	11.2
Nd	42.8	27.9	29.2	32.8	42.6	68.6	55.9	63.4	43.9	47.3	50.6	55.7	142	30.0	62.1	47.0
Sm	9.26	6.56	7.12	7.60	9.10	14.2	11.1	12.1	9.48	9.70	10.3	11.4	26.8	6.72	12.8	10.1
Eu	3.20	2.39	2.54	2.67	3.05	4.77	3.97	4.19	3.17	3.27	3.46	3.79	7.91	2.35	4.15	3.43
Gd	8.61	6.86	7.20	7.42	10.1	12.9	8.94	9.74	8.79	8.82	9.35	10.2	29.9	6.64	13.9	9.84
Tb	1.23	1.01	1.09	1.10	1.43	1.87	1.22	1.32	1.28	1.25	1.33	1.45	4.06	0.980	2.06	1.44
Dy	6.66	5.84	6.19	6.16	8.33	10.3	6.05	6.55	7.00	6.74	7.24	7.86	24.3	5.49	12.6	8.14
Ho	1.20	1.08	1.14	1.11	1.64	1.88	0.972	1.10	1.26	1.22	1.30	1.42	5.08	1.00	2.65	1.54
Er	2.96	2.70	2.85	2.82	4.30	4.71	2.24	2.60	3.20	3.03	3.28	3.60	13.6	2.51	7.46	3.99
Tm	0.391	0.358	0.387	0.379	0.562	0.639	0.277	0.323	0.428	0.403	0.437	0.483	1.79	0.332	1.06	0.536
Yb	2.41	2.19	2.40	2.35	3.41	3.93	1.62	1.93	2.65	2.49	2.76	3.04	10.9	2.07	6.93	3.38
Lu	0.331	0.306	0.333	0.322	0.504	0.540	0.208	0.259	0.373	0.352	0.380	0.420	1.63	0.287	1.07	0.484
Hf	6.53	3.96	4.99	5.30	5.10	9.81	9.30	8.73	6.69	6.82	7.17	7.87	10.4	4.78	7.53	6.78
Ta	2.33	1.11	1.34	1.62	1.51	3.84	3.83	3.93	2.62	2.89	2.98	2.71	3.04	1.64	2.43	2.66
Tl	0.065	0.020	0.031	0.028	0.124	0.234	0.110	0.270	0.013	0.049	0.030	0.074	0.172	0.045	0.752	0.057
Pb	2.13	1.26	1.47	1.62	3.18	2.76	2.51	3.30	1.99	2.17	2.25	2.51	24.7	1.46	7.35	3.57
Th	3.07	1.64	1.98	2.19	2.07	5.20	5.37	5.52	3.28	3.52	3.75	4.51	4.92	2.25	3.81	3.57
U	0.649	0.913	1.06	1.18	1.03	2.33	1.60	1.91	0.581	0.972	1.48	2.83	2.23	0.513	1.80	0.911

^a All sample numbers are prefixed by SO-167, major elements are reported in wt.% and trace elements in ppm.

Table 2 continued
 Geochemical analyses of Louisville lavas

Sample	149-1	150-1	152-1	154-1	154-2	157-1	157-2	157-3	158-1	158-2	158-3	158-7	159-1	159-2	159-3	159-6
SiO ₂	41.08	40.68	46.55	31.40	41.71	46.95	52.84	41.82	56.42	48.59	45.55	48.23	36.06	35.21	33.68	35.99
TiO ₂	3.46	3.86	2.03	2.86	3.94	3.17	1.35	4.83	0.85	2.56	2.67	2.45	3.51	3.30	3.05	3.84
Al ₂ O ₃	16.38	15.11	14.36	14.53	16.77	16.70	17.86	16.56	17.59	17.30	17.75	17.51	12.38	11.50	10.93	13.04
Fe ₂ O ₃	14.06	13.88	11.54	10.78	12.75	11.88	9.00	14.62	8.07	11.03	11.81	10.65	13.03	13.74	11.80	13.53
MnO	0.13	0.17	0.16	0.14	0.18	0.17	0.19	0.17	0.24	0.18	0.17	0.15	0.15	0.16	0.16	0.16
MgO	3.43	4.17	6.79	1.37	4.07	3.04	1.09	3.03	0.93	2.46	2.81	2.17	3.05	3.68	2.69	3.00
CaO	10.79	11.27	10.55	18.69	10.49	8.31	4.89	9.90	3.04	7.67	7.81	6.89	12.75	14.51	15.49	13.58
Na ₂ O	2.24	2.35	2.87	2.59	2.67	4.13	5.36	2.96	6.34	4.26	3.80	4.45	2.46	2.34	2.63	2.42
K ₂ O	1.19	1.19	0.50	1.20	1.04	1.74	2.76	1.33	3.34	2.14	1.51	2.48	2.44	2.16	2.85	1.85
P ₂ O ₅	1.34	1.86	0.34	4.11	0.99	1.08	1.00	1.21	0.30	1.11	1.26	1.28	4.71	4.87	6.88	4.58
LOI	5.16	4.22	3.53	12.14	4.21	1.44	2.34	2.56	1.64	1.76	3.62	2.56	8.15	7.14	8.38	6.75
Total	99.26	98.76	99.22	99.81	98.82	98.61	98.68	98.99	98.76	99.06	98.76	98.82	98.69	98.61	98.54	98.74
Li	21.8	31.3	25.8	41.8	36.0	13.2	15.8	12.3	3.31	10.2	28.1	28.7	20.4	12.5	6.66	17.4
Sc	35.8	23.1	23.4	13.0	11.3	9.83	3.17	22.1	5.61	7.17	9.04	7.66	29.3	32.1	25.5	28.7
V	337	371	208	197	240	135	45.2	337	0.440	61.5	81.1	93.6	281	316	223	297
Cr	93.5	50.5	391	37.8	0.529	2.32	0.702	61.6	0.126	1.24	0.862	0.816	428	567	425	218
Co	37.7	41.6	44.6	19.3	34.0	18.3	7.66	40.7	1.21	15.7	18.2	16.7	42.6	46.4	45.4	39.9
Ni	75.5	91.4	183	60.7	29.9	12.4	21.7	47.9	0.359	1.68	20.1	31.9	85.8	86.8	76.2	72.9
Cu	101	66.6	56.4	38.1	26.6	6.01	4.84	32.3	2.54	4.26	8.24	6.37	124	84.6	89.8	81.3
Zn	248	263	140	146	184	155	181	172	155	133	182	190	176	150	154	180
Ga	23.1	26.3	21.3	17.8	27.7	25.1	25.6	26.1	31.1	25.9	26.9	27.4	14.4	16.6	14.3	19.2
Rb	28.3	33.5	5.85	18.4	17.4	26.1	39.6	24.4	47.4	37.4	27.4	40.1	36.5	34.1	35.4	30.1
Sr	1048	776	467	1365	1343	1294	1216	1125	1649	1691	1285	800	781	712	1147	
Y	87.1	119	23.0	66.3	36.9	39.7	40.8	38.3	47.7	40.4	46.3	42.7	61.1	71.3	71.8	97.4
Zr	253	296	108	333	358	342	614	247	631	414	440	446	237	186	158	231
Nb	33.4	43.1	22.3	67.3	65.1	53.2	81.4	34.0	110	59.9	63.3	63.3	39.4	19.8	3.84	23.0
Cs	1.73	2.88	0.300	0.468	0.642	0.615	0.922	0.824	0.458	1.40	1.62	1.13	0.843	0.438	0.474	0.667
Ba	157	239	150	432	449	362	600	252	979	430	418	436	280	265	256	313
La	65.8	79.4	16.3	67.1	51.2	44.9	70.7	33.6	81.9	55.1	59.7	58.1	47.9	48.9	48.7	67.7
Ce	61.9	81.0	33.3	127	114	97.9	165	67.9	189	133	139	136	69.7	61.5	62.0	81.2
Pr	13.1	17.0	4.58	16.4	14.4	13.4	18.2	9.69	21.4	16.4	17.4	16.6	10.2	10.1	9.68	13.9
Nd	55.6	70.6	20.1	65.4	58.7	56.1	68.3	42.4	80.9	67.8	72.2	67.0	41.7	41.2	40.1	57.0
Sm	11.6	14.2	5.07	12.7	12.2	12.2	12.7	9.56	15.2	14.0	14.9	13.7	8.53	8.39	8.13	11.3
Eu	3.76	4.46	1.92	4.17	4.14	4.17	4.13	3.39	5.06	4.74	5.03	4.52	2.87	2.57	2.71	3.73
Gd	12.6	15.2	5.37	11.7	10.9	11.2	10.6	9.24	12.4	12.4	13.3	12.2	8.47	8.40	8.36	11.9
Tb	1.80	2.14	0.818	1.62	1.50	1.58	1.52	1.30	1.84	1.70	1.82	1.68	1.21	1.18	1.20	1.67
Dy	10.6	12.6	4.66	8.81	7.86	8.34	8.19	7.04	9.90	8.81	9.42	8.83	6.95	7.05	7.19	9.97
Ho	2.12	2.60	0.856	1.67	1.34	1.46	1.47	1.26	1.77	1.52	1.64	1.55	1.39	1.43	1.53	2.06
Er	5.66	7.06	2.15	4.43	3.21	3.60	3.80	3.06	4.46	3.69	3.95	3.79	3.83	3.95	4.39	5.69
Tm	0.757	0.969	0.289	0.586	0.407	0.468	0.526	0.393	0.606	0.477	0.513	0.492	0.531	0.549	0.635	0.790
Yb	4.64	6.04	1.79	3.71	2.44	2.84	3.33	2.38	3.79	2.85	3.09	3.03	3.40	3.50	4.19	5.02
Lu	0.688	0.900	0.249	0.559	0.333	0.388	0.473	0.330	0.523	0.390	0.425	0.421	0.531	0.531	0.667	0.777
Hf	5.93	6.65	3.05	6.89	7.73	7.78	12.9	5.61	13.5	9.13	9.44	9.35	5.38	3.77	3.61	5.14
Ta	2.09	2.65	1.39	3.95	4.05	3.38	5.25	2.10	6.17	3.82	3.79	3.85	2.43	1.07	0.186	1.20
Tl	0.154	0.335	0.024	0.075	0.163	0.033	0.181	0.039	0.176	0.311	0.097	0.093	0.191	0.125	0.232	0.111
Pb	7.45	9.27	1.05	5.39	3.38	3.08	5.73	2.66	6.25	3.86	4.05	4.45	3.53	3.50	2.70	5.50
Th	2.79	3.82	1.73	4.80	5.48	4.56	8.50	2.87	9.11	5.57	5.76	6.10	3.65	3.09	3.29	4.36
U	1.61	1.39	0.427	1.89	0.940	0.569	1.23	1.17	2.69	1.79	0.770	1.33	2.40	1.66	2.45	2.16

Table 2 continued
Geochemical analyses of Louisville lavas

Sample	161-1	162-1	162-3	162-8	163-1	165-1	165-2	165-8	167-1	168-1	168-2	168-3	168-4	171-1	171-2	171-3
SiO ₂	33.37	37.11	37.81	43.72	37.04	37.42	36.84	34.80	41.85	36.40	35.45	36.62	35.29	42.28	41.93	41.60
TiO ₂	4.55	3.18	3.04	2.67	4.55	4.03	3.80	3.78	4.00	3.27	3.56	3.39	3.60	4.17	2.32	2.51
Al ₂ O ₃	12.15	13.62	13.22	12.66	16.35	13.69	12.54	12.74	15.95	9.91	10.62	10.42	11.00	14.96	8.80	9.40
Fe ₂ O ₃	14.08	14.12	13.90	12.64	13.27	16.31	13.73	11.19	13.05	14.89	15.83	15.67	16.14	13.64	14.80	15.16
MnO	0.24	0.15	0.14	0.15	0.16	0.24	0.21	0.15	0.17	0.22	0.22	0.20	0.48	0.19	0.18	0.18
MgO	3.92	6.00	5.26	2.67	2.66	4.30	4.58	3.36	4.27	10.17	8.59	10.49	6.76	5.96	16.75	14.71
CaO	17.64	13.64	11.93	3.96	11.91	12.05	15.70	19.58	10.32	14.20	14.25	12.88	13.25	9.70	8.64	9.26
Na ₂ O	1.58	1.13	1.61	2.93	2.47	1.85	1.65	1.93	3.92	1.43	0.95	1.12	0.92	3.00	1.58	1.68
K ₂ O	1.34	0.89	1.57	3.73	1.26	1.03	0.94	1.02	1.38	1.00	0.74	0.86	1.18	1.32	0.66	0.72
P ₂ O ₅	1.32	1.31	2.02	1.44	1.32	2.32	1.01	1.27	1.23	0.76	1.05	0.91	1.53	0.80	0.45	0.52
LOI	9.34	9.01	9.30	13.34	8.61	5.71	8.91	10.31	2.46	7.03	8.15	6.76	8.65	2.60	3.03	3.12
Total	99.53	100.16	99.80	99.91	99.60	98.95	99.91	100.13	98.60	99.28	99.41	99.32	98.80	98.62	99.14	98.86
Li	19.5	61.5	36.1	29.0	33.1	18.4	24.7	15.8	24.3	44.6	62.1	41.3	44.0	9.98	30.8	27.5
Sc	22.3	25.5	24.0	21.2	17.4	29.2	24.0	19.1	9.69	27.0	28.8	27.3	32.8	16.9	20.3	22.6
V	344	330	301	129	259	384	325	282	209	307	345	318	365	237	195	226
Cr	283	467	474	382	53.0	441	281	195	0.942	699	710	781	870	48.9	1097	1286
Co	67.2	43.7	46.3	40.4	35.3	66.5	57.5	33.5	32.7	75.8	72.9	80.2	132	39.7	111	96.3
Ni	141	131	115	108	62.0	146	102	52.7	21.0	387	313	343	279	31.3	794	563
Cu	41.3	78.5	127	138	33.3	124	37.6	58.9	20.7	70.7	77.4	68.9	101	26.9	41.7	52.6
Zn	170	161	173	190	162	231	181	133	172	147	196	172	326	137	141	168
Ga	19.3	20.0	19.7	12.5	20.1	25.6	21.4	19.8	29.1	19.1	19.7	21.9	22.0	26.7	16.9	19.7
Rb	21.0	15.1	28.5	59.2	18.0	19.5	17.4	18.2	33.3	19.5	14.7	16.1	25.3	25.7	11.3	12.5
Sr	881	303	331	230	1122	757	612	744	1494	477	378	416	475	1160	492	552
Y	37.3	24.2	27.4	32.1	40.6	29.5	25.0	29.0	38.0	22.9	25.8	25.7	34.2	35.1	16.4	19.0
Zr	263	226	219	212	306	269	247	254	440	250	272	254	272	372	192	219
Nb	46.3	52.5	47.8	48.0	53.5	39.6	36.9	39.7	81.4	66.4	69.7	65.5	67.9	65.1	27.6	31.4
Cs	0.405	0.420	0.688	1.31	0.488	0.688	0.520	0.698	1.88	0.609	0.831	0.686	1.29	0.385	0.364	0.393
Ba	307	129	168	222	399	269	215	263	534	176	40.7	104	112	416	175	188
La	39.9	36.3	39.6	36.6	41.7	33.1	29.5	34.2	65.4	44.4	50.1	49.6	56.0	50.6	22.8	26.9
Ce	73.9	74.9	78.2	67.9	83.2	71.6	65.8	69.4	151	94.6	120	106	120	117	51.1	60.1
Pr	10.6	9.58	10.1	9.45	11.8	9.72	8.86	9.40	18.3	11.9	13.3	13.1	14.3	14.5	6.85	8.09
Nd	44.2	38.8	41.3	38.0	50.0	41.2	36.9	38.7	73.7	47.8	53.3	53.0	57.9	59.1	28.1	33.6
Sm	9.42	8.29	8.81	8.10	10.7	8.95	8.02	8.25	14.8	9.60	10.7	10.6	11.5	12.1	5.96	7.05
Eu	3.18	2.89	3.04	2.79	3.68	3.03	2.72	2.80	4.80	3.17	3.52	3.47	3.78	4.02	1.82	2.35
Gd	8.88	7.64	8.04	7.41	9.93	8.25	7.40	7.65	12.6	8.39	9.27	9.18	10.2	10.7	5.12	6.33
Tb	1.24	1.06	1.11	1.03	1.38	1.16	1.05	1.07	1.71	1.11	1.24	1.22	1.35	1.46	0.676	0.851
Dy	6.69	5.48	5.82	5.47	7.47	6.18	5.56	5.72	8.55	5.54	6.21	6.13	6.80	7.66	3.45	4.28
Ho	1.19	0.925	0.997	0.974	1.33	1.07	0.949	0.993	1.40	0.893	0.998	0.997	1.15	1.31	0.559	0.701
Er	2.95	2.17	2.36	2.46	3.31	2.57	2.28	2.44	3.23	2.05	2.32	2.28	2.67	3.14	1.28	1.61
Tm	0.380	0.270	0.300	0.326	0.430	0.331	0.290	0.311	0.393	0.244	0.277	0.272	0.329	0.401	0.157	0.198
Yb	2.26	1.60	1.80	2.05	2.57	1.96	1.74	1.88	2.28	1.41	1.60	1.59	1.91	2.40	0.935	1.18
Lu	0.317	0.215	0.245	0.315	0.360	0.269	0.237	0.260	0.299	0.186	0.214	0.207	0.261	0.322	0.119	0.159
Hf	6.03	5.02	5.05	4.54	6.72	6.12	5.57	5.66	9.16	5.66	6.18	6.00	6.35	8.31	3.97	4.97
Ta	2.85	3.13	2.94	2.89	3.28	2.40	2.36	2.53	5.17	3.80	4.06	3.96	3.86	4.06	1.59	1.98
Tl	0.217	0.053	0.049	0.587	0.077	0.734	0.249	0.137	0.053	0.071	0.134	0.086	0.289	0.053	0.054	0.040
Pb	4.89	1.90	2.08	2.47	3.10	2.10	1.65	1.91	3.84	2.34	2.72	2.70	3.39	3.24	1.56	2.08
Th	3.12	4.23	4.77	3.98	3.26	3.23	2.87	2.96	6.91	5.10	5.58	5.95	5.86	5.20	2.55	3.05
U	1.41	1.84	2.14	2.18	1.22	1.93	1.14	1.11	1.84	1.24	1.51	1.51	2.12	1.64	0.666	1.03

Table 2 continued
 Geochemical analyses of Louisville lavas

Sample	171-6	171-8	171-12	172-1	172-2	172-3	173-1	173-2	173-3
SiO ₂	41.83	41.16	43.56	36.08	32.87	26.19	53.03	52.69	52.36
TiO ₂	2.56	2.54	3.61	2.83	2.47	2.04	1.26	1.28	1.31
Al ₂ O ₃	11.92	11.75	14.58	14.22	12.71	9.79	17.66	17.78	17.59
Fe ₂ O ₃	10.45	10.70	12.40	11.07	9.72	7.74	8.85	9.20	9.37
MnO	0.14	0.14	0.18	0.19	0.17	0.14	0.22	0.23	0.23
MgO	7.43	7.08	5.54	2.59	2.14	1.88	1.64	1.58	1.65
CaO	14.42	15.00	10.70	14.44	17.51	26.04	4.53	4.52	4.49
Na ₂ O	2.12	2.14	2.41	2.49	2.44	2.16	5.60	5.48	5.47
K ₂ O	1.27	1.47	1.29	1.98	2.13	2.04	2.63	2.62	2.62
P ₂ O ₅	0.45	0.45	0.64	3.60	5.40	3.89	0.48	0.46	0.49
LOI	7.19	7.62	4.40	9.67	11.63	19.21	2.69	2.77	3.15
Total	99.78	100.05	99.31	99.16	99.19	101.12	98.59	98.61	98.73
Li	46.3	33.8	49.4	36.3	34.4	19.4	9.79	10.7	11.7
Sc	27.1	25.8	25.1	7.27	6.28	4.70	3.35	2.18	3.25
V	240	240	308	106	74.3	61.6	3.40	3.81	4.15
Cr	690	665	265	5.01	6.06	5.62	0.972	0.192	0.181
Co	44.9	44.0	48.4	22.0	17.1	14.0	7.34	6.96	7.55
Ni	256	244	166	54.9	54.8	39.2	1.87	5.96	4.71
Cu	62.2	53.0	61.3	27.8	36.9	20.8	8.89	9.38	9.88
Zn	125	123	163	180	165	127	135	135	128
Ga	18.1	18.2	23.6	21.2	15.8	12.2	28.8	28.2	25.4
Rb	31.6	40.2	33.7	39.5	41.0	35.6	54.4	53.3	56.9
Sr	445	445	554	1262	1192	968	745	779	738
Y	25.0	25.3	33.4	41.9	40.0	27.6	40.6	40.9	38.2
Zr	216	216	274	440	399	323	572	582	588
Nb	30.9	30.8	41.7	57.5	64.5	58.2	98.2	98.5	112
Cs	1.61	1.84	2.45	0.884	1.04	0.753	1.07	1.08	1.03
Ba	189	203	224	529	431	346	707	726	678
La	25.9	26.4	34.5	67.8	63.9	45.2	71.3	72.4	69.3
Ce	55.9	56.3	74.6	136	137	93.4	153	159	159
Pr	7.50	7.53	10.1	17.8	15.9	11.9	16.7	17.2	16.5
Nd	30.5	30.9	41.6	68.2	61.9	46.1	60.6	62.3	59.6
Sm	6.51	6.53	8.96	12.9	11.6	8.63	10.9	11.3	10.8
Eu	2.22	2.24	3.07	3.74	3.75	2.81	3.92	4.04	3.89
Gd	6.26	6.29	8.58	10.6	10.1	7.51	9.35	9.53	9.23
Tb	0.901	0.906	1.24	1.45	1.37	1.02	1.39	1.44	1.37
Dy	4.98	5.03	6.81	7.55	7.28	5.36	7.77	8.05	7.66
Ho	0.908	0.918	1.22	1.30	1.30	0.939	1.46	1.51	1.43
Er	2.30	2.34	3.05	3.27	3.30	2.37	3.89	4.02	3.83
Tm	0.307	0.308	0.402	0.423	0.433	0.316	0.558	0.580	0.542
Yb	1.93	1.94	2.45	2.64	2.70	1.98	3.63	3.77	3.53
Lu	0.269	0.272	0.344	0.355	0.396	0.282	0.521	0.547	0.514
Hf	4.96	4.95	6.26	7.75	8.40	6.71	10.7	11.3	10.9
Ta	1.98	1.98	2.60	2.98	3.90	3.53	5.84	6.19	5.98
Tl	0.038	0.043	0.034	0.066	0.099	0.076	0.087	0.168	0.121
Pb	1.87	1.89	3.43	3.69	3.39	2.59	5.16	5.26	4.78
Th	2.68	2.69	3.55	6.66	5.74	4.40	9.10	9.55	8.55
U	0.640	0.660	0.907	1.92	2.04	1.58	2.71	2.58	2.41

Table 3
Sr-Nd-Pb isotope data for Louisville lavas^a

Sample	⁸⁷ Sr/ ⁸⁶ Sr	¹⁴³ Nd/ ¹⁴⁴ Nd	ϵ_{Nd} ^b	²⁰⁶ Pb/ ²⁰⁴ Pb	²⁰⁷ Pb/ ²⁰⁴ Pb	²⁰⁸ Pb/ ²⁰⁴ Pb
116-4	0.703748 ± 5	0.512879 ± 2	4.70	19.149 ± 0	15.579 ± 0	38.928 ± 1
116-4 (u)	0.704845 ± 5	0.512864 ± 3	4.41			
116-4 (l)				19.408 ± 4	15.604 ± 3	39.347 ± 8
120-34	0.703669 ± 5	0.512931 ± 3	5.71	19.299 ± 1	15.588 ± 1	38.879 ± 2
120-34 (u)	0.703976 ± 5	0.512903 ± 2	5.16			
120-34 (l)				19.162 ± 2	15.579 ± 2	38.781 ± 5
135-2	0.703457 ± 5	0.512899 ± 2	5.09	19.608 ± 1	15.613 ± 0	39.318 ± 1
139-1	0.703268 ± 5	0.512890 ± 3	4.91	19.471 ± 1	15.609 ± 0	39.233 ± 1
139-1 (u)	0.703378 ± 5	0.512887 ± 2	4.86			
139-1 (l)				19.531 ± 1	15.614 ± 1	39.162 ± 2
147-1	0.703262 ± 5	0.512933 ± 2	5.76	19.516 ± 1	15.617 ± 1	39.231 ± 3
152-1	0.702935 ± 5	0.512953 ± 2	6.14	19.083 ± 1	15.561 ± 1	38.696 ± 3
154-2	0.703504 ± 5	0.512900 ± 2	5.11	19.198 ± 1	15.589 ± 0	39.061 ± 1
157-1	0.703599 ± 5	0.512894 ± 3	4.99	19.063 ± 1	15.575 ± 1	38.945 ± 2
159-6	0.703734 ± 5	0.512892 ± 2	4.96	19.247 ± 0	15.644 ± 0	39.066 ± 1
162-3	0.703130 ± 5	0.512957 ± 2	6.23	19.357 ± 1	15.578 ± 1	38.899 ± 2
165-1	0.703350 ± 5	0.512907 ± 2	5.24	19.436 ± 1	15.601 ± 1	39.044 ± 1
167-1	0.703384 ± 4	0.512900 ± 2	5.12	19.356 ± 1	15.591 ± 1	39.057 ± 2
168-3	0.703098 ± 4	0.512941 ± 2	5.90	19.406 ± 1	15.597 ± 1	39.015 ± 3
171-1	0.703521 ± 5	0.512869 ± 2	4.51	19.410 ± 1	15.601 ± 1	39.175 ± 2
172-3	0.703539 ± 5	0.512873 ± 3	4.59	19.396 ± 1	15.601 ± 1	39.185 ± 1
173-1	0.703205 ± 5	0.512905 ± 2	5.22	19.488 ± 1	15.592 ± 0	39.095 ± 1

^a Reported Sr-Nd isotope determinations were on leached powders with Pb isotope determinations on unleached aliquots except for samples suffixed with u (= Sr-Nd on unleached powder) or l (Pb on leached powder). All errors are 2 σ standard errors of the mean and apply to the last quoted digit of the analyzed ratio.

^b Calculated assuming present-day ϵ_{Nd} for CHUR = 0.512368; 2 σ error in ϵ_{Nd} is $\sim \pm 0.05$.

Figure Captions

- Fig. 1: Location map showing the principal features of the Pacific seafloor east of the Tonga–Kermadec Trench (predicted bathymetry from Smith and Sandwell, 1997). The white box encloses the area surveyed during this study.
- Fig. 2: Bathymetric map of the LR 34 and Klingon seamounts, both of which are flat-topped guyots. Dredging took place at the steep headwalls of sector collapse scarps at depths of 500–1000 m below the break in slope.
- Fig. 3: Plot of P_2O_5 versus MgO for all analyzed Louisville lavas, identifying a group of phosphatized lavas and a second group with aberrant geochemistry. No further use is made of these analyses. Lavas plotting below the dashed line have compositions that are little affected by marine weathering.
- Fig. 4: Panel A: total alkali ($Na_2O + K_2O$) versus SiO_2 plot with classification fields from Le Bas et al. (1986) and alkalic–tholeiitic boundary from Macdonald and Katsura (1964) demonstrating the alkalic character of Louisville lavas. Panel B: K_2O versus MgO plot showing that most foidites and the one lava plotting within the tholeiite field have high-MgO reflecting their cumulus enrichment in olivine.
- Fig. 5: Louisville lavas form tight linear arrays on plots of incompatible elements. Their values of $(Ce/Yb)_N$ and Nb/Zr are far greater than those of Mauna Kea tholeiites, reflecting their alkalic character. Note that Osbourn Seamount lavas fall to the left side in each plot.
- Fig. 6: Panels A-B: chondrite-normalized REE plots for representative Louisville lavas (chondrite after Sun and McDonough, 1989; MORB after Pearce and Parkinson, 1993). Note the light-REE enriched character and parallel (non-crossing) patterns. Panels C-D: primitive mantle-normalized plots for representative Louisville lavas (primitive mantle after Sun and McDonough, 1989; MORB after Pearce and Parkinson, 1993). Note the convex upward pattern that contrasts with MORB, and the negative anomalies at K, Pb and sometimes U.

- Fig. 7: Plots featuring strongly incompatible elements and distinguishing between melting within the garnet and spinel stability fields. Melting trajectories were determined using the non-modal partial melting equation of Shaw (1970) constrained by the experiments of Walter et al. (1995; 1999) with partition coefficients after the compilation of Sisson et al. (2002).
- Fig. 8: Changes in incompatible element values (Nb/Zr) and Sr-Nd-Pb isotope compositions with age along the sampled section of the Louisville Ridge. Note the similarity of the pattern in Nb/Zr with that in $^{143}\text{Nd}/^{144}\text{Nd}$ and $^{206}\text{Pb}/^{204}\text{Pb}$, whereas the $^{87}\text{Sr}/^{86}\text{Sr}$ pattern is a mirror image. Breaks in the trends correlate with the plume passing fractures at 173.5°W, 170°W and the major wishbone Scarp at ~45.5 Ma. The interval 62–47 Ma is also a period of faster than usual motion of the Louisville plume within the mantle reference frame (Koppers et al., 2004).
- Fig. 9: Sr, Nd and Pb isotope variation diagrams. Louisville lavas plot at the radiogenic end of the MORB spectrum adjacent to FOZO, but do not exhibit any evidence of HIMU, EM-I or EM-II components. Mantle component fields from Stracke et al. (2005).

Worthington et al., Louisville Ridge

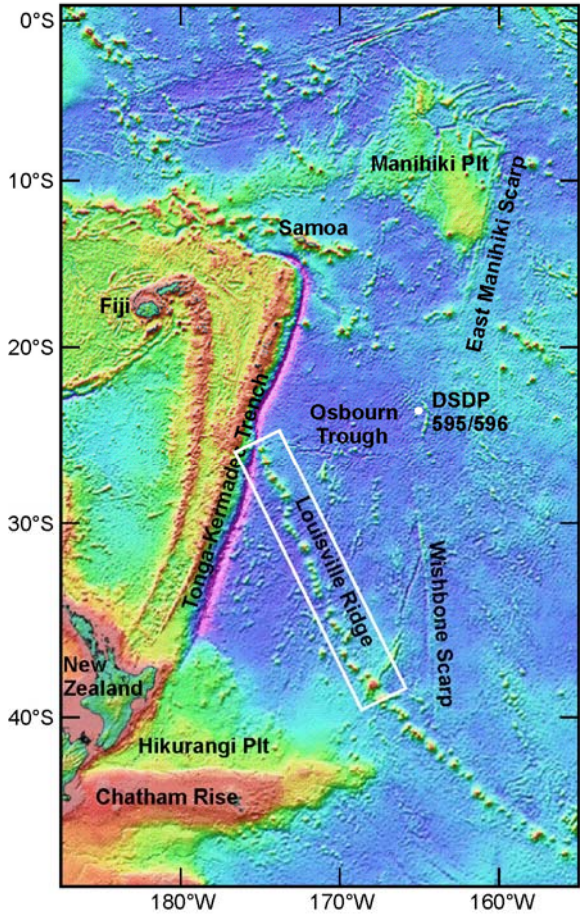


Figure 1

Worthington et al., Louisville Ridge

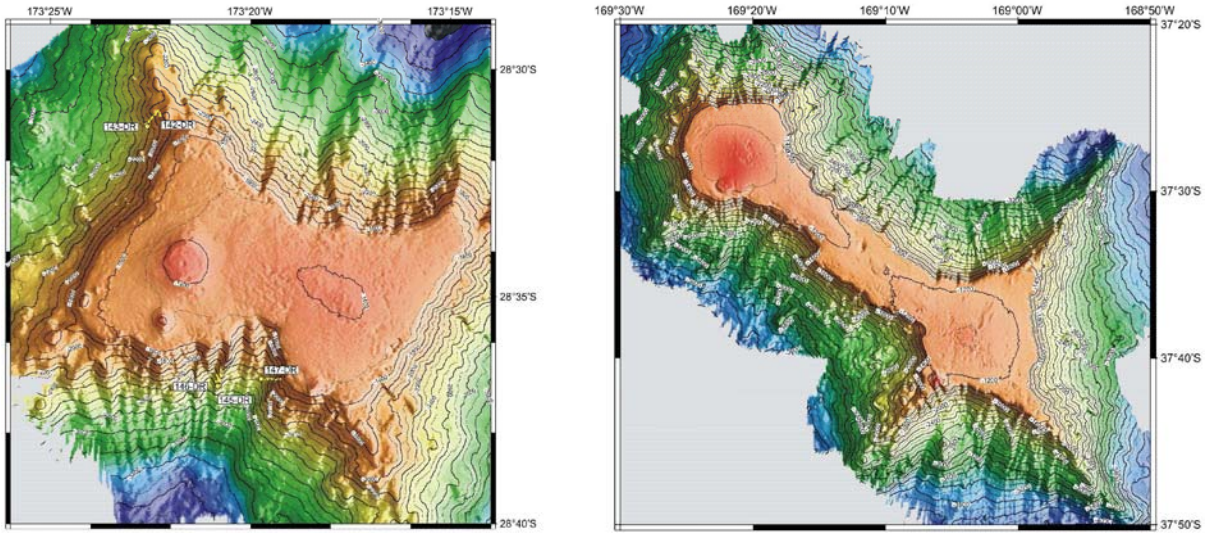


Figure 2

Worthington et al., Louisville Ridge

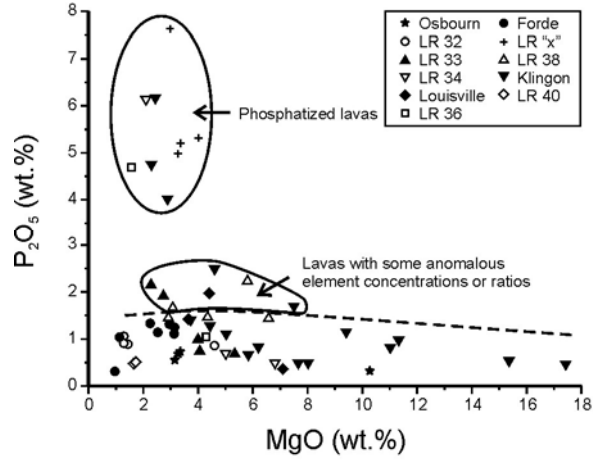


Figure 3

Worthington et al., Louisville Ridge

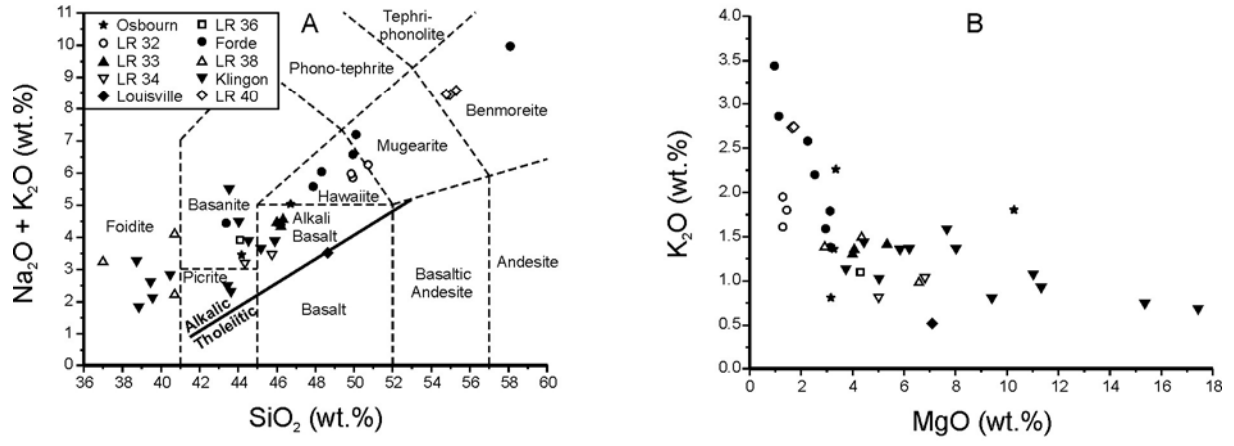
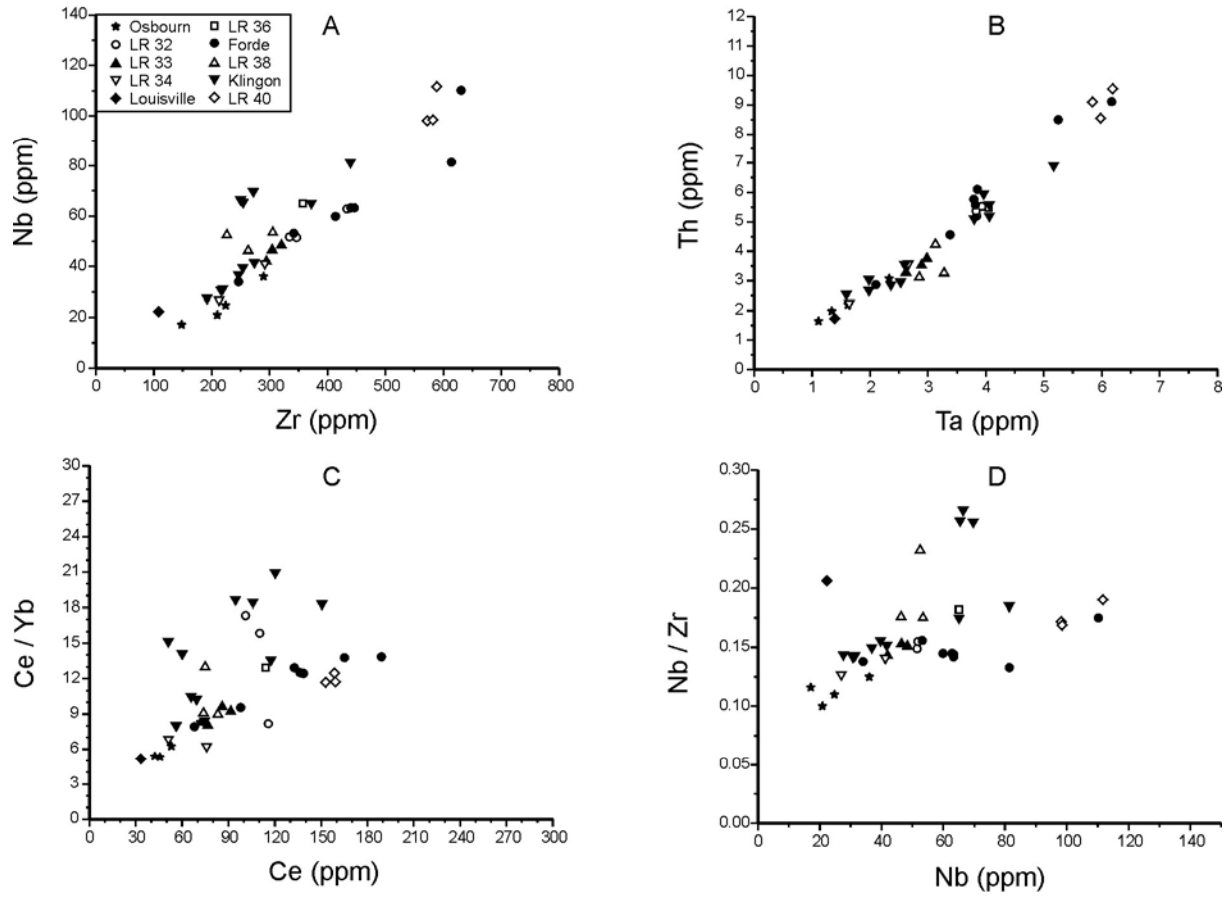


Figure 4

Worthington et al., Louisville Ridge



Worthington et al., Louisville Ridge

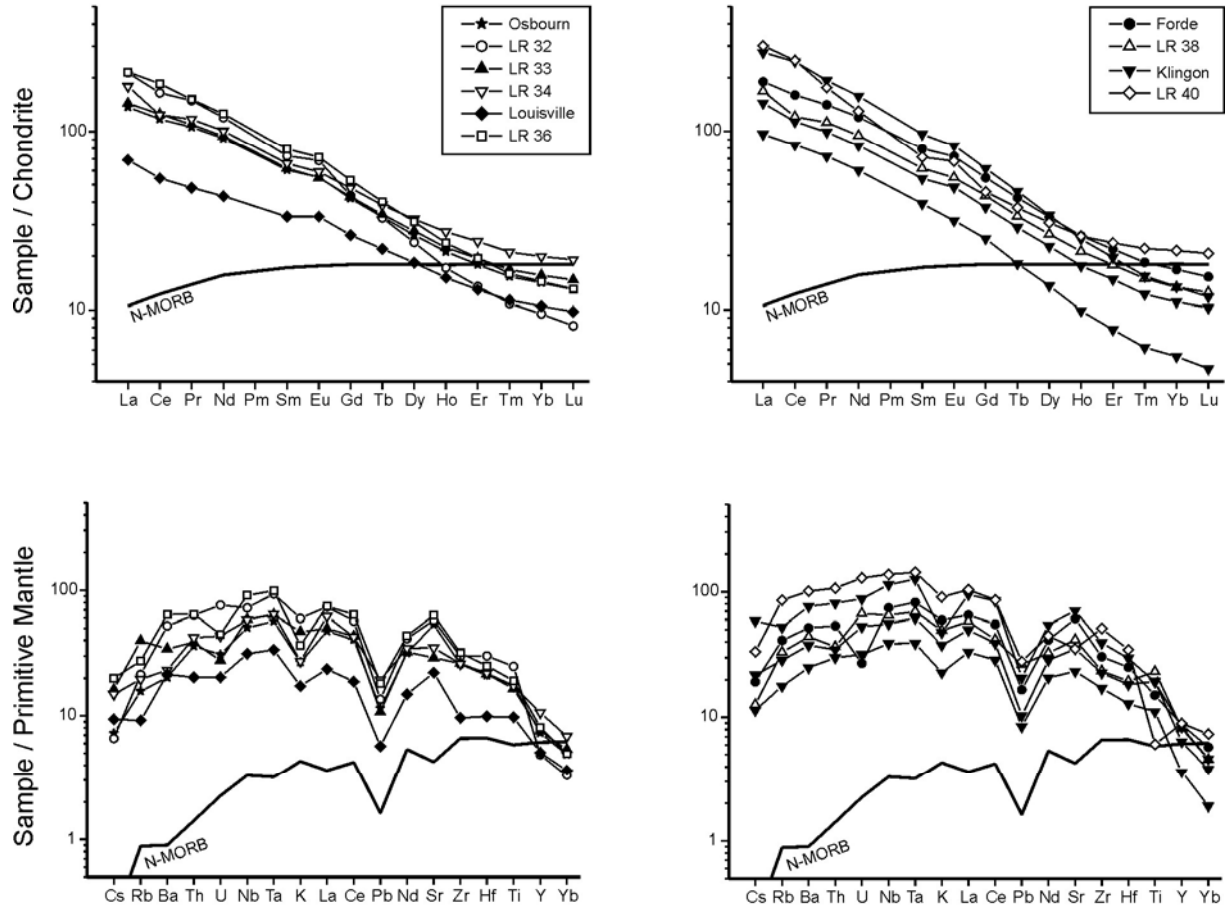


Figure 6

Worthington et al., Louisville Ridge

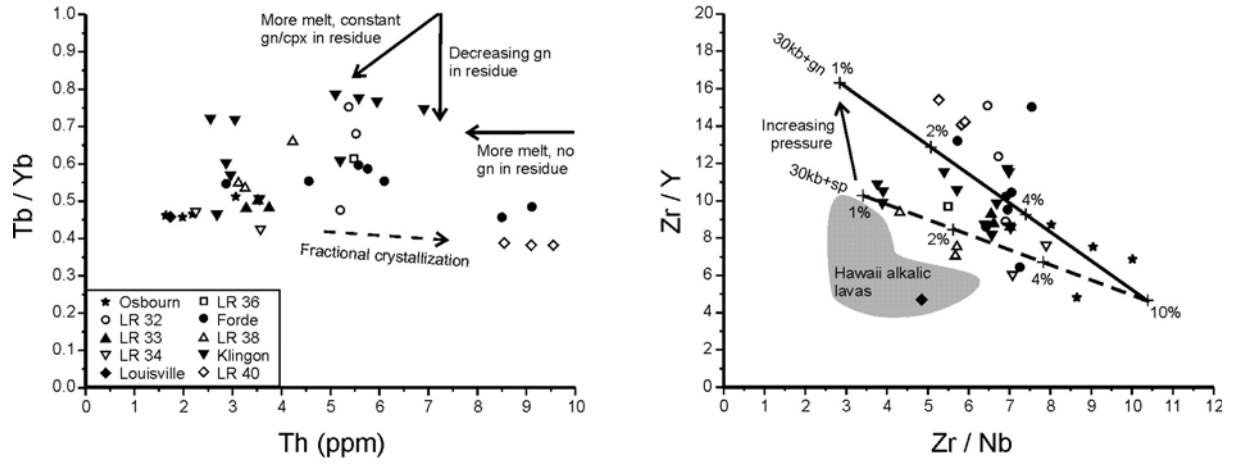


Figure 7

Worthington et al., Louisville Ridge

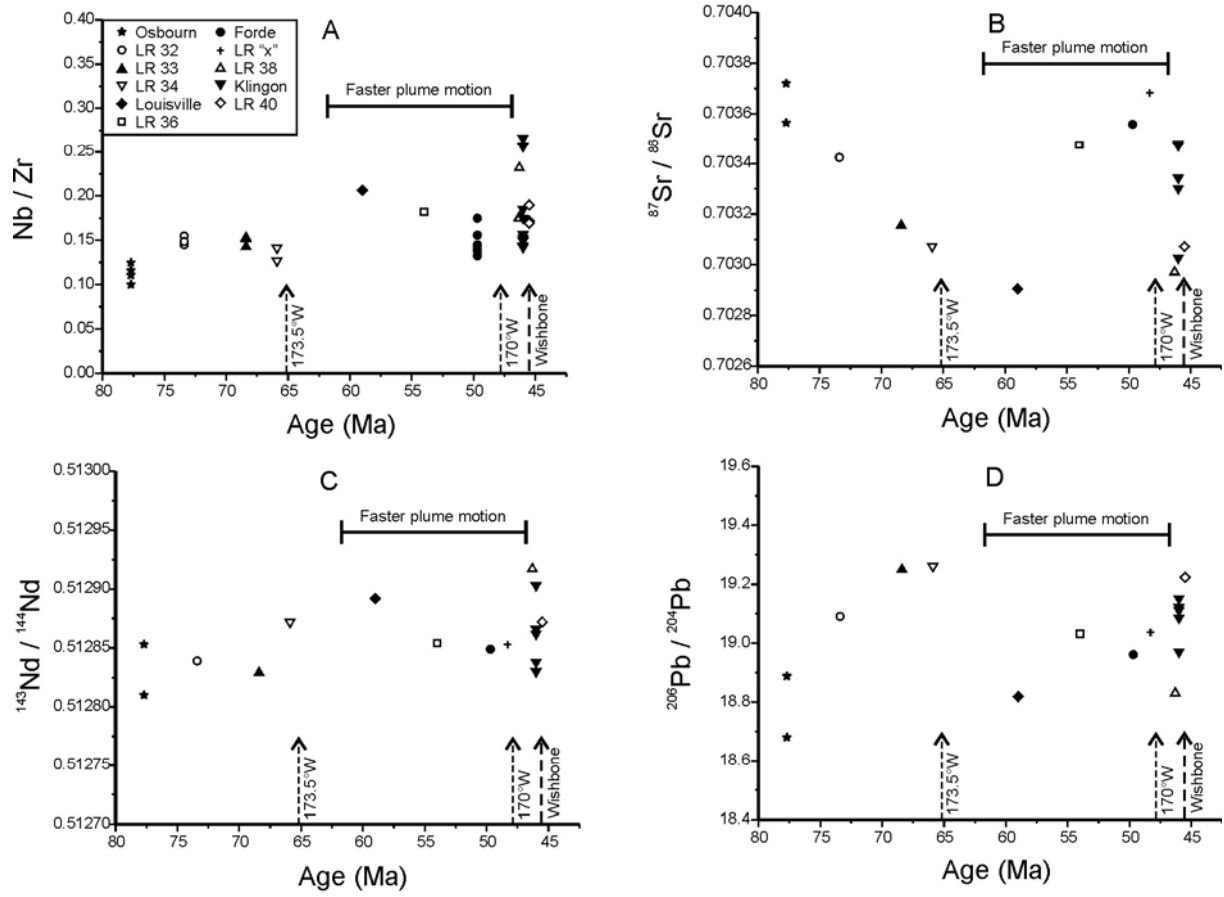


Figure 8

Worthington et al., Louisville Ridge

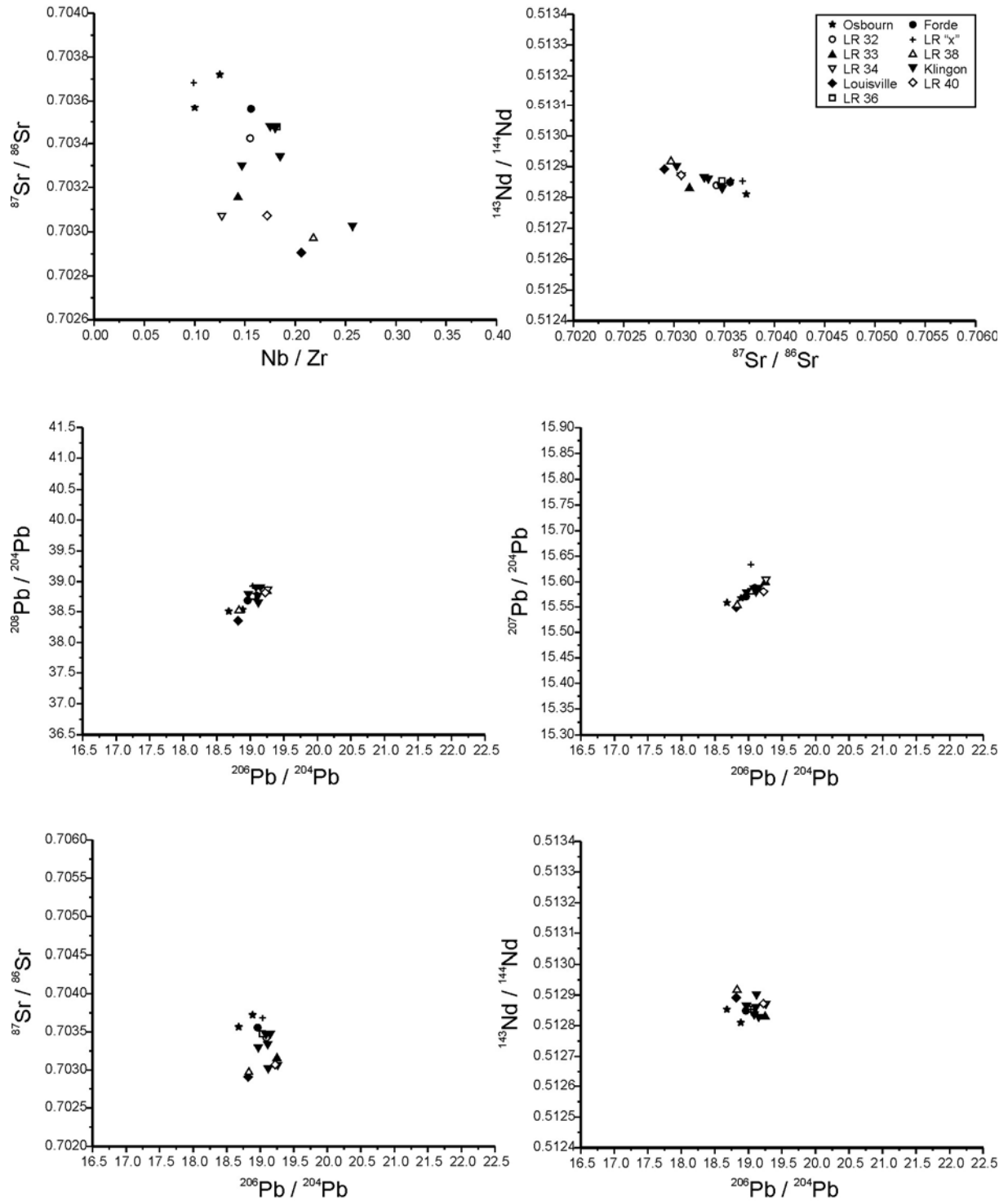


Figure 9

Forschungsfahrt SO-167 LOUISVILLE: Erste Ergebnisse

Stoffers, P.¹, Worthington, T.J.¹ and Shipboard Scientific Party

¹ Institut für Geowissenschaften, Christian-Albrechts-Universität zu Kiel, Olshausenstr. 40, 24118 Kiel

Mit der Forschungsfahrt Louisville sollte herausgefunden werden, inwieweit die Subduktion des Louisville Rückens (eine Kette von alten *hot spot* Vulkanen) und der Osbourn Trough (eine alte Spreizungszone) einen Einfluß haben auf die Häufigkeit der vulkanischen Eruptionen, auf die vulkanischen *Hazards* und auf die Zusammensetzung der Gesteine des Tonga Inselbogens.

Im Bereich des Tonga-Inselbogens wurden mit Hilfe der SIMRAD-Kartierung mehr als 20 bisher unbekannte große untermeerische Vulkane von mehr als 15 km Durchmesser und über 1000 m Höhe entdeckt und mit Dredgen beprobt. Die Palette der Vulkane reicht von jungen, aktiven Vulkankegeln mit deutlich ausgeprägten Kratern, über große, abgesunkene und durch Wellentätigkeit eingeebnete Vulkane, sog. Guyots, zu Vulkanen mit ausgedehnten Calderen und Vulkanen mit spektakulären Explosionskratern. Einer dieser Krater hat ein Durchmesser von 1.8 km und ist mehr als 1 km tief. Einige dieser Vulkane sind immer noch hydrothermal aktiv, d.h. heiße Lösungen treten aus und führen zu Vererzungen der Gesteine. Die Vulkane mit den tiefsten Kratern befinden sich im Gebiet des südlichen Tonga Inselbogens in einem Bereich, in dem sowohl die submarinen Vulkane der Louisville Kette als auch die fossile Osbourn Spreizungszone subduziert werden, was offenbar aufgrund des höheren Wassergehaltes der Gesteine zu einer intensiveren und stärker explosiven vulkanischen Aktivität führt. Die beprobten Gesteine reichen von Basalt bis Dazit und dazitischem Bims. Interessant ist das Vorkommen von Hornblende-Daziten, die einen höheren Volatilen- und Kaliumanteil anzeigen und womöglich mit einem stärkeren Sedimenteintrag durch die Subduktion des Osbourn Troughs erklärt werden können.

Ein weiteres Ziel der Forschungskampagne war der Osbourn Trough, eine erst kürzlich entdeckte 900 km lange Ost-West verlaufende Struktur auf der Pazifischen Platte bei rund 25°30 Süd. Über seine Entstehung und sein Alter gibt es sehr unterschiedliche Vorstellungen, die von fossiler Spreizungszone, rezenter Bruchspalte bis *fracture zone* reichen. Die Antwort auf diese Frage ist von großer Bedeutung für die Entwicklung des Südpazifiks. Außer drei geophysikalischen Traversen liegen bisher keine Daten aus diesem Gebiet vor. Ein Bereich von 100 x 150 km wurde detailliert mit SIMRAD kartiert. Unsere Daten zeigen jetzt ganz eindeutig, daß es sich bei dem Osbourn Trough um eine fossile Spreizungszone mit langsamer Spreizungsrate handelt. Der Osbourn Trough ist ein alter axialer Graben mit Tiefen zwischen 5500–6000 m und steilen Rändern, die bis zu 1200 m über den Meeresboden aufragen. Drei deutliche lineare Segmente konnten erkannt werden, wobei das mittlere Segment vollständig kartiert wurde. Diese Segmente sind durch senkrecht zum Trough verlaufende *transform faults* um 20–40 km versetzt. Das Ende der einzelnen Segmente ist durch eine morphologische Aufwölbung charakterisiert, was von uns als *inner corner high* interpretiert wird. Der Trough wird flankiert von einer Reihen paralleler Rücken, die mit zunehmender Entfernung von der Achse flacher werden und wahrscheinlich ältere Grabenränder (*rifted margins*) darstellen. Morphologie, Struktur und Größe des Osbourn Trough sind vergleichbar mit den langsam spreizenden Segmenten des Mittelatlantischen Rückens. Die meisten Dredgen wurden an den Flanken der *inner corner high* gezogen und enthielten aphyrische Olivin- und Plagioklas-Basalte zusammen mit Doleriten und Olivin-Gabbros. Der Olivin ist häufig ersetzt durch Iddingsit. Die Gesteine waren meist mit einer bis zu 80 mm mächtigen Mangankruste bedeckt.

Während der letzten Phase der Kampagne wurde eine Beprobung des Louisville Rückens durchgeführt. Alle untersuchten Vulkane sind Guyots. Der Gipfelbereich liegt bei den nördlicheren Vulkanen in rund 1500 m, im Süden bei etwa 800 m Wassertiefe. Kollapsstrukturen im Bereich der mittleren und oberen Flanken wurden erfolgreich beprobt. Die Gesteine bestehen meist aus aphyrischem Basalt und porphyrischem Olivinbasalt, wobei die Olivine meist durch Iddingsit ersetzt sind. Frische Olivine wurden trotz des vermuteten tertiären Alters in einigen Proben gefunden. Viele Gesteine sind sehr vesikulär. Von besonderem Interesse für uns war der Bereich des Louisville Rückens, in dem es zu einer Richtungsänderung des Rückens gekommen ist. Die beiden *seamounts*, die in diesem Knickbereich liegen, wurden vollständig kartiert. Im Gegensatz zu bisherigen Vorstellungen können wir jetzt zeigen, daß diese beiden *seamounts* durch einen schmalen ebenen Rücken miteinander verbunden sind, der ebenfalls oberhalb des Meeresspiegels entstanden ist. Diese für den Louisville Rücken ungewöhnliche Struktur scheint eine Änderung in Geschwindigkeit und Richtung der Pazifischen Platte vor rund 43-50 Millionen Jahren widerzuspiegeln, die für den Knick im Verlauf des Rückens verantwortlich ist. Mit Hilfe der gewonnenen Gesteine sollte es jetzt möglich sein, Alter und Zusammensetzung dieser kritischen Knickregion zu bestimmen.

Mineralisationsprozesse und ihre zeitliche Variabilität im Bereich des Tonga Inselbogens und des südlichen Lau Beckens: Erste Ergebnisse der Forschungsfahrt SO-167 LOUISVILLE

U. Schwarz-Schampera¹, P. Stoffers², R. Hekinian³, H. Gibson⁴, P. Herzig¹
Th. Kuhn¹, S. Fretzdorff^{1,2}, A. Kindermann¹, K. Schreiber¹

¹TU Bergakademie Freiberg, ²C.-A. Universität Kiel, ³Ifremer Brest, France, ⁴Laurentian University Sudbury, Canada

Einführung

Die Arbeiten im Bereich des südlichen Lau Back-Arc Beckens (Valu Fa Rücken) und des Tonga Inselbogens hatten die Untersuchung hydrothermalen Prozesse und ihrer zeitlichen Variabilität zum Ziel. Das Lau Becken gilt als rezentes Analogon für zahlreiche fossile Massivsulfid (VMS) -Lagerstättendistrikte. Die Kenntnis der Hydrothermalsysteme am Valu Fa Rücken aus früheren Forschungskampagnen (SO-35, SO-48, SO-67, NAUTILAU) und die daraus resultierenden Ergebnisse lassen auf eine enge Wechselwirkung mit zeitlich schnell aufeinander folgenden, magmatischen Ereignissen entlang struktureller Schwächezonen der nach Süden propagierenden Rückensegmente schließen. Anhaltender Wärmefluss und fortwährende magmatische Aktivität sind kritisch für die Entwicklung eines zeitlich stabilen Hydrothermalismus und gestatten die Anreicherung und Erhaltung hydrothermalen Präzipitate durch temporäre Bedeckung. Hohe Spreizungsraten und intensive Gesteinsdifferentiation wie im südlichen Lau Becken fördern möglicherweise die Freisetzung magmatischer Volatiler und deren Anreicherung in hydrothermalen Präzipitaten, wirken der Entwicklung einer langlebigen, stabilen hydrothermalen Konvektion und damit der Bildung großer Massivsulfidvorkommen jedoch entgegen. Die Untersuchung der zeitlichen Zusammenhänge magmatischer und hydrothermalen Prozesse am Beispiel des südlichen Lau Beckens besitzt daher eine große Bedeutung im Verständnis vergleichbarer fossiler Milieus seit dem Archaikum.

Die Arbeiten im Tonga Inselbogen schließen sich denen im weiter südlich gelegenen Kermadec Inselbogen (SO-135) an und hatten die Untersuchung des Potentials für aktiven, flachmarinen Hydrothermalismus in diesem Bereich zum Ziel. Wie sich am Kermadec Inselbogen gezeigt hat, besitzen die Mineralisationen (Clark und Brothers Seamount, Whakatane Graben) viele Charakteristika landgebundener epithermaler Goldlagerstätten; deutliche Unterschiede zwischen den Vorkommen in den Metallgehalten sowie im Sulfidierungs- und Alterationsgrad deuten jedoch auf Variationen während der Fluidentwicklung und Mineralisation hin. Die Nähe von Tonga Inselbogen und Lau Back-Arc (≤ 40 km) und der Nachweis magmatischer Volatiler auch in den Präzipitaten am Valu Fa Rücken lässt auf magmatisch-dominierte Hydrothermalsysteme in diesem Abschnitt der Tonga Subduktionszone schließen, deren Ursprung, Signatur und zeitliche Entwicklung Gegenstand des laufenden Projektes sind.

Südliches Lau Becken

Der aktive Valu Fa Rücken im südlichen Lau Back-Arc Becken ist durch das überaus häufige Auftreten junger, hochdifferenzierter vulkanischer Gläser charakterisiert, Beleg für eine intensive rezente magmatische Aktivität des Spreizungszentrums. Das Ziel der Identifikation propagierender Riftsegmente und potentieller neotektonischer und -vulkanischer Strukturen im zentralen und südlichen Teil des Valu Fa Rückens konnte mit einer detaillierten bathymetrischen Kartierung (SIMRAD) erreicht werden (Abb. 1A). Die ausgezeichnete Qualität der Daten erlaubt die Interpretation struktureller Schwächezonen am zentralen und südlichen Valu Fa Rücken und im Übergang zum Havre Trough zwischen 22°45'S und 23°00'S und damit der Lokationen zukünftiger seismischer, magmatischer und hydrothermalen Aktivität. Die Untersuchung des Vai Lili Hydrothermalfeldes ergab einen

signifikanten Wechsel in der Art der hydrothermalen Aktivität seit 1989. Das Feld ist derzeit durch weit verbreitete diffuse Fluidaustritte und niedrigtemperierte Präzipitate charakterisiert, die 1989 detailliert dokumentierten, aktiven Chimneys wurden auch bei mehreren OFOS- und TV-Greifer-Traversen über das Hydrothermalfeld nicht lokalisiert. Vielmehr deutet das Auftreten bisher nicht dokumentierter, unalterierter autobrekzierter Laven eine mögliche Bedeckung von Teilen des Vai Lili-Feldes und Beeinflussung der hydrothermalen Aktivität durch rezente magmatische Prozesse an. Das Auftreten von Xenolithen einer hydrothermal alterierten Stockwerkmineralisation in unalterierten Gesteinsgläsern belegt die Beeinträchtigung kontinuierlicher hydrothermalen Prozesse durch wiederkehrenden Vulkanismus im Vai Lili-Feld, wie es charakteristisch für landgebundene VMS-Lagerstätten ist. Eine partielle Überdeckung des Feldes findet in dem Auftreten abgestorbener bzw. junger Hydrothermalfauna auf diesen Gesteinsgläsern seine Bestätigung. Das südlich gelegene Hine Hina-Feld besitzt eine weitaus größere Ausdehnung als bisher bekannt und zeigt gegenüber seiner Ausbildung in 1989 keine signifikanten Änderungen. Aktiver Hydrothermalismus ist vor allem durch diffuse Lösungsaustritte charakterisiert. Inaktive Chimneys treten vereinzelt im Bereich hydrothermalen Inkrustationen (Fe- und Mn-Oxyhydroxide) auf. Signifikanterweise liegen diese Krusten vulkanischen Aschen auf, die keinerlei Hinweise auf hydrothermale Alteration liefern. Hine Hina ist an einen subrezent aktiven, andesitischen Aschenkegel gebunden, dessen Bildung wahrscheinlich auf explosiver Aktivität beruht.

Vergleichbare geologische Verhältnisse bestehen im südlichsten Teil des Valu Fa Rückens bei 22°41'S, etwa 20 km südlich des Hine Hina Feldes. Der südliche Bereich dieses Rückenabschnitts ist durch ausgedehnte hydrothermale Inkrustationen (Fe- und Mn-Oxyhydroxide) charakterisiert, die sich aufgrund diffuser, niedrigtemperierter Aktivität im Bereich weitgehend unalterierter pyroklastischer Aschen gebildet haben. Fehlende Hinweise auf rezent austretende hydrothermale Fluide sind Beleg dafür, dass dieser Rückabschnitt zur Zeit inaktiv ist. Ein weiteres südwärts propagierendes Riftsegment des zentralen Valu Fa Rückens bei 22°26'S ist durch konjugierte offene Störungssysteme charakterisiert, während neovulkanische Strukturen, rezenter Vulkanismus und Indizien für aktiven Hydrothermalismus fehlen.

Die auf der SIMRAD-Kartierung basierende Interpretation des sich südlich an den Valu Fa Rücken anschließenden, aktiven propagierenden Riftbereiches konnte durch einen OFOS-Einsatz bei 22°51.5'S bestätigt werden. Neotektonische und neovulkanische Strukturen belegen rezente Riftprozesse. Die Beprobung dieser Zone erbrachte einen jungen, aphyrischen, andesitisch-dazitischen Vulkanismus im Bereich einer aktiven Störungszone, der sich lithologisch deutlich von der umgebenden 'alten' Inselbogenkruste unterscheidet. Die kartierten Strukturen besitzen eine ausgeprägte *en echelon* Orientierung, die weitgehend derjenigen des Valu Fa Rückens folgt und eine Vorhersage zukünftiger tektonischer und magmatischer Aktivität weniger als 40 km westlich des Tonga Inselbogens sowie im Übergang zum südlich anschließenden Havre Trough ermöglicht.

Tonga Inselbogen

Detaillierte Arbeiten an 19 Vulkanbauten des Tonga Inselbogens erbrachten Mineralisationen an vier andesitischen Vulkanen (Nr. 1, 14, 18, 19). Etwa 37 Kilometer westlich Tongatapu ergaben die Arbeiten rezente vulkanische und hydrothermale Aktivität an einem ca. 5 x 7 km grossen Vulkanbau (Abb. 1B). Der Vulkan weist eine etwa 3 x 5 km große, zentrale Caldera-Struktur mit neovulkanischen Aschekegeln im westlichen und südlichen Teil auf, die bis in eine Wassertiefe von etwa 90 m reichen. Die Beprobung des Kegels zwischen etwa 470 und 200 m Wassertiefe sowie der nördlichen und südlichen Caldera-Ränder (700-280 m) erbrachte neben unmineralisierten, basaltisch-andesitischen vulkanoklastischen Brekzien eine signifikante Sulfid-Mineralisation, die eindeutige Rückschlüsse auf aktiven und ausgedehnten Hydrothermalismus erlauben. Die Vererzung besteht in einer intensiven Pyrit-Mineralisation mit einem disseminierten Auftreten von Chalkopyrit und möglicherweise Tennantit und Arsenopyrit sowie Realgar. Die Sulfide sind sehr feinkörnig und treten vor

allem im Porenraum der Aschenfragmente, aber auch in enger Verwachsung mit amorpher Kieselsäure in der Matrix auf und zeigen keinerlei Anzeichen von Oxidation. Kennzeichnend sind darüber hinaus eine durchgreifende Silifizierung (inklusive 'vuggy quartz') und argillitische Tonmineral-Alteration. Die Mineralisation besitzt damit charakteristische Kennzeichen landgebundener Epithermalvorkommen, die indikativ für eine typische Goldmineralisation in diesen Systemen sind. Hydrothermale Vererzungen mit einer vergleichbaren intensiven disseminierten Pyrit-Mineralisation und argillitischer Alteration wurden darüber hinaus etwa 200 km weiter südlich an einem andesitischen Aschekegel innerhalb einer zentralen Caldera des Vulkans Nr. 19 (ca. 8 x 10 km) in 600 bis 470 m Wassertiefe beprobt. Weitere Proben hydrothormaler Mineralisationen konnten an der oberen Nordflanke des Vulkans Nr. 18, der durch einen zentralen Krater von mehreren Kilometern Durchmesser und einer Tiefe von etwa 1 km charakterisiert ist, sowie von der Caldera-Wand des Vulkans Nr. 14 geborgen werden. Diese Mineralisationen ähneln sehr stark subaerischen Epithermalvererzungen und repräsentieren mineralisierende Prozesse vor der jüngsten pyroklastischen Aktivität. Die Vererzungen sind an stark alterierte, zum Teil brekziierte Andesite und dazitische Vulkanoklastite gebunden und manifestieren sich in einer durchgreifenden Silifizierung, Chloritisierung und disseminierten Pyritvererzung vor allem in Bimsfragmenten.

Ergebnisse

Die Ergebnisse während SO-167 haben gezeigt, dass die magmatische Aktivität entlang des schnell spreizenden und nach Süden propagierenden Valu Fa Rückens mit einer großen Variabilität hydrothormaler Prozesse verbunden ist. Auflebender Vulkanismus im Bereich des überlappenden Spreizungszentrums am zentralen Rückenabschnitt hat zur Bedeckung großer Teile des Vai Lili Hydrothermalfeldes und zum Erliegen der Hochtemperaturaktivität geführt. Niedrigtemperierte diffuse Fluidaustritte zeugen von anhaltender Aktivität und der Möglichkeit intensiver Sulfidpräzipitation unterhalb des Meeresbodens. Das Vai Lili Feld befindet sich damit in einem Stadium, das dem des Hine Hina Feldes vergleichbar ist. Das Auftreten eines weiteren, derzeit inaktiven Feldes zeigt, dass die hydrothermale Aktivität am Valu Fa Rücken in Abhängigkeit von vulkanischen Prozessen schnellen Veränderungen unterworfen ist, die Entwicklung eines (temporären) Hydrothermalismus aber gleichzeitig durch tektonische und magmatische Aktivität begünstigt wird. Diese Zusammenhänge erlauben Rückschlüsse für viele fossile Massivsulfid-Lagerstättendistrikte und deren zukünftige Exploration.

Neben den während SO-135 HAVRE TROUGH entdeckten und beprobten flachmarinen Hydrothermalvorkommen im südlich gelegenen Kermadec Inselbogen (Brothers and Clark Seamounts, Whakatane Graben) gelang während SO-167 der erste Nachweis einer ausgedehnten rezenter hydrothormalen Aktivität auch im Tonga Inselbogen. Die Alteration und Mineralisation sind charakteristisch für landgebundene Epithermalvorkommen und belegen das überaus große Potenzial flachmariner Inselbogen-Vulkane für assoziierte Goldmineralisationen. Darüber hinaus definieren sie den Tonga-Kermadec Inselbogen als ein beispielhaftes Arbeitsgebiet für zukünftige metallogenetische Untersuchungen. Die während SO-167 gewonnenen Daten werden in den Datensatz vorheriger 'Sonne'-Kampagnen integriert und bilden die Grundlage für eine rechnergestützte 3D-Modellierung, die für das derzeitige RIDGE 2000 Programm (Lau Basin Integrated Study Site) von zentralem Interesse sein wird.

Danksagung

Dieses Projekt wird durch Mittel des Bundesministeriums für Bildung und Forschung gefördert (Förderkennzeichen 03G0167B).

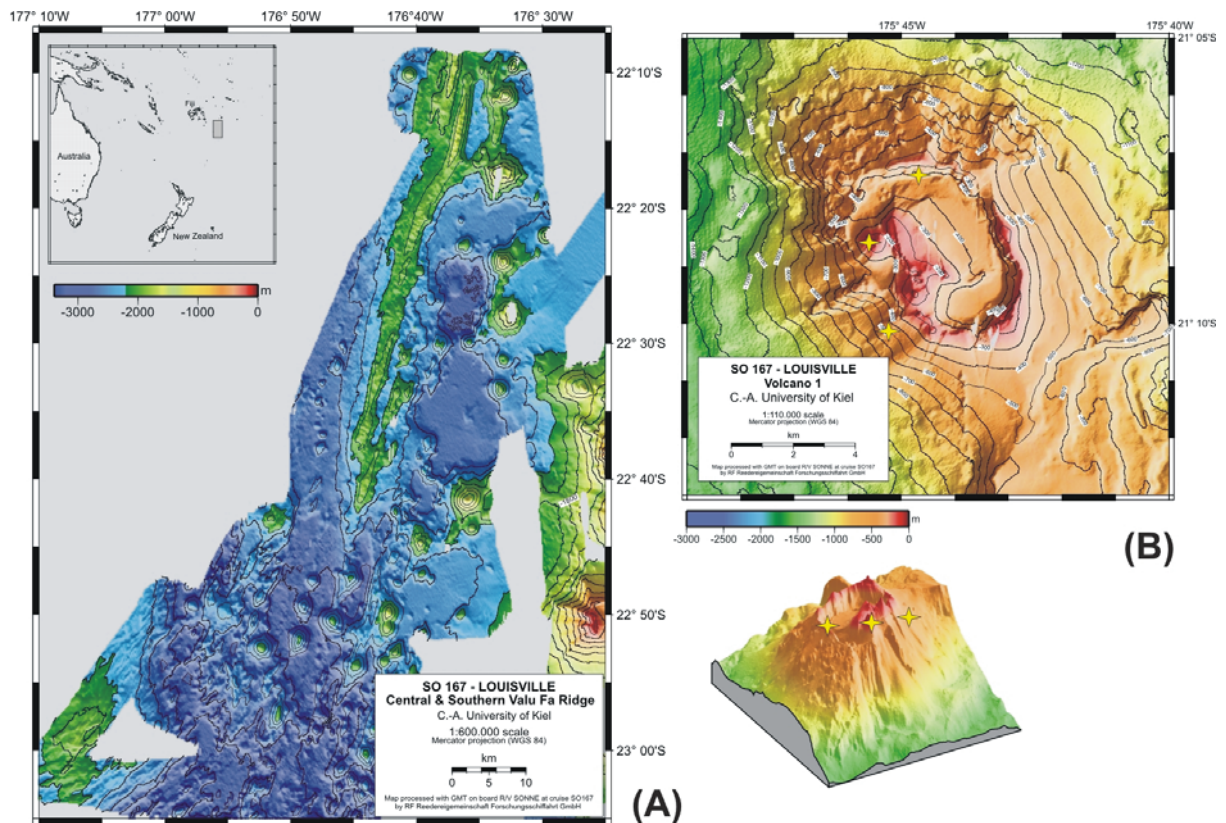


Abb. 1: (A) Bathymetrische Karte des Valu Fa Spreizungsrückens und der südwärts propagierenden Störungszone südlich 22°45'S, Lau Becken, SW-Pazifik. (B) Bathymetrische Karte und 3D-Modell des Vulkans Nr. 1 des Tonga Inselbogens. Die Sterne markieren die Lokationen hydrothermaler Aktivität am zentralen Aschenkegel sowie den äusseren südlichen und inneren nördlichen Calderawänden.

Magmatically induced hydrothermal processes and their temporal variability in the southern Lau basin and the nearby Tonga island arc, SW-Pacific

Ulrich Schwarz-Schampera, Harold Gibson, Peter Herzig, Peter Stoffers

R/V SONNE cruise SO-167 investigated the southern Tonga-Lau arc-back-arc complex for petrogenic, volcanologic, and hydrothermal purposes. The Tonga trench is a type example of an immature, intra-oceanic, convergent margin where Pacific plate lithosphere is subducted beneath a volcanic island arc chain. The Lau back-arc basin opened by the successive southward propagation of discrete seafloor spreading centers. The site of active rifting, the Valu Fa ridge, was identified as a site of intense tectonic, magmatic, and hydrothermal activity that also makes it a type example of rift-related volcanism, and associated hydrothermal processes. The back-arc ridge segments display active and fast southward propagation that resulted in rapid structural, volcanic, and hydrothermal evolution. The style of magmatism likely influenced the onset, type and longevity of hydrothermal activity. Elevated magma supply rates arrested hydrothermal activity and discharge during periods of volcanic eruption. Hydrothermal discharge at the Vai Lili vent field was affected by the eruption of andesitic lobate and aa-type flows suggesting the possibility of stratigraphically stacked mineralization beneath the present field. Hydrothermal activity at the Hine Hina field spanned the waning period of basaltic fissure eruptions and continued after fire-fountain eruptions that blanketed the ridge with deposits of volcanic tephra and bombs. Stable conditions at ridge segments, underlain by a high-level magma chamber, favour the onset and the development of sustainable hydrothermal convection cells, allowing for longer lived, and higher temperature discharge. Southward rift propagation is associated with a volcanically active fault zone that follows the regional left-stepping orientation of the ridge. The combination of tectonic and volcanic activity, however, is not preceded, or immediately associated, with hydrothermal activity. It is concluded that fairly fast spreading rates at the propagating rifts of single ridge segments are not associated with significant magmatic degassing or the development of a hydrothermal system.

In the southern Tonga island arc, more than 22 submarine stratovolcanoes that delineate the volcanic front, were surveyed for their hydrothermal activity. Four sites of transitional and epithermal-style shallow (< 700 m) submarine hydrothermal systems were discovered within calderas, either at the caldera walls or within intra-caldera scoria cones. The high sulfidation style of mineralization, its mineralogy, attendant argillic alteration and textural characteristics are similar to subaerial, epithermal-style, high-sulfidation Au deposits, and those reported from shallow submarine hydrothermal vent fields such as the Kermadec and Izu-Bonin arcs. The discoveries attest to a real potential for epithermal-style Au mineralization in the Tonga arc.

Auriferous pyrite mineralization in the Tonga island arc, SW-Pacific: first evidence for shallow submarine hydrothermal activity.

U. Schwarz-Schampera & P.M. Herzig

Institute of Mineralogy, Freiberg University of Mining and Technology, Germany

H. Gibson

Laurentian University, Sudbury, Canada

P. Stoffers

Institute of Geosciences, C.-A. University Kiel, Germany

Keywords: hydrothermal venting, shallow submarine, auriferous mineralization, Tonga-Kermadec island arc

ABSTRACT: The first occurrences of hydrothermal activity along the volcanic front of the Tonga island arc, SW-Pacific, were discovered during cruise SO-167 with R/V Sonne. The hydrothermal systems are associated with active and recently active andesitic and dacitic arc volcanoes. Active venting in water depths between 700 and 200 m meets the constraints for shallow submarine hydrothermal systems that are characterized by low base metal, but elevated precious metal contents. Mineralization at the Efuefu and Uli'uli sites is characterized by pervasive disseminated pyrite, marcasite and pyrite-magnetite intergrowths and variable amounts of chalcopyrite, arsenopyrite, realgar, orpiment, stibnite. The style of mineralization, its mineralogy and associated advanced argillic alteration, coupled with shallow water depths suggest a potential for auriferous shallow submarine hot springs at the Tonga arc volcanoes. The discoveries contribute to a number of epithermal-style and transitional types of mineralization now being recognized in the Tonga-Kermadec arc system.

1 INTRODUCTION

During cruise SO-167 LOUISVILLE with R/V SONNE, a total of 22 large and several smaller volcanic edifices along the southern Tonga island arc were mapped and sampled for petrogenic, volcanologic, and hydrothermal purposes. Two active (Efuefu, Uli'uli) and two inactive sites of shallow submarine hydrothermal systems were discovered at active or recently active volcanic centers. These are the first occurrences of hydrothermal activity along the volcanic front of the Tonga arc system. The associated mineralization contributes to a growing number of hydrothermal sites in the ~2500 km-long Tonga-Kermadec arc-back-arc system (Fig. 1.; Stoffers et al. 1998, 1999a; Schwarz-Schampera et al. 2001; de Ronde et al. 2001).

2 GEOLOGICAL SETTING

A total of 27 arc volcanoes represent the actual volcanic front of the southern Tonga arc. The basaltic to andesitic and dacitic edifices are often more than 1000 m high and 20 km² wide. Most of them are characterized by well-developed multiple basaltic-andesitic caldera structures while some developed subsequently pumice-dominated craters.

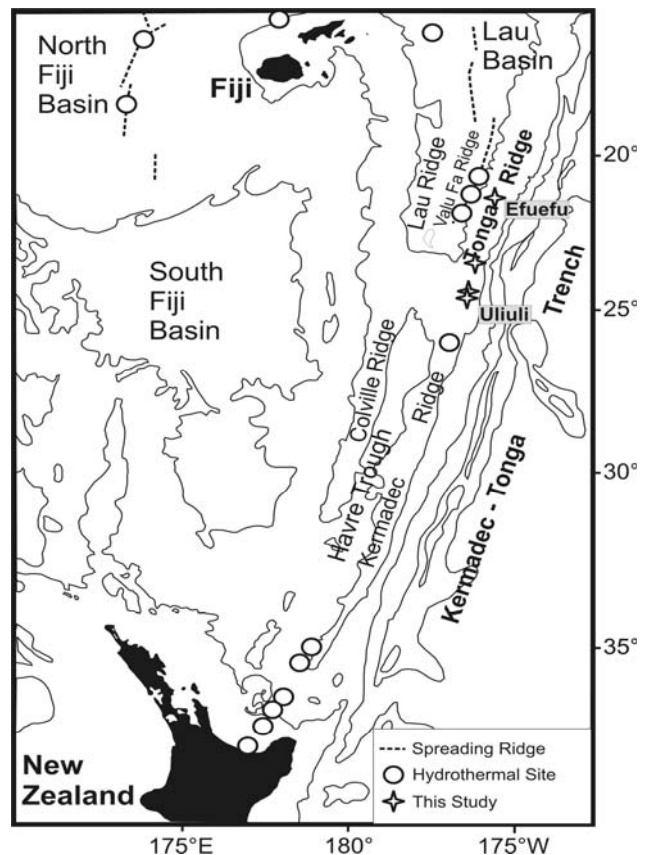


Figure 1. Tectonic setting of the Tonga-Kermadec arc and locations of active hydrothermal vents and known shallow submarine hydrothermal mineralization (circles) as well as the new sites along the southern Tonga ridge (stars).

Hydrothermal activity is closely associated with central to slightly offset (basaltic-) andesitic cinder cones, and prominent caldera and crater walls illustrating the structural control on hydrothermal discharge.

Host rocks are scoriaceous or pumiceous volcanoclastic and plagioclase porphyritic andesitic breccias. Setting, lithologies, volcanic textures, and water depths indicate that very shallow submarine pyroclastic eruptions (water depths of <1000 m up to 200 m) played a significant role in the formation of the arc volcanoes. The neovolcanic cones in water depths between 600 and 90 m are most likely a product of explosive strombolian to surtseyian eruptions.

The most extensive and strongest mineralization is associated with the Efuefu site offcoast Tongatapu. The host volcano (no. 1) is approximately 10 x 6 km in diameter, with a 5 x 3 km central caldera containing two young volcanoclastic cinder cones (Fig. 2).

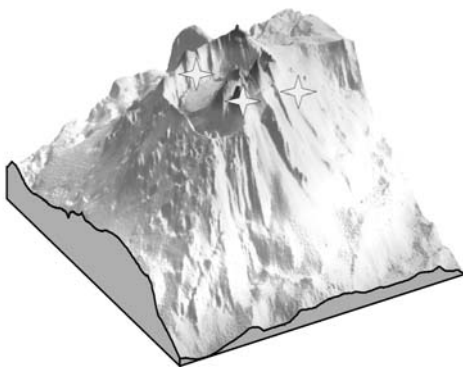
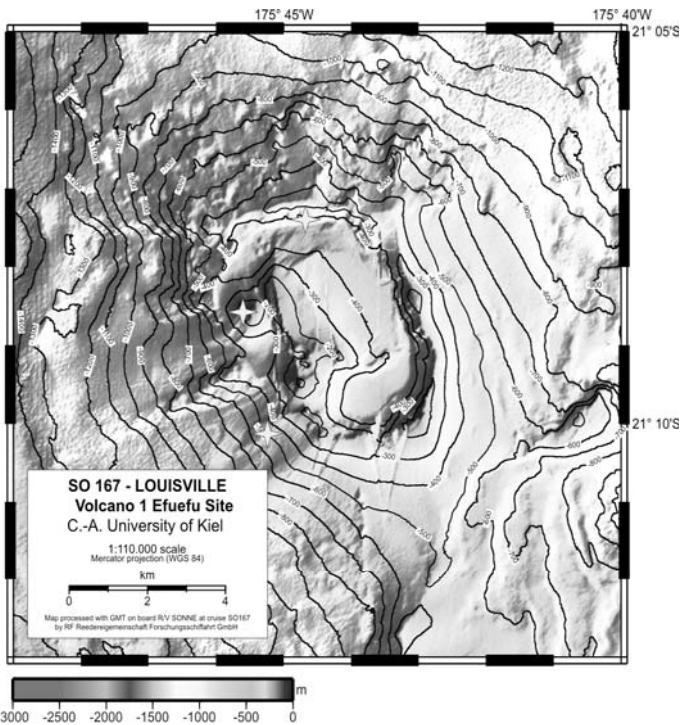


Figure 2. Bathymetry and 3D model of volcano no. 1, southern Tonga island arc, SW-Pacific and locations of the Efuefu hydrothermal sites (stars).

The mineralized cone rises to approximately 90 m below sea level and is localized along a regional, NE-SW trending structure. The widespread distribution of mineralization at the cone as well as at the southwestern and northern caldera walls suggest extensive hydrothermal activity.

The second site of active hydrothermal venting (Uli'uli site) is associated with the southernmost Tonga arc volcano (no. 19). The 13 by 15 km edifice is characterized by a large NW-SE elongated central caldera. Hydrothermal precipitates were collected from the western wall of a cone in the center of the caldera at water depths of 600 to 450 m.

Additional boulders of hydrothermally altered and mineralized andesitic and dacitic volcanoclastic breccias were retrieved from the crater and caldera walls of two other volcanic edifices. Volcano no. 18 exhibits a spectacular central crater two kilometers in diameter, interpreted as a product of major dacitic pyroclastic eruptions. Andesitic volcanoclastic rocks and younger pumiceous dacite are both affected by mineralization suggesting that the hydrothermal system persisted after dacitic eruptions. Volcano no. 14 is a 9 x 6 km edifice with a slightly offset central caldera. Sampling retrieved variably altered and weakly mineralized basaltic to andesitic flows and volcanoclastic rocks.

3 MINERALIZATION AND ALTERATION

Mineralization at all four sites is hosted by scoriaceous volcanoclastic material and consists of fine-grained, pervasive disseminated pyrite, marcasite, pyrite-magnetite intergrowths, and variable amounts of chalcopyrite, arsenopyrite, realgar, orpiment, stibnite (Fig. 3). The mineralization is finely dispersed in the matrix but is best developed where it occurs: 1) coating vesicles within scoriaceous fragments (coatings up to 2 mm thickness), 2) lining fractures and open spaces, and 3) within the matrix between larger fragments. However, a fine pyrite and/or marcasite dusting is also associated with smaller, more compact lithic fragments, interstices, and as a coating of larger scoria fragments. Pyrite and marcasite show the whole range from colloform to euhedral crystals whereas realgar, orpiment, chalcopyrite, and arsenopyrite are usually very fine-grained and euhedral. Magnetite ranges from mm-sized, equigranular crystals to rather platy varieties.

The host rocks suffered from an intense argillic and silica alteration. Similar to mineralization, the alteration assemblage is finely dispersed in the matrix and indurates single fragments as well as the breccia matrix. It results in distinct blue-green to pale grey bleaching of the andesitic volcanoclastics. Alteration mineralogy is dominated by amorphous silica, fine-grained quartz, kaolinite, illite, smectite,

and variable amounts of platy alunite, anhydrite, and native sulfur (Fig. 3).

Preliminary geochemical analyses of bulk rock samples have resulted in moderately elevated Au concentrations and coenrichments in Cu, Bi, As, Sb, Te, Tl. The base metal content is uniformly low.

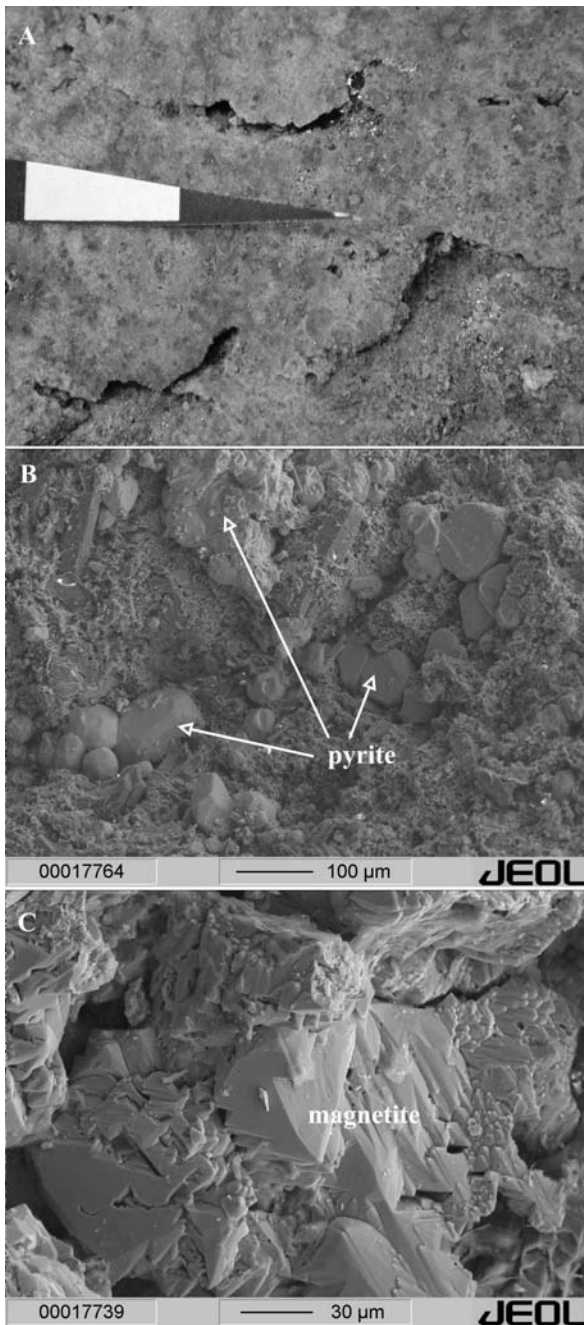


Figure 3. Representative mineralization from the Efuefu site, Tonga arc, SW-Pacific. A) Pyrite-magnetite mineralization in open cavities of highly silicified scoriaceous volcaniclastics (scale: 1 cm); B) Disseminated pyrite mineralization in a fine-grained silica-clay-altered matrix; C) Euhedral magnetite crystal syngenetic with pyrite-chalcopyrite mineralization.

4 DISCUSSION AND CONCLUSIONS

Alteration and mineralization of the four new hydrothermal sites show many characteristics that are typical of shallow submarine hydrothermal vent fields such as in the Kermadec and Izu-Bonin arcs

and the New Ireland fore-arc, but also of subaerial, epithermal-style, high-sulfidation Au deposits (e.g., Herzig et al. 1994, 1999; Hannington et al. 1999; Iizasa et al. 1999; Stoffers et al. 1999b; Glasby et al. 2000; de Ronde et al. 2001; Petersen et al. 2002). Similarities to high sulfidation epithermal-style mineralization are indicated by the occurrence of open spaces related to vuggy silica textures, strong silicification of lithic fragments and matrix, an advanced argillic alteration including the formation of alunite, and disseminated pyrite, chalcopryrite, tennantite, realgar, and orpiment. Mineralization along fractures and open spaces may indicate hydrothermal fracturing due to hydrothermal fluid overpressure (i.e., boiling) and sealing due to the rapid precipitation of pyrite, silica and clay minerals. The intense clay alteration of the scoriaceous ash is likely a product of acid-generating sulfurous gases emanating from the vents. The occurrence of platy alunite in the alteration assemblage and its close intergrowth with pyrite suggest contributions and subsequent disproportionation of magma-derived SO_2 . Close intergrowths of pyrite with magnetite attest to elevated oxygen fugacities in the mineralizing fluids; a possible prerequisite for enhanced Au transportation (Mungall 2002). However, moderate precious metal and low base metal contents are characteristic of settings where the mineralizing fluids have undergone phase separation. If this is the case, significant mineral precipitation in the feeder zones due to boiling processes can be expected.

The recent discoveries in the Tonga-Kermadec arc system contribute to the growing number of epithermal-style mineralization now being recognized in shallow submarine hot springs (Herzig et al. 1994, 1998, 1999; Herzig and Hannington 1995a, b; Hannington et al. 1999; Wright et al. 1998; de Ronde et al. 2001; Petersen et al. 2002). Volcanic arcs represent a potentially extensive source of shallow hydrothermal vent fields and auriferous to Au-rich sulfide precipitates. These discoveries have significant implications for land-based mineral exploration in ancient volcanic belts, which are traditionally targeted for volcanic-hosted massive sulfide deposits but are largely unexplored for epithermal-style gold mineralization.

5 ACKNOWLEDGEMENTS

This work was funded by the German Federal Ministry of Education and Research grants 03G0135D and 03G0167B and supported by the Leibniz Program of the German Research Association.

REFERENCES:

- de Ronde, C., Baker, E.T., Massoth, G.J., Lupton, J.E., Wright, I.C., Feely, R.A., and Greene, R.R. 2001. Intra-oceanic subduction-related hydrothermal venting, Kermadec volcanic arc, New Zealand. *Earth Planetary Science Letters* 193: 359-369.
- Glasby, G. P., Iizasa, K., Yuasa, M., and Usui, A., 2000, Submarine hydrothermal mineralization on the Izu-Bonin Arc, south of Japan: an overview. *Marine Georesources and Geotechnology* 18: 141-176.
- Hannington, M.D., Poulsen, K.H., Thompson, J.F.H., and Sillitoe, R.H. 1999. Volcanogenic gold in the massive sulfide environment. In: Barrie, C.T. and Hannington, M.D. (Eds.): *Volcanic-associated massive sulfide deposits: Processes and examples in modern and ancient settings. Reviews in Economic Geology* 8: 325-356.
- Herzig, P.M., Hannington, M.D., McInnes, B., Stoffers, P., Villinger, H., Seifert, R., Binns, R., Liebe, T., and Scientific Party RV Sonne Cruise SO-94 1994. Submarine volcanism and hydrothermal venting studied in Papua New Guinea. *Eos, Transactions American Geophysical Union*, 75: 513-516.
- Herzig, P. and Hannington, M.D. 1995a. Hydrothermal activity, vent fauna, and submarine gold mineralization at alkaline fore-arc seamounts near Lihir Island, Papua New Guinea. *Proceedings Pacific Rim Congress 1995*, Australasian Institute of Mining and Metallurgy: 279-284.
- Herzig, P. and Hannington, M.D. 1995b. Polymetallic massive sulfides at the modern seafloor - A review. *Ore Geology Reviews* 10: 95-115.
- Herzig, P.M., Hannington, M.D., and Arribas Jr., A. 1998. Sulfur Isotope Composition of Hydrothermal Precipitates from the Lau Back-Arc: Implications for Magmatic Contributions to Seafloor Hydrothermal Systems. *Mineralium Deposita* 33: 226-237.
- Herzig, P.M., Petersen, S. and Hannington, M.D. 1999. Epithermal-type gold mineralization at Conical Seamount: A shallow submarine volcano south of Lihir Island PNG. In: Stanley, C.J., et al., (Eds.): *Mineral Deposits: Processes to Processing*, Proceedings of the Fifth Biennial SGA Meeting and 10th IAGOD, London, England, Balkema, Rotterdam, 527-530.
- Iizasa, K., Fiske, R. S., Ishizuka, O., Yuasa, M., Hashimoto, J., Ishibashi, J., Naka, J., Horii, Y., Fujiwara, Y., Imai, A., and Koyama, S., 1999. A Kuroko-type polymetallic sulfide deposit in a submarine silicic caldera. *Science* 283: 975-977.
- Mungall, J.E. 2002. Roasting the mantle: Slab melting and the genesis of major Au and Au-rich Cu deposits. *Geology* 30: 915-918.
- Petersen, S., Herzig, P.M., Hannington, M.D., Jonasson, I.R., and Arribas, 2002. Submarine vein-type gold mineralization near Lihir island, New Ireland fore-arc, Papua New Guinea. *Economic Geology* 97(8): 1795-1813.
- Schwarz-Schampera, U., Herzig, P.M., Hannington, M.D., and Stoffers, P., 2001. Shallow submarine epithermal-style As-Sb-Hg-Au mineralization in the active Kermadec arc, New Zealand In: Piestrzynski, A. et al., (Eds.): *Mineral Deposits at the Beginning of the 21st century*. Proceedings of the Joint Sixth Biennial SGA-SEG Meeting Krakow, Poland, Balkema, Rotterdam, 333-335.
- Stoffers, P., Wright, I.C., de Ronde, C., Hannington, M.D., Villinger, H., Herzig, P.M., and the Shipboard Scientific Party 1998. Little studied arc-backarc system in the spotlight. *Eos, Transactions* 80/32: 353, 359.
- Stoffers, P., Wright, I.C., de Ronde, C., Hannington, M.D., Herzig, P.M., Villinger, H., and the Shipboard Scientific Party 1999a. Longitudinal transect of the Kermadec - Havre arc - back-arc system: initial results of R/V Sonne Cruise SO-135. *InterRidge News* 8: 45-50.
- Stoffers, P., Hannington, M.D., Wright, I., Herzig, P.M., de Ronde, C., and Shipboard Scientific Party 1999b. Elemental mercury at submarine hydrothermal vents in the Bay of Plenty, Taupo Volcanic Zone, New Zealand. *Geology* 27: 931-934.
- Wright, I.C., de Ronde, C.E.J., Faure, K., and Gamble, J.A. 1998. Discovery of hydrothermal sulfide mineralization from southern Kermadec arc volcanoes (SW Pacific). *Earth and Planetary Science Letters* 164: 335-343.

LOUISVILLE RIDGE AND THE SOUTH TONGA ARC: FIRST RESULTS

Worthington, T.J., Stoffers, P., Timm, C., Zimmerer, M., Garbe-Schönberg, C.-D.

Institut für Geowissenschaften, Universität Kiel, D-24118 Kiel, Germany

(email: tw@gpi.uni-kiel.de)

Subduction of the hotspot-generated Louisville Ridge at the Tonga–Kermadec Trench has long intrigued geologists (Fig. 1). One early notion postulated that the volcanic islands of Tonga and the Kermadec group were separated by a "volcanic gap", where magmatism was switched off due to subduction of the Louisville Ridge (Nur and Ben-Avraham, 1983). Others have suggested a Louisville Ridge-derived component is present in young (<10 ka) lavas from the northernmost two volcanic islands of Tonga (Tafahi and Niuaotupapu), which may have overlain the Louisville Ridge at 3–4 Ma (Turner et al., 1997; Ewart et al., 1998).

Projecting the Louisville Ridge into the subduction system, it should presently be 100 km below the arc at ~22.5°S (near but south of 'Ata Island). This locus moves southwards at ~145 km/Ma. However, reliable past reconstructions are hampered by possible plume–ridge interactions between the Louisville hotspot and the late Cretaceous Osborn Trough paleo-spreading centre. To examine how Louisville subduction affects arc magma genesis, we mapped and sampled the south Tonga arc between Hunga and Monowai in late 2002 (SO 167 cruise; FS *SONNE*). Further constraints on possible end-members and the evolution of this system were established by mapping and sampling of Louisville Ridge and Osborn Trough.

Southwards from Hunga, the 10–15 km-wide volcanic front of the south Tonga arc consists of 27 semi-regularly spaced large submarine stratovolcanoes.

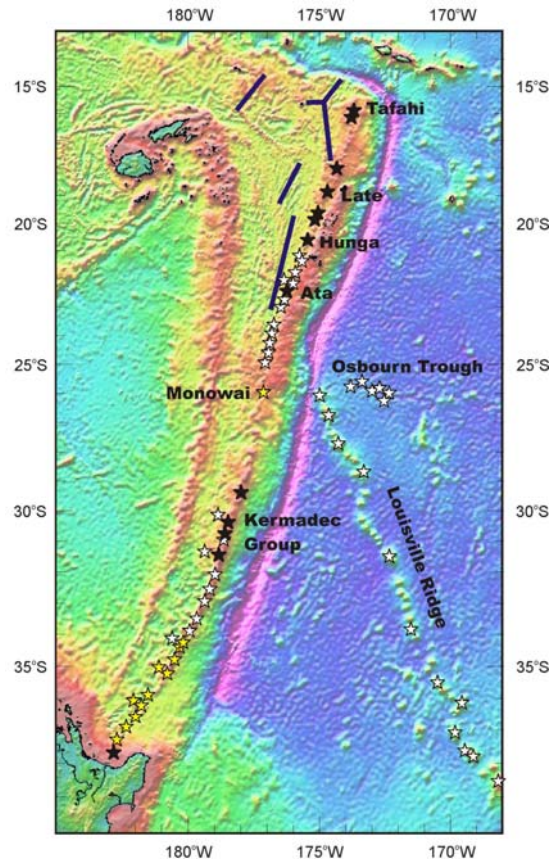


Fig. 1: Major features of the Tonga-Kermadec subduction system

- ★ Subaerial volcanoes
- ☆ Submarine, sampled during the 1990s
- ☆ Submarine, sampled 2002-2003

Each has a basal diameter of 10–25 km and rises 1–2 km from the surrounding seafloor. Evidence of recent volcanism abounds at most (e.g. fresh lavas, well-preserved sediment-free craters, steep slump-free calderas, ongoing hydrothermal activity). Volcano summits north of 23°05'S are often <200 mbsl, whereas the summits of those further south are somewhat deeper (most >400 mbsl). Apart from a 50 km-long stretch devoid of major edifices between 23°05' and 23°30'S, the volcanic front is essentially continuous.

A striking change in character of the volcanic front affects the 'Ata region from 21°56' to 22°30'S, where 10 major volcanoes and numerous smaller volcanic features extend the width of the front to ~40 km (Fig. 2). The oldest volcanoes are two large stratocones that plot along a southward projection of the volcanic front (5A, 6A). Both feature wave-cut thickly sedimented summits at 150 mbsl with much slumping, erosion and faulting of their flanks. Further west is a parallel chain of three inactive, eroded and/or sedimented, stratocones (5B, 5C and 'Ata). 'Ata Island consists of remnant lavas/volcaniclastics buttressed by three coastal plug-dyke complexes and surrounded by a wave-cut platform at 150 mbsl. The dissected southern flanks of the 5D stratocone suggest a comparable age. Westward migration of volcanism terminated at a morphologically complex ridge capped predominantly by weathered lavas (4C). More recently, volcanism has migrated back to the east. Moderately to weakly weathered lavas outcrop on the little dissected 4A stratocone and in its well preserved crater. Fresh lavas cover much of the youthful, active, 4B and 5E stratocones.

The field evidence indicates: (i) westward migration of the volcanic front, (ii) possible stabilisation of the front 40 km west of its initial position, and (iii) recent eastward migration of the front towards its initial position. The westward migration was accompanied by a decrease in lava production, and the more recent eastward migration by an increase in lava production. The wave-cut broad summits, degree of erosion and sedimentation on stratocones 5A and 6A are consistent with the westward migration commencing either prior to 180 ka or early in the interval 140–180 ka (last long-lived sea-level low-stand).

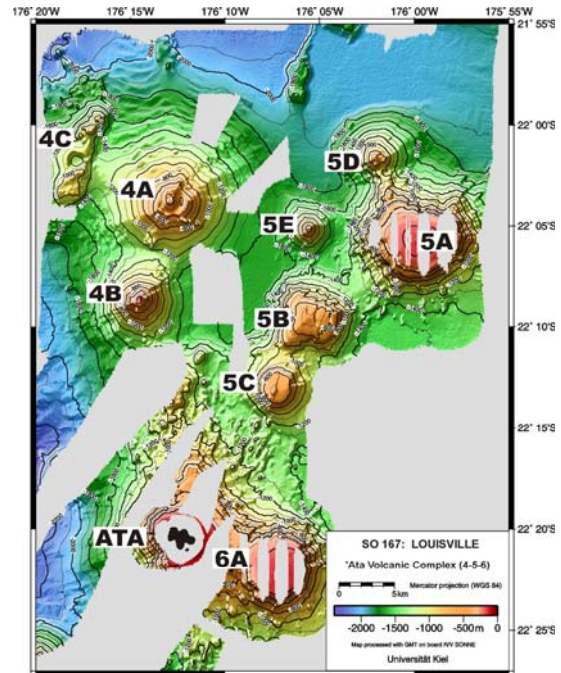


Fig. 2: Bathymetry of the Ata Region

Lavas from the central–south Tonga arc range from high-Mg basalt to rhyolite, and can be classified as a low-K series. Mafic and felsic lavas were recovered from about half of the stratovolcanoes, with the remainder being unimodal. Samples from the 'Ata region are unremarkable in this regard, but have a higher prevalence of mafic lavas. However, whereas lavas from other central–south Tonga arc volcanoes are characterised by chondrite-normalised REE patterns that are either flat or weakly LREE-depleted with $(La/Yb)_N < 1.1$, those from four volcanoes in the 'Ata region have $(La/Yb)_N > 1.1$ (4C, 5D, 6A, 'Ata; Fig. 3). This anomaly is most marked for lavas from 6A, where $(La/Yb)_N \sim 2.4$. These same four volcanoes are also characterised by higher Th/U (>2.25) and more subtle anomalies in other trace element ratios (e.g. Ba/Th). Isotope analyses are in progress, but the few literature analyses of 'Ata Island lavas have $^{143}Nd/^{144}Nd$ and $^{206}Pb/^{204}Pb$ values that overlap the high end of the central Tonga array with no offset in $^{87}Sr/^{86}Sr$.

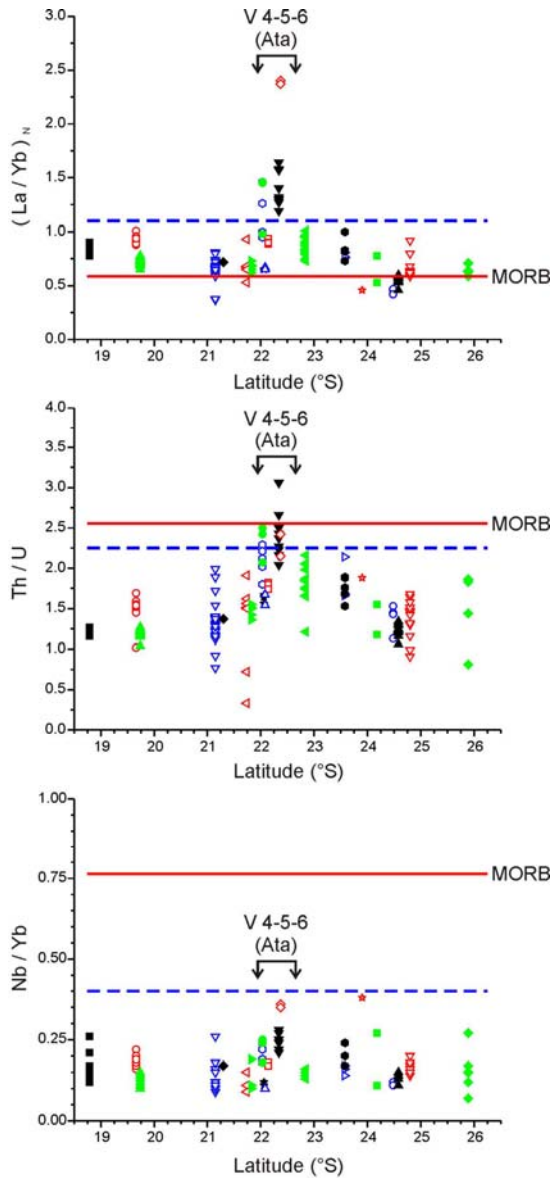


Fig. 3: Plots of $(La/Yb)_N$, Th/U and Nb/Yb vs latitude for the central - south Tonga arc volcanoes (Late - Monowai; Uni Kiel analyses only). Red line = MORB, blue line = arbitrary.

We attribute the complex migration, waning and waxing, and anomalous trace element geochemistry of 'Ata region volcanism to passage of the Louisville Ridge through the sub-arc magma generation zone. No other part of the 800 km-long central-south Tonga arc displays comparable features. Therefore, although alternate models invoking a local mantle anomaly beneath 'Ata are possible, these carry the corollary that either the Louisville Ridge was never subducted north of

26°S or it has no effect on magma generation. Louisville seamounts consist of stacked weathered pillow lavas, hyaloclastite and breccia, and represent significant water reservoirs on the slab. We concur with Nur and Ben-Avraham (1983) that subduction of this relatively hydrous and low density pile will tend to flatten the subducting slab, resulting in the observed temporary westward migration of magmatism and decline in volcanism until new magma conduits are established through the crust.

Why does Louisville Ridge subduction generate high $(La/Yb)_N$ in the arc lavas? Central-south Tonga arc lavas (excluding the 'Ata region) have $(La/Yb)_N < 1.1$ and are strongly depleted in the HFSE and REE relative to MORB (e.g. Nb/Yb ~ 0.20, Yb ~10 x chondrite). In contrast, Louisville lavas are LREE-enriched with $(La/Yb)_N \sim 10$ and La concentrations ~140 x chondrite (Fig. 4). Therefore, the inferred strongly depleted sub-'Ata mantle will be highly sensitive to any addition of a LREE-bearing fluid derived from the Louisville Ridge. A MORB comparison requires >60% of La in all central-south Tonga arc lavas to be subduction-related.

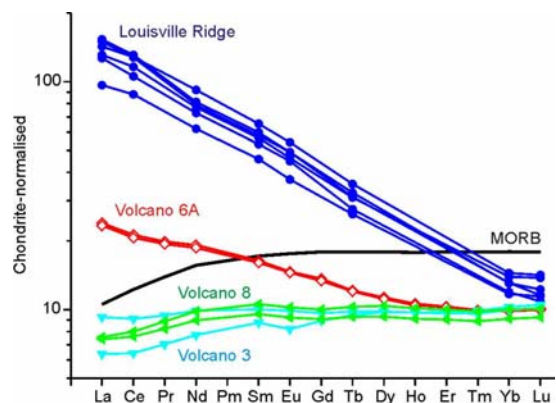


Fig. 4: Chondrite-normalised REE analyses for representative lavas. Volcano 3 is north of the 'Ata region (21.8°S; Louisville component gone/going). Volcano 6A is adjacent to 'Ata (22.4°S; strong Louisville component). Volcano 8 is south of 'Ata (22.8°S; not yet affected by the Louisville component). Louisville analyses from Hawkins et al. (1987).

Similar reasoning can explain other trace element anomalies associated with 'Ata region lavas (e.g. Louisville Th/U ~ 3.5, MORB Th/U ~ 2.5). We are presently verifying the absence of any conspicuous Sr-Nd-Pb isotope anomaly in published 'Ata analyses. If confirmed, this absence may reflect the similarity of Louisville and central-south Tonga arc lavas for $^{87}\text{Sr}/^{86}\text{Sr}$ and $^{143}\text{Nd}/^{144}\text{Nd}$. For Pb, the more radiogenic Louisville contribution may be swamped by that from the underlying oceanic crust or obscured by interactions between the plume (~70 Ma at the trench) and the paleo-Osborn spreading centre (70–80 Ma at the trench).

Provisional conclusions

- A major structural and geochemical disturbance of the central-south Tonga volcanic front affects only the region presently underlain by the subducting Louisville Ridge.
- Subduction of the Louisville Ridge causes a temporary westward migration and waning in volcanism along the south Tonga volcanic front.
- The geochemical signature of the Louisville Ridge in the arc lavas is best seen in elevated $(\text{La}/\text{Yb})_{\text{N}}$, reflecting the strongly depleted character of the south Tonga mantle wedge and the high LREE concentration of Louisville lavas.
- The Louisville component first appears in arc lavas before the volcanic front begins to migrate westwards. It may also attain maximum magnitude before the westward migration.
- All unambiguous vestiges of the Louisville component have been flushed from the sub-arc magma generation zone by the time the

volcanic front commences its eastwards return migration.

- The Louisville component is only found in volcanoes along a ~30 km-long strip of the volcanic front at any point in time. This approximates the diameter of the large Louisville Ridge seamounts.
- Louisville Ridge is surrounded by a 250 km-wide turbidite apron, but no evidence of a contribution from these sediments to the south Tonga arc lavas has been observed either at volcanoes preceding or following the locus of Louisville Ridge subduction.
- Rapid tectonic erosion occurs along the Tonga Trench (~4 km strip of forearc per Ma), where Eocene arc complexes are exposed. The absence of any Louisville sediment signature in south Tonga arc lavas probably reflects mixing and extreme dilution of the <250 m-thick sediment blanket by the re-cycled arc material.
- Despite the very high Nb and Ta content of Louisville lavas and the strongly depleted character of the south Tonga mantle wedge, only lavas with the maximum Louisville component have marginally higher Nb/Yb (and Ta/Yb, Nb/Ta; Fig. 3). Slight mobility of Nb and Ta relative to Yb in slab-derived fluids is suggested.

References

- Ewart, A., et al., 1998. *J. Petrol.* 39: 331–368.
- Hawkins, J., et al., 1987. *AGU Geophys. Mono.* 43: 235–254.
- Nur, A., Ben-Avraham, Z.; 1983. *Tectonophysics* 99: 355–362.
- Turner, S., et al., 1997. *Geochim. Cosmochim. Acta* 61: 4855–4884.

Hydrothermal Processes in Island Arcs: New Evidences from the Tonga Arc

U. Schwarz-Schampera¹, H. Gibson², P. Stoffers³
¹BGR, ²Laurentian University, ³University Kiel

A total of 27 submarine stratovolcanoes delineate the volcanic front along the southern Tonga island arc. The basaltic to andesitic and dacitic edifices are often more than 1000 m high and 20 km² wide. Most of them are characterized by well-developed multiple basaltic-andesitic caldera structures while some developed subsequently pumice-dominated craters. Volcanic rocks are scoriaceous or pumiceous volcanoclastic and plagioclase porphyritic andesitic breccias. Setting, lithologies, volcanic textures, and water depths indicate that very shallow submarine pyroclastic eruptions played a significant role in the formation of the arc volcanoes.

The first occurrences of hydrothermal activity along the volcanic front of the Tonga island arc, SW-Pacific, were discovered during cruise SO-167 with R/V Sonne. Four sites of shallow submarine hydrothermal systems were discovered at active and recently active andesitic and dacitic volcanic centers: Efuefu, Uli'uli (active) and Mutu'a ŋutu, Mo'uŋa (inactive). Hydrothermal activity is closely associated with central to slightly offset (basaltic-) andesitic cinder cones, and prominent caldera and crater walls illustrating the structural control on hydrothermal discharge. The mineralization is characterized by pervasive disseminated chalcopyrite, pyrite, marcasite, and pyrite-magnetite intergrowths and variable amounts of hematite, arsenopyrite, realgar, orpiment, stibnite, pyrrhotite. The high sulfidation style of mineralization, its mineralogy, associated advanced argillic alteration, and textural characteristics, coupled with shallow water depths share many similarities with other auriferous shallow submarine hot spring systems and contribute to a number of epithermal-style and transitional types of mineralization now being recognized in the Tonga-Kermadec arc system.

The Tonga suprasubduction zone represents a favorable tectonic setting for the generation of large epithermal-style Au and Cu deposits. The present southern Tonga arc is affected by the collision and subduction of the intensely altered aseismic Louisville ridge. The style of magmatism and associated hydrothermal activity at volcanoes along the collision zone suggest enrichment of volatiles in the subduction zone and their recycling during magmatic processes. This may produce melts with elevated oxygen fugacities and enriched in fluid-mobile elements. The removal of chalcophile elements from the mantle wedge into the Tonga

arc magmas strongly depends on the absence of sulfide, requiring oxidation of the mantle wedge by ferric iron, carried in solution by slab-derived partial melts from the aseismic Louisville ridge. Partial melting and addition of Fe_2O_3 may brought the Tonga arc mantle wedge to higher oxygen fugacities and above the SSO buffer (cf., Mungall, 2002) potentially leading to elevated Cu and Au contents in the arc volcanic rocks and associated hydrothermal fluids and precipitates.

The present sampling of the southern Tonga arc suggests a large potential for Cu and Au mineralization. The lack of careful and detailed seafloor mapping and sampling, however, largely prevents a proper assessment of the extent and character of mineralization.

FIRST EVIDENCE FOR SHALLOW SUBMARINE HYDROTHERMAL ACTIVITY IN THE TONGA ISLAND ARC, SW-PACIFIC

The first occurrences of hydrothermal activity along the volcanic front of the Tonga island arc, SW-Pacific, were discovered during R/V Sonne cruise SO-167. Two active (Efuefu, Uli'uli) and two inactive sites (Mo'uŋa, Mutu'a ŋutu) of shallow submarine hydrothermal systems are associated with active and recently active andesitic and dacitic arc volcanoes. Hydrothermal activity is closely associated with central to slightly offset (basaltic-) andesitic cinder cones and prominent caldera and crater walls. Host rocks are scoriaceous or pumiceous volcanoclastic and plagioclase porphyritic andesitic breccias. Setting, lithologies, volcanic textures, and water depths indicate that very shallow submarine pyroclastic eruptions (water depths of <1000 m up to 200 m) played a significant role in the formation of the arc volcanoes. The neovolcanic cones in water depths between 600 and 90 m are most likely a product of explosive strombolian to surtseyian eruptions.

The most extensive and strongest mineralization is associated with the Efuefu site offcoast Tongatapu. The host volcano is approximately 10 x 6 km in diameter, with a 5 x 3 km central caldera containing two young volcanoclastic cinder cones (Fig. 1). The mineralized cone raises to approximately 90 m below sea level and is localized along a regional, NE-SW trending structure. The widespread distribution of mineralization at the cone as well as at the southwestern and northern caldera walls suggests extensive hydrothermal activity. The Uli'uli site is associated with the southernmost Tonga arc volcano. The 13 by 15 km edifice is characterized by a large NW-SE elongated central caldera. Hydrothermal precipitates were collected from the western wall of a cone in the center of the caldera at water depths of 600 to 450 m.

Boulders of hydrothermally altered and mineralized andesitic and dacitic volcanoclastic breccias were retrieved from the crater and caldera walls of two other volcanic edifices. Volcano Mutu'a ŋutu exhibits a spectacular central crater two kilometers in diameter, interpreted as a product of major dacitic pyroclastic eruptions. Andesitic volcanoclastic rocks and younger pumiceous dacite are both affected by mineralization suggesting that the hydrothermal system persisted after the dacitic eruptions. Volcano Mo'uŋa is a 9 x 6 km edifice with a slightly offset central caldera. Sampling retrieved variably altered and weakly mineralized basaltic to andesitic flows and volcanoclastic rocks.

Mineralization at all four sites consists of fine-grained, pervasive disseminated pyrite, marcasite, pyrite-magnetite intergrowths, and variable amounts of chalcopyrite, hematite, arsenopyrite, realgar, stibnite. The mineralization is finely dispersed in the matrix but is best developed where it occurs: 1) coating vesicles within scoriaceous fragments, 2) lining fractures and open spaces, and 3) within the matrix between larger fragments. The host rocks suffered from an intense argillic and silica alteration. Similar to mineralization, the alteration assemblage is finely dispersed in the matrix and indurates single fragments as well as the breccia matrix. Alteration mineralogy is dominated by amorphous and opaline silica, fine-grained quartz, kaolinite, illite, smectite, and variable amounts of platy alunite, anhydrite, and native sulfur. Bulk rock analyses have resulted in moderately elevated Au concentrations and coenrichments in Cu, Bi, As, Sb, Te, Tl. The base metal contents are uniformly low.

Alteration and mineralization of the four new hydrothermal sites show many characteristics that are typical of shallow submarine hydrothermal vent fields such as in the Kermadec and Izu-Bonin arcs and the New Ireland fore-arc, but also of subaerial, epithermal-style Au deposits. The recent discoveries in the Tonga-Kermadec arc system contribute to the growing number of epithermal-style mineralization now being recognized in shallow submarine hot springs.

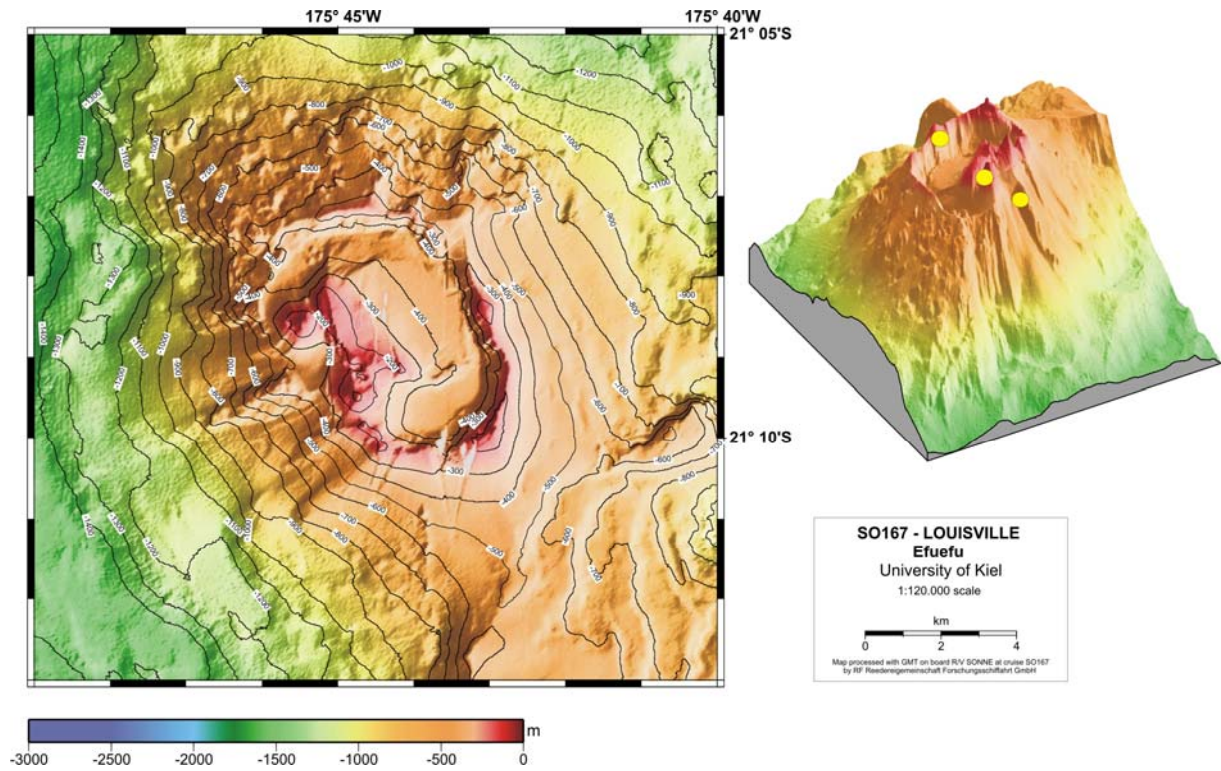


Figure 1. Bathymetry and 3D model of the volcano Efuefu, southern Tonga island arc, SW-Pacific and locations of the hydrothermal sites (dots).

Submitted by Ulrich Schwarz-Schampera, Peter Stoffers, Harold Gibson, and Peter M. Herzig, Federal Institute for Geosciences and Natural Resources, University of Kiel, Germany and Laurentian University, Canada; contact: u.schwarz-schampera@bgr.de

Effects of subducting the Louisville Ridge and Osborn Trough beneath the South Tonga arc

TIM WORTHINGTON, PETER STOFFERS, CHRISTIAN TIMM, MARCUS ZIMMERER, AND DIETER GARBE-SCHÖNBERG

Institut für Geowissenschaften, Universität Kiel, Germany tw@gpi.uni-kiel.de; pst@gpi.uni-kiel.de; ct@gpi.uni-kiel.de; zimmi.kiel@freenet.de; dgs@gpi.uni-kiel.de

Subduction of both the plume-generated Louisville Ridge and the late Cretaceous Osborn Trough paleo-spreading centre takes place beneath the 450 km-long South Tonga segment of the Tonga–Kermadec subduction system. The predominantly submarine South Tonga arc was previously unsurveyed and features only 1 volcanic island (Ata). Surveying and sampling during cruise SO 167 of the FS *SONNE* revealed a continuous volcanic front, 10–15 km wide, comprising 27 semi-regularly spaced active stratovolcanoes typically with basal diameters of 10–25 km and heights of 1–2 km. The volcanic front is disturbed only in the vicinity of Ata, where 10 major edifices and numerous smaller constructs extend the width of the front to 50 km. This greater width reflects a transient 40 km westward migration of the front and enhanced constructional volcanism as the Louisville Ridge dehydrates and passes under the arc.

The South Tonga arc volcanoes show considerably more geochemical and isotopic variation than the better-known subaerial Central Tonga volcanoes. High-Mg basalt, andesite, and rhyodacite associated with calderas (often > 6 km in diameter) are common. Overall, these lavas define a low-K suite with strong enrichment in the fluid-mobile elements and extreme depletion in the fluid-immobile elements relative to MORB [e.g., $(La/Yb)_N < 1.1$; Nb/Yb 0.09–0.27]. Specific incompatible element ratios distinguish some volcanoes and are randomly distributed along the arc segment. These characteristics are long-lived, and best explained by interaction of ascending magma with sub-arc lithosphere in a volcano-specific manner. They provide support to models invoking significant lithospheric processing of magma in oceanic settings.

Passage of the Louisville Ridge beneath the arc is associated with the eruption of lavas with $(La/Yb)_N > 1.1$, higher Th/U, and other anomalies prior to and during the westward migration of the volcanic front. In contrast, lavas erupted during the eastward return of the front have relatively normal South Tonga compositions, suggesting rapid flushing of ridge-derived fluids from the sub-arc mantle. Volcanoes that overlie the subducting Osborn Trough at 23.5–24.7°S exhibit a marked change in caldera-style to diatreme-like craters up to 1.1 km-deep. Associated changes in magmatic volatile content driving these eruptions probably reflect dehydration of mantle extensively serpentinised when spreading stalled at the Osborn Trough.

Hf-Nd Isotope Characterization of the Tonga-Kermadec Sub-Arc Mantle

¹Tim J. Worthington, ²Carsten Muenker, ¹Peter Stoffers, ³John A. Gamble, ⁴Ian C. Wright

¹Institute fuer Geowissenschaften, Universitaet Kiel, Olshausenstr. 40, D-24118 Kiel, Germany

(tw@gpi.uni-kiel.de; pst@gpi.uni-kiel.de)

²Institut fuer Mineralogie, Universitaet Muenster, Corrensstr. 24, D-48149, Muenster, Germany (muenker@nwz.uni-muenster.de)

³Dept. of Geology, National University of Ireland, University College, Cork, Ireland (j.gamble@ucc.ie)

⁴National Institute for Water and Atmospheric Research, PO Box 14-901, Wellington, New Zealand (i.wright@niwa.cri.nz)

Subduction-related magmatism involves fluxing of the mantle wedge by a slab-derived fluid and/or melt. Uncertainty surrounds the thermal, physical and chemical state of the slab and slab-wedge interface beneath the volcanic front, creating doubt over the application of experimental data on slab dehydration and melting to models of magma genesis and mass balance. Constraining the composition of the wedge should provide an important control on such models. However, simple models of wedge convection from the backarc to sub-arc environment are clearly incomplete (e.g. do not explain the lack of correlation between depletion of the sub-arc mantle and either backarc width or extension rate). To investigate the dynamics of wedge convection, we undertook Hf-Nd isotope determinations for lavas spanning most of the Tonga-Kermadec arc. Advantages of these elements include their fluid-immobile character (Hf strongly, Nd moderately) relative to the highly mobile, and thus predominantly slab-derived, Sr and Pb. Previous Sr-Nd-Pb isotope studies of backarc Lau Basin lavas revealed that Indian MORB mantle (IMM) replaced Pacific MORB mantle (PMM) during basin opening, and that IMM underlies the central Tonga arc. In contrast, the backarc mantle south of Valu Fa Ridge and under the Havre Trough remains PMM. Thus, a transition from IMM to PMM was anticipated beneath the south Tonga arc.

Hf isotope compositions of the Tonga-Kermadec arc lavas range from +12 to +16 ϵ_{Hf} -units and are 1-2 ϵ_{Hf} units below those of the Lau Basin spreading centres. Tonga lavas are generally in the upper part of this range, whereas Kermadec lavas are more varied. All Tonga-Kermadec lavas plot within the IMM field in ϵ_{Hf} vs ϵ_{Nd} -space, indicating IMM-like mantle is under the entire arc from 15-35°S. This result is further enhanced by subtracting the $\sim 20-40\%$ Nd added from the subducting slab (PMM-composition). ϵ_{Hf} exhibits a mild negative correlation with Hf/Yb and increasing latitude, consistent with a minor Hf contribution from subducting volcanogenic sediment in the Kermadec arc sector. Our data provide no evidence for a slab melt, even in the southern Kermadecs where the slab is warmer due to slow subduction. The occurrence of IMM beneath the Tonga-Kermadec arc, but PMM below the southern Lau Basin-Havre Trough, is inconsistent with simple models invoking progressive southeastward migration of IMM into the Tonga-Kermadec system accompanying the opening of the Lau-Havre backarc basin. Instead, considerably complexity is required in the geometry of the IMM-PMM interface, the sub-arc wedge flow, or the origin of the IMM-like signature.

Mineralisationsprozesse und ihre zeitliche Variabilität im Bereich des südlichen Tonga Inselbogens: Ergebnisse der Forschungsfahrt SO-167 LOUISVILLE

U. Schwarz-Schampera¹, P. Stoffers², K. Schreiber³, S. Fretzdorff², H. Gibson⁴,
P. Herzig⁵, T. Kuhn⁵, R. Hékinian², T. Worthington²

¹BGR-Lagerstättenforschung, ²C.-A. Universität Kiel, ³TU Bergakademie Freiberg,
⁴Laurentian University Sudbury, Canada, ⁵Leibniz-Institut für Meereswissenschaften

Einführung

Das Forschungsvorhaben SO-167 LOUISVILLE wurde mit dem Ziel petrogenetischer, vulkanologischer und hydrothormaler Arbeiten im Bereich des südlichen Tonga Inselbogens und des angrenzenden Lau Back-Arc Beckens (Valu Fa Rücken) durchgeführt. Im Rahmen der Arbeiten zum Hydrothermalismus standen die Untersuchung metallogenetischer Prozesse in flachmarinen Milieus einer intraozeanischen Subduktionszone sowie die Interaktion und zeitliche Variabilität vulkanischer, magmagenetischer und hydrothormaler Prozesse im Vordergrund.

Die Arbeiten im südlichen Tonga Inselbogen schließen sich denen im weiter südlich gelegenen Kermadec Inselbogen (SO-135) an und hatten die Untersuchung des Potenzials für aktiven, flachmarinen Hydrothermalismus zum Ziel. Die Bildung großer Cu-Au-Lagerstätten ist eng mit einem Suprasubduktionsmilieu, wie es entlang des Tonga-Kermadec Inselbogens entwickelt ist, assoziiert. Die spezielle geotektonische Situation mit der Kollision und Subduktion des alten Louisville Rückens im Bereich des südlichen Tonga Inselbogens ermöglicht die Anreicherung volatiler Elemente im Mantelkeil und den Transport magmatogener fluider Phasen in den Bereich der Inselbogenvulkane und sorgt somit für ein hohes Potenzial für epithermale und porphyrische Vererzungen.

Im südlichen Lau Becken ist die magmatische Aktivität entlang des schnell spreizenden und nach Süden entlang struktureller Schwächezonen propagierenden Valu Fa Rückens mit einer großen Variabilität hydrothormaler Prozesse verbunden. Anhaltender Wärmefluss und fortwährende magmatische Aktivität sind kritisch für die Entwicklung eines zeitlich stabilen Hydrothermalismus und gestatten die Anreicherung und Erhaltung hydrothormaler Präzipitate durch temporäre Bedeckung. Hohe Spreizungsraten und intensive Gesteinsdifferentiation fördern die Freisetzung magmatischer Volatiler und deren Anreicherung in hydrothermalen Präzipitaten, wirken der Entwicklung einer langlebigen, stabilen hydrothermalen Konvektion und damit der Bildung großer Massivsulfidvorkommen jedoch entgegen.

Die geringe Distanz zwischen rücken- und inselbogenbezogenen Mineralisationen und die Untersuchung der zeitlichen Zusammenhänge magmatischer und hydrothormaler Prozesse haben eine große Bedeutung für das Verständnis fossiler Lagerstättensysteme. Der Tonga-Kermadec Inselbogen gilt als rezentes Äquivalent für zahlreiche fossile Lagerstättendistrikte. Die Untersuchung rezenter geologischer, vulkanologischer und hydrothormaler Prozesse und ihr Vergleich mit fossilen Systemen ermöglicht die detaillierte Analyse metallogenetischer Prozesse an ehemals aktiven Plattenrändern seit dem Präkambrium und liefert wichtige Rückschlüsse im Verständnis fossiler Stoffflüsse.

Südlicher Tonga Inselbogen

Die Kartierung und Beprobung von insgesamt 27 submarinen Inselbogenvulkanen führte zur Identifizierung von neuen flachmarinen Hydrothermalsystemen (Efuefu, Mo'ūna, Mutu'a ŋutu, Uli'uli) an vier aktiven oder subrezentem Vulkanen. Zwei Inselbogenvulkane (Efuefu, Uli'uli) erbrachten Präzipitate einer rezenten, hochtemperierten, hydrothermalen Aktivität in geringer Wassertiefe (Abb. 2), während die Felder Mo'ūna und Mutu'a ŋutu derzeit vermutlich inaktiv sind. Die Alteration, Mineralisation und geochemischen Signaturen zeigen

signifikante Charakteristika subaerischer Geothermalfelder. Die Felder Efuefu (Vulkan 1) und Uli'uli (Vulkan 19) sind mit stark alterierten und mineralisierten vulkanoklastischen Andesiten assoziiert und an Calderastrukturen und neovulkanische Kegel in den oberen Partien aktiver Inselbogenvulkane gebunden (Abb. 1). Aktive Fluidaustritte in Wassertiefen zwischen 600 und 200 m können als charakteristisch für flachmarine Hydrothermalsysteme angesehen werden, die durch geringe Buntmetall-, aber erhöhte Au- und Ag-Gehalte gekennzeichnet sind. Die Gesteine zeigen eine intensive argillitische Alteration und Silifizierung. Die Alterationsparagenese führt die für epithermale Mineralisationen diagnostischen Minerale Natroalunit, Illit-Kaolinit, Christobalit, rhombischer Kalifeldspat, Anhydrit, Baryt und gediegen Schwefel. Die disseminierte Vererzung besteht vor allem aus Chalkopyrit-Hämatit und Pyrit-Magnetit sowie variablen Anteilen von Markasit, Pyrrhotin, intermediate solid solution (iss), Arsenopyrit, Realgar, Rutil, Stibnit und gediegen Gold. Hinweise auf ein Kochen und subkritische Phasenseparation der hydrothermalen Lösungen unterhalb bzw. im Bereich der Austrittsstelle finden sich in stark variablen Redoxbedingungen in den mineralisierenden Fluiden nahe des $\text{Fe}^{2+}/\text{Fe}^{3+}$ -Puffers, in unterschiedlichen Sulfidierungsgraden, niedrigen Buntmetallgehalten und in leichten Schwefelisotopensignaturen. Die Koexistenz von Natroalunit und Pyrit, und Schwefelisotopensignaturen nahe dem Gleichgewicht in der Folge der Disproportionierung von magmatischem SO_2 deuten auf die Beteiligung magmatischer Volatiler an den hydrothermalen Systemen hin. Die Abschätzung der Bildungstemperaturen ergibt einen Temperaturbereich zwischen 280° und 310°C für Efuefu und zwischen 360° und 390°C für die Proben des Uli'uli-Feldes.

Weitere Proben hydrothermalen Mineralisationen konnten an der oberen Flanke des Vulkans Nr. 18 (Mutu'a ŋutu) sowie von der Caldera-Wand des Vulkans Nr. 14 (Mo'ūŋa) geborgen werden. Die disseminierte Mineralisation besteht aus Pyrit, Magnetit, Chalkopyrit und untergeordnet Pyrrhotin und Markasit und ist an stark alterierte, zum Teil brekziierte Andesite und dazitische Vulkanoklastite gebunden. Die Proben sind durch eine intensive propylitische und argillitische Alteration mit Bildung von Chlorit, Epidot, Calcit und Quarz gekennzeichnet.

Die hydrothermale Aktivität geht bei allen vier Lokationen nicht mit den jüngsten vulkanischen Ereignissen einher. Vielmehr entstammen die Proben dezentralen und distalen Strukturen und werden zum Teil von vulkanischen Aschen überprägt. Es wird angenommen, dass die Platznahme neovulkanischer Intrusionen den Antrieb (kleinerer) Konvektionszellen ermöglicht; ein (geringer) Einfluss von Meerwasser spiegelt sich in den Schwefelisotopenwerten wider.

Südliches Lau Becken

Die Arbeiten im südlichen Lau Becken haben gezeigt, dass der schnell spreizende und nach Süden propagierende Valu Fa Rücken durch einen episodischen, phreatomagmatischen Vulkanismus geprägt ist. Das überaus häufige Auftreten junger, hochdifferenzierter vulkanischer Gläser ist Beleg für eine intensive magmatische Aktivität des Spreizungszentrums. Die Segmente und Vulkanbauten des Valu Fa Rückens und südwärtsgerichtete Störungszonen in dessen Verlängerung folgen einem regionalen linkslateralen, en echelon-orientierten Muster. Die Identifikation propagierender Riftsegmente und potenzieller neotektonischer und neovulkanischer Strukturen führt zu einer Neuinterpretation struktureller Schwächezonen am zentralen und südlichen Valu Fa Rücken und im Übergang zum Havre Trough zwischen $22^\circ45'\text{S}$ und $23^\circ00'\text{S}$, und damit möglicher Lokationen zukünftiger seismischer, magmatischer und hydrothermalen Aktivität. Das schnelle und aktive südwärtsgerichtete Spreizen des Valu Fa Rückens resultiert in kurzfristigen strukturellen, vulkanischen und hydrothermalen Veränderungen. Die hydrothermale und jüngste vulkanische Aktivität ist mit westwärts gerichteten Strukturen und Vulkanbauten an der Westseite des Valu Fa Rückens assoziiert und spiegelt hiermit die starke magmatische Kontrolle der Rückengeometrie wider. Der südliche Valu Fa Rücken ist durch ein breites Spektrum an Laven basaltisch-andesitisch bis rhyolithischer Zusammensetzung gekennzeichnet. Bei $22^\circ25'\text{S}$ wurden die bisher am höchsten differenzierten Gesteine des gesamten Lau Beckens identifiziert. Die Zusammensetzung der Vulkanite belegt die Zufuhr von Fluiden aus der subduzierten Platte in die Magmenquelle

(siehe Kurzfassung Fretzdorff et al.). Die südwärtige Verlängerung des Valu Fa Rückens mündet in einer Störungszone, die weitgehend dem regionalen linkslateralen Strukturmuster folgt. Die tektonische und magmatische Aktivität belegt die Existenz tiefreichender Strukturen, die jedoch (noch) nicht mit hydrothermalen Prozessen (Freisetzung magmatogener Fluide) assoziiert sind.

Die hydrothermale Aktivität ist derzeit durch diffuse Austritte gekennzeichnet. Ein wiederauflebender andesitisch-dazitischer Vulkanismus hat zur Bedeckung großer Teile des Vai Lili Hydrothermalfeldes und zum Erliegen der 1989 dokumentierten Hochtemperaturaktivität geführt. Tote Kolonien einer ehemals intensiven Hydrothermalfauna und isolierte inaktive und oxidierte Chimneys zwischen andesitischen Laven sowie das Auftreten alterierter und mineralisierter Xenolithe in andesitischen Gläsern belegen die weitreichende Bedeckung des Hydrothermalfeldes. Das weit verbreitete Auftreten diffuser Lösungsaustritte, die Existenz niedrigtemperierter Fe-Mn-Präzipitate und die Beprobung einer intensiven und jungen Stockwerkmineralisation belegen jedoch ein Andauern hydrothermalen Prozesse im Untergrund und lassen einen fortgesetzten Absatz von Metallen in der Tiefe möglich erscheinen. Die disseminierte Stockwerkmineralisation zeigt eine intensive Vererzung aus Pyrit, Markasit, Sphalerit, Chalkopyrit und Galenit. Die Alteration (Kaolinit-Illit, Alunit, Rhodochrosit) ist typisch für distale Bereiche epithermaler Lagerstätten unter dem Einfluss magmatogener Fluide.

Das Hine Hina Hydrothermalfeld ist an einen subrezent aktiven, basaltisch-andesitischen Aschenkegel gebunden, dessen Bildung wahrscheinlich auf explosiver Aktivität beruht. Das Feld besitzt eine wesentlich größere Ausdehnung als bisher bekannt. Die hydrothermale Aktivität hat sich seit 1989 nicht wesentlich verändert und markiert die vulkanologische Entwicklung von einem basaltischen Pillowvulkan zu phreatomagmatischem Vulkanismus. Aktiver Hydrothermalismus zeigt sich in diffusen Fluidaustritten, Fe-Mn-Oxyhydroxidkrusten, und einer charakteristischen Vent-Fauna.

Ergebnisse

Mit dem Forschungsvorhaben SO-167 gelang der erste Nachweis einer ausgedehnten rezenten hydrothermalen Aktivität im Tonga Inselbogen. Die Alteration und Mineralisation sind charakteristisch für landgebundene Epithermalvorkommen und belegen das überaus große Potenzial flachmariner Inselbogen-Vulkane für assoziierte Cu-Au-Mineralisationen. Darüber hinaus definieren sie den Tonga-Kermadec Inselbogen als ein beispielhaftes Arbeitsgebiet für zukünftige metallogenetische Untersuchungen. Die Nähe von Inselbogen zum Back-Arc (≤ 40 km) und der Nachweis magmatischer Volatiler auch in den Präzipitaten am Valu Fa Rücken lässt auf magmatisch-dominierte Hydrothermalsysteme in diesem Abschnitt der Tonga Subduktionszone schließen. Normale Subduktionsprozesse führen selten zur Bildung großer Au und Cu Lagerstätten. Vielmehr ist die Oxidation des Mantelkeiles ein bedeutender Parameter in der Bildung großer Cu-Au- und möglicherweise auch vieler Buntmetallagerstätten, der eine frühe Fraktionierung der Metalle verhindert. Die Vulkanite im Bereich der Subduktion des Louisville Rückens zeigen eine deutliche geochemische Anomalie, die sich in der Anreicherung volatiler Elemente manifestiert. Das Auftreten tephritischer Aschen und basaltisch-andesitischer Bomben und ihre geochemische Zusammensetzung belegen einen explosiven Vulkanismus und somit hohe Volatilingehalte in den Magmen. Die Fraktionierung chalkophiler Elemente in die Magmen des südlichen Tonga Inselbogens bedingt die Abwesenheit sulfidischer Phasen durch Oxidation des Mantelkeiles, vermutlich verursacht durch das hohe Redoxpotenzial des Louisville-Rückens und einen massiven Eintrag von dreiwertigem Eisen in der Subduktionszone.

Danksagung

Dieses Projekt wird durch Mittel des Bundesministeriums für Bildung und Forschung gefördert (Förderkennzeichen 03G0167A und B).

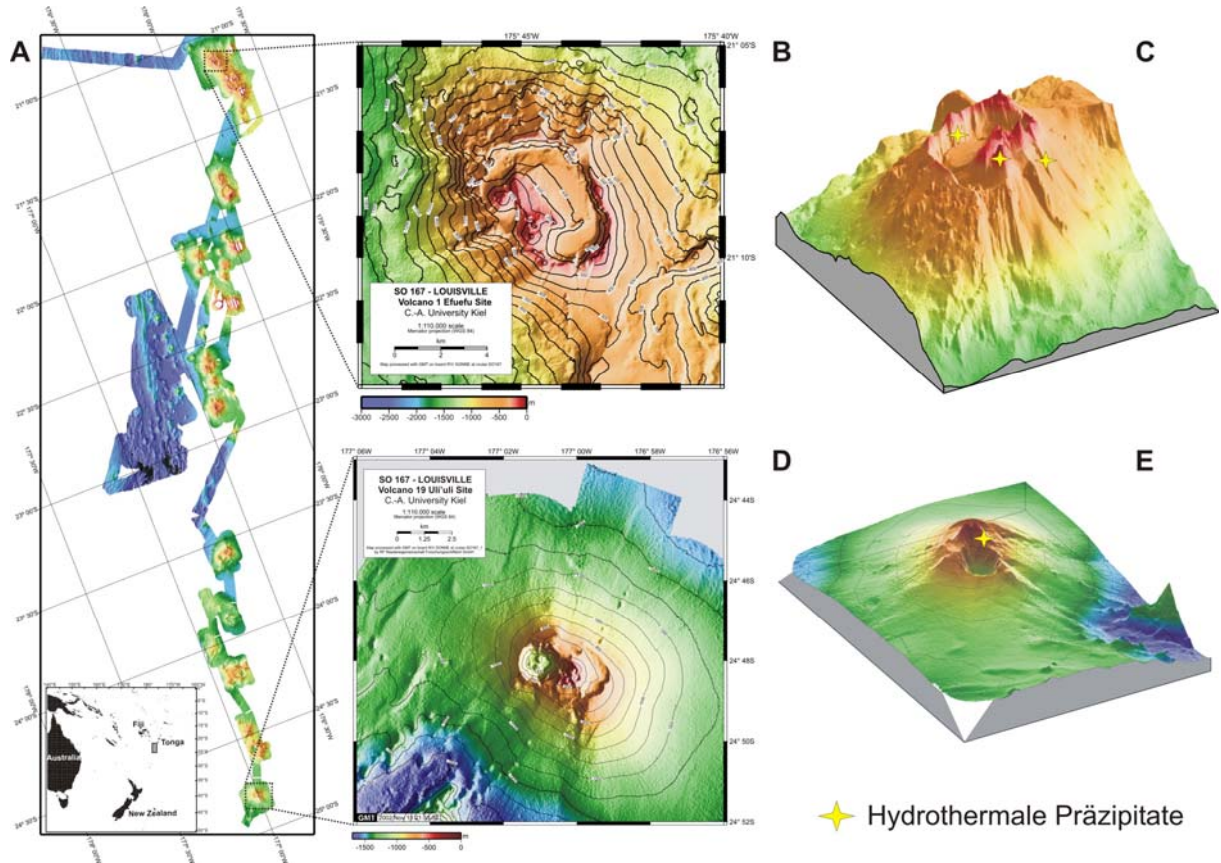


Abb. 1. A. Lokation und Bathymetrie des südlichen Tonga Inselbogens und Lau Back-arc Beckens, SW-Pazifik. B. Bathymetrie des Vulkans 1. C. Dreidimensionale Darstellung des Vulkans 1 und Lokation der drei aktiven Efuefu-Hydrothermalfelder. D. Bathymetrie des Vulkans 19. E. Dreidimensionale Darstellung des Vulkans 19 und Lokation des Uli'uli Hydrothermalfeldes.

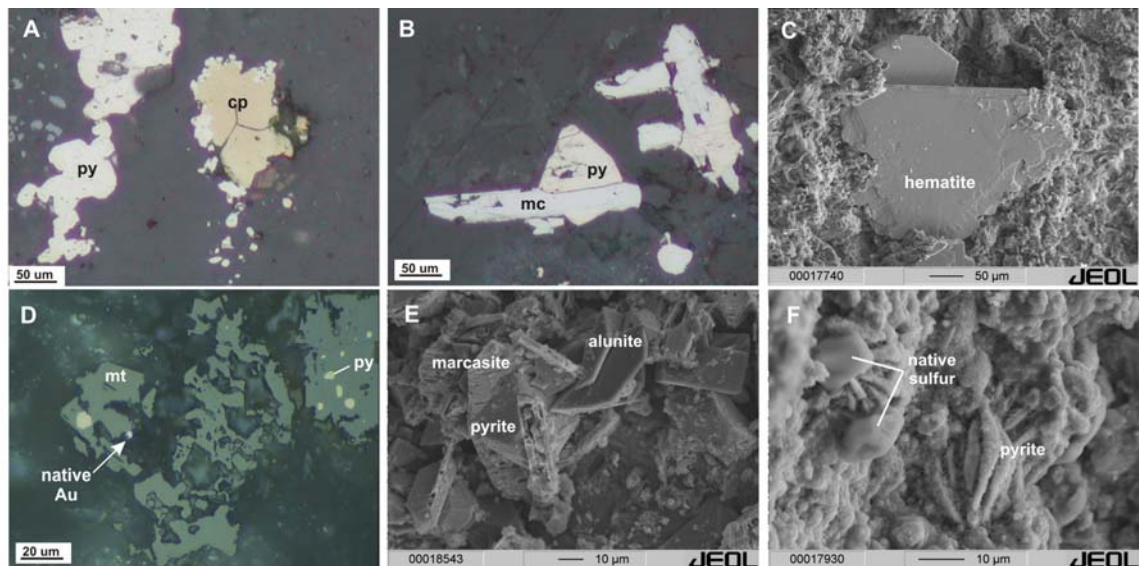


Abb 2. A. Chalkopyrit (cp) und kolloidale Pyrit (py) – Aggregate im Efuefu-Hydrothermalfeld. B: Verwachsung aus kogenetischem Pyrit und Markasit (mc), Uli'uli-Hydrothermalfeld. C. Tafeliger hydrothermalmer Hämatit (Efuefu). D. Hydrothermalmer Magnetit (mt) mit Einschlüssen aus Pyrit und gediegen Gold (Efuefu). E. Kogenetische Verwachsung von Pyrit-Markasit und Alunit aufgrund der Disproportionierung von magmatischem SO_2 (Efuefu). F) Verwachsung von Pyrit und gediegen Schwefel infolge variierender Redoxbedingungen durch hydrothermale Siedeprozesse (Efuefu).

Magmengenetische Prozesse entlang des Valu Fa Rückens, Lau Becken, SW-Pazifik (SO 167)

S. Fretzdorff¹, P. Stoffers¹, U. Schwarz-Schampera², T. Worthington¹

¹Institut für Geowissenschaften, Universität zu Kiel; ²BGR Hannover

Einführung

Der Valu Fa Rücken, die südliche Fortsetzung des Lau Beckens, ist ca. 165 km lang und 5 bis 6 km breit. Südlich von 22°45'S propagiert die Spreizungsachse in miozäne Inselbogenkruste (Taylor et al., 1996; Wiedicke und Collier, 1993). Geophysikalische Studien zeigen, dass die aktive Spreizungsachse in 11 Rückensegmente unterteilt werden kann (V3 – V14; Abb. 1), wobei der jeweilige Rückenversatz 0.4 bis 2.3 km beträgt und damit nur die neovulkanische Zone beeinflusst (Wiedicke und Collier, 1993). Der zentrale Bereich des Valu Fa Rückens ist durch eine Magmenkammer in 3.2 km Krustentiefe gekennzeichnet, die auf einer Länge von bis zu 20 km anhand seismischer Profile verfolgt werden kann (z.B. Morton und Sleep, 1985; Collier und Sinha, 1990; Abb. 1).

Während der Forschungsfahrt SO 167 wurde die Spreizungsachse des Valu Fa Rückens zwischen 22°12'S und 22°52'S mit insgesamt 19 Dredge- und TV-Greifer Einsätzen erfolgreich beprobt (Abb. 1). Die Untersuchungen der vulkanischen Gesteine konzentrieren sich im Wesentlichen auf magmengenetische Fragestellungen. Dabei sollen die Haupt- und Spurenelementzusammensetzungen sowie die Isotopenverhältnisse (Sr, Nd, Pb) der Laven Einblicke in fraktionelle Kristallisations- und Aufschmelzprozesse sowie die Zusammensetzung der Mantelquelle des südlichen Valu Fa Rückens geben. Desweiteren soll der Einfluss der Subduktionsvorgänge auf die Laven der Valu Fa Spreizungszone untersucht werden, insbesondere welche Komponenten aus der subduzierten Platte in den Mantelkeil transportiert werden.

Ergebnisse

Die geochemischen Untersuchungen zeigen, dass entlang des südlichen Valu Fa Rückens ein breites Spektrum an Laven von basaltischen Andesiten bis hin zu Rhyoliten vorkommt (Abb. 2). Die untersuchten Laven fallen in die Gruppe der „K-armen“ Gesteine, sind allerdings bei gleichen SiO₂ Gehalten K-reicher als die Vulkanite des Lau Beckens.

Im Bereich von 22°25'S sind Laven mit SiO₂ Gehalten von bis zu 72 Gew.% eruptiert (Abb. 2). Bisher ist das Auftreten von solch hoch-differenzierten Gesteinen einzigartig und unterstützt die geophysikalischen Beobachtungen, dass eine Magmenkammer im zentralen Bereich des Valu Fa Rückens vorhanden ist, in der die Magmen unter intensiven fraktionellen Kristallisationsprozessen generiert worden sind.

Um Aussagen über Aufschmelzprozesse der Laven zu treffen, wurden die Na₂O Gehalte auf einen MgO-Wert von 8 Gew.% fraktionierungskorrigiert. Niedrige Na_{8,0}-Konzentrationen weisen auf einen hohen Aufschmelzgrad der Proben hin, wobei hohe Werte einen vergleichsweise niedrigen Aufschmelzgrad anzeigen (Plank und Langmuir, 1992). Entlang des Valu Fa Rückens ist eine deutliche Abnahme der Na_{8,0}-Gehalte in Richtung Süden zu beobachten, was auf eine Erhöhung des Aufschmelzgrades hindeutet (Abb. 3). Dies korreliert mit der Abnahme der Entfernung zum Inselbogen in südlicher Richtung (siehe Abb. 1), was bedeutet, dass der Eintrag von Subduktionskomponenten z.B. Fluide aus der alterierten ozeanischen Kruste in die Magmenquelle der Laven mit abnehmender Distanz zum Inselbogen ansteigt. Die Proben des südlichen Valu Rückens sowie Seamount-Laven mit niedrigen Na_{8,0}-Gehalten weisen erhöhte Uran-Konzentrationen auf (Abb. 4). Uran ist mobil in Fluiden z.B. aus der subduzierten alterierten ozeanischen Kruste und kann im Mantelkeil angereichert werden (z.B. Pearce und Peate, 1995). Ein hoher Fluideintrag hat eine Erhöhung des Aufschmelzgrades zur Folge, wie es bei den südlichsten Valu Fa Laven zu beobachten ist (Abb. 3, 4). Den Magmenquellen südlich von Hine Hina und einigen

Seamounts südlich der Spreizungsachse wurde demnach in hohem Maße eine fluidreiche Phase aus der subduzierten Platte zugeführt.

Generell sind die Uran- und Ytterbium-Konzentrationen des Valu Fa Rückens und des Lau Beckens positiv korreliert, wobei die Laven des Lau Beckens bei gleichen Ytterbiumgeringere Uran-Gehalte aufweisen. Dies bedeutet, dass die Laven des Valu Fa Rückens im Vergleich zu denen des Lau Beckens in höherem Maße an Fluiden angereichert sind (Abb. 4). Die geochemischen Trends innerhalb der Valu Fa und Lau Becken Probensuiten können größtenteils auf fraktionelle Kristallisationsprozesse zurückgeführt werden.

Bei vergleichbaren Nd-Isotopenverhältnissen ist eine Variation der Sr-Isotopenzusammensetzung innerhalb der Valu Fa Probenserie zu beobachten. Die leicht erhöhten Nd-Isotopenverhältnisse einzelner Proben im Bereich südlich von Hine Hina und der Seamounts spiegeln den erhöhten Eintrag von Material aus der subduzierten Platte in die Magmenquelle wider. Die Pb-Isotopenzusammensetzung der untersuchten Probensuite ist bis auf vereinzelte Laven von Vai Lili und Hine Hina relativ homogen (Abb. 5). Die Laven mit den höchsten $^{206}\text{Pb}/^{204}\text{Pb}$ Gehalten sind ebenfalls an Uran angereicht, was die Beobachtung unterstützt, dass südlich von Hine Hina ein erhöhter Fluideintrag aus der subduzierten Platte in den Mantelkeil stattfindet. Dies gilt im umgekehrten Fall für die Probe mit den niedrigsten $^{206}\text{Pb}/^{204}\text{Pb}$ -Verhältnissen und Uran-Gehalten; hier ist eine relativ geringe Beeinflussung der Magmenquelle durch die subduzierte Platte zu vermuten.

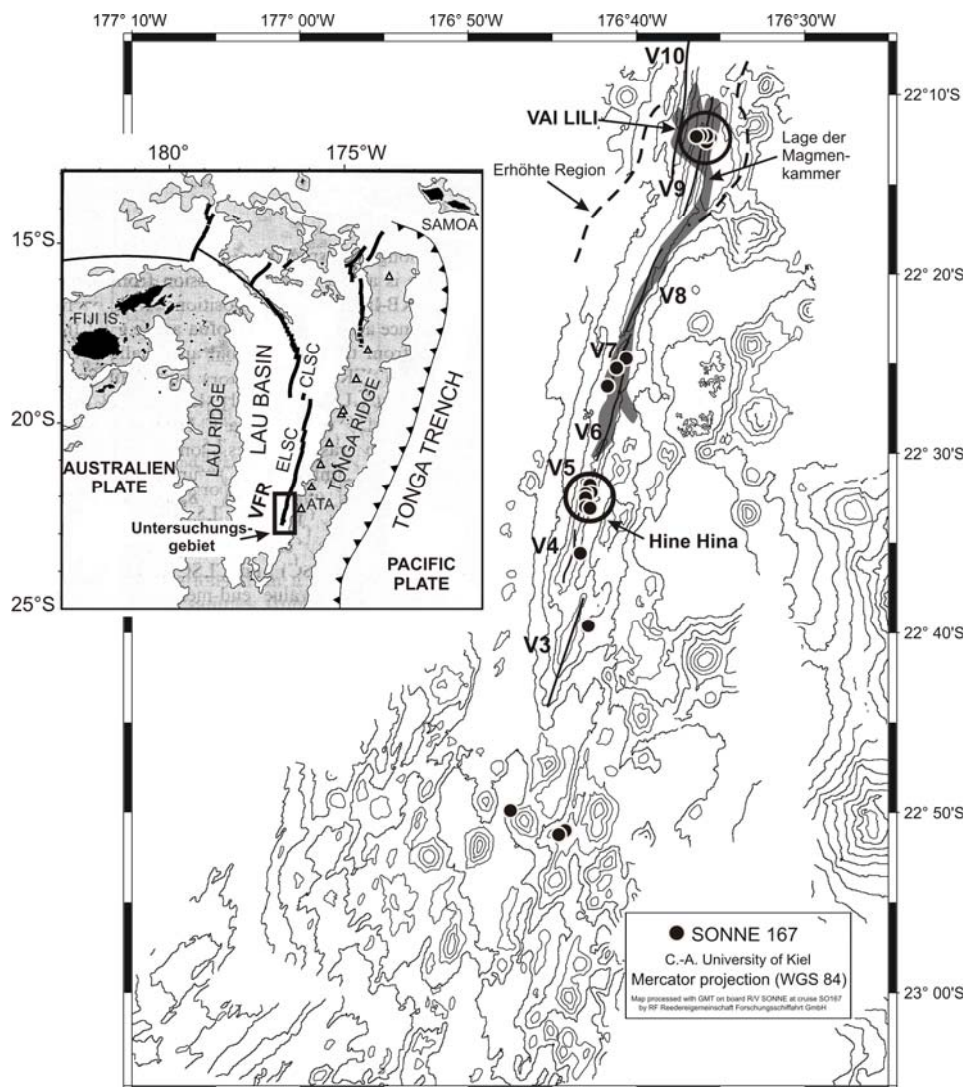


Abbildung 1: Bathymetrische Karte des zentralen und südlichen Valu Fa Rückens mit Lage der Hydrothermalfelder Vai Lili und Hine Hina und Probenahmestationen. Darüber hinaus sind die Spreizungssegmente nach Wiedicke und Collier (1993) eingezeichnet, sowie die Lage der Magmenkammer nach Day et al. (2001).

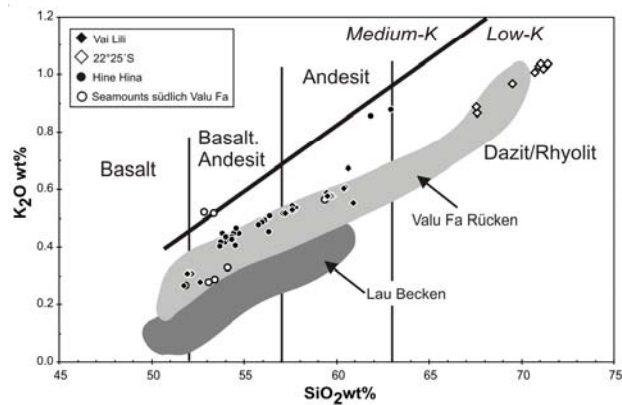


Abbildung 2: K₂O- versus SiO₂-Gehalte der SO167 Laven im Klassifizierungsdiagramm nach Peccerillo & Taylor (1976). Literaturdaten Lau Basin und Valu Fa Rücken: Jenner et al., 1987; Volpe et al., 1988; Boesflug et al., 1990; Frenzel et al., 1990; Look et al., 1990; Vallier et al., 1991; Pearce et al., 1995; Bach et al., 1998; Peate et al., 2001.

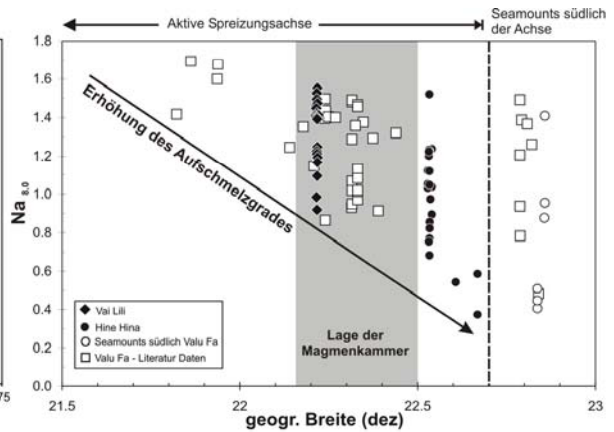


Abbildung 3: Na_{8.0} Gehalte der Valu Fa Rücken Laven berechnet nach Plank und Langmuir (1992; Proben mit MgO Gehalten < 3 Gew. % sind nicht dargestellt) aufgetragen gegen die geographische Breite. Lage der Magmenkammer nach Day et al. (1992) und Literaturdaten siehe Abb. 2.

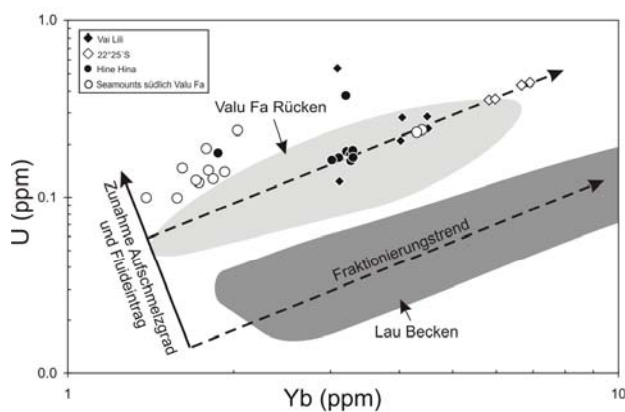


Abbildung 4: U (ppm) und Yb (ppm) Konzentration der Valu Fa Probensuite im Vergleich zu den Lau Becken Laven. Die gestrichelte Linie markiert schematisch den Fraktionierungstrend innerhalb der Probensuiten. Die durchgezogene Linie zeichnet den steigenden Fluidgehalt mit gleichzeitig ansteigendem Aufschmelzgrad nach. Literaturdaten wie in Abb. 2.

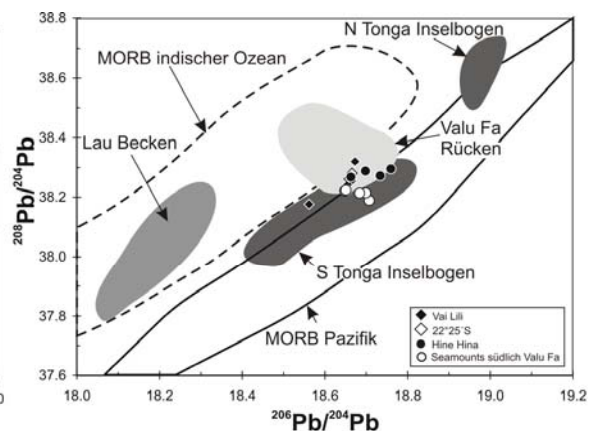


Abbildung 5: Pb-Isotopenverhältnisse des Valu Fa Rückens im Vergleich zum Lau Becken, Tonga Inselbogen (Ewart et al., 1994; Turner et al., 1997) und mittelozeanischen Rückenbasalten (MORB) vom indischen Ozean (Ito et al., 1987; Mahoney et al., 1989) und Pazifik (Prinzhofer et al., 1989; Mahoney et al., 1994; Bach et al., 1996; Vlastelic et al., 1999). Fehlerbalken der gemessenen Pb Isotopenverhältnisse liegen innerhalb der Symbole. Literaturdaten für Lau Becken und Valu Fa Rücken siehe Abb. 2.

Danksagung

Dieses Projekt wird durch Mittel des Bundesministeriums für Bildung und Forschung gefördert (Förderkennzeichen 03G0167A und B).

Literatur

- Bach, W., E. Hegner, and J. Erzinger, Chemical fluxes in the Tonga subduction zone: Evidence from the southern Lau Basin, *Geophys. Res. Letts.*, 25, 1467-1470, 1998.
- Bach, W., J. Erzinger, L. Dosso, J. Bollinger, H. Bougault, J. Etoubleau, and J. Sauerwein, Unusually large Nb-Ta depletions in North Chile ridge basalts at 36°50' to 38°56'S: major element, trace element, and isotopic data, *Earth Planet. Sci. Letts.*, 142, 223-240, 1996.
- Boesflug, X., L. Dosso, and H. Bougart, Trace element and isotopic (Sr, Nd) geochemistry of volcanic rocks from the Lau Basin, *Geol. Jb.*, D92, 503-516, 1990.
- Collier, J.S., and M.C. Sinha, Seismic mapping of a magma chamber beneath the Valu Fa Ridge, Lau Basin, *J. Geophys. Res.*, B, 97, 14,031-14,053, 1992.
- Day, A.J., C. Peirce, and M.C. Sinha, Three-dimensional crustal structure and magma chamber geometry at the intermediate-spreading, back-arc Valu Fa Ridge, Lau Basin; results of a wide-angle seismic tomographic inversion, *Geophysical Journal International*, 146 (1), 31-52, 2001.
- Ewart, A., J.M. Hergt, and J.W. Hawkins, Major element, trace element, and isotope (Pb, Sr, and Nd) geochemistry of Site 839 basalts and basaltic andesites; implications for arc volcanism, edited by W.e.a. Hawkins James, pp. 519-531, Texas A & M University, Ocean Drilling Program, College Station, TX, United States, 1994.

- Frenzel, G., R. Mühe, and P. Stoffers, Petrology of the volcanic rocks from the Lau Basin, southwest Pacific, *Geol. Jb.*, D92, 395-479, 1990.
- Ito, E., W.M. White, and C. Göpel, The O, Sr, Nd and Pb isotope geochemistry of MORB, *Chem. Geol.*, 62, 157-176, 1987.
- Jenner, G.A., P.A. Cawood, M. Rautenschlein, and W.M. White, Composition of back-arc basin volcanics, Valu Fa Ridge, Lau Basin: evidence for a slab-derived component in their mantle source, *J. Volcanol. Geotherm. Res.*, 32, 209-222, 1987.
- Loock, G., W.F. McDonough, S.L. Goldstein, and A.W. Hofmann, Isotopic compositions of volcanic glasses from the Lau Basin., *Marine Mining*, 9, 235-245, 1990.
- Mahoney, J.J., J.H. Natland, W.M. White, S.H. Poreda, S.H. Bloomer, R.L. Fisher, and A.N. Baxter, Isotopic and geochemical provinces of the western Indian Ocean spreading centers, *J. Geophys. Res.*, 94, 4033-4052, 1989.
- Mahoney, J.J., J.M. Sinton, M.D. Kurz, J.D. Macdougall, K.J. Spencer, and G.W. Lugmair, Isotope and Trace Element Characteristics of a Super-Fast Spreading Ridge: East Pacific Rise, 13-23°S, *Earth Planet. Sci. Letts.*, 121, 173-193, 1994.
- Pearce, J.A., and D.W. Peate, Tectonic implications of the composition of volcanic arc magmas, *Annu. Rev. Earth Planet. Sci. Letts.*, 23, 251-285, 1995.
- Pearce, J.A., M. Ernewein, S.H. Bloomer, L.M. Parson, B.J. Murton, and L.E. Johnson, Geochemistry of Lau basin volcanic rocks: influence of ridge segmentation and arc proximity, *Volcanism associated with extension of consuming plate margins*. In: J.L. Smellie (ed.). *Geol. Soc. Spec. Publ.*, 81, 53-75, 1995.
- Peate, D.W., T.F. Kokfelt, C.J. Hawkesworth, P.W. van Calsteren, J.M. Hergt, and J.A. Pearce, U-series Isotope Data on Lau Basin Glasses: the Role of Subduction-related Fluids during Melt Generation in Back-arc Basins, *J. of Petrol.*, 42, 1449-1470, 2001.
- Peccerillo, A., and S.R. Taylor, Geochemistry of Eocene calc-alkaline volcanic rocks from the Kastamonu area, northern Turkey, *Contrib. Mineral. Petrol.*, 58, 63-81, 1976.
- Plank, T., and C.H. Langmuir, Effects of melting regime on the composition of the oceanic crust, *J. Geophys. Res.*, 97, 19,749-19,770, 1992.
- Prinzhofer, A., E. Lewin, and C.J. Allegre, Stochastic melting of the marble cake mantle: evidence from local study of the East Pacific Rise at 12° 50'N, *Earth Planet. Sci. Letts.*, 92, 189-206, 1989.
- Taylor, B., K. Zellmer, F. Martinez, and A.M. Goodliffe, Sea-floor spreading in the Lau back-arc basin, *Earth Planet. Sci. Letts*, 144, 35-40, 1996.
- Turner, S., N.R. Hawkesworth, J. Bartlett, T. Worthington, J. Hergt, J. Pearce, and I. Smith, 238U-230Th disequilibria, magma petrogenesis, and flux rates beneath the depleted Tonga-Kermadec island arc, *Geochim. Cosmochim. Acta*, 61, 4855-4884, 1997.
- Vallier, F.T.L., G.A. Jenner, F.A. Frey, J.B. Gill, A.S. Davis, A.M. Volpe, J.W. Hawkins, J.D. Morris, P.A. Cawood, J.L. Morton, D.W. Scholl, M. Rautenschlein, W.M. White, R.W. Williams, A.J. Stevenson, and L.D. White, Subalkaline andesite from Valu Fa Ridge, a back-arc spreading center in southern Lau Basin: petrogenesis, comparative chemistry, and tectonic implications, *Chem. Geol.*, 91, 227-256, 1991.
- Vlastelic, I., D. Aslanian, L. Dosso, H. Bougault, J.L. Olivet, and L. Geli, Large-scale chemical and thermal division of the Pacific mantle, *Nature*, 399, 345-350, 1999.
- Volpe, A.M., J.D. Macdougall, and J.W. Hawkins, Lau Basin basalts (LBB): trace elements and Sr-Nd isotopic evidence for heterogeneity in backarc basin mantle, *Earth Planet. Sci. Letts.*, 90, 174-186, 1988.
- Wiedicke, M., and J.S. Collier, Morphology of the Valu Fa spreading ridge in the southern Lau Basin, *J. Geophys. Res.*, B, 98, 11,769-11,782, 1993.

The South Tonga Arc: Influence of the Subducting Louisville Ridge and Osbourn Trough on Arc Magmatism

Tim Worthington, Peter Stoffers, Christian Timm, Marc Zimmerer, Dieter Garbe-Schönberg

Institut für Geowissenschaften, Universität Kiel (tw@gpi.uni-kiel.de; pst@gpi.uni-kiel.de; ct@gpi.uni-kiel.de; zimmi.kiel@freenet.de; dgs@gpi.uni-kiel.de)

Subduction of both the plume-generated Louisville Ridge and the late Cretaceous Osbourn Trough paleo-spreading centre takes place beneath the 450 km-long South Tonga segment of the Tonga–Kermadec subduction system. The predominantly submarine South Tonga arc was previously unsurveyed and features only 1 volcanic island (Ata). Surveying and sampling during cruise SO 167 of the FS *SONNE* revealed a continuous volcanic front, 10–15 km wide, comprising 27 semi-regularly spaced active stratovolcanoes typically with basal diameters of 10–25 km and heights of 1–2 km. The volcanic front is disturbed only in the vicinity of Ata, where 10 major edifices and numerous smaller constructs extend the width of the front to 50 km. This greater width reflects a transient 40 km westward migration of the front and enhanced constructional volcanism as the Louisville Ridge dehydrates and passes under the arc.

The South Tonga arc volcanoes show considerably more geochemical and isotopic variation than the better-known subaerial Central Tonga volcanoes. High-Mg basalt, andesite, and rhyodacite associated with calderas (often > 6 km in diameter) are common. Overall, these lavas define a low-K suite with strong enrichment in the fluid-mobile elements and extreme depletion in the fluid-immobile elements relative to MORB [e.g., $(La/Yb)_N < 1.1$; Nb/Yb 0.09–0.27]. Specific incompatible element ratios distinguish some volcanoes and are randomly distributed along the arc segment. These characteristics are long-lived, and best explained by interaction of ascending magma with sub-arc lithosphere in a volcano-specific manner. They provide support to models invoking significant lithospheric processing of magma in oceanic settings.

Passage of the Louisville Ridge beneath the arc is associated with the eruption of lavas with $(La/Yb)_N > 1.1$, higher Th/U, and other anomalies prior to and during the westward migration of the volcanic front. In contrast, lavas erupted during the eastward return of the front have relatively normal South Tonga compositions, suggesting rapid flushing of ridge-derived fluids from the sub-arc mantle. Volcanoes that overlie the subducting Osbourn Trough at 23.5–24.7°S exhibit a marked change in caldera-style to diatreme-like craters up to 1.1 km-deep. Associated changes in magmatic volatile content driving these eruptions probably reflect dehydration of mantle extensively serpentinised when spreading stalled at the Osbourn Trough.

This project was funded by the BMBF, grant 03G0167A.

Hf-Nd Isotope Characterization of the Tonga–Kermadec Sub-Arc Mantle

Tim J. Worthington¹, Carsten Münker², Peter Stoffers¹, John A. Gamble³, Ian C. Wright⁴

¹ Institut für Geowissenschaften, Universität Kiel, Olshausenstr. 40, D-24118 Kiel, Germany (tw@gpi.uni-kiel.de; pst@gpi.uni-kiel.de)

² Institut für Mineralogie, Universität Münster, Corrensstr. 24, D-48149, Münster, Germany (muenker@nwz.uni-muenster.de)

³ Dept. of Geology, National University of Ireland, University College, Cork, Ireland (j.gamble@ucc.ie)

⁴ National Institute for Water and Atmospheric Research, PO Box 14-901, Wellington, New Zealand (i.wright@niwa.cri.nz)

Subduction-related magmatism involves fluxing of the mantle wedge by a slab-derived fluid and/or melt. Uncertainty surrounds the thermal, physical and chemical state of the slab and slab-wedge interface beneath the volcanic front, creating doubt over the application of experimental data on slab dehydration and melting to models of magma genesis and mass balance. Constraining the composition of the wedge should provide an important control on such models. However, simple models of wedge convection from the backarc to sub-arc environment are clearly incomplete (e.g. do not explain the lack of correlation between depletion of the sub-arc mantle and either backarc width or extension rate). To investigate the dynamics of wedge convection, we undertook Hf-Nd isotope determinations for lavas spanning most of the Tonga–Kermadec arc. Advantages of these elements include their fluid-immobile character (Hf strongly, Nd moderately) relative to the highly mobile, and thus predominantly slab-derived, Sr and Pb. Previous Sr-Nd-Pb isotope studies of backarc Lau Basin lavas revealed that Indian MORB mantle (IMM) replaced Pacific MORB mantle (PMM) during basin opening, and that IMM underlies the central Tonga arc. In contrast, the backarc mantle south of Valu Fa Ridge and under the Havre Trough remains PMM. Thus, a transition from IMM to PMM was anticipated beneath the south Tonga arc.

Hf isotope compositions of the Tonga–Kermadec arc lavas range from +12 to +16 ϵ -units and are 1-2 ϵ Hf units below those of the Lau Basin spreading centres. Tonga lavas are generally in the upper part of this range, whereas Kermadec lavas are more varied. All Tonga–Kermadec lavas plot within the IMM field in ϵ Hf vs ϵ Nd-space, indicating IMM-like mantle is under the entire arc from 15–35 °S. This result is further enhanced by subtracting the ~20–40 % Nd added from the subducting slab (PMM-composition). ϵ Hf exhibits a mild negative correlation with Hf/Yb and increasing latitude, consistent with a minor Hf contribution from subducting volcanogenic sediment in the Kermadec arc sector. Our data provide no evidence for a slab melt, even in the southern Kermadecs where the slab is warmer due to slow subduction. The occurrence of IMM beneath the Tonga–Kermadec arc, but PMM below the southern Lau Basin–Havre Trough, is inconsistent with simple models invoking progressive southeastward migration of IMM into the Tonga–Kermadec system accompanying the opening of the Lau–Havre backarc basin. Instead, considerably complexity is required in the geometry of the IMM–PMM interface, the sub-arc wedge flow, or the origin of the IMM-like signature.

This project was funded by the BMBF, grant 03G0167A.

Shallow submarine hydrothermal activity in the Tonga island arc, SW-Pacific

Schwarz-Schampera, Ulrich¹; Stoffers, Peter²
¹BGR, ²C.-A.-U. Kiel

Three active sites (Efuefu, Mutu'a nutu, Uli'uli) of shallow submarine hydrothermal systems were discovered in 2002 during R/V Sonne cruise SO-167 and revisited with the submersible Pisces in 2005. The sites are associated with recently active andesitic and dacitic arc volcanoes. Setting, lithologies, volcanic textures, and water depths indicate that very shallow submarine pyroclastic eruptions (water depths of <1000 m up to 200 m) played a significant role in the formation of the arc volcanoes. The most extensive and strongest mineralization occurs at the Efuefu site offcoast Tongatapu. The host volcano is approximately 10 x 6 km in diameter, with a 5 x 3 km central caldera containing two young volcanoclastic cinder cones. Acid-sulfate and argillic alteration, and chalcopyrite-hematite and pyrite-magnetite mineralization with traces of native gold, arsenopyrite, stibnite, realgar and iss are associated with the cone and the southwestern and northern caldera walls. The Uli'uli site occurs at the southernmost Tonga arc volcano. The 13 by 15 km edifice is characterized by a large NW-SE elongated central caldera. Hydrothermal precipitates were collected from a cone in the center of the caldera at water depths of 600 to 450 m. The basaltic andesites show pronounced advanced argillic and silica alteration; mineralization includes disseminated but pervasive pyrite-marcasite. The volcano Mutu'a nutu exhibits a spectacular central crater two kilometers in diameter, interpreted as a product of major dacitic pyroclastic eruptions. Andesitic volcanoclastic rocks and younger pumiceous dacite are both affected by pyrite-chalcopyrite mineralization and a wide range of propylitic, argillic, and silica alteration. All three sites show sulfur isotope signatures that are different from regular seawater-dominated hydrothermal systems but are regarded characteristic for the introduction of magmatic SO₂. Isotope fractionation suggests equilibrium conditions and formation temperatures can be calculated in the range between 280° and 390°C. Alteration and mineralization of the new hydrothermal sites show many characteristics that are typical of shallow submarine hydrothermal vent fields such as in the Kermadec and Izu-Bonin arcs, but also of subaerial, epithermal-style Au deposits.